Materials for depollution based on the model of manganese dioxygenases

Jérémy Chaignon

THÈSE

en vue de l'obtention du grade de

Docteur de l'Université de Lyon, délivré par l'École Normale Supérieure de Lyon en cotutelle avec la Universitat de València

Discipline : Chimie

Laboratoire de Chimie de l'ENS de Lyon / ICMol, Universitat de València

École Doctorale de Chimie

présentée et soutenue publiquement le 20 décembre 2013

par Monsieur Jérémy CHAIGNON

Materials for depollution based on the model of manganese dioxygenases

---

Directrices de thèse : *Mme Belén ALBELA et Mme Isabel CASTRO*

Après l'avis de : *Mme Teresa BLASCO LANZUELA*

Mme Rosa LLUSAR BARELES

Devant la commission d'examen formée de :

Mme Belén ALBELA, Membre/Directrice, ENS de Lyon

Mme Teresa BLASCO LANZUELA, Membre/Rapportrice, Universidad Politécnica de Valencia

M. Laurent BONNEVIOT, Membre, ENS de Lyon

Mme Isabel CASTRO, Membre/Directrice, Universitat de València

M. Miguel JULVE OLCINA, Membre, Universitat de València

M. Francisco LLORET PASTOR, Membre, Universitat de València

Mme Rosa LLUSAR BARELES, Membre/Rapportrice, Universidad Jaume I de Castellon

Summary

Intensive use of pesticides led to an excess of polluting molecules in water and soil. These molecules requires expensive treatments to be degraded, therefore cheaper alternative solutions are of interest. In the case of catechol derivatives, some enzymes called catechol dioxygenase perform an oxidative cleavage of the aromatic ring using O_2 as oxidant. The mild conditions and the large availability of the oxidant make these enzymes a clever solution in such depollution issues.

This work aims at providing mimics of a particular kind of dioxygenase enzymes, the manganese-dependent dioxygenases. Given that both first and second coordination spheres plays an important role in enzymes, our model must consider these two aspects.

The active site is modelled by a manganese(II) complex that imitates the direct metal ion environment in the enzyme. The second coordination sphere is mimicked by incorporating these complexes inside a functionalized mesoporous silica. Then mesoporosity recreates the confinement present in the enzyme while side functions can play the role of the stabilizing enzymatic amino acids.

Chapter I

This chapter relates the synthesis and characterization of manganese(II) complexes. First, ligands were designed in such a way that complexation with metal ions and grafting on material would not interfere. Second, manganese(II) complexes were synthesized. The first two crystals we obtained with manganese(II) led us to investigate in two directions:

- The synthesis of mononuclear species, which would be closer to the actual enzymatic site.
- The synthesis of bridged dinuclear species, in order to study the evolution of the interaction between the two manganese(II) ions upon changes in the nature of the bridge or in the ligand.

In total, four dinuclear complexes were obtained with chloride, bromide or azide bridges. Chloride-bridged complex exhibited a weak antiferromagnetic behaviour at low temperature, whereas a ferromagnetic coupling was observed in the three others. Comparing the value of coupling J in the azido-bridged species with other similar species described in the literature allowed us to link this magnetic parameter with structural ones such as the Mn-X-Mn angle (where X is the bridging atom) and the Mn-Mn distance.

The EPR study in both solid and liquid states led us to conclude that although these complexes crystalize as a dinuclear unit, manganese centres do not interact anymore when dissolved.

Chapter II

This chapter compares two synthetic ways of LUS mesoporous silica with conventional and microwave ovens. Microwave synthesis is then optimized to provide mesoporous materials in a shorter time with a good porosity. The total synthesis time was reduced from one day to a couple of hours using the microwave irradiation. More important, characterizations of those materials showed that mesoporous properties are maintained through the process, *i.e.*, the final materials possess similar pore sizes (between 3 and 4 nm), porous volumes (between 0.7 and 0.9 $cm^3.g^{-1}$) and specific surface areas (900 to 1000 $m^2.g^{-1}$).

A maximal temperature of 190 °C, impossible to reach without damaging the surfactant in classical syntheses, was reached with microwave oven. Furthermore, increasing the temperature in both protocols enlightened different behaviours:

- In the classical synthesis, the pores tend to enlarge upon such increase, the porous volume remains quasi-unchanged, and the specific surface area drops.
- In microwave synthesis, porous volume and surface area follow the same trend: a decrease between 130 °C and 170 °C followed by an increase until 180 °C and stabilization at 190 °C. Hence increasing temperature has not the same effect than for classical syntheses which was interpreted by both purely thermal and heating homogeneity effects.

We showed that microwave irradiation is a method that allows synthesis of mesoporous silica in much shorter time with a better homogeneity of the final material. The effects of thermal agitation become much less visible compared to the condensation speed ones.

Chapter III

This last chapter details the design of host materials to support the manganese(II) complexes synthesized in the first chapter. Mesoporous LUS silica synthesized at 180 °C using microwave irradiation described in chapter II were functionalized using the Molecular-Stencil Patterning (MSP) strategy. Host materials synthesized in this study were separated in two families, whether they contain a tethering azide function and a simple spacing function (trimethylsilyl) or a tethering azide function and a coordinating spacing function (pyridine). X-ray powder diffraction allowed controlling the integrity of the porous structure.

Huisgen copper-catalyzed cycloaddition was adapted to the grating of complexes into the pores of these silica hosts. Tris(triphenylphosphine) copper bromide was employed as catalyst for this ultimate grafting step, providing solids with an average manganese content of 2 wt%.. EPR study showed that isolated manganese(II) species were indeed present in the final material, and nitrogen sorption isotherm demonstrated that the complexes were inside the pores and that there was enough remaining porous volume to allow catalytic reactions inside the mesopores of the solid.

Catalytic reactions were then carried out using some free complexes as catalyst and 4-*ter*-butylcatechol (4-TBC) and 3,5-di-*ter*-butylcatechol (3,5-DTBC) as substrates. The complexes exhibit an oxidase activity, contrary to the dioxygenase one in the enzyme: the substrate is oxidized from alcohol to ketone without incorporation of oxygen atoms from dioxygen. However, these catalysts are thus relatively specific compared to other model catalysts described in literature. Oxidation of 4-TBC with supported complexes only provided the *o*-quinone. While the free catalysts also provided some by-products, this is no longer the case as supported complexes exclusively oxidize the catechol to its quinone form.

Resumen

La utilización intensiva de pesticidas ha traído consigo la presencia de una gran cantidad de moléculas contaminantes en aguas y suelos. Los tratamientos para degradar estas moléculas son caros, por lo que es de gran interés la búsqueda de soluciones más baratas. En el caso de los catecoles, existen enzimas, las catecol-dioxigenasas, que abren el ciclo aromático por oxidación con dioxígeno. Las condiciones suaves y la gran disponibilidad de este oxidante podrían ofrecer una solución para esos problemas de polución.

El objetivo de este trabajo de tesis es mimetizar un tipo particular de dioxigenasa, la dioxigenasa de manganeso. Dado que tanto la primera esfera de coordinación como la segunda juegan un papel en la reacción enzimática, el modelo tiene que considerar estos dos aspectos.

El sitio activo se modeliza mediante un complejo de manganeso(II) que imita el entorno directo del metal en la enzima. La segunda esfera de coordinación se mimetiza mediante la incorporación de los complejos en sílices mesoporosas funcionalizadas. Éstas recrean el confinamiento presente en la enzima, mientras que los sustituyentes pueden estabilizar los intermedios de la misma manera que los amino ácidos enzimáticos.

Capitulo I

Este capitulo describe la síntesis y la caracterización de los complejos de manganeso(II). En primer lugar, se han diseñado y caracterizado los ligandos para que no haya interferencias entre la complejación con el ion metálico y el anclaje en la sílice. A continuación, se procedió a la síntesis de los complejos. Los dos primeros cristales obtenidos nos hicieron investigar en dos direcciones:

- La síntesis de complejos mononucleares, ya que éstos pueden ser mejores modelos del sitio activo que los dinucleares.
- La síntesis de otros complejos dinucleares con objeto de estudiar la interacción entre los dos iones manganeso(II) bajo diferentes ligandos puente o ligandos terminales.

En total, se han cristalizado cuatro complejos dinucleares, con cloruro, bromuro o azida. Los complejos con ligandos puente cloro presentan un comportamiento antiferromagnético a baja temperatura mientras que en el resto se observa acoplamiento ferromagnético. En el caso de los compuestos con ligando azida puente, se ha podido establecer, junto con otros valores del acoplamiento magnético J encontrados en la literatura, una relación entre este parámetro magnético y los parámetros estructurales.

El estudio EPR del solido y de una disolución de complejos dinucleares nos permitió concluir que los puentes se destruyen al disolver el complejo.

Capitulo II

En este capítulo se compara la síntesis de sílices mesoporosas LUS clásicas con las sintetizadas con microondas. Hemos optimizado la síntesis con microondas para obtener un material mesoporoso de calidad en un tiempo de síntesis más corto. El tiempo de síntesis ha sido reducido desde un día hasta un par de horas. Más aún, la caracterización de estos materiales ha demostrado que las propiedades mesoporosas se mantienen, es decir, que el material final posee poros de dimensión (3-4 nm) y volumen (0.7-0.9 $cm^3.g^{-1}$) comparables, así como superficies porosas similares (900-1000 $m^2.g^{-1}$). Se puede alcanzar una temperatura máxima de 190 °C en la síntesis con microondas, mientras que esta temperatura degrada el tensoactivo en la síntesis clásica. Además, el aumento de temperatura muestra diferentes comportamientos:

- En la síntesis clásica, los poros se agrandan con la temperatura, el volumen permanece constante y la superficie disminuye.
- En la síntesis con microondas, el volumen de poro y la superficie siguen la misma tendencia: una disminución entre 130 y 170 °C seguido por un aumento hasta 180 °C y estabilización a 190 °C. Por lo tanto, el aumento de temperatura no tiene el mismo efecto que para la síntesis clásica. Esa diferencia de comportamiento fue interpretada por efectos térmicos y por cambios en la homogeneidad de la calefacción.

Demostramos que la síntesis por microondas permite obtener sílices mesoporosas mucho más rápidamente y con una mejor homogeneidad del material. Los efectos de la agitación térmica son mucho menos importantes que los de la velocidad de condensación.

Capitulo III

En este último capítulo se detalla el diseño de materiales que soportarán los compuestos sintetizados en el primer capitulo. La sílice LUs mesoporosa sintetizada con microondas a 180 °C descrita en el capítulo II, se ha funcionalizado usando la estrategia de Molecular-Stencil Patterning (MSP). Esos materiales se dividen en dos familias: los que contienen una función de anclaje azida y una simple función espaciadora (trimetilsilano) y los que contienen una función de anclaje azida así como una función espaciadora coordinante (piridina). La difracción de rayos X en polvo nos permitió controlar la calidad de la estructura porosa.

La cicloadición de Huisgen catalizada con cobre(I) ha sido adaptada para el anclaje de los complejos en las sílices funcionalizadas. Se ha utilizado $CuBr(PPh_3)_3$ como catalizador para esta última etapa de anclaje, obteniéndose materiales con un contenido medio en manganeso del 2 % en peso. El estudio EPR ha mostrado que en el material final estaban presentes especies aisladas de manganeso(II) y la adsorción de N_2 que los compuestos de manganeso(II) estaban dentro de los poros y que el volumen poroso restante es suficiente para permitir la catálisis dentro del sólido mesoporoso.

Las reacciones catalíticas se llevaron a cabo con complejos de manganeso(II) libres como catalizadores y con 4-*ter*-butilcatecol (4-TBC) así como 3,5-di-*ter*-butilcatecol (3,5-DTBC) como substratos. Los compuestos de manganeso(II) se comportan como oxidasas, al contrario que la actividad dioxigenasa del enzima: el substrato es oxidado desde alcohol hasta cetona sin incorporación de átomos de oxigeno del dioxígeno. Sin embargo, estos catalizadores son relativamente específicos comparados con otros encontrados en la literatura. La oxidación del 4-TBC con el complejo soportado produce la *o*-quinona sin otros subproductos como era el caso con los complejos libres.

Résumé

L'utilisation intensive de pesticides a conduit à un excès de molécules polluantes dans les eaux et les sols. L'élimination de ces molécules requérant des traitements couteux, il est intéressant de développer des alternatives bon marché. Dans le cas des dérivés du catéchol, des enzymes appelées catéchol-dioxygénases effectuent le clivage du cycle aromatique en utilisant O_2 comme oxydant. Les conditions douces et la disponibilité de l'oxydant font de ces enzymes des solutions élégantes dans le cas de ces problèmes de dépollution.

Ce travail a pour objectif de mimer un type particulier de dioxygénases, appelées manganese-dependent dioxygenases. Etant donné que les premières et secondes sphères de coordination jouent un rôle important dans l'enzyme, notre modèle se doit se considérer ces deux aspects.

Le site actif est modélisé par un complex de manganèse(II) qui imite l'environnement direct du métal dans l'enzyme. La seconde sphère de coordination est mimée en incorporant ces complexes au sein d'une silice mésoporeuse fonctionnalisée. La mésoporosité recréé le confinement présent dans l'enzyme et les fonctions auxiliaires peuvent jouer le rôle stabilisant qui incombe aux acides aminés enzymatiques.

Chapitre I

Ce chapitre retrace la synthèse et la caractérisation de complexes de manganèse(II). Tout d'abord, les ligands ont été dessinés afin que la complexation et le greffage sur silice n'interfèrent pas. Ensuite, les complexes de manganese(II) ont été synthétisés. Les deux premiers cristaux obtenus nous ont poussé à travailler dans deux directions:

- La synthèse d'espèces mononucléaires, qui seraient des modèles plus proches du site actif.
- La synthèse d'espèces dinucléaires pontées, afin d'étudier l'évolution de l'interaction entre deux manganèse(II) en fonction de la nature des ponts et du ligand.

Au total, quatre complexes dinucléaires ont été obtenus, avec des ponts chlorure, bromure ou azoture. Les complexes contenant les chlorures ont un comportement antiferromagnétique, alors qu'un couplage ferromagnétique est observé dans les autres complexes. En comparant les valeurs du couplage J des complexes à pont azotures avec d'autres complexes similaires de la littérature, nous avons pu relier ce paramètre magnétique avec des paramètres structuraux.

L'étude RPE des états solide et liquide nous ont permis de conclure quant à la disparition des ponts après dissolution, étant donné qu'il n'y a plus d'interaction entre centres métalliques en solution.

Chapitre II

Ce chapitre compare deux méthodes de synthèse de silice mésoporeuse LUS avec des fours conventionnels ou micro-onde. La synthèse micro-onde a été optimisée pour fournir un matériaux mésoporeux dans un temps plus court et possédant une bonne porosité. Le temps de synthèse total a été réduit d'un jour à deux heures grâce aux micro-ondes. Plus important, la caractérisation de ces matériaux a montré le maintien des propriétés poreuses avec des matériaux synthétisés possédant des tailles de pores (entre 3 et 4 nm), des volumes poreux (entre 0.7 et 0.9 $cm^3.g^{-1}$) et des surfaces spécifiques (entre 900 et 1000 $m^2.g^{-1}$) similaires

Une température maximale de 190 °C, impossible à atteindre sans endommager le surfactant dans les synthèses classiques, a été utilisée dans les fours micro-onde. L'augmentation de température démontre deux comportements différents:

- Dans les synthèses classiques, les pores ont tendance à grossir lorsque la température augmente, le volume poreux ne change pas et la surface spécifique chute.
- Dans les synthèses micro-onde, le volume poreux et la surface suivent les mêmes tendances que précédemment jusqu'à 170 °C, avant d'augmenter à 180 et 190 °C. Ainsi l'augmentation de température n'a pas le même effet en synthèse classique qu'en synthèse micro-onde, ce qui a été interprété par des effets à la fois thermiques et d'homogénéité de chauffage.

Nous avons montré que le chauffage micro-onde est une méthode qui permet la synthèse de silices mésoporeuses dans des temps bien plus courts avec une meilleure homogénéité du matériau final. Les effets thermiques sont beaucoup moins visibles comparés aux effets de vitesse de condensation.

Chapitre III

Ce dernier chapitre détaille le développement de matériaux hôtes pour le support des complexes synthétisés précédemment. Une silice mésoporeuse LUS synthétisée à 180 °C a été functionalizsée en utilisant la stratégie de pochoir moléculaire (Molecular-Stencil Patterning). Les matériaux hotes ont été séparés en deux familles, selon qu'ils contiennent une fonction d'ancrage azoture et une fonction simplement espaçante (trimethylsilyl), ou bien qu'ils

contiennent une fonction d'ancrage azoture et une fonction espaçante (pyridine) et coordinante. La diffraction de rayons X sur poudre nous a permis de controler l'intégrité de la mesoporosité.

La cycloaddition de Huisgen a été adaptée au greffage de complexes au sein des pores de ces silices. $CuBr(PPh_3)_3$ a été utilisé comme catalyseur pour la dernière étape de greffage, fournissant des solides avec une charge de manganèse de 2 % en masse. L'étude RPE montre que des espèces isolées manganèse(II) sont présentes, et l'adsorption d'azote a démontré qu'il restait assez de volume poreux pour effectuer la catalyse.

Les réactions catalytiques ont été effectuées en utilisant les complexes libres comme catalyseurs, et le 4-*ter*-butylcatéchol (4-TBC) et le 3,5-di-*ter*-butylcatéchol (3,5-DTBC) comme substrats. Les complexes ont une activité oxydase, contrairement à l'activité dioxygénase de l'enzyme: l'alcool est oxydé en cétone sans incorporation d'atomes d'oxygène. Ces catalyseurs sont cependant relativement plus spécifiques que d'autres exemples reportés dans la littérature. L'oxydation du 4-TBC par les catalyseurs supportés n'a conduit qu'au dérivé o-quinone. Cependant, alors que les catalyseurs libres créaient des sous-produits, ce n'est plus le cas avec ces complexes supportés, qui oxydent exclusivement le substrat en quinone.

Acknowledgement

Un peu de repos maintenant, les derniers mots de cette thèse seront écrits en français. Je voudrais tout d'abord remercier mes directrices de thèse, Belén et Isabel, pour m'avoir supporté/encadré pendant ces 3 ans…et quelques. Belén, c'est grâce à toi que cette cotutelle a pu être démarrée, je te dois beaucoup. Isabel, merci pour ta patience, ton aide précieuse dedans et en dehors du laboratoire, et désolé de t'avoir causé tant de soucis à certains moment. Evidemment je ne peux pas oublier Laurent, qui, en plus de servir de relai en attendant une HDR espagnole, m'a formé à la recherche pendant toutes ces années.

Je tiens également à remercier ma famille, mes parents Pierre et Nadine (referred as Papa and Maman in the rest of the manuscript), et ma sœur Sandrine, là encore pour m'avoir supporté, encouragé, et pour leur patience durant ces trois années…et quelques.

Un merci spécial à Halima, qui aura elle aussi été très patiente, j'adore ta gestion des bourses de mobilité, j'esaierai de ne pas me comporter comme les thésards littéraires qui ne connaissent plus personne quand ils sont docteurs !

Merci aussi au laboratoire espagnol de Valencia, en vrac merci à Jesus (siempre nos quedará Grenoble, y ya sabes quien va a lluitar), Maria (loca), Julia (aún más loca), Fran (los pelirojos si que tienen alma al final) y Thais (una buena sorpresa encontrarte). Merci aux permanents aussi, Joan, pour la théorie de tout et le calme impressionant, Miguel et Paco, les sages du magnétisme, Salah pour l'aide en chimie organique, et Rafa, pour les couscous du vendredi midi/après-midi. Merci à Emilio, qui me fait apprécier de plus en plus les victoires sportives françaises.

Merci au laboratoire français également, Lin et Yuting pour les plats chinois et l'aide précieuse à des moments où j'en avais vraiment besoin, Younes pour le stage de M2 où j'étais ton padawan, et enfin Hanène et Sonia pour m'apprendre l'arabe petit à petit. Merci aussi à Nathalie pour l'aide en DRX.

Bien entendu un grand merci aux gens qui m'ont aidé pour les résultats expérimentaux, Sandrine pour la RMN (et les nombreuses soirées aussi remarque), Xelo et Guillaume pour la cristallographie, un énorme merci à Fabienne pour la catalyse, un tout petit merci à Marie aussi, à qui j'ai du mentir en prétendant que je devais repartir en Espagne au bout de deux semaines de stages, je n'en pouvais plus. Merci à Pascal Perriat pour la microscopie, et enfin Lhoussain pour la RPE et les discussions de repas de Noël !

Finalement, même si la science c'est bien, la vie sociale c'est mieux, merci à tous les gens rencontrés durant ces trois ans…et quelque. En vrac, sans aucune logique, merci à Aline

et Laure-Lise, qui me connaissent depuis les débuts, merci à Edouard, Sophie et Jérémy, LA FAMILLE QUOI, merci à Saralafolle, qui a de très bons gouts en matière de tee-shirts, merci aussi à Kevin et Anne-Gaëlle, pour les soirées chez Kévin, et accessoirement pour toute l'aide administrative, merci à Delphine pour savoir quand je suis sérieux et quand je le suis pas (indice: je suis tout le temps sérieux), à Benjamin pour les rappels charlotte, merci à Simon, Marie et Marion qui m'ont fait passer des nuits blanches à des moments où je n'en avais absolument pas besoin, merci à Léa, Pepe, Gloria, Alessia pour la colocation espagnole, merci à Hoëlle pour les soirées "vas-y on va boire un verre j'en ai trop marre", Mélanie pour les moments culture, Lucia pour ces rhums arrangés qui passent crème, Yoan et Flo pour les moments moins culture, et Alex et Mauri pour les terrasses valenciennes.

J'en oublie surement, j'en suis désolé, merci à vous aussi, vous-même vous savez (genre !).

List of abbreviations

3,5-DTBC	3,5-Di-*Tert*-ButylCatechol
4-TBC	4-*Tert*-ButylCatechol
A	4-*tert*-butyl-5-methoxy-*o*-quinone
B	4-*tert*-butyl-2-hydroxy-4,5-dimethoxycyclohexa-2,5-dienone
BdB	Broekhoff and De Boer
BET	Brunauer-Emmett-Teller
BJH	Barrett-Joyner-Halenda
C	3,5-di-*tert*-butyl-*o*-quinone
C1	$[Mn_2(\mu\text{-}Cl)_2(Cl)_2(L^1)_2]$
C2	$[Mn_2(\mu\text{-}Br)_2(Br)_2(L^1)_2]$
C3	$[Mn_2(\mu\text{-}N_3)_2(N_3)_2(L^1)_2]\cdot 2CH_3OH$
C4	$[Mn_2(\mu\text{-}N_3)_2(N_3)_2(L^2)_2]$
C5	$[Mn(NO_3)(H_2O)_2L^1]\ NO_3$
C6	$[MnCl_2L^2]$
C7	$[Mn(H_2O)_3L^1]\cdot(BPh_4)_2$
C8	$[Mn(H_2O)_3L^3]\cdot(BPh_4)_2$
cmc	critical micelle concentration
CP/MAS	Cross Polarization/Magic Angle Spinning
CTA^+	CetylTrimethylAmmonium
DDT	DichloroDiphenylTrichloroethane
EG	Ethylene Glycol
EPR	Electron Paramagnetic Resonance
EXAFS	Extended X-Ray Absorption Fine Structure
HK	Horvath Kawazoe
HMDS	HexaMethylDiSilazane
HPDEC	High Power Decoupled
IR	InfraRed
L^1	*N*,*N*-bis((pyridin-2-yl)methyl)prop-2-yn-1-amine
L^2	*N*-((1-methyl-1H-imidazol-2-yl)methyl)-*N*-(pyridin-2-ylmethyl)prop-2-yn-1-amine
L^3	2-(prop-2-ynyl(pyridin-2-ylmethyl)amino)acetate
LUS	Laval University Silica
MCM	Mobil Composition of Matter
MndD	Manganese-dependent Dioxygenases
MSP	Molecular Stencil Patterning
MW	Microwave
NMR	Nuclear Magnetic Resonance
OECD	Organisation for Economic Co-operation and Development
PMOS	Periodic Mesoporous OrganoSilicas
SBA	Santa-BArbara silica

SEM	Scanning Electronic Microscopy
SOD	SuperOxide Dismutase
SOMC	Surface Organo Metallic Chemistry
STP	Standard Temperature and Pressure
TEM	Transmission Electron Microscopy
TGA	ThermoGravimetric Analysis
TMA^+	TetraMethylAmmonium
TMS	TriMethylSilyl
Tos	Tosylate
TPA	Tris(2-Pyridylmethyl)Amine
SQUID	Superconducting Quantum Interference Device
XRD	X-Ray Diffraction

Contents

Introduction

The use of chemicals agents against pests finds its roots in the earlier classical Antiquity. Back then, sulphur and arsenic were already used for crop protection as insecticides. During Middle Age, plants such as aconites were employed and reported in treatises such as Maimonides' "*Treatise on poisons and their antidotes"* around the 12th century.[1, 2] In Europe, taking advantage of natural pesticides continued later during 17th century with the introduction of tobacco and more particularly nicotine.[3] Although well known in Asia, equatorial Africa and Amazonia, naturally extracted rotenone and pyrethrum appeared later in Europe during the 19th century.[4]

This was also the century of the development of mineral chemistry, leading to new inorganic pesticides, especially copper-based ones. For instance, the Bordeaux mixture spilled over vineyards as a fungicide was composed of copper sulphate and slaked lime.[5] In the early 20th century, sowings were treated with mercury salts. Although soil pollution was observed in both cases, only mercury salts were prohibited in OECD (Organisation for Economic Co-operation and Development) countries in 1991.[6]

The development of inorganic chemistry and the rise of organic chemistry in the 30's combined with better knowledge on chemical weapons after World War I led to the emergence of new kinds of pesticides. One of the most famous, DDT (DichloroDiphenylTrichloroethane, Figure 1), opened the way to the organochlorinated family. Though it had been synthesized by Zeidler in 1874, its insecticide properties were only discovered in 1939 by Müller, bringing him the Nobel Prize in 1948.[7] During World War II, researches on combat gas brought organophosphorus compounds such as malathion (Figure 2). After those first synthetic families of pesticides, other kinds of molecules successively appeared. Amongst them, substituted ureas like linuron or diuron were developed around 1950 in the U.S. along with quaternary ammoniums or triazines.[8] Two decades later, new insecticides called pyrethroids appeared, inspired from the pyrethrin chemical structure (Figure 3). This family of pesticides is now one of the most employed for household utilization, as these compounds are found in pesticides such as Raid or Baygon.[9]

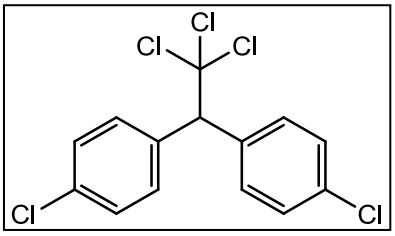

Figure 1: DDT.

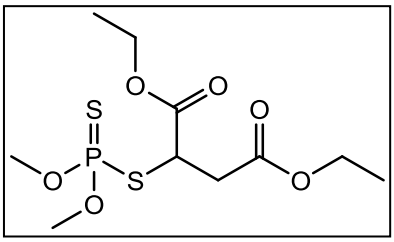

Figure 2: Malathion.

Nowadays, a large number of pesticides used in crops contain halogens such as chloride or bromide. Pentachlorophenol, diuron, chlorpyrifos are a small sample of what is currently employed in fields. Through pesticide treatments, crop yields have undeniably

increased by eliminating funguses, insects or weeds. However, those molecules revealed themselves as a problem because of their very nature. Indeed, their toxicity towards pests may also cause severe intoxications to human being. In addition, the persistence of pesticides in soils is worsened by its uses in excess in crops or private gardens. [10, 11] Soil contamination led to water contamination, affecting the whole chain of alimentation. [12] As a response to those problems, the Stockholm Convention on Persistent Organic Pollutants signed in 2001 restricted or prohibited the use of compounds such as DDT, due to their effects on environment and human health. Along with pesticides, pharmaceutical active molecules such as hormones were also classified as pollutants of used water and recognized as detrimental to health and environment.

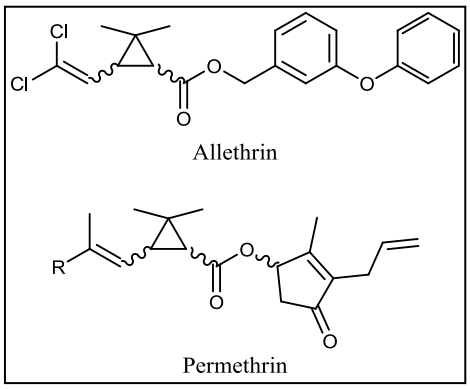

Figure 3: Two pyrethroids found in commercial insecticides

In water-treatment plants, the elimination of these organic molecules requires expensive treatments based on total oxidation such as chlorination, ozonation or membrane filtration. [13, 14, 15] These methods are not selective and not fully effective. [16] In France, the AMPERES project carried on between 2006 and 2007 revealed that 30 % of targeted species are still present in water after treatment, a proportion that can rise up to 90 % in the case of some pharmaceutical compounds. [17]

To overcome the limitation of the actual processes, new kind of treatments must be developed. Instead of using heavy and expensive methods such as strong oxidation, softer methods could appear at once cheaper and even more effective. In that matter, Mother Nature has proven to be an inspiring source. In particular, a class of protein called enzymes can perform a large number of chemical conversions under physiological, thus mild, conditions. In other words, enzymes are biocatalysts with high selectivity and yield.

This difficulty of elimination is not trivial: in particular, though some of them are biodegradable, most of halogenated compounds revealed themselves extremely persistent. [18] Actually, most of these organic molecules find their source in the human production and cannot be found naturally, hence their recalcitrance to microbial degradation. [19, 20, 21] However, even in only a few decades, microbes have evolved to perform their degradation. [22] Though those pollutants are reluctant to be degraded in water-treatment plants, they can be metabolized by microorganisms by following two pathways where dehalogenation plays a key role. The first one consists in the early removal of the halogen atom from the aromatic cycle

(Scheme 1),[23] while the second begins with the ring aperture which is then followed by a dehalogenation. [22] In both cases, many examples can be found where intermediates are catechol derivatives.

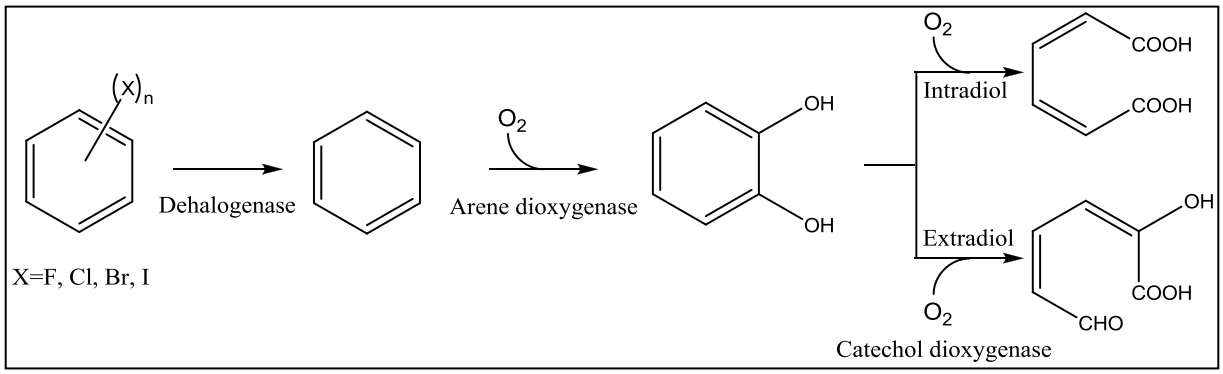

Scheme 1: Natural degradation of halogenated aromatic rings.

In the first case, halogens are removed from the ring by dehalogenase enzymes. Most of the time, those enzymes operate a reductive biological process to remove the halogen atoms. [22] After the aromatic ring has lost all its halogens the arene ring undergoes the action of another family of enzymes called arene dioxygenases. [24, 25, 26] This latter uses dioxygen as oxidant to *cis*-dihydroxylate the aromatic ring yielding catechol moieties. This moiety acts as a chelating ligand into the coordination sphere of the metal ion contained in the last family of enzymes where it is finally degraded by ring aperture. These metalloenzymes are called catechol dioxygenases. [27, 28]

Both arene dioxygenases and catechol dioxygenases are metalloenzymes that use molecular dioxygen as oxidant agent. Whereas the metallic centre of arene dioxygenases is often composed by a ferredoxin, [24, 25] catechol dioxygenases can host either iron or manganese metal ions. This difference of metal ion monitors the enzyme reactivity: an intradiol catechol cleavage will be observed with Fe(III) while an extradiol cleavage is carried out with Fe(II), Mn(II) or more rarely with Mg(II). [29, 30, 31, 32, 33]

Though iron-dependent dioxygenases are known since the middle 50's, [34] manganese-dependent dioxygenases (MndD) were only discovered in 1981. [35] Crystallographic structure of homoprotocatechuate 2,3-dioxygenases, a kind of catechol dioxygenase, was not available until 2004 (Figure 4). [36, 37] In this particular metalloenzyme as well as in other dioxygenases, a recurrent metal coordination was noticed, composed by two histidines and one carboxylic acid, either from glutamate or aspartate. [38] This spread structural motif, called the 2-His-1-carboxylate facial triad, manifests versatility toward dioxygen activation in various metalloproteins such as catechol dioxygenases, Rieske dioxygenases, α-ketoglutarate dependent enzymes, pterin dependent hydroxylases or other oxidases. [38]

Despite this similarity in metal coordination, catechol extradiol cleavage by iron and manganese-dependent catechol dioxygenases exhibits some differences. First, manganese-dependent enzymes are less quenched than iron-dependent ones, which cannot perform catechol cleavage in the presence of H_2O_2, or which are inhibited by azide or cyanide ions. [35] Second, maybe because of the more recent crystallographic resolution, the mechanism of catechol cleavage by MndD is still under discussion (Scheme 2). [39] Studies tend to prove that the substrate binds to manganese, displacing two water molecules. In a second time dioxygen displaces the remaining water molecule and manganese(II) undergoes an oxidation to pass to manganese(III). Oxygen is then activated as superoxide. This latter oxidizes in turn catechol and dioxygen forms an alkylperoxo species with the radical thus created. Rearrangement and protonation occurs, providing the opened ring and returning the active site to its initial form. During the whole process, not only the active site is relevant to observe but also the second coordination sphere, *i.e.*, amino acids that are not directly bound to the metal ion. In particular, the effect of Histidine 200 has been reported to stabilize activated dioxygen species during the

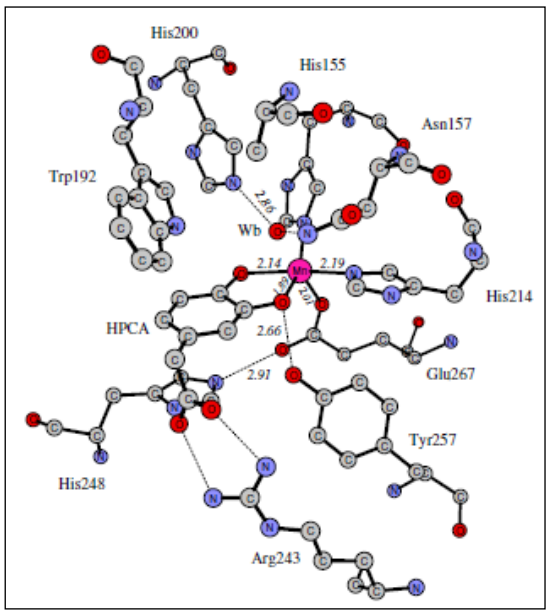

Figure 4: X-ray structure of the active site of MndD with the substrate (HPCA) coordinated to the metal ion [37]

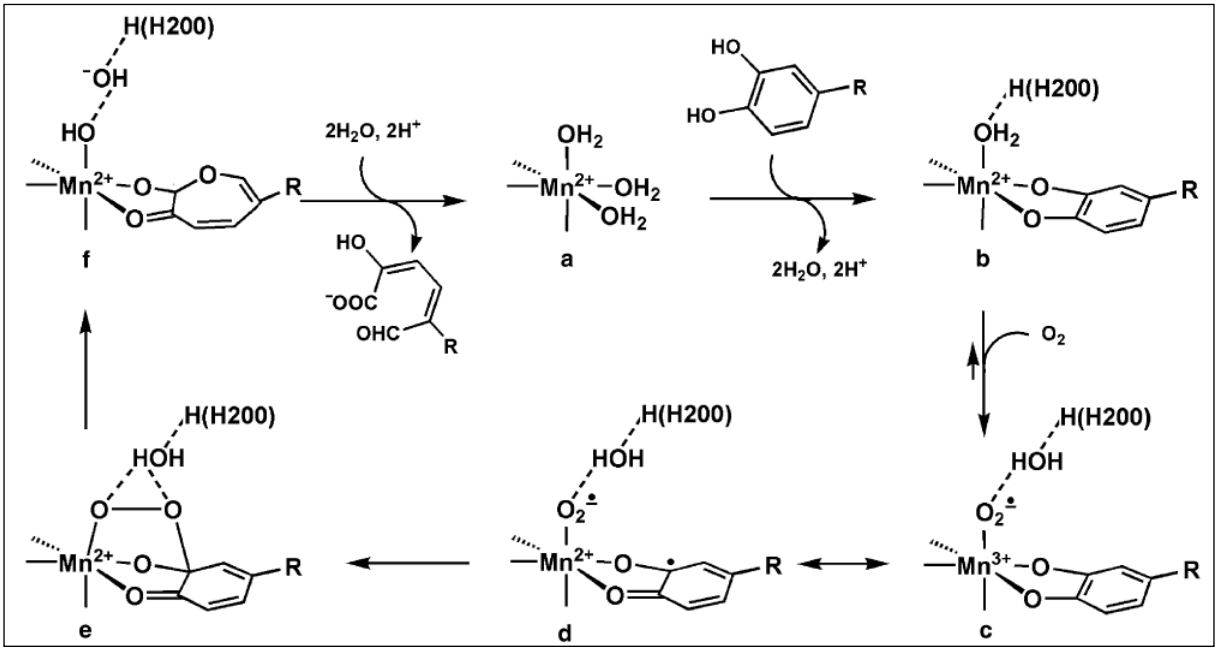

Scheme 2: Proposed mechanism for extradiol cleavage in MndD [39]

reaction. [39] Therefore, to fully understand the mechanism, focus cannot only be made on the first coordination sphere, which does not suffice to stabilize intermediate species and consequently to carry out the whole process.

Unravelling the mechanisms that govern enzymatic reactions is a key-step to understand their specificity. Since purifying those enzymes in large quantities has proven to be quite challenging, chemists started to develop functional model complexes to mimic active sites. This bio-inspired approach has two beneficial effects: it allows a better comprehension of the catalytic reaction itself and it provides new efficient catalysts, *i.e.*, catalysts with high specificity and yield. As explained before, iron-dependent catechol dioxygenases have been more intensively studied than their manganese counterparts. In this work, emphasis will be made on this particular kind of enzymes for two reasons. First, the reactive pathway is still under discussion, thus new models could lift the veil on remaining uncertainties. Second, the more difficult inhibition or quenching of those enzymes would provide in principle better complexes for future applications.

The objective of this thesis is to design new functional models of MndD for the cleavage of catechol derivatives. Some studies already report such models however those approaches were models of the active site only. [40] In fact, we chose not only to mimic the first coordination sphere by designing manganese complexes, but also to take into account the non-futile effect of the second coordination sphere, by grafting those complexes inside the pores of functionalized mesoporous silicas (Figure 5). This anchoring is expected to recreate both confinement and proximity of stabilizing functions.

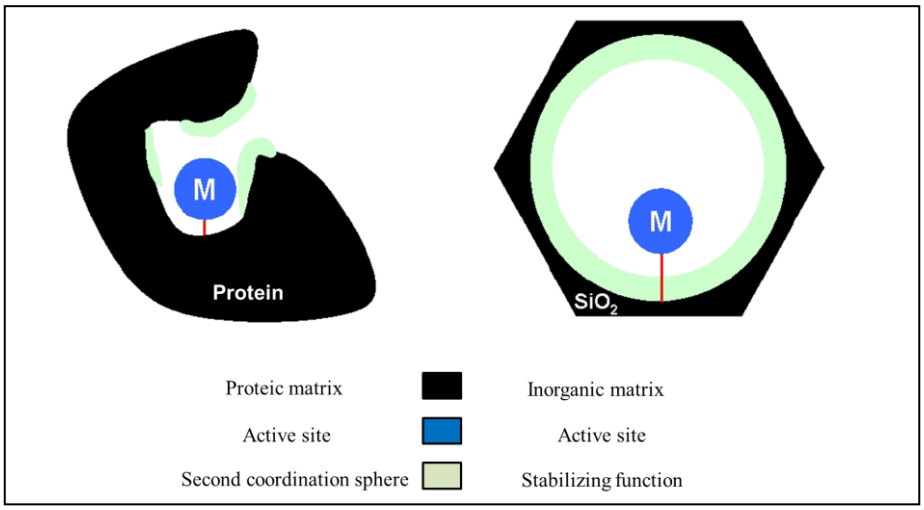

Figure 5 : Comparison between a protein (left) and a functionalized silica pore (right)

Three different chapters will develop the main aspects of this thesis. Considering that these chapters will explore different fields of chemistry, bibliographic reports will be written at the beginning of each one for more clarity. The first chapter will explain the ligand design, synthesis and characterization of manganese complexes. These syntheses provided both mononuclear and dinuclear complexes. The latter are bridged by different atoms allowing a magnetic coupling between metal ions: magnetic study of these species will also be reported in the first chapter. The second chapter will enlighten the synthesis of the silica support via microwave irradiation. Optimization of the microwave treatment and comparison with the classical thermal heating will compose this second chapter. The last chapter before conclusion will be the link between the two previous ones as it will explain silica functionalization for complexes hosting. Preliminary catalysis results will end this chapter, detailing the tests performed with both free and silica-supported complexes.

Bibliography

[1] F. Rosner, "Treatises on Poisons, Hemorrhoids and Co-habitation", *Maimonides Research Institute, Israel*, **1984**

[2] F. Rosner, *Einstein Quart. J. Biol. Med.*, **2002**, *19*, *3*, 125

[3] I. Ujváry, "Nicotine and Other Insecticidal Alkaloids", *Ed. I. Yamamoto and J. E. Casida, Tokyo: Springer-Verlag*, **1999**, 29

[4] R. L. Metcalf, "The Mode of Action of Organic Insecticides", *National Research Council, Washington DC*, **1948**

[5] B. Ginestet, "La bouillie bordelaise, ou Petite anthologie anecdotique et chronologique du vignoble, des gens et du vin de Bordeaux", *Flammarion, Paris*, **1975**, 241

[6] Commission Directive 91/188/EEC of 19 March 1991 amending for the fifth time the Annex to Council Directive 79/117/EEC prohibiting the placing on the market and use of plant protection products containing certain active substances, OJ L 92, 13.4.1991, 42

[7] http://www.nobelprize.org/nobel_prizes/medicine/laureates/1948/

[8] S Giacomazzi, N Cochet, *Chemosphere*, **2004**, *56*, *11*, 1021

[9] R. L. Metcalf, "Insect Control" in "Ullmann's Encyclopedia of Industrial Chemistry", *Wiley-VCH, Weinheim*, **2002**

[10] S. Navarro, N. Vela, G. Navarro, *Span. J. Agric. Res.*, **2007**, *5*, *3*, 357

[11] L. Alletto, Y. Coquet, P. Benoit, D. Heddadj, E. Barriuso, *Agron. Sustain. Dev.*, **2010**, *30*, 367

[12] R. C. Gilden, K. Huffling, B. Sattler, *J. Obstet. Gynecol. Neonat. Nurs.*, **2010**, *39*, 103

[13] K. Ikehata, M. G. El-Din, *Ozone Sci. Eng.*, **2005**, *27*, *2*, 83

[14] V. Camel, A. Bermond, *Wat. Res.*, **1998**, *32*, *11*, 3208

[15] S. Babel, T.A. Kurniawan, *J. Hazard. Mater. B*, **2003**, 97, 219

[16] P. E. Stackelberg, J. Gibs, E. T. Furlong, M. T. Meyer, S. D. Zaugg, R. L. Lippincott, *Sci. Total Environ.*, **2007**, *377*, 255

[17] C. Soulier, V. Gabet, K. LeMenach, P. Pardon, M. Esperanza, C. Miège, J.-M. Choubert, S. Martin-Ruel, A. Bruchet, M. Coquery, H. Budzinski, *Techniques Sciences et Méthodes*, **2011**, *1/2*, 63

[18] D.D. Kaufman, P. C. Kearney, "Herbicides: Physiology, Biochemistry, Ecology", *Ed. L. J. Audus, Academic Press, London*, **1976**, *2*, 29

[19] D. Ghosal, I.-S. You, D. K. Chatterjee, A. M. Chakrabarty, *Science*, **1985**, *228*, 135

[20] M. Alexander, *Science*, **1981**, *211*, 132

[21] D. T. Gibson, "Microbial Degradation of Organic Compounds", *Dekker, New York*, **1984**

[22] M. M. Häggblom, FEMS Microbiol. Lett., **1992**, *103*, *1*, 29

[23] N. Raffard, V. Balland, J. Simaan, S. Létard, M. Nierlich, K. Miki, F. Banse, E. Anxolabéhère-Mallart, J.-J. Girerd, *C. R. Chimie*, **2002**, *5*, 99

[24] E. Carredano, A. Karlsson, B. Kauppi, D. Choudhury, R. E. Parales, J. V. Parales, K. Lee, D. T. Gibson, H. Eklund, S. Ramaswamy, J. Mol. Biol., **2000**, *296*, 701

[25] B. Kauppi, Y. Lee, E. Carredano, R. E. Parales, D. T. Gibson, H. Eklund, S. Ramaswamy, Structure, **1998**, *6*, 571

[26] F. H. Vaillancourt, J. T. Bolin, L. D. Eltis, *Crit. Rev. Biochem. Mol. Biol.*, **2006**, *41*, 241

[27] O. Hayaishi, M. Katagiri, S. Rothberg, *J. Am. Chem. Soc.*, **1955**, *77*, 5450

[28] T. D. H. Bugg, *Tetrahedron*, **2003**, *59*, 7075

[29] Y. R. Boldt, M. J. Sadowsky, L. B. Ellis, L. Que Jr, L. P. Wackett, *J. Bacteriol.*, **1995**, *177*, *5*, 1225

[30] E. L. Neidle, C. Hartnett, S. Bonitz, L. N. Ornston, *J. Bacteriol.*, **1988**, *170*, *10*, 4874

[31] D. H. Ohlendorf, J. D. Lipscomb, P. C. Weber, *Nature*, **1988**, *336*, 403

[32] S. Han, L. D. Eltis, K. N. Timmis, S. W. Muchmore, J. T. Bolin, *Science*, **1995**, *270*, 976

[33] A. K. Whiting, Y. R. Boldt, M. P. Hendrich, L. P. Wackett, L. Que Jr., *Biochem.*, **1996**, *35*, 160

[34] R. Y. Stanier, J. L. Ingraham, *J. Biol. Chem.*, **1954**, *210*, 799

[35] L. Que Jr, J. Widom. R. L. Crawford, *J. Biol. Chem.*, **1981**, *256*, 10941

[36] M. W. Vetting, L. P. Wackett, L. Que Jr., J. D. Lipscomb, D. H. Ohlendorf, *J. Bacteriol.*, **2004**, *186*, *7*, 1945

[37] V. Georgiev, T. Borowski, P. E. M. Siegbahn, *J. Biol. Inorg. Chem.*, **2006**, *11*, 571

[38] K. Koehntop, J. Emerson, L. Que Jr., *J. Biol. Inorg. Chem.*, **2005**, *10*, 87

[39] J. P. Emerson, M. L. Wagner, M. F. Reynolds, L. Que Jr., M. J. Sadowsky, L. P. Wackett, *J. Biol. Inorg. Chem.*, **2005**, *10*, 751

[40] See Introductory aspects in Chapter I for more details of these models.

Chapter I:

Manganese(II) complexes:

synthesis and characterization

Introductory aspects

This first chapter will detail our approach in the synthesis of manganese(II) complexes to mimic the first coordination sphere in the manganese-dependent catechol dioxygenases (MndD).

Beyond industrial applications such as alloys, manganese is an essential element for living organisms. It is indeed present in several metalloproteins, in particular in photosystem II, responsible for photosynthesis in plants. [1, 2] It can also be found in enzymes like superoxide dismutase (SOD) or other oxidoreductases such as catechol dioxygenase. [3]

Understanding the underlying mechanisms of those enzymes has proven to be a challenging issue, as isolation and purification of biological proteins remain difficult. Therefore, model complexes were developed to mimic the activity of those macromolecules and to afford an easier material to work on. Discovery of the importance and occurrence of cytochrome P-450 in oxidation reactions led to the development of functional models from the beginning of the 80's. [4, 5, 6] Those models, metalloporphyrins containing either iron or manganese, were used in the oxidation of various compounds such as hydrocarbons, amines, or sulfoxides. Dinuclear manganese oxo/hydroxo/alkoxo bridged complexes have also been studied as models to the manganese catalase, an enzyme involved in the regulation of hydrogen peroxide. [7, 8]

Concerning oxidoreductases, emphasis will be put on enzymes involving molecular oxygen. Contrary to oxidases, that use dioxygen as an oxidant, oxygenases and dioxygenases incorporate atoms of oxygen in the substrate during the enzymatic reaction. [9] In the first case, only one atom is added to the substrate while both atoms are involved in the latter case.

I.0.1 Oxygen activation

From a thermodynamic point of view, the difference of bond energies between the created bonds (C-O and O-H bonds) and broken bonds (C-H, C-C and O-O bonds) during the oxidation of hydrocarbons with dioxygen is positive: the reaction is exothermic and thus thermodynamically favoured. [10] However, and that is quite comforting, no spontaneous reaction of dioxygen with hydrocarbons is observed. This absence of reaction is caused by the spin forbidden reaction between dioxygen triplet ground state $^3O_2$ and spin-paired singlet state of the substrate (Figure 1). [9] However, due to the difference of energy between those two

states (*ca.* 22 kcal.mol^{-1}), transition metals from enzymes cannot excite dioxygen to its singlet state. [11] Activation can be made using three different detours:

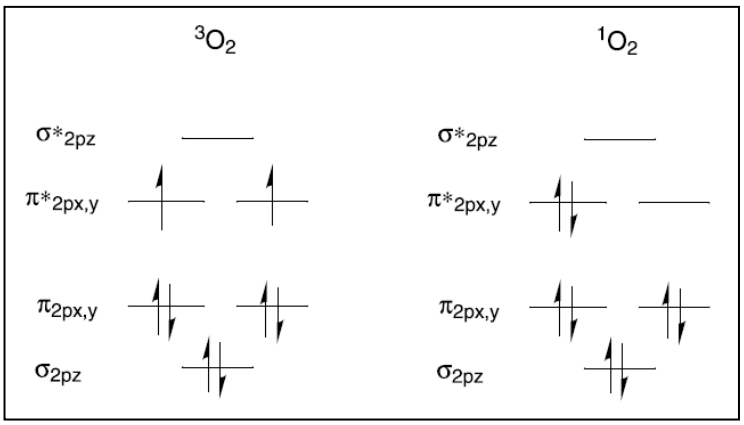

Figure 1: Molecular diagrams of $^3O_2$ (ground state) and $^1O_2$ (excited state) [9]

- Overlapping the π* orbitals from O_2 with the orbitals containing unpaired electrons from the metal ion can allow the reaction with singlet species.
- Formation of superoxide O_2^- by single electron transfer from the metal to the dioxygen, which is much more reactive toward organic substrates.
- Creation of a substrate radical, which turns the previously spin-forbidden reaction into a spin-allowed one.

I.0.2 Catechol dioxygenase models

As the crystal structure of iron-dependent catechol dioxygenase has been resolved decades before its manganese-dependent homologue, most of the models reported in the literature use iron as metal ion. [9, 12] Models containing iron(III) usually mimic the intradiol cleavage while models with iron(II) attempt to catalyse the extradiol cleavage. The review of models reported here is not exhaustive, only major works are presented.

The first models of intradiol cleaving enzymes used nitrilotriacetate (NTA) as ligand, to yield the furanone derivative after 4 days (Scheme 1). [13, 14] Reaching this final product was consistent with the mechanism of the intradiol cleavage.

Few years later, a much more reactive Fe(III) complex was reported with tris(2-pyridylmethyl)amine (TPA) as ligand. [15, 16] Instead of 4 days, this complex could perform the same oxidation within minutes in a higher yield. Though the active site of the intradiol cleaving dioxygenase is a 3N1O coordination sphere, most of the reported intradiol dioxygenase functional models contain 4N ligands. [17] Likewise, extradiol dioxygenase models generally use 3N or 4N ligands while the enzymatic metal ion is complexed by two histidine amino acids and one carboxylate moiety.

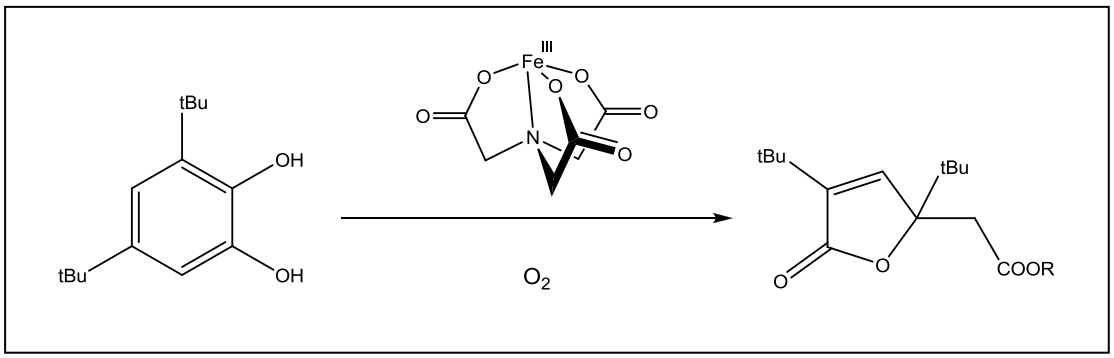

Scheme 1: Oxidation of 3,5-di-tert-butylcatechol by Fe-NTA complex, with R = H or Me [13, 14]

Iron complexes have been much more investigated than manganese complexes to study the extradiol cleavage of catechol. Models by Funabiki *et al.* in 1986 were the first Fe(III) complexes with bipyridine/pyridine ligands that oxidized 3,5-di-*tert*-butylcatechol into a mixture of its quinone equivalent, some intradiol products and some pyrones stemmed from an intermediate lactone (Scheme 2). [18] Iron(III) complex with triazacyclononane provided the same pyrones. [19, 20] However, addition of pyridine in the reacting mixture led to both extradiol and intradiol opened-ring products. [21] Over the years, other model complexes with iron(II) or iron (III) were studied, with ligands containing pyridine, carboxylate or imidazole moieties. [22, 23, 24, 25, 26] In most cases, the obtained products were heterocycles coherent with the supposed extradiol cleavage mechanism.

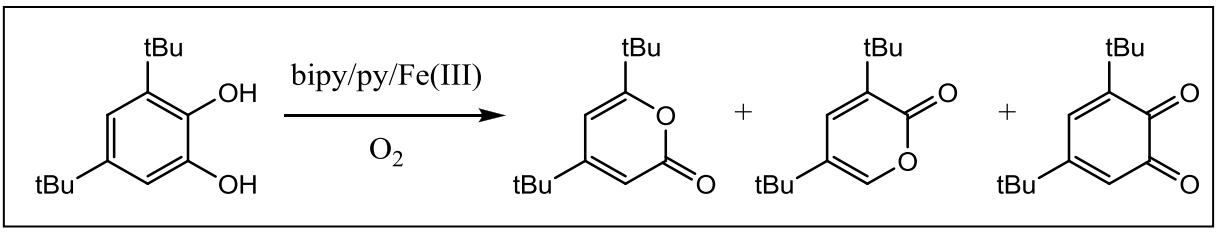

Scheme 2: Oxidation products of extradiol dioxygenase model by Funabiki [18]

In comparison, models that contain a manganese centre are much less frequent. Only few examples in the literature report manganese(II) complexes as mimics of the catechol dioxygenase. The first reported model to our knowledge was synthesized by Sakurai *et al.* in 1983, *i.e.*, two years after the discovery of the manganese-dependent dioxygenase. [27] This report describes the use of penicillamine with manganese(II) in the oxidation of catechol. However, very low conversion rates were achieved (< 2 %). In 1998, Ramadan and El-Mehasseb investigated the oxidative properties of tridentate pyridyl hydrazone ligands with manganese(II) (Figure 2.a). [28] They reported the transformation of catechol into *o*-benzoquinone in presence of catalyst and O_2, which would correspond to an oxidase activity (oxidation without incorporation of oxygen atom in the substrate). Similar results were obtained a few years later with tetradentate ligands containing imidazole, phenolate and/or

pyridine moieties (Figure 2.b). [29] The same year, the complex of another tetradentate ligand, N,N'-bis(2-pyridylmethyl)-1,2-ethanediamine (bispicen, Figure 2.c), with manganese(II), managed to oxidize the 4-tert-butylcatechol into a mixture of its quinone equivalent and extradiol intermediate products. [30] Reaction conditions turned out to have an important effect on the resulting products.

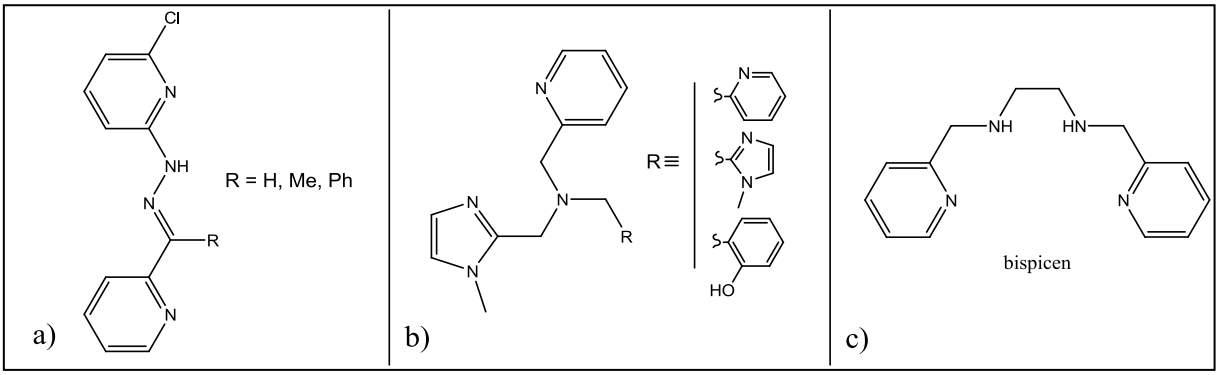

Figure 2: Ligands used for model complexes of MndD with manganese(II) [28, 29, 30]

First, this chapter will tackle the synthesis and characterisation of ligands that mimic the first coordination sphere of the enzyme. Then, the synthesis, the characterization and the study magnetic properties of manganese(II) complexes with these latter will be discussed.

I.1. Strategy

The same pattern was used in every ligand design: a tertiary amine linking an alkyne-containing arm and two coordinating moieties such as pyridine, 1-methylimidazole or carboxylate groups. By design, the ligands chemical functions that intervene in complexation and grafting processes are orthogonal. Given that the interferences between these reactions are greatly reduced, this approach affords much more room for manoeuvre in each one of those mentioned steps.

The alkyne function is used for the silica-grafting step. Indeed, due to the advantages of the copper(I) catalyzed Huisgen azide-alkyne cycloaddition, also known as "click chemistry", in terms of yield and selectivity, we chose this reaction for the grafting process. [31] Given that this click reaction involves an alkyne and an azide, we had the choice to design our ligands either with an azide or an alkyne arm. The latter was preferred for two reasons: first, the incorporation of an azide function in the ligand could have been more problematic for the synthesis of the complex than the incorporation of an alkyne arm because of the coordinating potential of the azide moiety, and second, it was easier to synthesize the azide tethering silane than the alkyne tether one. Grafting strategy and particularly the choice of involved chemical functions in both complexes and grafted silanes will be discussed in further details in the third chapter. Beyond our further utilisation of this alkyne moiety, these ligands possess a broader versatility than the mesoporous silica grafting. On the first hand, they can act as a tridentate coordinating group toward metal ions, and on the second hand their alkyne arm allows them to be coupled to a wide range of molecules, polymers or solids whom only condition would be to possess an azide moiety. Many research projects in the literature involve azide-functionalized polymers, surface or materials efficiently modified through the use of click chemistry. [32, 33, 34] Furthermore, even though our work only reports the use of manganese(II), other metal ions can be coordinated to tune the properties of the resulting complex.

As for the coordinating moiety, the tertiary amine and the two side-functions mimic the three amino-acids coordinated to the manganese(II) ion in the enzyme, *i.e.*, the two histidines and the glutamate. We mainly focused our work on three different ligands, differentiated one from another by their two coordinating groups (Figure 3). Though the first two ligands do not contain a carboxylic acid moiety, many functional models of catechol dioxygenase enzyme are actually metals coordinated to three or more nitrogen atoms without any actual carboxylic acid. [35]

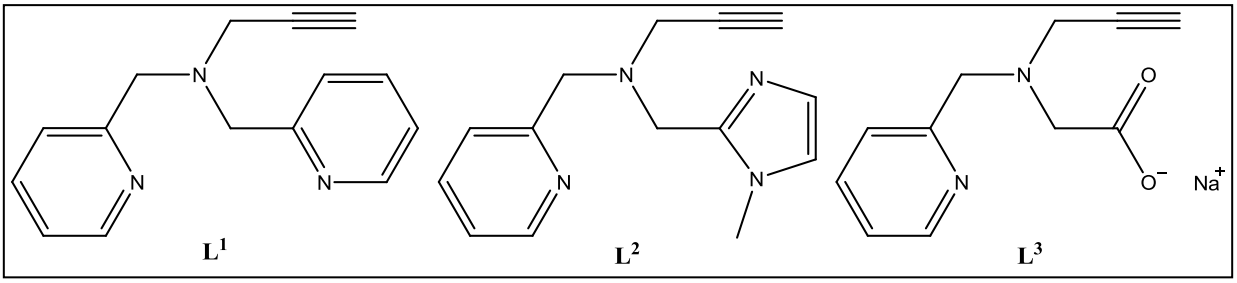

Figure 3: Ligands targeted in this study

While L^1 synthesis has already been published in the literature and involved in the synthesis of copper and rhenium complexes, [36, 37, 38] both L^2 and L^3 were new designed ligands. Characterizations such as nuclear magnetic resonance (NMR) and infrared (IR) spectra are given in the experimental part and the spectra are given in appendix.

I.2. Ligand synthesis

This part describes the synthesis of L^1-L^3, as well as the attempts performed to synthesize other ligands. Protocols are detailed in the experimental part.

I.2.1 Ligand L^1

Two methods have been explored to synthesize L^1. Method A is a two-step pathway (Scheme 3), starting with the formation of a Schiff base from the condensation of the 2-picolylamine with the 2-pyridinecarboxaldehyde which is further reduced with sodium borohydride. The second step consists in an electrophilic substitution with propargyl bromide to obtain the desired ligand. [37] The first step yield was 96% with a simple work-up whereas the purification column chromatography on silica for the second step only allowed us to recover the product in an 11 % yield. However the yield of this second-step should not be taken as a standard yield for this reaction. In fact, this purification has only been performed once, and results found in the literature report average yields above 80 %. [37, 39]

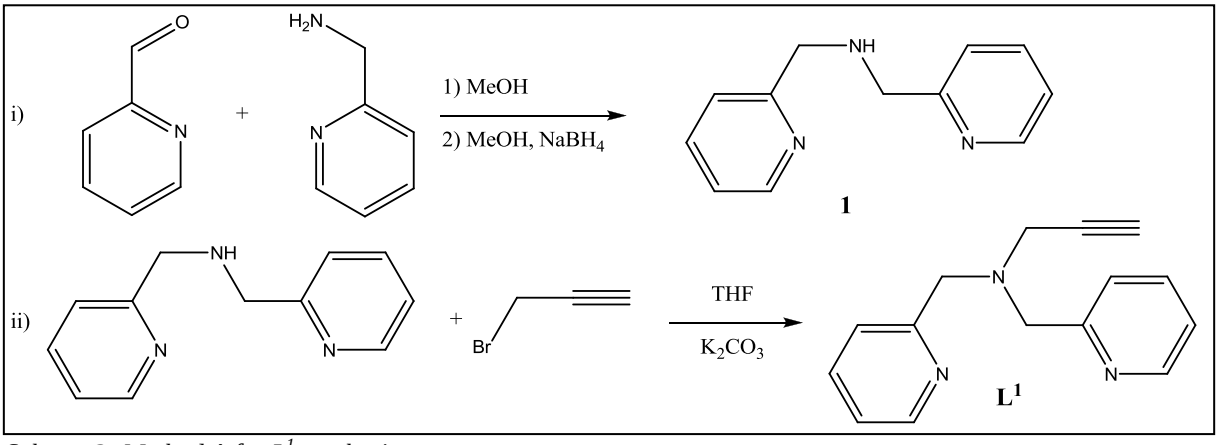

Scheme 3: Method A for L^1 synthesis

Nonetheless another method has been tested, in one step (Scheme 4). This reaction is a double electrophilic substitution involving the propargyl amine and two 2-picolylchloride molecules. The mixture was stirred at 65 °C for five days allowing us to retrieve L^1 in a 90 to 96 % yield. Once again this reaction has already been reported, however the synthesis time found in the literature was much shorter, around 12 h. [37] The product was then obtained in a 32 % yield, leading the authors to conclude the first method was much more efficient.

Though method B is much longer than the first one from a reaction time point of view (five days in that case, against two days for method A), it presents some advantages. First,

only one step is necessary to afford the desired ligand. Furthermore both proton and carbon NMR show that a pure product can be obtained with simple wash-up, *i.e.*, an extraction in this case, in a convenient yield. Therefore this synthetic method was adopted for the synthesis of L^1 ligand.

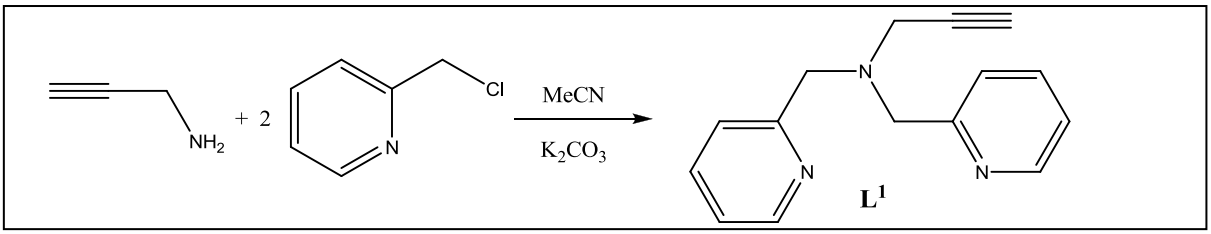

Scheme 4: Method B for L^1 synthesis

I.2.2 Ligand L^2

To our knowledge, ligand L^2 had never been synthesized before according to the available literature. Therefore the trials were inspired from the synthesis of L^1 and method A was attempted first (Scheme 5), *i.e.*, condensation between an amine and an aldehyde followed by an electrophilic substitution.[40] Consequently the first step was a condensation between the 2-picolylamine and the 1-methyl-2-imidazolecarboxaldehyde, followed by a reduction of the Schiff base formed by sodium borohydride. The secondary amine thus

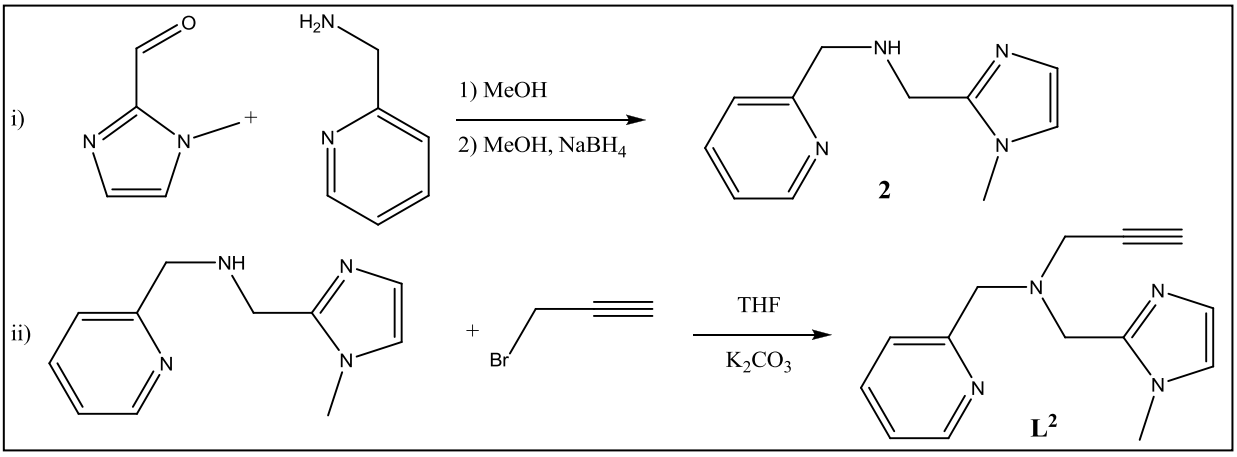

Scheme 5: Synthesis of L^2

formed was then treated with propargyl bromide.

It is interesting to note the absence of undesired by-products in the second step, contrary to the second step of method A in the synthesis of L^1 that requires purification by column chromatography. In fact, simple redissolution in dichloromethane and filtration through potassium bromide provided the pure ligand L^2 in an 80 % yield.

I.2.3 Ligand L^3

This third ligand, like L^2, was an original synthesis and necessitated an adapted strategy. It was synthesized in three steps (Scheme 6). The first two steps consist in two successive nucleophilic substitutions to afford a secondary (**3**) [41] and then a tertiary amine, containing an ester and a pyridine arm (**4**). The last one consists in the deprotection of the ester moiety to obtain the carboxylic acid. While the first product was purified to get rid of by-products such as the double substituted amine, the product obtained in the second step was deprotected without any previous purification. After extraction and acidification, ligand L^3 was obtained as a sodium salt.

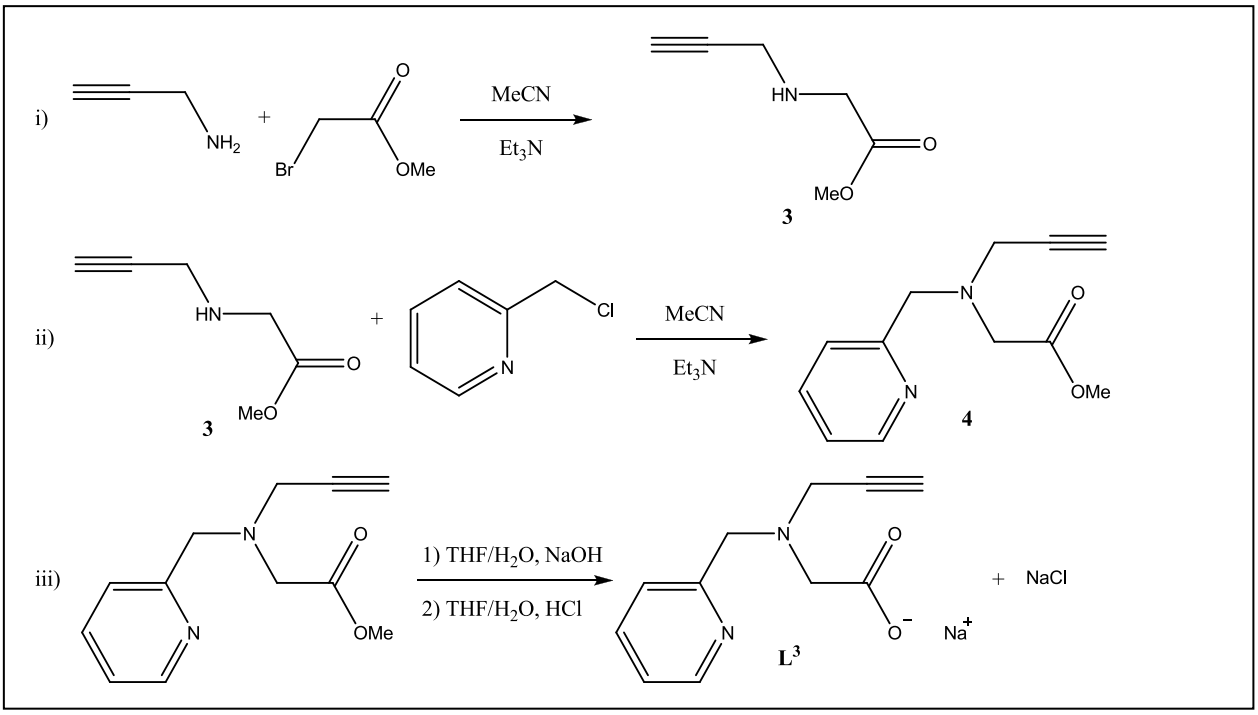

Scheme 6: Synthesis of L^3

The first step was the limiting one. Indeed, using the conditions described in the literature (1.2 equivalent of bromide derivative), a comparable fraction of double substituted by-product was obtained. In the end only a stoichiometric amount of reactive was used. The second reaction was almost total after one night, according to the ^{1}H-NMR spectrum of the crude product. Finally, the deprotection was a classic saponification, leading to the product in a 60 % yield. Without any acidic treatment, and due to the basic medium required by the saponification, a deprotonated alkyne was first obtained.

The use of hydrochloride acid to protonate the final alkyne provided a product containing both ligand L^3 and sodium chloride.

I.2.4 Other ligands

Different attempts to obtain other ligands were carried out. For instance, we tried to synthesize the *N*,*N*-bis((1-methyl-1*H*-imidazol-2-yl)methyl)prop-2-yn-1-amine, L^4 (Scheme 7). A similar reaction than the one used for L^1, *i.e.*, a double electrophilic substitution on a primary amine, was tested. The chlorinated derivative of methylimidazole was first synthesized in two steps starting from 1-methyl-1*H*-imidazole and paraformaldehyde to provide the alcohol (1-methyl-1*H*-imidazol-2-yl)methanol, before substitution of the hydroxyl moiety by chloride through reaction with thionyl chloride. [42, 43, 44]

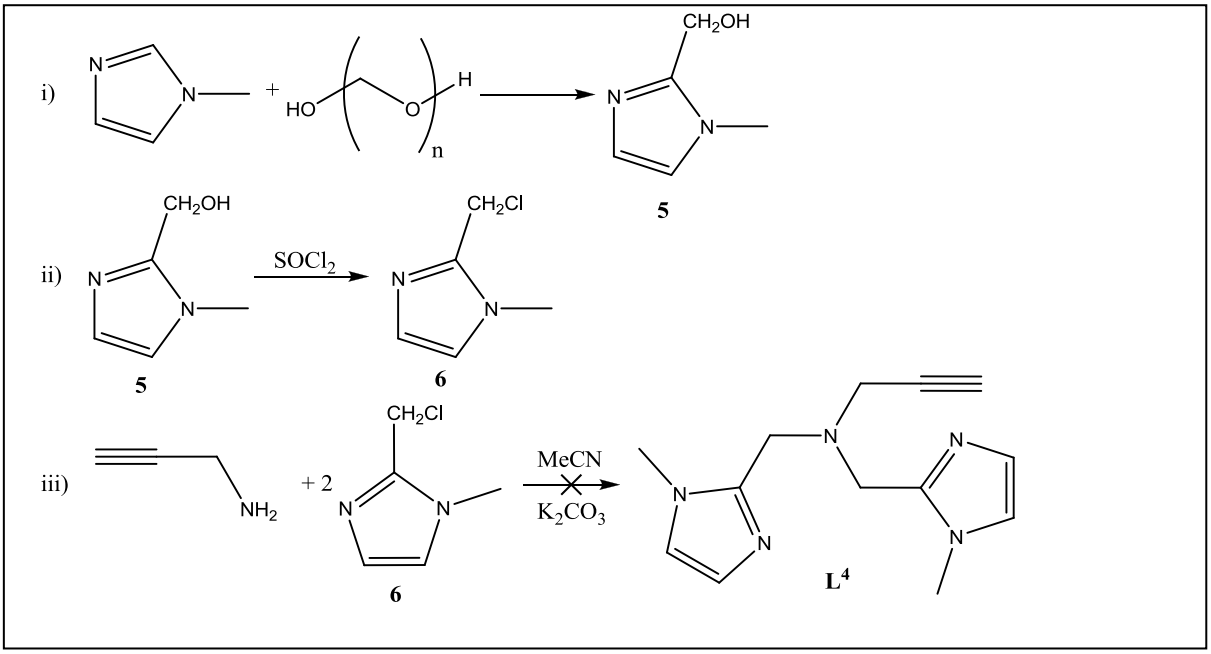

Scheme 7: Attempt of synthesis of L^4

Unfortunately, this chlorinated derivative was much less reactive toward the amine than picolyl chloride used in the synthesis of L^1. Indeed, when this latter could be carried out with 6 equivalents of base per amine, such excess was not enough in the case of methylimidazole thus the desired product was not obtained according to the ^{1}H-NMR spectra. This difference of reactivity between pyridine and imidazole chlorinated derivatives was also observed in the synthesis of L^2: under the same synthetic conditions, **1** and **2** reacted differently with propargyl bromide as **2** led to L^2 with a much simpler purification than the one required to obtain L^1 from **1**.

The synthesis of sodium 2-(((1-methyl-1*H*-imidazol-2-yl)methyl)(prop-2-ynyl)amino)acetate, L^5, was also tried, with several methods as described on Scheme 8. As there are three different arms on the final desired tertiary amine, two pathways were possible:

one similar to method A for L^1, formation of a Schiff base followed by reduction, before addition of a halogenated equivalent of the third arm, and one similar to the synthesis of L^3, sequential addition of the halogenated equivalent of each arm on a primary amine. Obviously, those are the simplest pathways; most complicated strategies could have been elaborated. However our previous failed attempts with 2-(chloromethyl)-1-methyl-1*H*-imidazole led us to prefer the Schiff base pathway over the other one.

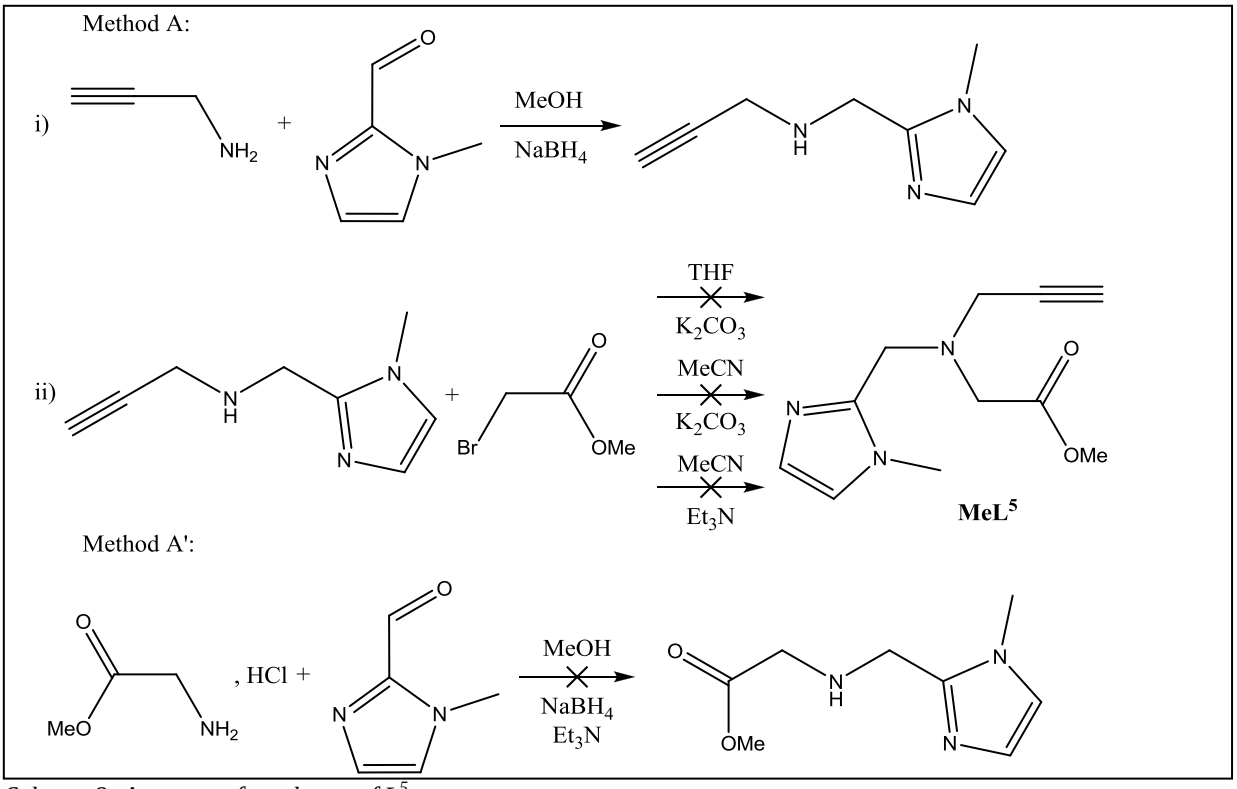

Scheme 8: Attempts of syntheses of L^5

Reaction between propargylamine and 1-methyl-2-imidazolecarboxaldehyde followed by reduction with $NaBH_4$ gave N-((1-methyl-1*H*-imidazol-2-yl)methyl)prop-2-yn-1-amine in an average 95 % yield. However, we could not obtain the desired product by adding methylbromoacetate, in spite of the different conditions used. Indeed, neither changing the solvent from tetrahyfrofurane to acetonitrile nor using another base allowed us to achieve the reaction (Scheme 8.ii).

Another strategy (method A') was then employed: instead of trying to obtain an intermediate containing the alkyne and imidazole arms, the aim was now an intermediate containing both coordinating moieties, hence a reaction between 1-methyl-2-imidazolecarboxaldehyde and glycine methylester hydrochloride was performed. However, this reaction did not give the desired product but a mixture of byproducts and triethylamine.

I.3. Synthesis of the metal complexes

Once the ligands synthesized, our next goal was obtaining manganese(II) complexes and the resolution of their crystal structure. All the manganese complexes were synthesized by metallation of ligands L^1, L^2 and L^3 described above using manganese(II) salts. At the beginning some insights about the ligand and their coordination toward this metal were necessary. In fact, those ligands, even the known one, had never been tried to coordinate manganese(II). Our first attempt was manganese chloride, for this choice was the most common one. Both ligands L^1 and L^2 were tested with this manganese(II) salt, and though those ligands are relatively close in structure, their complexes with $MnCl_2$ were quite different: complex with L^1 crystallized as a dinuclear species containing two metal ions bridged by two chloride anions, while complex with L^2 crystallized as a mononuclear species. Those two crystals actually led us to investigate in two directions:

- First the synthesis of dinuclear complexes, to compare their magnetic and structural properties.
- Second the synthesis of mononuclear complexes, in principle closer to the active site of the enzyme.

This paragraph describes first the syntheses of the two chloride-containing complexes, then the synthesis of the dinuclear species with azido and bromide bridges, followed by the synthesis of mononuclear species with nitrate and tetraphenylborate, and finally the synthesis of complexes with L^3.

Crystal structures and magnetic properties of the manganese(II) complexes are detailed in paragraphs I.4 and I.5, the aim of this part being to describe the syntheses.

I.3.1 $[Mn_2(\mu\text{-}Cl)_2(Cl)_2(L^1)_2]$

This complex was synthesized using a stoichiometric amount of ligand and manganese(II) chloride in methanol. After a 30 min stirring, the precipitate thus formed was filtered, washed with methanol and dried to obtain the complex in a 52 % yield. Apart from methanol, ethanol and acetonitrile were tested as solvent, without any significant change in the yield, all of them around 50 %. Because of the better solubility of both ligand and metal salt in methanol, this solvent was used in the following syntheses. Pale yellow crystals were obtained by slow diffusion of diethyl ether in a methanolic solution of the precipitated solid

within a few days. The crystal structure resolution showed that the complex crystallizes as a dinuclear compound, with two chloro-bridges between two manganese(II) centres (Figure 4).

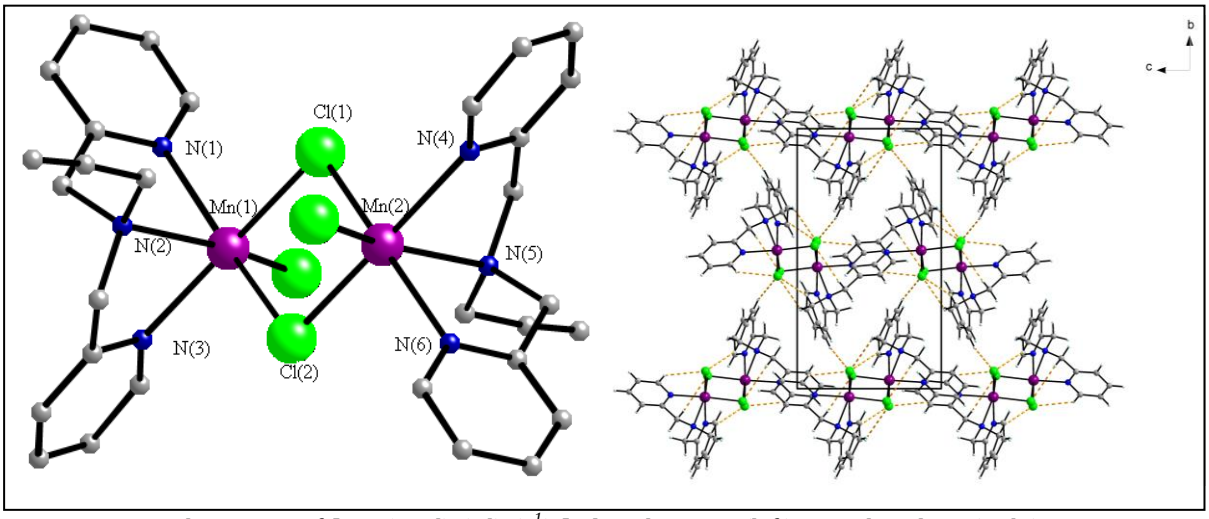

Figure 4: Crystal structure of [$Mn_2(\mu\text{-}Cl)_2(Cl)_2(L^1)_2$], dinuclear unit (left) crystal packing (right)

I.3.2 [$Mn(Cl)_2L^2$]

The protocol is similar to the one used for L^1, *i.e.*, a stoichiometric amount of ligand and manganese(II) chloride was stirred in methanol during one hour. The solution was filtered and the filtrate was let to evaporate at room temperature. After 48 h, large brown crystals (from 1 to 3 mm) of the complex were obtained. This crystallization method was actually so efficient that it provided enough matter to perform grafting and catalytic tests. Given that most of those large crystals were twinned, one of them was redissolved in methanol in order to afford suitable crystals for X-ray diffraction. The solution was then let to evaporate again so smaller crystals could be collected. Crystal structure exhibits some differences in comparison to its equivalent with L^1 (Figure 5). The manganese(II) centre is pentacoordinated by three nitrogen atoms from the ligand and two chloride anions from the initial manganese(II) salt. Chloride atoms do not act as bridges anymore therefore this complex is a mononuclear complex instead of the dinuclear complex obtained before with L^1.

In order to verify whether the crystallization method influenced, or not, the nuclearity of the final product, crystals of [$Mn(Cl)_2L^2$] were grown by diffusion of ether in a methanolic solution of the complex. Once again, the same crystal structure was obtained, without any chloride bridge between to manganese(II) centres.

Though this synthesis directly provided crystals of this complex, small changes in the process can have drastic effects. In fact, the first tests were done with a ligand kept at room

temperature. When the ligand was stocked in the fridge and used immediately for the synthesis, the complex actually precipitated within minutes. Keeping the same stock at room temperature before its utilization allowed us to retrieve a solubilized complex leading to crystals within a couple of days.

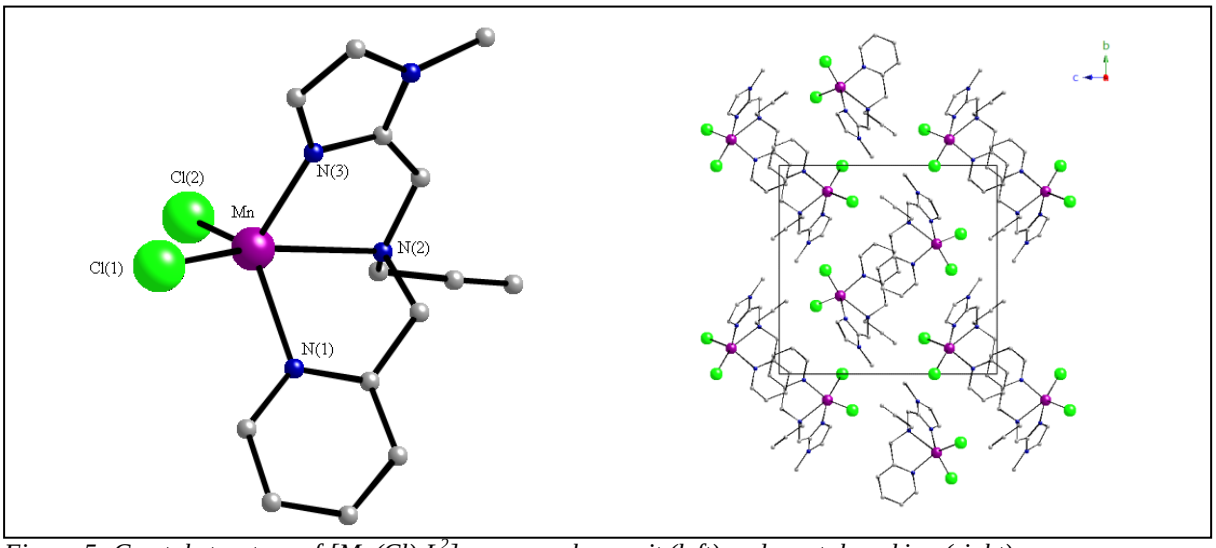

Figure 5: Crystal structure of [Mn(Cl)$_2$L^2], mononuclear unit (left) and crystal packing (right)

The differences between crystals synthesized with L^1 and L^2 led us to investigate in two different directions. The first one was the synthesis of other anion-bridged dinuclear species, to compare their magnetic properties, their structures and to study the effects of both ligands and anions. The second one was obtaining mononuclear species, in principle more efficient when used in catalysis purposes. Indeed, a less coordinating counter-anion would be more easily displaced by the substrate and the catalytic reaction would be favoured. In this sense, nitrate was tested first, followed by tetraphenylborate, an even less coordinating counter-anion.

Therefore different manganese(II) salts were tested with L^1. In the case of chloride, bromide, nitrate, acetate and sulphate counter-anions, the complexation was directly performed using the corresponding manganese(II) salt. However, complexes with azide and tetraphenylborate were synthesized in two steps: a first complexation with manganese(II) nitrate followed by an addition of 5 equivalents of the desired counter-anion (NaN_3 and $NaBPh_4$).

I.3.3 $[Mn_2(\mu\text{-}Br)_2(Br)_2(L^1)_2]$

The choice of bromide as counter-anion was initially motivated by its tendency to give mononuclear complexes with manganese(II). Examples found in the literature mainly report

mononuclear complexes of Mn(II) with bromide anions. Due to the greater size of bromide anions, one can assume they would not bridge two manganese(II) centres. To our knowledge, only one crystal structure containing a bromide bridge between two manganese(II) has been published. [45] Finally another member of those bromide-bridged manganese(II) compounds was added to the family when the structure of $[Mn_2(\mu\text{-}Br)_2(Br)_2(L^1)_2]$ was resolved (Figure 6).

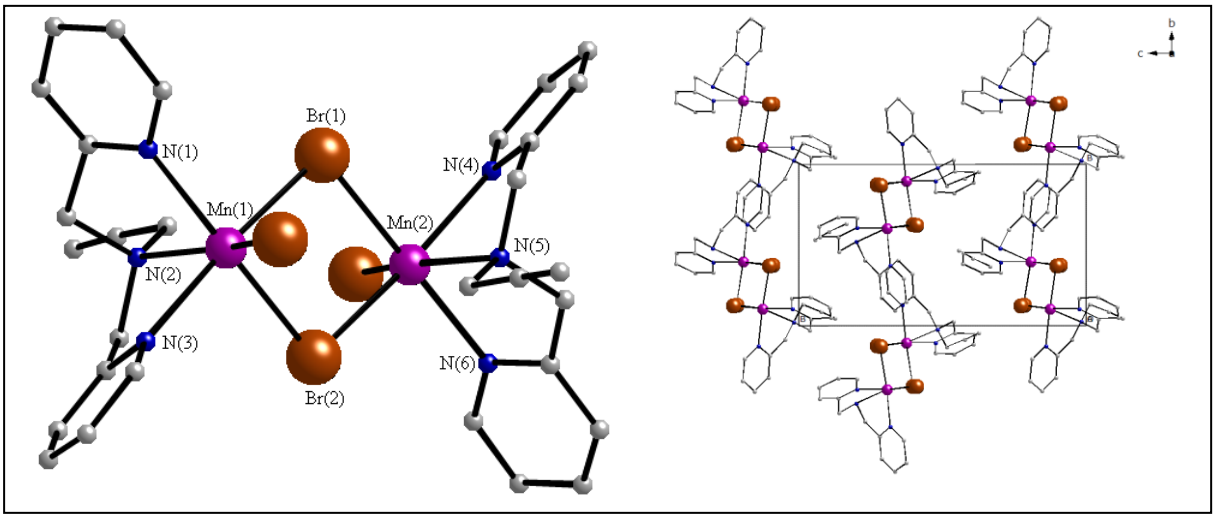

Figure 6: Crystal structure of $[Mn_2(\mu\text{-}Br)_2(Br)_2(L^1)_2]$, dinuclear unit (left) and crystal packing (right)

This complex was synthesized using a stoichiometric amount of ligand and manganese(II) bromide, again in methanol. Contrary to the previous synthesis with L^1, the complex did not precipitate. However, dark brown crystals suitable for X-ray diffraction were obtained within couple of days by slow diffusion of diethyl ether in the latter methanolic solution. A dinuclear complex was obtained (Figure 6), with two bromide bridges between the manganese(II) centres.

I.3.4 $[Mn_2(\mu\text{-}N_3)_2(N_3)_2(L^1)_2]\cdot 2MeOH$

Using the azide counter-anion in the synthesis of bridged manganese(II) complexes was more usual than using the bromide one. However, azide anions can be coordinated in

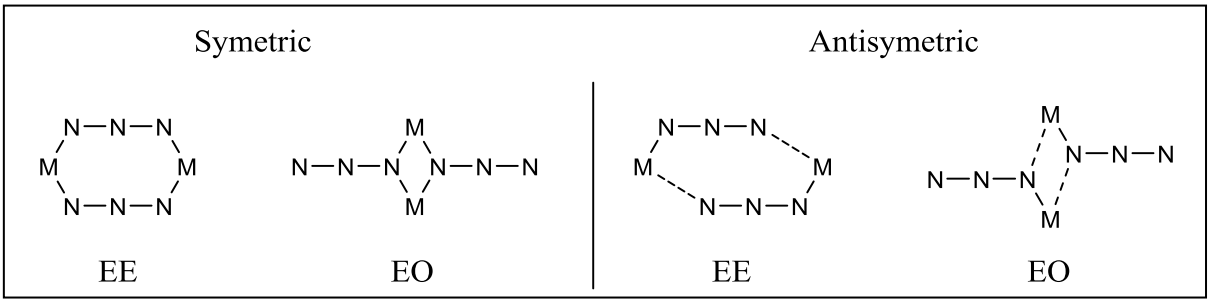

Figure 7: Symmetric EE and EO and asymmetric EE and EO coordination modes for azido bridges (M = metal ion)

different ways (Figure 7): *end-to-end* ($\mu_{1,3}$-N_3, EE) and *end-on* ($\mu_{1,1}$-N_3, EO) are the most common ways. In order to obtain a $\mu_{1,1}$ bridge and thus an exploitable comparison with chloride and bromide complexes, EO coordination was needed.

In this case, the synthesis was adapted given that the manganese(II) azide was not available. Thus the complex was synthesized starting from a solution of manganese(II) nitrate to which was added a stoichiometric amount of ligand L^1. After one hour under stirring, a solution of five equivalents of sodium azide was added, leading to the apparition of a pale brown precipitate. After filtration and washing with methanol, crystals were obtained once again by slow diffusion of diethyl ether in a methanolic solution of the complex.

The resolution of the crystal structure showed another dinuclear complex, containing one molecule of methanol per manganese atom. This slight difference with the two other complexes could be predicted considering the instability of the crystals when let at room temperature, due to the evaporation of the structural solvent molecule. As proven by the crystal structure, EO coordination of the bridging azide anions was obtained (Figure 8).

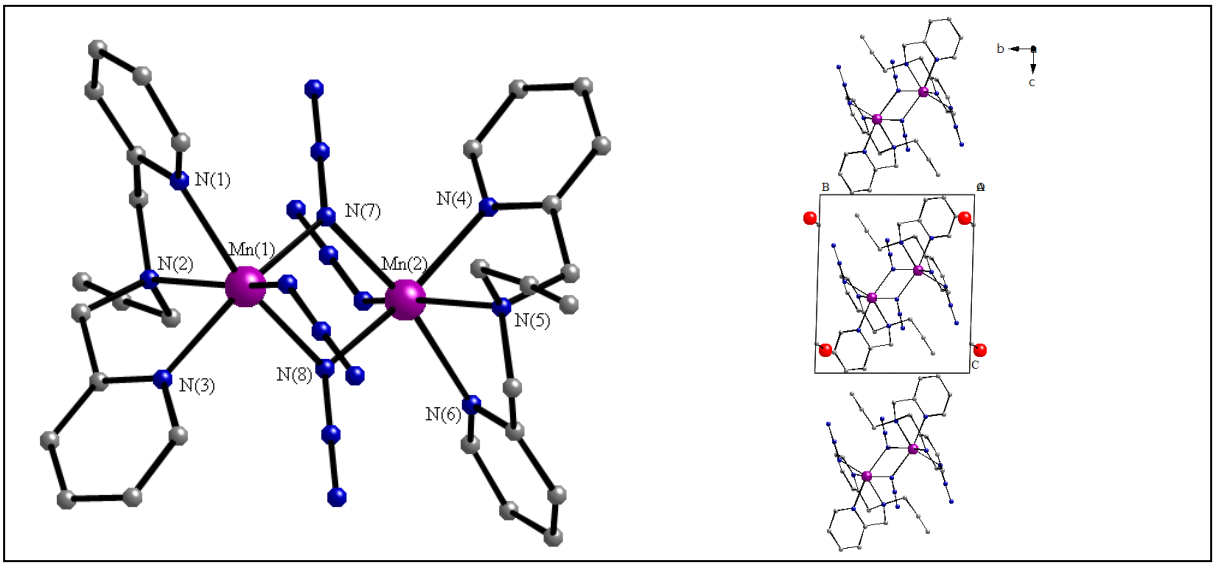

Figure 8: Crystal structure of [$Mn_2(\mu$-$N_3)_2(N_3)_2(L^1)_2$]·2MeOH, dinucealr unit (left) and crystal packing (right)

I.3.5 $[Mn_2(\mu\text{-}N_3)_2(N_3)_2(L^2)_2]$

This complex was synthesized and crystallized to be compared to the equivalent with L^1. Actually, it was the only dinuclear complex we achieved with L^2. The same synthetic method than before was followed: a first reaction with a stoichiometric amount of manganese(II) nitrate and ligand L^2 was stirred at room temperature during 30 min. A methanolic solution of sodium azide was added to this first solution and the mixture was further stirred. After 30 min, the precipitate thus formed was filtered and washed with methanol. The solid was redissolved in methanol, and crystals were obtained after a slow diffusion of ether. The resolved structure showed a dinuclear complex with two azide anions bridging two manganese(II) centres, once again in EO coordination (Figure 9). Contrary to its equivalent with L^1, no solvent molecule was observed in this crystal structure.

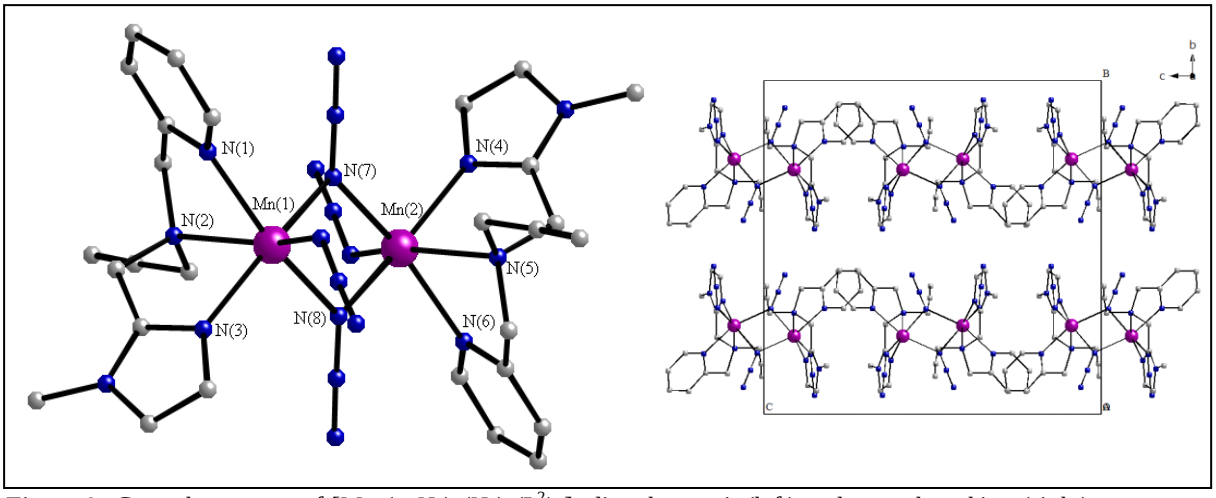

Figure 9: Crystal structure of $[Mn_2(\mu\text{-}N_3)_2(N_3)_2(L^2)_2]$, dinuclear unit (left) and crystal packing (right)

Though obtaining those dinuclear complexes showed an interest from a magnetic point of view, our initial purpose was the synthesis of catalysts. Therefore other complexes with less coordinating, *i.e.*, more labile, counter anions were synthesized, in order to increase the accessibility of the manganese(II) centre. However, gaining in accessibility was not the only advantage. As those catalysts are meant to be used for depollution, it is important to keep them relatively non-toxic. Hence the use of counter-anions such as azide or bromide was not the most interesting choice in terms of toxicity. The first and most obvious one was the complex containing the nitrate counter anion.

I.3.6 $[Mn(NO_3)(H_2O)_2L^1]\cdot NO_3$

Two different syntheses were performed, depending on the purpose sought. Indeed, in order to get crystals, the synthesis was performed in methanol, with a stoichiometric amount of ligand and manganese(II) nitrate. The complex thus formed was soluble in methanol, but small crystals appeared when the solvent was let to evaporate at room temperature. Given that those crystals were not suitable for X-ray diffraction, they were dissolved again in methanol and ether was slowly diffused in this new solution to afford suitable crystals. As expected due to the chosen counter-anion, this complex was mononuclear and only one nitrate was coordinated to the manganese(II) centre (Figure 10).

However, this method was not appropriate to obtain a consequent amount of product. Therefore the solvent was changed and absolute ethanol was used instead of methanol. This small difference was enough as the complex precipitated after stirring the mixture for a dozen of minutes. The precipitate was filtrated and washed with ethanol. To ensure that this precipitate was the same complex than the one synthesized by the previous method, IR spectrum were compared, resulting in the same absorption for crystal and precipitate.

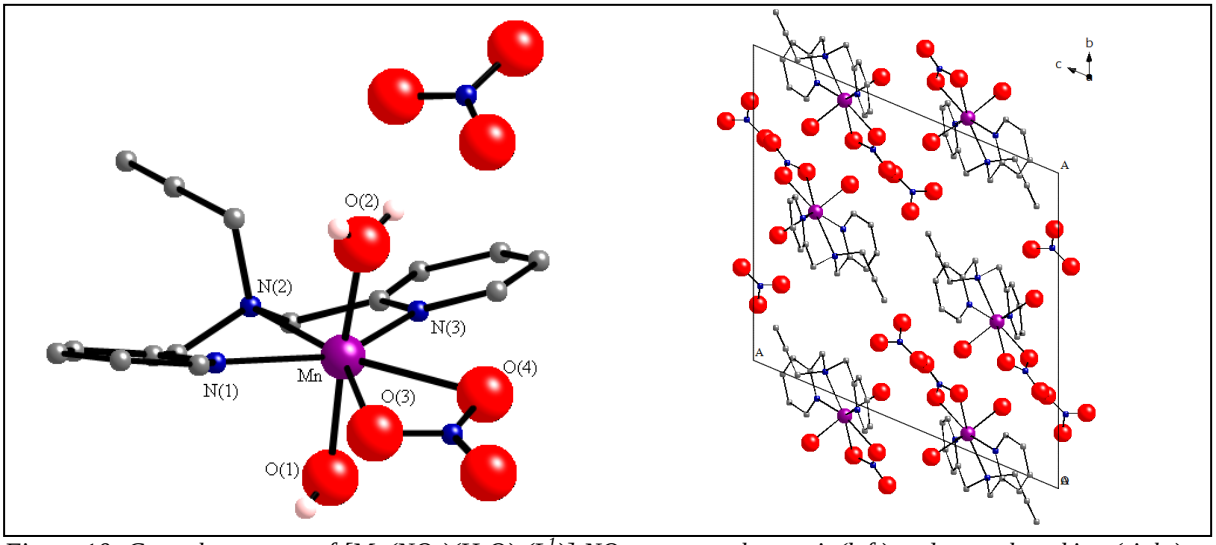

Figure 10: Crystal structure of $[Mn(NO_3)(H_2O)_2(L^1)]\cdot NO_3$, mononuclear unit (left) and crystal packing (right)

I.3.7 $[Mn(H_2O)_3L^1]\cdot(BPh_4)_2$

Previous results with nitrate showed the coordination of a unique anion to the metal centre. Therefore, the use of tetraphenylborate as counter-anion was motivated by its lower ability to coordinate the metal centre: such counter-anion could let even more space around the manganese(II) ion for the substrate to coordinate. This synthesis was quite similar to the

synthesis involving the azide counter-anion. Indeed, upon reaction of L^1 with the manganese(II) nitrate, addition of an excess of sodium tetraphenylborate salt in methanol led to the apparition of a pale brown precipitate. This latter was filtrated and washed with methanol to obtain the tetraphenylborate equivalent of the manganese(II) complex. Nonetheless, we did not succeed in obtaining any crystal of this version of the MnL^1 complex.

I.3.8 Complexes with ligand L^3

This ligand was the most problematic one. We did not manage to crystallize any manganese(II) complex synthesized with L^3, with any counter anion used. Table 1 reports the synthesis conditions tried with this ligand to obtain and crystallize a usable $[MnX_2L^3]$ complex.

Methanol, water and ethanol were used as solvents for they could solubilise the ligand while possessing a relatively low boiling point (100 °C maximum, against 150 °C for DMF and 189 °C for DMSO). Solubility tests with chlorinated solvents (dichloromethane or chloroform) and acetonitrile showed that L^3 was not dissolved in any of them.

When water was used, colourless crystals appeared after slow evaporation of the solvent. Unfortunately, those crystals turned out to be NaCl crystals, from the remaining synthesis salts. This assertion was supported by their IR spectrum, which did not exhibit any of the ligand bands. In the case of entry 10, the reaction was performed in a mixture of water and methanol. Dimethylformamide was added after stirring the reacting solution for 1 h. This method was inspired from a reported synthesis that used carboxylate-containing ligands with copper(II): both reactant and product where soluble in the mixture methanol/water, while the product was insoluble in DMF. [46] Evaporation of H_2O and MeOH led to increase the percentage of DMF in the resulting mixture and thus to decrease the complex solubility. By doing so, crystals could grow. In our case, we did obtain light yellow crystals with this method. However they did not appear before quasi-total evaporation of the solvent, which provided crystals covered with brown oil supposed to be unreacted ligand.

Precipitation only occurred when tetraphenylborate was used as counter-anion providing $[Mn(H_2O)_3L^3]\cdot(BPh_4)_2$ as a powder; otherwise the product was soluble in the solvent used. Crystallization conditions employed in entry 14 did not provide any crystal. However by slow evaporation of a mixture H_2O/acetone, small yellowish crystals grew. Unfortunately, those crystals were not suitable for X-ray diffraction and their structure could not be resolved.

Table 1: Summary of the synthesis conditions for $[MnX_2L^3]$ complexes

Entry	Counter-anion[a]	Solvent	M/L[b]	Product[c]	Crystallization[d]
1	Cl^-	H_2O	1	S	SE
2	Cl^-	H_2O	1	S	Dif MeOH→H_2O
3	Cl^-	H_2O	1	S	Dif EtOH→H_2O
4	Cl^-	MeOH	1	S	Dif Et_2O→MeOH
5	NO_3^-	H_2O	1	S	SE
6	NO_3^-	MeOH	1	S	SE
7	NO_3^-	MeOH	2	S	SE
8	NO_3^-	H_2O	1	S	Dif MeOH→H_2O
9	NO_3^-	H_2O	1	S	Dif EtOH→H_2O
10	NO_3^-	H_2O/MeOH/DMF (2/2/1)	1	S	SE
11	AcO^-	H_2O	1	S	SE
12	SO_4^{2-}	H_2O	1	S	SE
13	ClO_4^-	H_2O	1.5	S	SE
14	BPh_4^-	H_2O	1	P	Dif H_2O→DMSO
15	BPh_4^-	H_2O/Acetone (1/1)	1	P	SE

a) For entry 14 and 15, NO_3^- was exchanged by BPh_4^-, b) M/L is the molar ratio of metal salt over ligand, c) Product obtained after 1 h stirring at room temperature: S = Soluble, P = Precipitate, d) Crystallization method attempted after reaction: SE = Slow Evaporation, Dif A→B = Slow diffusion of solvent A in solvent B.

I.4. Crystal structure description

Mononuclear or dinuclear species were obtained, depending on the couple ligand/counter-anion used in the synthesis. All the crystals obtained are summed up in Table 2. For the sake of convenience, those crystallized complexes will be named **C1-C6**. **C1** to **C4** crystals are dinuclear units while **C5** and **C6** are mononuclear species. The list of hydrogen bonds and crystallographic tables are reported in appendix.

Table 2: Summary of the obtained crystals

Complex	Name	Ligand	Counter-anion	Nuclearity
$[Mn_2(\mu\text{-}Cl)_2(Cl)_2(L^1)_2]$	**C1**	L^1	Cl^-	Di
$[Mn_2(\mu\text{-}Br)_2(Br)_2(L^1)_2]$	**C2**	L^1	Br^-	Di
$[Mn_2(\mu\text{-}N_3)_2(N_3)_2(L^1)_2]\cdot 2CH_3OH$	**C3**	L^1	N_3^-	Di
$Mn_2(\mu\text{-}N_3)_2(N_3)_2(L^2)_2]$	**C4**	L^2	N_3^-	Di
$[Mn(NO_3)(H_2O)_2L^1]\cdot NO_3$	**C5**	L^1	NO_3^-	Mono
$[MnCl_2L^2]$	**C6**	L^2	Cl^-	Mono

I.4.1 Dinuclear complexes

This series of crystals were designed and grown to be compared on both structural and magnetic bases. Table 3 gathers some relevant crystallographic data that differences the four dinuclear complexes.

Complexes **C1-C4** are dimers of Mn(II) and exhibit the same structural layout (Figure 11) though they differ by the nature of the atom composing the double bridge between the metal ions and those completing the metal environment (chlorine for **C1**, bromine for **C2**, nitrogen for **C3** and **C4**).

Table 3: Comparison of selected angles and distances in the four dinuclear complexes

Distance (Å) or angle (°)	**C1**	**C2**	**C3**	**C4**
d Mn(1)-N(1)	2.27(1)	2.26(6)	2.26(5)	2.28(4)
d Mn(1)-N(2)	2.38(8)	2.37(5)	2.38(4)	2.46(2)
d Mn(1)-N(3)	2.28(0)	2.26(4)	2.25(4)	2.18(4)
d Mn(2)-N(4)	2.28(0)	2.27(7)	2.25(4)	2.18(4)
d Mn(2)-N(5)	2.38(8)	2.40(3)	2.38(4)	2.46(2)
d Mn(2)-N(6)	2.27(1)	2.26(8)	2.26(5)	2.28(4)
d Mn(1)-X(1)[a]	2.51(4)	2.66(4)	2.24(4)	2.20(1)
d Mn(1)-X(2)[a]	2.57(4)	2.73(2)	2.22(5)	2.22(0)
d Mn(2)-X(1)[a]	2.57(4)	2.73(6)	2.22(5)	2.22(0)
d Mn(2)-X(2)[a]	2.51(4)	2.66(4)	2.24(4)	2.20(1)
d Mn(1)-Mn(2)	3.82(7)	4.00(7)	3.55(3)	3.48(3)
θ Mn(1)-X(1)-Mn(2)[a]	97.52(8)	95.81(8)	104.49(8)	103.97(1)
θ Mn(1)-X(2)-Mn(2)[a]	97.52(9)	95.89(7)	104.49(8)	103.97(1)

a) For complex **C3** and **C4**, X(1) = N(7) and X(2) = N(8)

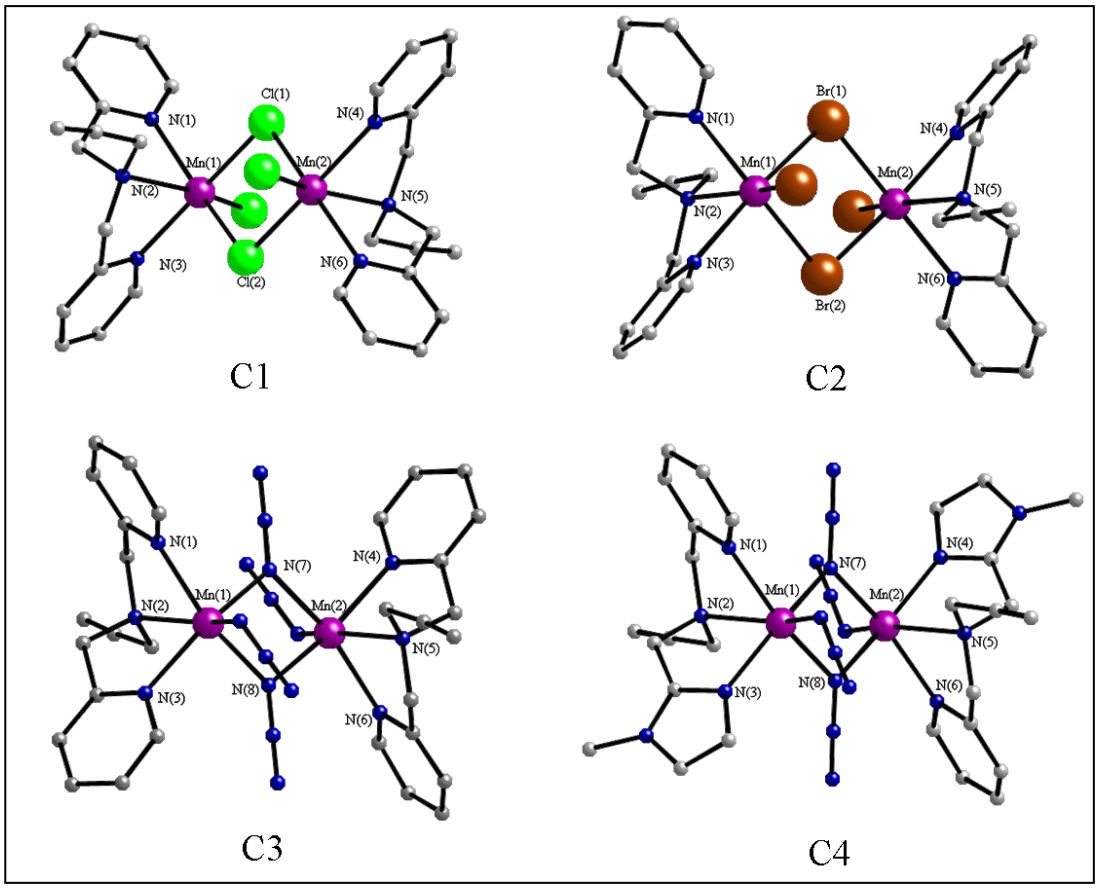

*Figure 11: Crystal structure of complexes **C1**-**C4***

Within all complexes, Mn(II) ions are located in a distorted N_3X_3 (X = Cl for **C1**, Br for **C2** and N for both **C3** and **C4**) octahedral environment. Mn-N bond lengths (nitrogen atoms from the tridentate ligand) are similar in all four complexes and in good agreement with similar complexes involving double bridge with chlorine atoms [47, 48, 49], bromine atoms [45] and azido groups [50, 51, 52, 53] referenced in the literature. It is important to note that the Mn-N bond length involving the central nitrogen atom of the ligand is usually *ca.* 0.1 Å longer than the two others. In the case of complex **C4**, involving L^2, Mn-N bond lengths are noticeably shorter (*ca.* 0.1 Å) for the external nitrogen atoms of the ligand and longer (*ca.* 0.1 Å) for the central one than those observed for complexes **C1**-**C3** involving L^1. The environment of the metal ions is completed by three X atoms with two of which involved in the double bridge between the two Mn(II) ions. As expected, Mn-Cl bond lengths are shorter than the Mn-Br ones. Moreover, Mn-X bond lengths, for X involved in the double bridge (Cl(1), Br(1)), for both Cl and Br, are longer (*ca.* 0.1 Å) the other one (Cl(3), Br(3)), coordinated to only one metallic centre.

The distortion of the metal ion octahedral environment is also exemplified by the distribution, far from the ideal values of 90° and 180°, of the X-Mn-X angles (X = N, Br and Cl) ranging from 70.9(1)° to 102.57(4)° (theoretical value of 90° for a perfect octahedral environment) and from 157.83(7)° to 163.87(7)° (ideal value: 180°) for **C1**; from 71.45(8)° to 101.69(2)° and from 159.85(5)° to 165.10(6)° for **C2**; from 72.6(5)° to 105.08(6)° and from 154.43(6)° to 163.57(6)° for **C3**; from 69.7(1)° to 103.3(1)° and from 154.7(1)° to 161.8(1)° for **C4**.

In the case of complexes **C1** and **C2**, the metal ions are linked together by a symmetrical double μ_2-halogen bridge (Cl and Br for **C1** and **C2**, respectively) with Mn-X bond lengths equal to 2.574(1) Å and 2.515(2) Å for **C1**; 2,6641(5) Å and 2.7333(5) Å for **C2**. The Mn-X-Mn angles are equal to 97.52(4)° and 95.88(1)° for **C1** and **C2**, respectively.

Within complexes **C3** and **C4**, Mn(II) metal ions are linked together via a double EO azido-bridge (Figure 7). In both cases, this bridge is almost symmetrical as the Mn-N bond distances are close: 2.225(2) Å and 2.244(2) Å for **C3**; 2.201(3) Å and 2.221(3) Å for **C4**. Mn-N-Mn angles are equal to 104.50(6)° and 104.0(1)° for **C3** and **C4**, respectively.

Structural packing in complexes **C1** and **C2** is realized by H-X (X = Cl and Br for **C1** and **C2**, respectively) weak interactions leading to a dense 3D network. In case of complex **C3**, the co-crystallized methanol molecule, through the hydrogen atom of the alcoholic group, forms hydrogen bonds with the terminal nitrogen atom of the double azido-bridge. Finally, for

complexes **C3** and **C4**, the crystal packing, in both cases, is assumed by weak interactions as Van der Waals ones for example.

I.4.2 Mononuclear complexes

Crystals of complexes **C5** and **C6** are mononuclear species. Contrary to the dinuclear species, the structure will be described independently because their structure is not related.

- Crystal structure of **C5**:

Compound **C5** is made up of a cationic monomer $[Mn(NO_3)(H_2O)_2L^1]^+$ which reaches electroneutrality with a nitrate counter-anion (Figure 12). In this complex, the Mn(II) metal ion is located in a heptacoordinated N_3O_4 distorted pentagonal bipyramidal environment. Three nitrogen atoms (N(1), N(2) and N(3)) from L^1 and two oxygen atoms (O(3) and O(4)) from the bidentate nitrate counter-anion occupy the equatorial positions while two coordinating oxygen atoms (O(1) and O(2)) from water molecules are placed in axial position (Figure 12). Contrary to the previous dinuclear complexes, the manganese(II) centre is not in an octahedral environment anymore. The second nitrate counter-anion is not coordinated to the metallic centre but co-crystallized. The bidentate nitrate anion is asymmetrically coordinated to the manganese(II), as one bond is noticeably longer than the other (*ca.* 0.3 Å). The two Mn-O(1) and Mn-O(2) length bonds are almost equal, as they only differ by 0.04 Å (2.18(9) Å for Mn-O(1) and 2.15(3) Å for Mn-O(2)). In the meantime, the distance Mn-O(3) (2.29(5) Å) is around 0.1 Å longer than the Mn-O(1) one. While Mn-N(1) and Mn-N(3) bond lengths are really close (2.26(1) and 2.24(8) respectively), the Mn-N(2) bond length involving central nitrogen atom from the ligand (2.38(7) Å) is as expected a little bit longer (*ca.* 0.1 Å). Those values are comparable with the bond lengths in **C1**-**C3**.

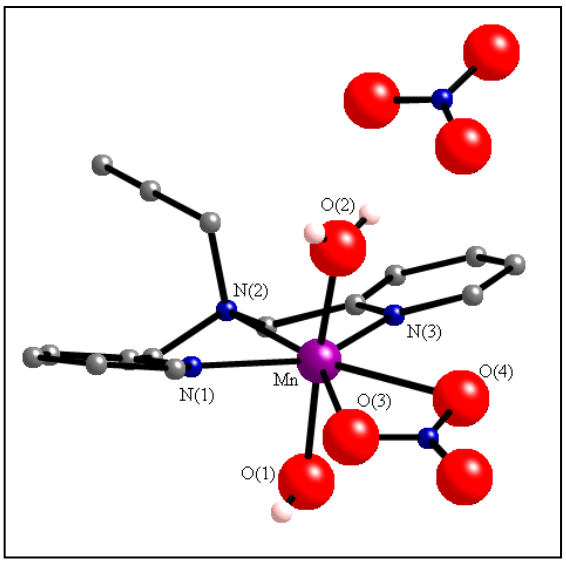

*Figure 12: Crystal structure of **C5***

This complex also displays a distorted geometry, with bond angles differing from the ideal case. Considering the two oxygen atoms from water molecules as the axial atoms of the pentagonal bipyramid would imply an O(1)-Mn-O(2) angle of 180° instead of the actual value of 173.93(4)°. Likewise, the angle X-Mn-X' where X and X' are two adjacent atoms from the

plane should be 72°. The crystal structure of **C5** exhibits a range of angle between 51.04(0)° (for O(3)-Mn-O(4)) and 83.41(6)° (for N(1)-Mn-O(1)). The two N(1)-Mn-N(2) and N(2)-Mn-N(3) bond angles are actually really close to the ideal values as they measure respectively 72.07(1)° and 72.58(4)°. The metallic centre is displaced of 0.046(3) Å from the main plane towards the O(2) atom.

A major difference between **C5** and **C1**-**C3** lies in the coordination of the ligand. While in the first three crystals the nitrogen atoms were in facial position, they adopt a meridional conformation in **C5**. This can be measured with the torsion angle between N(1)-Mn-N(2)-N(3) in both cases: in **C1** for instance this torsion angle measures 106.01(7)° while its equivalent in **C5** measures 174.48(1)°.

The structure adopts a 2D dimensionality by the hydrogen bond interactions between the coordinated water molecules (O(1) and O(2)) and the oxygen atoms of the free nitrate molecules as well as π–π interactions between the pyridyl rings of neighbour monomeric units.

- Crystal structure of **C6**:

Complex **C6** is a neutral mononuclear complex of formula $[MnCl_2L^2]$ (Figure 13). The manganese(II) centre is positioned in a five-coordinated N_3Cl_2 environment, which is not common for a manganese(II) ion. The three nitrogen atoms (N1, N2 and N3) from L^2 and two chloride atoms (Cl(1) and Cl(2)) make up the coordination sphere. The Mn-N distances vary in the range of 2.15(0)-2.45(0) Å. The Mn-N(2) bond length involving central nitrogen atom of the ligand (2.45(0) Å) is as expected longer than the Mn-N(1) distance (2.21(7) Å) and the Mn-N3 one (2.15(0) Å). As for the coordination with the ligand, Mn-N bond lengths are similar to the Mn-N bond lengths found in **C4**. Both Mn-Cl bond lengths are similar, 2.34(3) Å and 2.39(2) Å. They are shorter than in **C1** because in this case they are terminal ligands while in the first one they were bridged ligands.

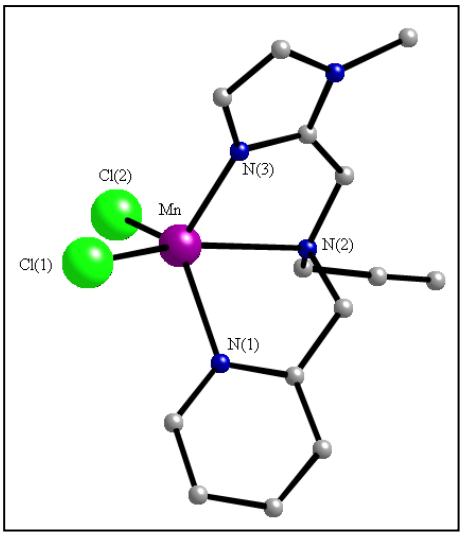

Figure 13: Crystal structure of C6

This complex presents a structure between distorted square pyramidal geometry and distorted trigonal bipyramid geometry. The distortion parameter τ quantifies from 0 to 1 the transition from square pyramidal to trigonal bipyramidal respectively (Equation 1, Figure 14).

[54] So, a parameter τ = 0 is a perfect square pyramidal geometry while a parameter τ = 1 corresponds to a perfect trigonal bipyramidal geometry.

$$\tau = \frac{(\beta - \alpha)}{60} \qquad \textit{Equation 1}$$

In our case, β stands for the N(1)-Mn-N(3) bond angle and α corresponds to the Cl(1)-Mn-Cl(2) one, resulting a distortion parameter τ of 0.28. Therefore the geometry is closer to a distorted square pyramid.

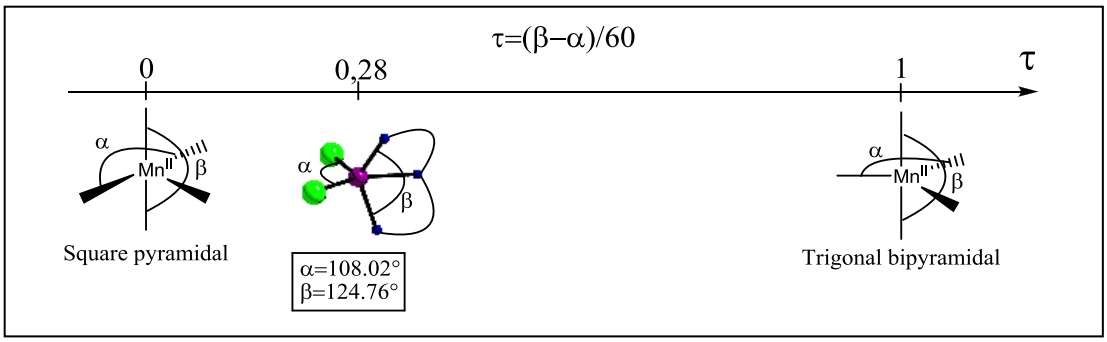

Figure 14: Definition of τ parameter

Both Mn-Cl bond lengths are similar, 2.34(3) Å and 2.39(3) Å. As for the coordination with the ligand, Mn-N bond lengths are similar to the Mn-N bond lengths found in **C4**.

Once again, comparing the dihedral angle N(1)-N(2)-Mn-N(3) in **C4** and **C6** crystals (respectively di- and mononuclear species) enlightens the difference of coordination of the ligand. Though this separation is much less pronounced than in the case of L^1, the two dihedral angles are quite different, with a dihedral angle of 136.09(3) for **C6** against 110.06(8) for **C4**. Therefore, the three nitrogen atoms and the manganese(II) centre are no longer in the same plane like their equivalent in **C5** but their orientation is not as inclined as in **C4**.

The structure holds it by very weak π-π interactions between the pyridyl rings of neighbour monomeric units, electrostatic and Van der Waals forces.

I.5. Study of the magnetic properties

In this part, fundamentals of molecular magnetism will be reminded. Then SQUID (for Superconducting Quantum Interference Device) measurements of all four dinuclear complexes will be used to discuss the magnetic properties of those complexes. Finally EPR spectra have been measured to compare the behaviour of these complexes in liquid and solid states.

I.5.1. Fundamentals of molecular magnetism

It has been known for a long time that every substance possesses magnetic properties. Indeed, when a magnetic field H is applied, then the magnetic induction B is given by Equation 2.

$$B = H + 4\pi I \qquad \textit{Equation 2}$$

In this equation, I represents the volumetric magnetic moment. Dividing this equation per H provides Equation 3.

$$P = 1 + 4\pi\kappa \qquad \textit{Equation 3}$$

P and κ are respectively called volumetric permeability and susceptibility. To obtain the molar susceptibility χ_M, in practice more convenient to use, κ is divided by the density and multiplied by the molar weight.

Substances are classified by using Equation 3:

- If P<1, *i.e.*, κ and χ are negative, then the substance is called diamagnetic. Consequently, the density of lines of force is reduced within the sample. Measured values of χ are really small, around -1×10^{-6}.
- If P>1, *i.e.*, κ and χ are positive, then the substance is called paramagnetic. Contrary to the previous case, the density of lines of forces within the sample is increased.

However, every substance contains an underlying diamagnetism. The overall magnetic susceptibility of a compound is thus the sum of both its paramagnetic and diamagnetic susceptibility (χ^D and χ^P), as written in Equation 4

$$\chi = \chi^D + \chi^P \qquad \textit{Equation 4}$$

This diamagnetic contribution can be corrected to retrieve the paramagnetic component alone. From now on, χ will design the paramagnetic susceptibility alone, *i.e.*, the magnetic susceptibility corrected from its diamagnetic part.

Determining this susceptibility can be done using Van Vleck's formula (Equation 5):

$$\chi = \frac{N\sum_n E_n^{(1)2} \exp(-E_n^{(0)}/kT)}{kT\sum_n \exp(-E_n^{(0)}/kT)} \qquad \textit{Equation 5}$$

Here N is the Avogadro number, k is the Boltzmann constant, $E_n^{(0)}$ is the energy of level n in zero field, and $E_n^{(1)}$ represents the first order Zeeman coefficient.

Let's consider now a molecule possessing a spin number S, a large separation between excited states (*i.e.*, no coupling between those states) and no first-order angular momentum. The application of an external magnetic field H will remove the degeneracy of the ground state into 2S+1 Zeeman components whose energies will be given by:

$$E_n = M_S g\beta H \qquad \textit{Equation 6}$$

In this equation M_S varies by an integer from –S to +S, g is the g-factor and β the Bohr magneton. When H/kT is small, then $E_n^{(0)} = 0$ and $E_n^{(1)} = M_S g\beta$. Applying this approximation in Van Vleck's formula leads after simplification to:

$$\chi = \frac{Ng^2\beta^2}{3kT} S(S+1) \qquad \textit{Equation 7}$$

Then χ varies linearly as a function of 1/T. Indeed, the reduced expression χ = C/T known empirically since 1910 as the Curie law obtained theoretical foundations with Van Vleck who shade into light the relation between C and the spin state of the considered matter.

Ferromagnetic and antiferromagnetic compounds are subdivisions of paramagnetic substances. When coupling between two paramagnetic centres is possible, a spin ordering can be observed at low temperature. For ferromagnetic substances, this coupling implies a parallel orientation of spins, whereas for antiferromagnetism, antiparallel organisation is generated (Figure 15). For ferromagnetic compounds, the temperature below which this interaction can be observed is called the Curie temperature (or Curie point), while it is called the Neel temperature for antiferromagnetic species.

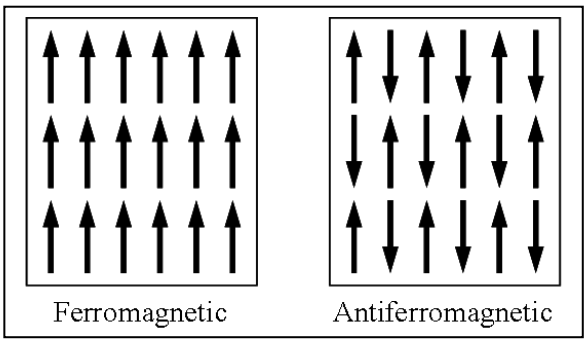

Figure 15: Spin organization in ferro- and antiferromagnetic materials

As our studied complexes crystallized in a dinuclear fashion, let us consider the case of two metal ions bridged by a diamagnetic ligand able to transmit the electronic effects between the two paramagnetic centres. A simple case would be two local spins S_A and S_B with $S_A = S_B = 1/2$. Total spin S can therefore be equal to 0 or 1, and the energies of both states are separated by an energy gap J defined as E(S = 0)-E(S = 1) and called the isotropic

interaction parameter. Depending on the ground state, coupling constant J can be either positive or negative. If J > 0, then S = 1 is the ground state, the interaction is ferromagnetic, while if J < 0, S = 0 is the ground state and the interaction is antiferromagnetic.

Upon application of a magnetic field, the triplet state will split in three states corresponding to the three values of M_s. As explained before, if no interaction between this triplet state (chosen as origin of energies) and the singlet state is considered, the magnetic susceptibility can be written using Van Vleck's formula:

$$\chi = \frac{2Ng^2\beta^2}{kT\left[3+\exp\left(-J/kT\right)\right]} \qquad \textit{Equation 8}$$

Under those hypotheses, the spin Hamiltonian, also known in this case as the Heisenberg-Dirac-Van Vleck Hamiltonian (HDVV), can be expressed as:

$$\mathbf{H} = -J\mathbf{S_A}\cdot\mathbf{S_B} \qquad \textit{Equation 9}$$

Writing that $\mathbf{S} = \mathbf{S_A}+\mathbf{S_B}$ and developing this Hamiltonian leads to the eigenvalues:

$$E(S,S_A,S_B) = -\frac{J}{2}\left[S(S+1)-S_A(S_A+1)-S_B(S_B+1)\right] \qquad \textit{Equation 10}$$

or, after a change of origin:

$$E(S) = -\frac{J}{2}S(S+1) \qquad \textit{Equation 11}$$

Let us consider now a little more complicated case, when $S_A > 1/2$. The spin Hamiltonian taking into account the Zeeman perturbation can now be written as:

$$\mathbf{H} = -J\mathbf{S_A}\cdot\mathbf{S_B} + \beta\left(\mathbf{S_A}\cdot\mathbf{g_A}+\mathbf{S_B}\cdot\mathbf{g_B}\right)\cdot H \qquad \textit{Equation 12}$$

where $\mathbf{g_A}$ and $\mathbf{g_B}$ are the **g**-tensors associated with the two interacting centres. For two high spin Mn(II) centres, $S_A = S_B = 5/2$, therefore S varies by an integer from 0 to 5. This Hamiltonian neglect both zero-field splitting and anisotropic interactions. Therefore magnetic susceptibility can be expressed as:

$$\chi = \frac{Ng^2\beta^2}{kT}\frac{\sum_S\sum_{M_S=-S}^{+S}M_S^2\exp\left[-E(S)/kT\right]}{\sum_S(2S+1)\exp\left[-E(S)/kT\right]} \qquad \textit{Equation 13}$$

which can be rewritten as:

$$\chi = \frac{Ng^2\beta^2}{kT}\frac{\sum_S S(S+1)(2S+1)\exp\left[-E(S)/kT\right]}{\sum_S(2S+1)\exp\left[-E(S)/kT\right]} \qquad \textit{Equation 14}$$

In the case of high spin Mn(II) centres, Zeeman perturbation splits every energy level in 2S+1 components (Figure 16).

Consequently, the molar magnetic susceptibility is expressed as:

$$\chi = \frac{2Ng^2\beta^2}{kT}\frac{e^x + 5e^{3x} + 14e^{6x} + 30e^{10x} + 55e^{15x}}{1 + 3e^x + 5e^{3x} + 7e^{6x} + 9e^{10x} + 11e^{15x}} \qquad \textit{Equation 15}$$

with x = J/kT.

Fitting the experimental curve with this expression of χ leads to the value of J.

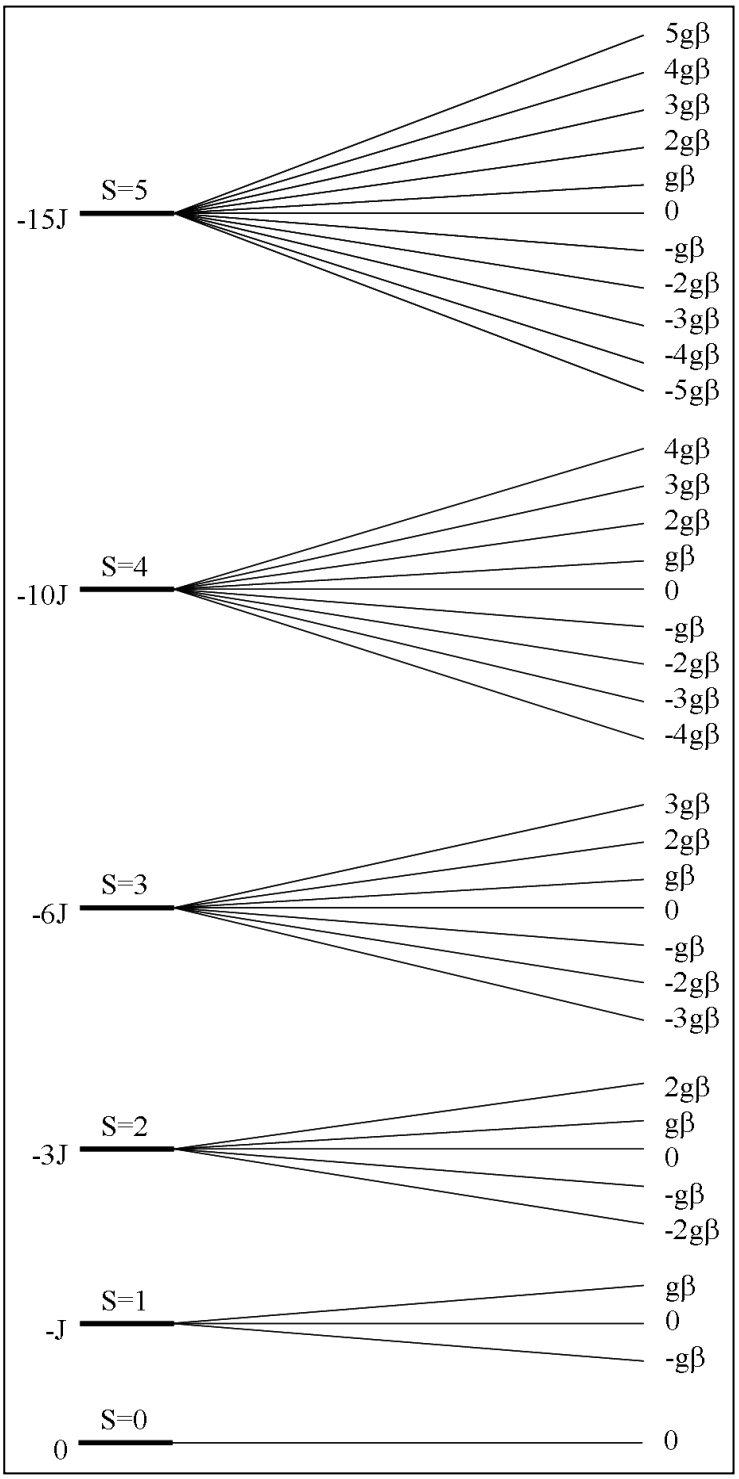

Figure 16: Energy levels and Zeeman first order coefficients in the case of a spin S=5

I.5.2. Magnetic susceptibility

Figures 17-19 exhibit the $\chi_M T$ *versus* T plots for compounds **C1-C4** respectively, χ_M being the magnetic susceptibility per two Mn(II) ions. At room temperature, $\chi_M T$ for **C1** and **C2** is *ca*. 8.75 $cm^3.mol^{-1}.K$. Whereas this value is expected for two magnetically isolated Mn(II) metal ions, the corresponding values of $\chi_M T$ for **C3** and **C4** are somewhat greater (*ca*. 9.5 $cm^3.mol^{-1}.K$). Upon cooling, the value of $\chi_M T$ for **C1** remains constant until 25.0 K and it further decreases to 7.70 $cm^3.mol^{-1}.K$ at 2.0 K, suggesting the occurrence of a very weak antiferromagnetic interaction. In contrast, the values of $\chi_M T$ for **C2-C4** continuously increase while the temperature decreases to reach maxima at 5.5 K (*ca*. 11.3 $cm^3.mol^{-1}.K$) for **C2** and 10 K (*ca*. 14.8 $cm^3.mol^{-1}.K$) for **C3** and **C4**. After these maxima, $\chi_M T$ decreases to 7.5 (**C2**), 13.7 (**C3**) and 13.9 $cm^3.mol^{-1}.K$ (**C4**) at 2.0 K. The increase of the values of $\chi_M T$ in the high temperature region for **C2-C4** is indicative of the occurrence of a ferromagnetic interaction between the paramagnetic Mn(II) ions, whereas the decrease at low temperatures can be attributed to weak intermolecular antiferromagnetic interactions and/or zero-field splitting of the S = 5 ground spin state. However, because of the large isotropic character of the six-coordinate high-spin Mn(II) ion, the zero-field splitting effects are expected to be negligible.

As explained earlier, the expression for the magnetic susceptibility for a dimanganese(II) unit derived from the Van Vleck's equation is given by Equation 16: [55]

$$\chi_M = \frac{2N\beta^2 g^2}{k(T-\theta)} \frac{e^x + 5e^{3x} + 14e^{6x} + 30e^{10x} + 55e^{15x}}{1 + 3e^x + 5e^{3x} + 7e^{6x} + 9e^{10x} + 11e^{15x}} \qquad \textit{Equation 16}$$

where x = J/kT and θ is the Weiss constant defined as θ = zJ'S(S+1)/3k with zJ' accounting for the magnetic interaction between the *z* nearest dinuclear units. The other parameters have their usual meaning. The best-fit parameters obtained are listed in Table 4.

*Table 4: Best-fit parameters for complexes **C1-C4***

Complex	*g*	J (cm^{-1}) [a]	zJ' (cm^{-1})
C1	1.99	-0.06	0.0
C2	1.99	+1.04	-0.20
C3	2.01	+5.30	-0.060
C4	2.02	+4.99	-0.052

a) Accuracy: ± 0.01 cm^{-1}

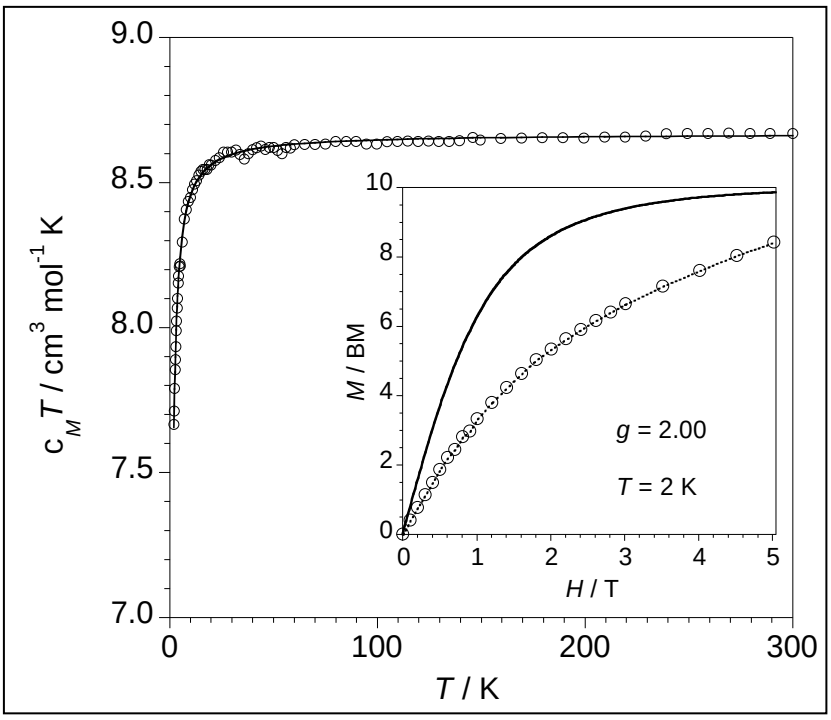

*Figure 17: Temperature dependence of $\chi_M T$ for **C1**. The solid line represents the best fit based on the parameters discussed in the text while the inset shows the magnetization curve at 2.0 K and the solid line is the theoretical Brillouin curve for two magnetically independent spin sextuplets, S = 5/2.*

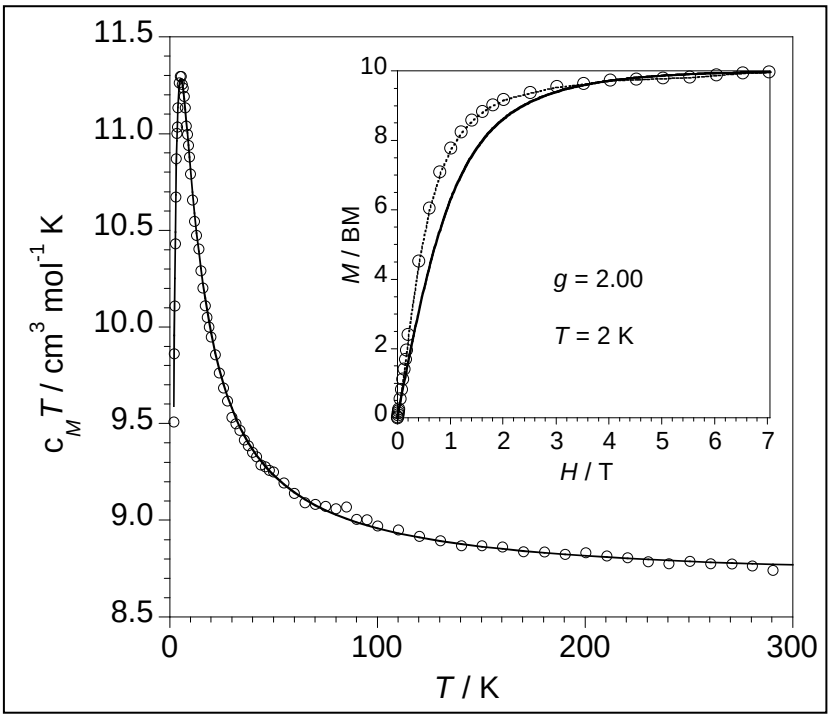

*Figure 18: Temperature dependence of $\chi_M T$ for **C2**. The solid line represents the best fit based on the parameters discussed in the text while the inset shows the magnetization curve at 2.0 K and the solid line is the theoretical Brillouin curve for two magnetically independent spin sextuplets, S = 5/2.*

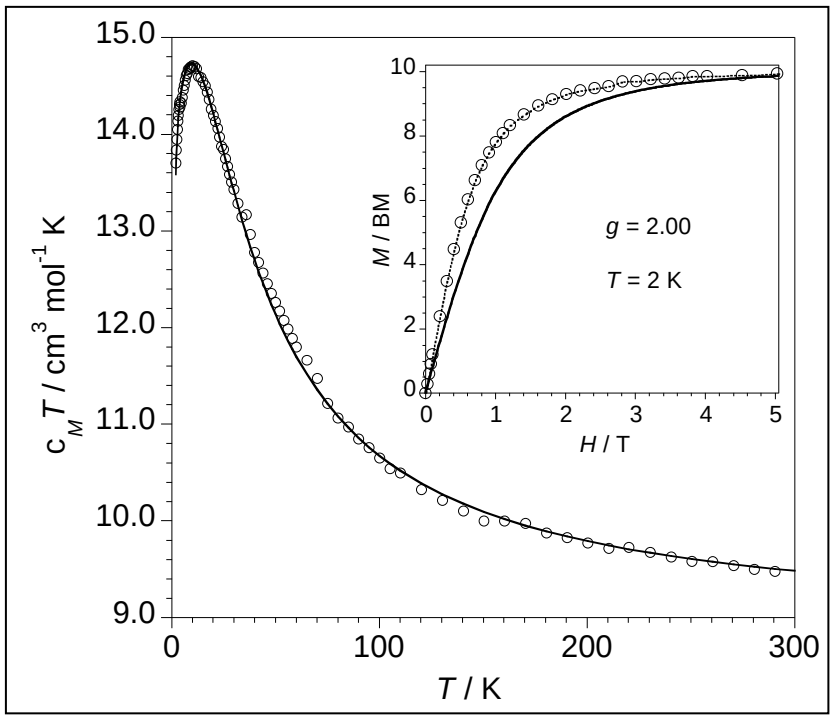

*Figure 20: Temperature dependence of $\chi_M T$ for **C3**. The solid line represents the best fit based on the parameters discussed in the text while the inset shows the magnetization curve at 2.0 K and the solid line is the theoretical Brillouin curve for two magnetically independent spin sextuplets, S = 5/2.*

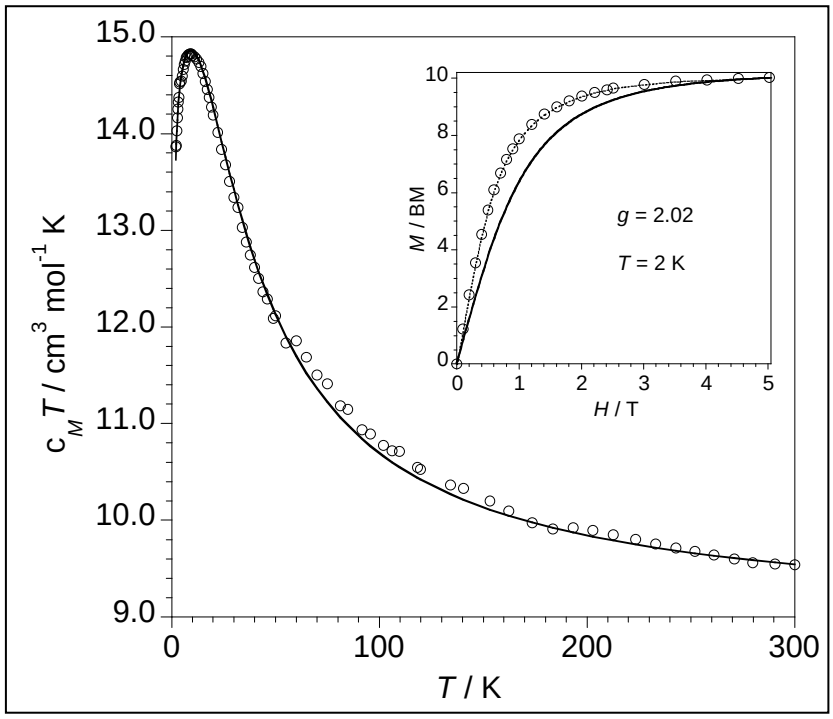

*Figure 19: Temperature dependence of $\chi_M T$ for **C4**. The solid line represents the best fit based on the parameters discussed in the text while the inset shows the magnetization curve at 2.0 K and the solid line is the theoretical Brillouin curve for two magnetically independent spin sextuplets, S = 5/2.*

As indicated above, the decrease of $\chi_M T$ at low temperatures could be alternatively interpreted by the presence of a zero-field splitting (D). Having this possibility in mind, the magnetic data for **C2-C4** were also analyzed through the Hamiltonian of Equation 17 by using the VPMAG FORTRAN program that allows us to determine these values through numerical matrix diagonalization. [56, 57]

$$H = -J\mathbf{S_{Mn1}} \cdot \mathbf{S_{Mn2}} + D(\mathbf{S}^2_{\mathbf{z\,Mn1}} + \mathbf{S}^2_{\mathbf{z\,Mn2}} + 35/6) \qquad \textit{Equation 17}$$

The least-squares fit of the experimental data to this equation gave values for the g and J parameters similar to those obtained through Equation 16 (Table 4). However the values for the D parameter (4.9 cm^{-1} for **C2**, 1.4 cm^{-1} for **C3** and 1.1 cm^{-1} for **C4**) are too high to be considered real and they are meaningless. Therefore the decrease of the $\chi_M T$ values has to be certainly attributed to intermolecular antiferromagnetic interactions between near dinuclear units.

Field dependence magnetization plots of **C1-C4** at 2.0 K are shown in the inset of the corresponding Figures 17-19. The magnetization data for **C1** are well below the Brillouin curve for two magnetically isolated S = 5/2 Mn(II) ions, while they are well above for **C2-C4**, in agreement with the occurrence of antiferro- (**C1**) or ferromagnetic (**C2-C4**) interactions between the Mn(II) ions.

The magneto-structural parameters obtained with both **C1** and **C2** were compared with a series of $[Mn^{II}(\mu\text{-}X)_2Mn^{II}]$ (X = Cl or Br) dinuclear complexes, which were subject of previous studies (Table 5). As far as we know, no theoretical magneto-structural correlation has been reported for this family. By observing the results reported in the table, no correlation seems to exist between the structural parameters (angles or distances) and magnetic coupling parameter (J), this circumstance being most likely due to the scarce number of compounds, the small variation of the structural parameters and the experimental errors. However, there must exist a correlation between the size and nature of the magnetic exchange and the structural parameters, the value of the Mn-X-Mn angle being the most determinant one, as it is known for other metal ions or other bridging ligands. [58] In fact, experimental data from Table 5 predict a change from ferro- to antiferromagnetic behaviour at an angle of *ca.* 97^o for the bridgehead chloro atom. The value of this crossover Mn-Cl-Mn angle is very close to that observed for the di-μ-hydroxodicopper(II) complexes (*ca.* 97.5^o). [59] Compound **C2** is the first di-μ-bromodimanganese(II) complex reported and thus we can only compare it with the chloro derivatives listed in Table 5.

Table 5: Selected magneto-structural parameters for $[Mn^{II}(\mu\text{-}X)_2Mn^{II}]$ complexes (X = Cl or Br)

Compound[a]	$d_{Mn\text{-}Mn}$ (Å)	$d_{Mn\text{-}Cl}$ (Å)	Mn-Cl-Mn (°)	J (cm^{-1})	Reference
$[Mn_2(biz)_2(\mu\text{-}Cl)_2]Cl_2$	3.74	2.57	93.5	+0.66	[49]
$[Mn_2Cl_2(bpea)_2(\mu\text{-}Cl)_2]$	3.79	2.48	95.7	+0.68	[47]
$[Mn_2Cl_2(mpba)_2(\mu\text{-}Cl)_2]$	3.9	2.50	96.4	+1.1	[48]
C1		2.54	97.5	–0.06	This work
C2		2.69	95.9	+1.04	This work

a) biz = 2,2'-biimidazoline, bpa = N,N'-bis(2-pyridylmethyl)ethylamine, mpbpa = N-(3-methoxypropyl)-N,N'-bis(pyridin-2-ylmethyl)amine.

Concerning the di-$\mu_{1,1}$-azidodimanganese(II) complexes (**C3** and **C4**), an experimental relationship between the magnetic coupling (J) and the Mn-N-Mn bridging angle (θ) was proposed. [52, 60] Expressing J in cm^{-1} and θ in degree would verify the relation:

$$J = 0.552\theta - 53.8 \qquad \textit{Equation 18}$$

Table 6 shows the magneto-structural parameters for double end-on azido-bridged Mn(II) complexes. **C3** and **C4** follow roughly the above relationship and they are in good agreement with the fact that the value of the exchange coupling constant increases with the Mn-N-Mn bridging angle, which is consistent with theoretical predictions. [58] A careful inspection of the data listed in Table 6 shows that the values of the coupling parameter J generally increase with an increase in the difference between the two Mn-N(bridging azide) bond distances (Δd in Table 6), [52] which is an increase in the asymmetry of the azido bridging. In this sense, a better magneto-structural correlation is observed when both structural parameters θ and Δd were used. Figure 21 shows the values of J *versus* the corresponding values of $(\theta + 10\Delta d)$ from Table 6. The best linear fit gives the equation:

$$J = 0.553(\theta + 10\Delta d) - 54.111 \qquad \textit{Equation 19}$$

In this equation, J is expressed in cm^{-1}, θ in degrees and Δd in angstrom.

This linear fit is slightly better than:

$$J = 0.576\theta - 54.040 \qquad \textit{Equation 20}$$

where the influence of Δd was neglected.

Table 6: Selected magneto-structural parameters for di-$\mu_{1,1}$-azidodimanganese(II) complexes.[a]

Compound	Δd(Å)	θ(°)	θ+10Δd	J (cm^{-1})	Reference
$[Mn_2(ttp)_2(N_3)_2(\mu_{1,1}\text{-}N_3)_2]$	0.236	103.45	105.81	4.92	52
$[Mn_2(ttp\text{-}N_3)_2(N_3)_2(\mu_{1,1}\text{-}N_3)_2]$	0.252	103.13	105.65	4.50	52
$[Mn_2(ttp\text{-}N_3)_2(N_3)_2(\mu_{1,1}\text{-}N_3)_2]_2[Mn(ttp\text{-}N_3)(N_3)_3]$	0.150	105.29	106.79	3.84	52
$[Mn_2(terpy)_2(N_3)_2(\mu_{1,1}\text{-}N_3)_2]\cdot 2H_2O$	0.090	104.60	105.50	4.86	61
$[Mn_2(L^A)_2(\mu_{1,1}\text{-}N_3)_2](ClO_4)_2$	0.030	102.12	102.42	1.54	60
$[Mn_2(L^B)2(\mu_{1,1}\text{-}N_3)_2](ClO_4)_2$	0.072	104.29	105.01	4.09	60
$[Mn_2(L^C)2((\mu_{1,1}\text{-}N_3)_2](ClO_4)_2$	0.053	103.58	104.11	3.50	60
$[Mn_2(phen)_4(\mu_{1,1}\text{-}N_3)_2][Co(bpb)(CN)_2]_2\cdot H_2O$	0.002	102.60	102.62	2.54	62
$[Mn_2(phen)_4(\mu_{1,1}\text{-}N_3)_2][Cr(bpb)(CN)_2]_2\cdot H_2O$	0.003	102.55	102.58	2.20	62
$[Mn_2(phen)_4(\mu_{1,1}\text{-}N_3)_2][Fe(bpb)(CN)_2]_2\cdot H_2O$	0.006	101.40	101.46	2.40	62
$[Mn_2(2,2'\text{-}dpa)_2(N_3)_2(\mu_{1,1}\text{-}N_3)_2]$	0.059	103.11	103.70	2.24	50
$[Mn(tptz)(\mu_{1,1}\text{-}N_3)_2]_n$	0.002	106.16	106.18	4.06	63
$[Mn(pyz)(\mu_{1,1}\text{-}N_3)_2]$	0.000	98.80	98.800	1.22	64
$[Mn(2\text{-}bzpy)(\mu_{1,1}\text{-}N_3)_2]_n$	0.032	100.50	100.82	0.80	65
$[Mn_2L^B(N_3)_2(\mu_{1,1}\text{-}N_3)_2]$	0.202	100.38	102.40	2.62	53
C3: $[Mn_2(L^1)_2(N_3)_2(\mu_{1,1}\text{-}N_3)_2]\cdot 2CH_3OH$	0.019	104.50	104.69	5.30	This work
C4: $[Mn_2(L^2)_2(N_3)_2(\mu_{1,1}\text{-}N_3)_2]$	0.020	103.96	104.16	4.99	This work

a) Average values. $\Delta d = d(Mn–N_{azido}) – d(Mn–N'_{azido})$. ttp = 4'-*p*-Tolyl-2,2':6',2''-terpyridine, ttp-N_3 = 4'-*p*-Azidomethylphenyl-2,2':6',2''-terpyridine, L^A = [N,N-bis(pyridine-2-yl)benzylidene]ethane-1,2-diamine, L^B = [N,N-bis(pyridine-2-yl)-benzylidene]propane-1,3-diamine, L^C = [N,N-bis(pyridine-2-yl)benzylidene]butane-1,4-diamine, bpb^{2-} = 1,2-bis(pyridine-2-carboxamido)benzenate, 2,2'-dpa = 2,2'-dipicolylamine, tptz = 2,4,6-tris(2-pyridyl)-1,3,5-triazine, pyz = pyrazine, 2-bzpy = 2-benzoylpyridine.

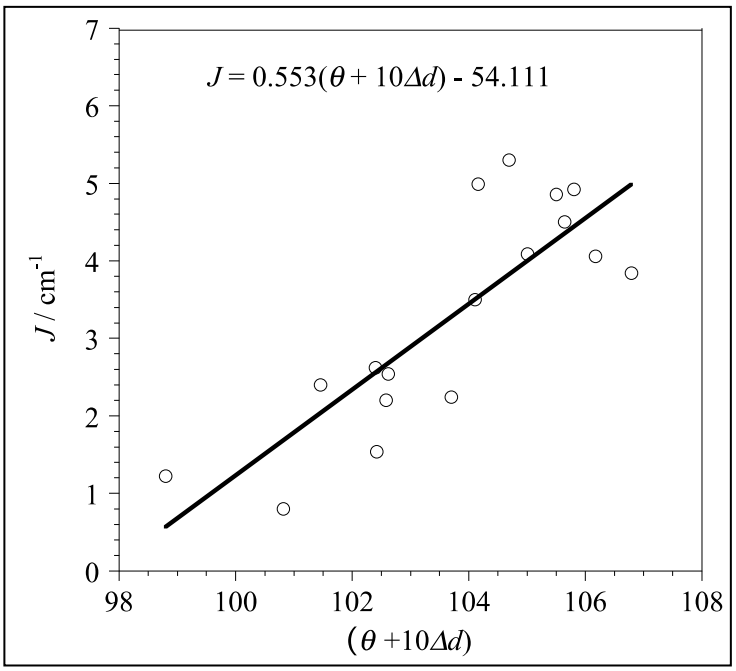

Figure 21: Plot of J versus (θ + 10Δd), θ being the average Mn-N-Mn angles and Δd the average Mn-N(azido-bridge) bond distances (see text), for double EO azido-bridged Mn(II) complexes (Table 6). The solid straight line represents the best linear fit to Equation 19

I.5.3. Electron paramagnetic resonance study

Electronic paramagnetic resonance (EPR) takes advantage of the interaction between electromagnetic radiations and magnetic moments from electrons. Herein will be explained the basics of this technique.

In an EPR spectrometer, the sample is placed in a resonant cavity immerged in a magnetic field H where a microwave irradiation by a wave-guide at a given frequency ν is maintained constant at the resonant value during measurement. Let us consider the spin ½ of an electron. When the magnetic field varies, Zeeman effect will split the energy levels in two distinct levels ±½ which energy will be $\pm\frac{1}{2}g_e\beta_e H$. Therefore, when the difference of energy between the two levels is equal to hν (the energy of the exciting irradiation), transition occurs. The EPR spectrometer measures this transition.

However when this electron is close to a nucleus possessing a spin quantum number I, the energy levels are perturbed, and the energy diagram is modified (Figure 22). Transition will occur for $\Delta M_S = \pm 1$ and $\Delta M_I = 0$.

Now, instead of a single resonance value of magnetic field, there are two values, one for each possible value of M_I. Those results can also be applied to larger values of I, for instance 5/2 in the case of Mn(II) metal ions. In this case, their will be 6 possible transitions (2I + 1) that will respect the conditions $\Delta M_S = \pm 1$ and $\Delta M_I = 0$.

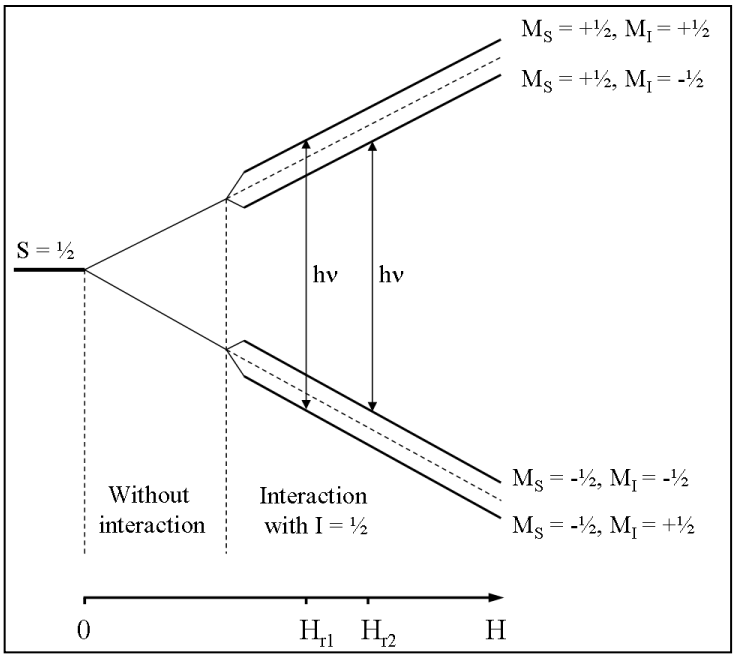

Figure 22: Energy levels of a single electron in interaction with a nucleus with I = 1/2. Two resonnances can be observed for H = H_{r1} or H = H_{r2}

EPR spectra in liquid and solid states were measured for two complexes, **C1** and **C6**. Solid state spectra were performed at 117 K using mashed crystals of the complexes to ensure both absence of impurities and metal coordination: dinuclear species and hexacoordinated metal ion for **C1**, mononuclear species and pentacoordinated metal ion for **C6**. Liquid spectra were measured at 116 K in a mixture EtOH/MeOH 1/1.

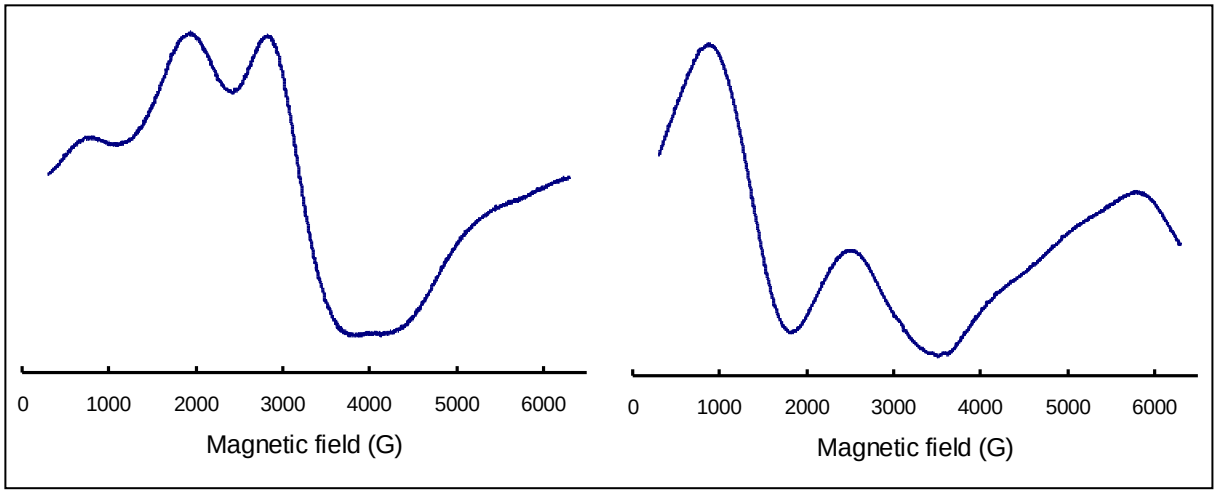

*Figure 23: Solid-state EPR spectra of **C1** (left) and **C6** (right) at 117 K. Microwave frequency: 9.41 GHz, amplitude modulation: 1 G, gain: 60 dB, power: 6 mW.*

Figure 23 present solid state EPR spectra of **C1** and **C6** complexes. As determined with SQUID measurements, the coupling constant J between the two Mn(II) centres in **C1** is really weak ($|J| = 0.06$ cm^{-1}) which means the states S = 0-5 are not well separated in energy. The exciting energy provided by the microwave irradiation, which is around 0.3 cm^{-1} (9.4

GHz), is ten times greater than this coupling constant. Therefore, in order to fully understand the solid state EPR spectra of **C1**, interaction between metallic centres cannot be omitted. Furthermore, the crystal structure shows a distorted octahedral geometry for each manganese(II). This distortion can induce an additional zero-field splitting D that, once again, has an influence on the final spectra. These distortion and coupling will generate new transitions which will mean a much more complicated spectrum. Therefore further investigations and simulations would require supplementary measurements, in particular a temperature-dependence study of the EPR signal.

Frozen solution spectra in a MeOH/EtOH (1/1) mixture at 116 K turned out to be much simpler to interpret (Figure 24 and 25). Indeed, the behaviour of the dissolved complexes completely changes compared to their solid-state equivalent. EPR spectra now exhibit six main bands characteristic of a hyperfine interaction between an electron and an isolated nucleus spin of 5/2, even for **C1** that crystallizes as a dinuclear species. The small bands in each spectrum are likely due to spin-forbidden transitions $\Delta M_I = \pm 1$. [66] The absence of zero-field splitting D in the dissolved complexes was deduced from the simulated spectra of **C1** and **C6** (see appendix for details of the simulation). The calculation provided an average g-value of 2.001 ± 0.001 and an average value of the hyperfine isotropic coupling constant A of 97 ± 1 G. Therefore we can conclude that in solution, those complexes are mainly present as monomers, no matter how they crystallize. This information is actually quite important: either for catalysis or for incorporation in the mesoporous support, these complexes will be dissolved. Thus their behaviour in solution must be considered, rather than their solid state one.

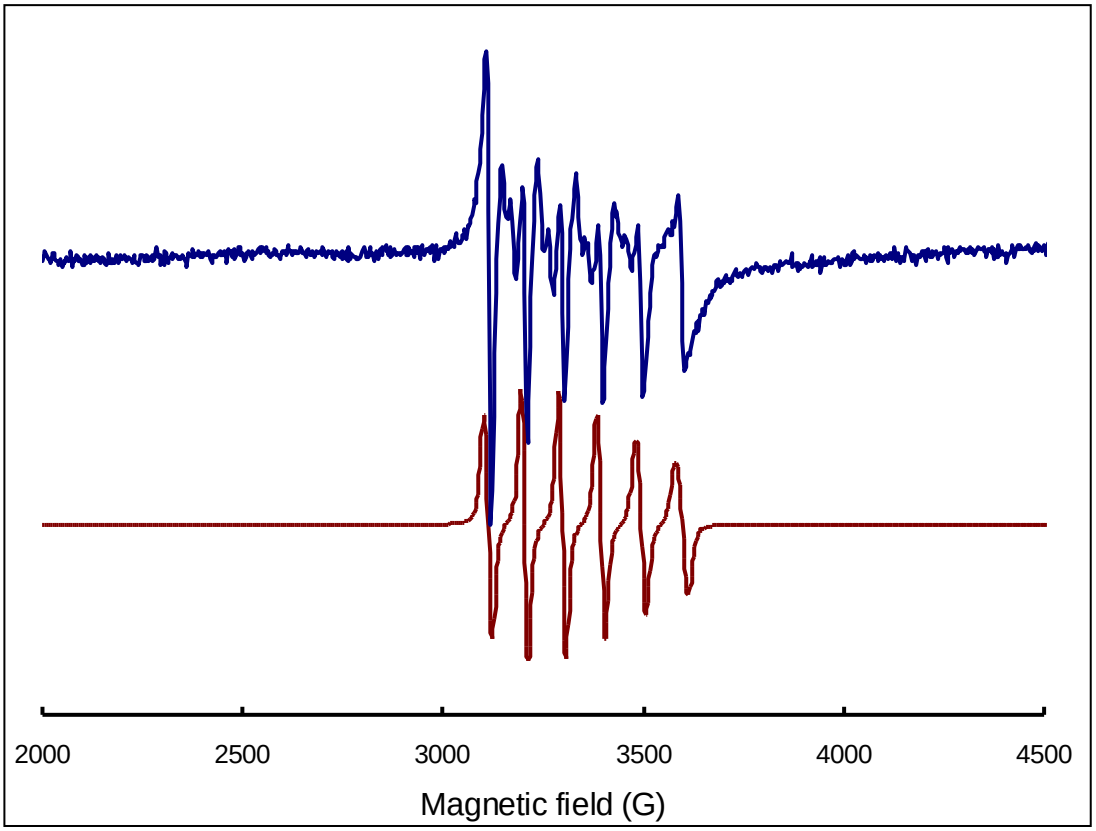

*Figure 24: Liquid-state EPR spectra of **C1** in MeOH/EtOH (1/1) (blue line) at 116 K and its simulation (red line). Microwave frequency: 9.41 GHz, amplitude modulation: 1 G, gain: 60 dB, power: 4 mW*

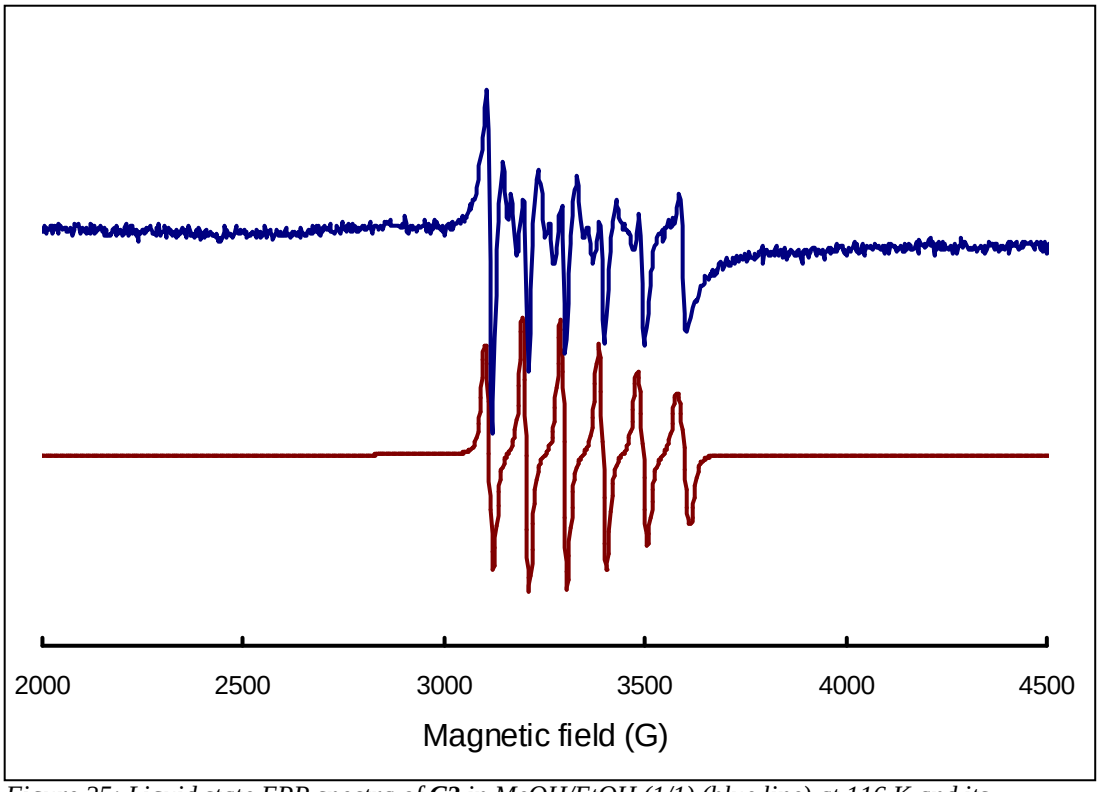

*Figure 25: Liquid state EPR spectra of **C2** in MeOH/EtOH (1/1) (blue line) at 116 K and its simulation (red line). Microwave frequency: 9.41 GHz, amplitude modulation: 1 G, gain: 60 dB, power: 2 mW.*

I.6. Electrochemistry

Given that these complexes were meant to be used as catalysts for oxidation, some of them were studied by cyclic voltametry. This analytical technique allowed us to determine the electrochemical behaviour of the complexes, for a better comprehension of the catalysis mechanism. Herein are studied five complexes: **C1**, **C5**, **C6**, $[Mn(H_2O)_3L^1]\cdot(BPh_4)_2$ (**C7**) and $[Mn(H_2O)_3L^3]\cdot(BPh_4)_2$ (**C8**). These complexes were in principle better candidates for catalysis as they did not possess toxic counter-anions.

Each voltamogram, complex was dissolved in MeCN (10^{-3} $mol.L^{-1}$) and tetrabutylammonium perchlorate (TBAP) was used as supporting electrolyte (0.1 $mol.L^{-1}$). A glassy carbon electrode and a $Ag/AgNO_3$(10^{-2} $mol.L^{-1}$) electrode were used as working and reference electrodes, respectively.

I.6.1 Cyclic voltametry

Cyclic voltamograms were recorded for each complex. Both complexes **C1** and **C6** exhibit a reversible redox process, while the others (**C5**, **C7** and **C8**) show an irreversible oxidation. The oxidation and reduction peak potentials of these complexes were measured, as well as the half-wave potentials in the case of reversible processes (Table 7). All the potentials are measured *versus* the $Ag/AgNO_3$ electrode. Cyclic voltamograms of complexes **C1**, **C5** and **C8** are represented on Figure 26.

*Table 7: Oxidation and reduction peak potentials vs $Ag/AgNO_3$ of complexes **C1** and **C5-C8***

Compound	E_{Ox} (V)	E_{Red} (V)	$E_{1/2}$ (V)
C1	0.70	0.57	0.64
C5	1.14	0.16	/
C6	0.64	0.52	0.58
C7	0.52	/	/
C8	0.54	/	/

Reversible processes were only observed in the presence of chloride, which tends to prove that these latter stabilize the manganese(III) species formed by oxidation. In the case of **C5**, **C7** and **C8**, the complexes are oxidised to an electrochemically inactive species. Given that the ligand is the only difference between complexes **C1** and **C6**, the higher oxidation potential of **C1** proves that L^2 is a more electrodonor ligand than L^1.

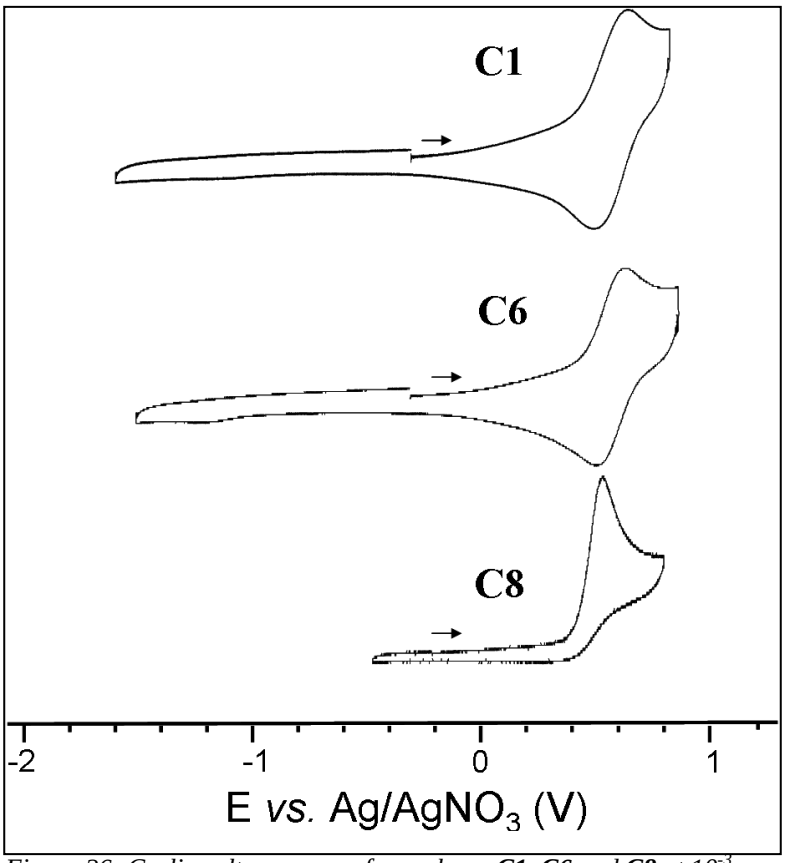

*Figure 26: Cyclic voltamogram of complexes **C1**, **C6** and **C8** at 10^{-3} mol.L^{-1} in MeCN, TBAP was used as supporting electrolyte (0.1 mol.L^{-1}).*

I.6.2 Addition of chloride

The voltamogram of **C6** recorded until 1.5 V was actually more complex than the simple reversible process previously displayed (black curve on Figure 27). This voltamogram exhibits three waves (B, C and D) at 0.64, 1.03 and 1.43 V. Wave B is likely due to the oxidation of mononuclear $[Mn^{II}Cl_2L^2]$ to $[Mn^{III}Cl_2L^2]$ as this monomer is supposed to be the main species in solution. Given that wave D exhibits a similar intensity than wave B, it could correspond to the oxidation of $[Mn^{III}Cl_2L^2]$ to $[Mn^{IV}Cl_2L^2]$. The values of those oxidation potentials are in good agreement with similar complexes found in the literature. [29] The presence of wave C was more difficult to explain.

To investigate a little further results obtained with **C6**, cyclic voltamograms were recorded after progressive additions of tetrabutylammonium chloride (TBACl) to a solution of **C6** (Figure 27). Before one equivalent, drastic changes occur in the voltamogram. First, a new wave (wave A) appears at E = 0.42 V, *i.e.*, before wave B in the genuine voltamogram. Second, wave B at diminishes in intensity, while wave C at E = 1.03 V increases.

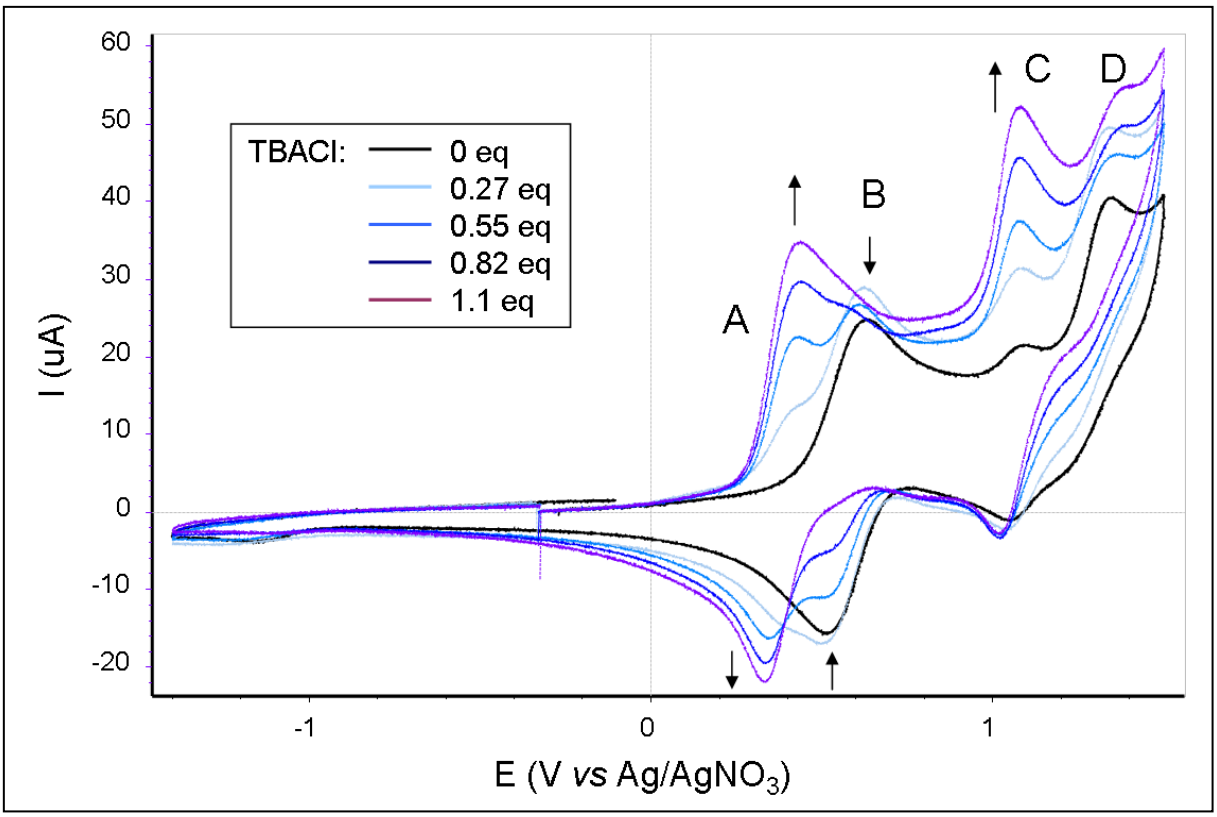

*Figure 27: Evolution of cyclic voltamogram of **C6** upon addition of tetrabutylammonium chloride (TBACl) up to 1 equivalent.*

Given that wave A only appears when there is an excess of chloride in the solution, one can suppose that this wave comes from the oxidation of a new species, $[Mn^{II}Cl_3L^2]$ to $[Mn^{III}Cl_3L^2]$. Indeed, adding a chloride ion or replacing a solvent molecule by a chloride ion (more electrodonor) in the coordination sphere will facilitate the manganese(II) oxidation.

Wave C is present before and after addition of chloride, at a higher potential than the oxidation potential of monomeric Mn(II), but its intensity increases upon chloride addition. Our hypothesis is that this wave is relative to a dimeric complex (bridged by chloride anions), because of its lower intensity. The position of this wave led us to believe that it is not due to a Mn(II) to Mn(III) oxidation, which would occur at lower potential than the oxidation of monomeric species. Therefore, wave C could be the oxidation of a $[(Mn^{III})_2(\mu\text{-}Cl)_xCl_yL^2]$ dimer to a $[Mn^{III}Mn^{IV}(\mu\text{-}Cl)_xCl_yL^2]$ dimer (Scheme 9). Presence in excess of chloride anion would favour the formation of chloride bridges between metallic centres, which would explain the higher intensity.

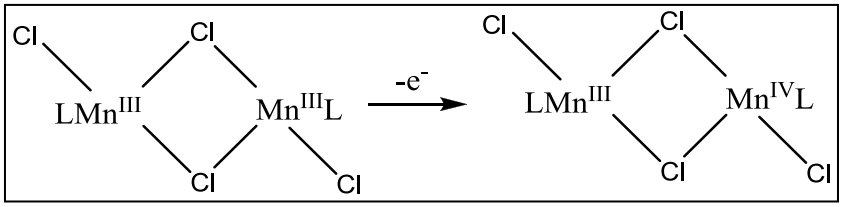

Scheme 9: Possible oxidation reaction occuring at wave C.

I.7 Experimental part

I.7.1 Ligands synthesis

Synthesis of *N,N*-bis((pyridin-2-yl)methyl)prop-2-yn-1-amine (L^1) (Method A). [36, 37]

*Synthesis of 2,2'-dipicolylamine **1**:* a solution of 2-pyridinecarboxaldehyde (5.35 g, 50 mmol) in 20 mL of methanol was added to a solution of 2-picolylamine (5.48 g, 50 mmol) in 80 mL of methanol. The resulting solution was stirred at room temperature for 8 h, and sodium borohydride (3.8 g, 100 mmol) was added portionwise. The solution was then stirred for 2 h and the solvent was removed under reduced pressure. The oil thus obtained was redissolved in 100 mL of water, and extracted twice with 100 mL of dichloromethane. The organic phases were gathered and dried over sodium sulphate. After filtration, the solvent was removed under vacuum to give the product as brown oil in a 96 % yield. ^{1}H NMR ($CDCl_3$, 300 MHz): δ (ppm) 8.55 (ddd, J = 4.80, 1.80, 0.90 Hz, 2H), 7.63 (td, J = 7.50, 1.80 Hz, 2H), 7.34 (d, J = 7.80 Hz, 2H), 7.14 (ddd, J = 7.50, 4.80, 1.20 Hz, 2H), 3.97 (s, 4H).

Synthesis of L^1: propargyl bromide (649 mg, 4.4 mmol) was added dropwise to a mixture of 2,2'-dipicolylamine (879 mg, 4.4 mmol) and potassium carbonate (2.4 g, 17.6 mmol) in 10 mL of dry THF. The mixture was heated at 70 °C for 24 h and diluted with 40 mL of dichloromethane. The solution was filtered through a pad of potassium carbonate and the solvent was removed under vacuum. The resulting product was purified on an alumina column eluted with ethylacetate in dichloromethane (0 - 40 %) and L^1 was obtained as a dark brown oil in an 11 % yield. ^{1}H NMR ($CDCl_3$, 300 MHz): δ (ppm) 8.55 (ddd, J = 4.80, 1.80, 0.90 Hz, 2H), 7.64 (td, J = 7.50, 1.80 Hz, 2H), 7.50 (d, J = 7.80 Hz, 2H), 7.15 (ddd, J = 7.50, 4.80, 1.20 Hz, 2H), 3.91 (s, 4H), 3.41 (d, J = 2.40 Hz, 2H), 2.29 (t, J = 2.40 Hz, 1H). ^{13}C NMR (300 MHz, $CDCl_3$): δ (ppm) 158.76, 149.26, 136.47, 123.14, 122.10, 78.32, 73.62, 59.44, 42.54. IR (KBr): 3294 (w), 3062 (w), 3011 (w), 2921 (w), 2839 (w), 2095 (m, C≡C) cm^{-1}.

Synthesis of *N,N*-bis((pyridin-2-yl)methyl)prop-2-yn-1-amine (L^1) (Method B). [37] The synthesis was based on a published protocol. A mixture of propargylamine (1.50 g, 27.3 mmol) and potassium carbonate (22.8 g, 163.8 mmol) was stirred in 140 mL of acetonitrile for 5 min. Then 2-picolyl chloride hydrochloride (9.84 g, 60.0 mmol) dissolved in 140 mL of acetonitrile was added. The resulting solution was stirred under reflux for 5 days. The solution

was filtered and the filtrate was evaporated under reduced pressure. The resulting brown oil was redissolved in 100 mL of distilled water and extracted thrice with dichloromethane. The organic phases were gathered and dried with sodium sulphate. The solvent was finally evaporated to afford L^1 in a 94 % yield. ^{1}H NMR ($CDCl_3$, 300 MHz): δ (ppm) 8.55 (ddd, J = 4.80, 1.80, 0.90 Hz, 2H), 7.64 (td, J = 7.50, 1.80 Hz, 2H), 7.50 (d, J = 7.80 Hz, 2H), 7.15 (ddd, J = 7.50, 4.80, 1.20 Hz, 2H), 3.91 (s, 4H), 3.41 (d, J = 2.40 Hz, 2H), 2.29 (t, J = 2.40 Hz, 1H). ^{13}C NMR (300 MHz, $CDCl_3$): δ (ppm) 158.76, 149.26, 136.47, 123.14, 122.10, 78.32, 73.62, 59.44, 42.54. IR (KBr): 3294 (w), 3062 (w), 3011 (w), 2921 (w), 2839 (w), 2095 (m, C≡C) cm^{-1}.

Synthesis of *N*-((1-methyl-1H-imidazol-2-yl)methyl)-*N*-(pyridin-2-ylmethyl)prop-2-yn-1-amine (L^2). This second ligand was synthesized in two steps.

*Synthesis of N-(1-methyl-1H-imidazol-2-ylmethyl)pyrid-2-ylmethylamine **2**:* [40] 2-picolylamine (2.45 g, 22.7 mmol) in 25 mL of methanol was added dropwise to a solution of 1-methyl-2-imidazolecarboxaldehyde (2.5 g, 22.7 mmol) in 50 mL of methanol. The resulting solution was stirred for 3 h at room temperature. Sodium borohydride (0.86 g, 22.7 mmol) was added portionwise and the solution was further stirred for two more hours at room temperature. The solvent was evaporated under reduced pressure and the orange oil thus obtained was redissolved in a mixture of water/methanol (25 mL/50 mL), before being extracted thrice with 50 mL of dichloromethane. The combined organic phases were washed with 50 mL of water and dried over Na_2SO_4. The solvent was finally removed to obtain the product as orange oil in a 96 % yield. ^{1}H NMR ($CDCl_3$, 300 MHz): δ (ppm) 8.54 (ddd, J = 4.80, 1.80, 0.90 Hz, 1H), 7.63 (td, J = 7.50, 1.80 Hz, 1H), 7.31 (d, J = 7.80 Hz, 1H), 7.15 (ddd, J = 7.50, 4.80, 1.20 Hz, 1H), 6.92 (d, J = 1.20 Hz, 1H), 6.80 (d, J = 1.20 Hz, 1H), 3.93 (s, 2H), 3.89 (s, 2H), 3.66 (s, 3H).

Synthesis of L^2: *N*-(1-methyl-1*H*-imidazol-2-ylmethyl)pyrid-2-ylmethylamine (3 g, 14.8 mmol) and potassium carbonate (8.18 g, 59.2 mmol) were dissolved in 40 mL of THF. Then propargyl bromide was added dropwise, and the resulting solution was heated at 50 °C for 18 h. The solvent was removed under reduced pressure, and the brown oil thus obtained was dissolved in dichloromethane before being passed over several pads of potassium carbonate until disappearance of the hydrobromic acid. Dichloromethane was removed under reduced pressure and ligand L^2 was obtained in an 80 % yield. ^{1}H NMR ($CDCl_3$, 300 MHz): δ (ppm) 8.51 (ddd, J = 4.80, 1.80, 0.90 Hz, 1H), 7.60 (td, J = 7.50, 1.80 Hz, 1H), 7.32 (d, J = 7.80 Hz, 1H), 7.12 (ddd, J = 7.50, 4.80, 1.20 Hz, 1H), 6.88 (d, J = 1.20 Hz, 1H), 6.76 (d, J = 1.20 Hz,

1H), 3.80 (s, 2H), 3.79 (s, 2H), 3.58 (s, 3H), 3.32 (d, J = 2.40 Hz, 2H), 2.27 (t, J = 2.40 Hz, 1H). ^{13}C NMR (300 MHz, $CDCl_3$): δ (ppm) 158.28, 149.26, 144.59, 136.45, 127.27, 123.44, 122.21, 121.58, 78.27, 73.74, 59.29, 49.54, 42.44, 32.84. IR (KBr): 3010 (w), 2926 (w, br), 2839 (w), 2100 (m, C≡C) cm^{-1}.

Synthesis of Sodium 2-(prop-2-ynyl(pyridin-2-ylmethyl)amino)acetate (L^3).

*Synthesis of methyl 2-(prop-2-ynylamino)acetate **3**:* [41] triethylamine (2.79 g, 27.6 mmol) was added to a mixture of propargylamine (1.27 g, 23 mmol) and methyl bromoacetate (4.22 g, 27.6 mmol) in 75 mL of acetonitrile. The solution was stirred for 12 hours at 50 °C and the solvent was removed under reduced pressure. The oil was redissolved in 100 mL of dichloromethane and washed twice with 25 mL of water. The solvent was evaporated and the product was purified on a silica gel column (CH_2Cl_2/MeOH: 96/4) to obtain **3** in a 24% yield. ^{1}H NMR ($CDCl_3$, 300 MHz): δ (ppm) 3.73 (s, 3H), 3.51 (s, 2H), 3.47 (d, J = 7.80 Hz, 2H), 2.23 (t, J = 2.4 Hz, 1H), 1.77 (br s, 1H).

*Synthesis of methyl 2-(prop-2-ynyl(pyridin-2-ylmethyl)amino)acetate **4**:* in 15 mL of acetonitrile, potassium carbonate (1.269 g, 9.18 mmol) and **3** (389 mg, 3.06 mmol) were stirred during 5 min. Then 2-picolyl chloride (552 mg, 3.37 mmol) was added portionwise and the solution was heated at reflux for 18 hours. The solution was filtered and the solvent removed under reduced pressure and used without further purification in the next step.

Synthesis of L^3: sodium hydroxide (240 mg, 6 mmol) and **4** (654 mg, 3mmol) were dissolved in a mixture THF/H_2O (5 mL/1 mL) and stirred at room temperature for 2 h. The solvent was then evaporated and the brown oil thus obtained was redissolved in 25 mL and washed twice with 25 mL of ethyl acetate. The solvent was removed under reduced pressure and the product was redissolved in the minimum amount of water. The resulting solution was acidified to pH 6 with a solution of HCl 1 $mol.L^{-1}$. The solvent was finally evaporated to provide L^3 in a 60% yield. ^{1}H NMR (D_2O, 300 MHz): δ (ppm) 8.41 (dm, J = 4.80, 1H), 7.65 (td, J = 7.50, 1.80 Hz, 1H), 7.33 (d, J = 7.80 Hz, 1H), 7.17 (ddd, J = 7.50, 4.80, 1.20 Hz, 1H), 3.71 (s, 2H), 3.26 (d, J = 2.40 Hz, 2H), 3.10 (s, 2H), 2.54 (t, J = 2.40 Hz, 1H).

Synthesis of (1-methyl-1*H*-imidazol-2-yl)methanol 5. Two different protocols were followed for the synthesis of this molecule.

Protocol 1: [43] a mixture of paraformaldehyde (1.8 g, 60 mmol) and 1-methyl-1*H*-imidazole (4.92 g, 60 mmol) in 22 mL of acetonitrile were heated in an autoclave at 120 °C overnight. After cooling at room temperature, acetonitrile was removed under reduced pressure. The

solid was quickly washed with acetone and recrystallized from ethanol to give the product in a 33 % yield.

Protocol 2: [42] paraformaldehyde (30.15 g, 1 mol) and 1-methyl-1*H*-imidazole (30.2 g, 0.365 mol) were heated at 160 °C for 2 h. After cooling at room temperature, the mixture was dissolved in methanol, and precipitated at -20 °C. The solid was filtered and recrystallized from chloroform to provide the product in a 25 % yield. ^{1}H NMR (DMSO-d6, 300 MHz): δ (ppm) 7.06 (d, J = 1.20 Hz, 1H), 6.75 (d, J = 1.20 Hz, 1H), 4.46 (s, 2H), 3.63 (s, 3H).

Synthesis of 2-(chloromethyl)-1-methyl-1H-imidazole 6. [44] A solution of **5** (3 g, 27 mmol) in 34 mL of $CHCl_3$ was added at 0 °C to a solution of thionyl chloride (18.7 g, 0.156 mol) in 10 mL of $CHCl_3$. The resulting mixture was heated under reflux for 90 min. The solvent was evaporated under reduced pressure and the resulting yellowish powder was stirred in diethyl ether overnight. After decantation of the ether, the solid was dried under vacuum to give the desired product as an off-white powder in a 96 % yield. ^{1}H NMR (DMSO-d6, 300 MHz): δ (ppm) 7.75 (d, J = 1.20 Hz, 1H), 7.68 (d, J = 1.20 Hz, 1H), 5.16 (s, 2H), 3.87 (s, 3H). ^{13}C NMR (DMSO-d6, 300 MHz): δ (ppm) 141.39, 124.65, 119.23, 34.18, 31.59.

I.7.2 Manganese(II) complexes synthesis

Synthesis of $[Mn_2(\mu\text{-}Cl)_2(Cl)_2(L^1)_2]$ C1. A solution of L^1 (47 mg, 0.2 mmol) in 2 mL of methanol was slowly added to a solution of $MnCl_2{\cdot}4H_2O$ (40 mg, 0.2 mmol) in 2 mL of methanol. The solution was stirred for 1 h then the solid was filtered and washed with methanol to obtain 38 mg of the complex in a 52 % yield. This powder was redissolved in the minimum amount of methanol, and pale yellow crystals of complex were obtained by slow diffusion of diethylether into this solution. IR (KBr): 3247 (s), 3092 (w), 3079 (w), 3052 (w), 3017 (w), 2947 (m), 2925 (m), 2898 (m), 2851 (m), 2108 (m, C≡C) cm^{-1}.

Synthesis of $[MnCl_2L^2]$ C6. A solution of L^2 (49 mg, 0.2 mmol) in 2 mL of methanol was slowly added to a solution of $MnCl_2{\cdot}4H_2O$ (40 mg, 0.2 mmol) in 2 mL of methanol and the resulting mixture was stirred for 1 h. The solvent was let to evaporate, and crystals were obtained in a couple of days. IR (KBr): 3202 (s), 3139 (w), 3117 (m), 2920 (m, br), 2103 (m, C≡C) cm^{-1}.

Synthesis of $[Mn_2(\mu\text{-}Br)_2(Br)_2(L^1)_2]$ C2. A solution of L^1 (47 mg, 0.2 mmol) in 2 mL of methanol was slowly added to a solution of $MnBr_2 \cdot 4H_2O$ (57 mg, 0.2 mmol) in 2 mL of methanol. This solution was let under stirring for 1 h. Brown crystals were obtained by slow diffusion of diethylether in the latter solution.

Synthesis of $[Mn_2(\mu\text{-}N_3)_2(N_3)_2(L^1)_2] \cdot 2CH_3OH$ C3. A solution of L^1 (24 mg, 0.1 mmol) in 2 mL of methanol was added to a solution of $Mn(NO_3)_2 \cdot 4H_2O$ (25 mg, 0.1 mmol) in 2 mL of methanol. The resulting solution was stirred during 30 min, then a solution of NaN_3 (26 mg, 0.4 mmol) in 3 mL of methanol was added. The mixture was further stirred for 1 h, and the solid thus formed was filtered and washed with methanol. The solid was redissolved in methanol, and slow diffusion of diethylether in that solution provided crystals suitable for X-ray diffraction.

Synthesis of $[Mn_2(\mu\text{-}N_3)_2(N_3)_2(L^2)_2]$ C4. The synthesis is similar to the $[Mn_2(\mu\text{-}N_3)_2(N_3)_2(L^1)_2] \cdot 2CH_3OH$ synthesis, the only difference being that L^2 (24 mg, 0.1 mmol) was used instead of L^1. Suitable crystals for X-ray diffraction were obtained following the same diffusion protocol.

Synthesis of $[Mn(NO_3)(H_2O)_2L^1] \cdot NO_3$ C5. Two different approaches were used depending on the purpose.

Crystal synthesis: a solution of L^1 (24 mg, 0.1 mmol) in 2 mL of methanol was added to a solution of $Mn(NO_3)_2 \cdot 4H_2O$ (25 mg, 0.1 mmol) in 2 mL of methanol and the mixture was stirred for 1 h. Solvent was let to evaporate and small crystals were collected after few days and redissolved in methanol. Ether was slowly diffused in this solution to afford suitable crystals for X-ray diffraction.

Powder synthesis: the same amount of L^1 and $Mn(NO_3)_2 \cdot 4H_2O$ was mixed in absolute ethanol (2+2 mL) and stirred for 1 h. The precipitate thus formed was filtered and carefully washed with absolute ethanol to afford the complex as a light brown powder.

Synthesis of $[Mn(H_2O)_3L^1] \cdot (BPh_4)_2$ C7. A solution of L^1 (47 mg, 0.2 mmol) in 2 mL of methanol was added to a solution of $Mn(NO_3)_2 \cdot 4H_2O$ (50 mg, 0.2 mmol) in 2 mL of methanol. The solution was stirred during 30 min, then a solution of $NaBPh_4$ (784 mg, 2 mmol) in 10

mL of methanol was added. The mixture was further stirred for 1 h, and the solid thus formed was filtered and washed with methanol to afford $[Mn(H_2O)_3L^1]\cdot(BPh_4)_2$.

Synthesis of $[Mn(H_2O)_3L^3]\cdot(BPh_4)_2$ C8. A solution of L^3 (45 mg, 0.2 mmol) in 1 mL of distilled water was added to a solution of $Mn(NO_3)_2\cdot 4H_2O$ (50 mg, 0.2 mmol) in 1 mL of distilled water. The solution was stirred during 30 min, then a solution of $NaBPh_4$ (342 mg, 1 mmol) in 8 mL of distilled water was added. The mixture was further stirred for 1 h, and the solid thus formed was filtered and washed carefully with distilled water to afford the complex $[Mn(H_2O)_3L^3]\cdot(BPh_4)_2$. IR (KBr): 3293 (w), 3053 (w), 2996 (w), 2920 (w), 2850 (w), 2584 (w), 2515 (w), 2116 (w, C≡C) cm^{-1}.

Conclusion

This chapter relates the synthesis and characterization of manganese(II) complexes as mimics of the first coordination sphere of MndD. First, ligands were designed in such a way that complexation with metal ions and grafting on material would not interfere. Indeed, while complexation is achieved with pyridine, imidazole or carboxylate moieties, grafting will involve a triple bond C≡C which has no coordinating ability toward manganese(II). Three different ligands were synthesized, and two of them were new molecules.

Second, manganese(II) complexes were synthesized. The first two crystals we obtained with manganese(II) chloride were mono and dinuclear species (**C6** and **C1**, using L^2 and L^1 respectively), which led us to investigate in two directions:

- The synthesis of mononuclear species, which would be closer to the actual enzymatic site.
- The synthesis of bridged dinuclear species, in order to study the evolution of the interaction between the two manganese(II) ions upon changes in the nature of the bridge or in the ligand.

Apart from **C6**, another mononuclear complex has been crystallized, **C5**, using manganese(II) nitrate salt with L^1. The structures exhibit unusual coordination numbers for such metal ion, as **C5** and **C6** are hepta and pentacoordinated respectively. Two other complexes were obtained using tetraphenylborate as counter anion with L^1 and L^3, and though these complexes were not crystallized, one can assume that the anions are not coordinated to the metal centre due to steric hindrance.

In addition to **C1**, three dinuclear complexes **C2**, **C3** and **C4** were obtained. To our knowledge, complex **C2** (obtained with L^1 and manganese(II) bromide) was the first crystallized complex containing bromide bridges between two Mn(II) ions that has been magnetically studied. Complexes **C3** and **C4** were crystallized to obtained two azide bridges between the metal ions, using respectively L^1 and L^2 as ligands. Amongst those dinuclear complexes, **C1** was the only one that exhibited a weak antiferromagnetic behaviour at low temperature, contrary to the ferromagnetic coupling observed in **C2**-**C4**. Comparing the value of coupling J in the azido-bridged species with other similar species described in the literature allowed us to link this magnetic parameter with structural ones such as the Mn-X-Mn angle (where X is the bridging atom) and the Mn-Mn distance.

The EPR study of **C1** in both solid and liquid states led us to conclude that although this complex crystalizes as a dinuclear unit, manganese centres do not interact anymore when dissolved. Therefore, in solution, the bridges (chloride ions here) do not exist anymore, *i.e.*, the complex behaves like a mononuclear species. This information is actually of great importance as further utilisations of these complexes, either for catalysis or for silica grafting, will require the complexes to be dissolved.

Bibliography

[1] V. K. Yachandra, K. Sauer, M. P. Klein, *Chem. Rev.*, **1996**, *96*, *7*, 2927

[2] A. Zouni, H.-T. Witt, J. Kern, P. Fromme, N. Krauss, W. Saenger, P. Orth, *Nature*, **2001**, *409*, 739

[3] G. E. O. Borgstahl, H. E. Parge, M. J. Hickey, M. J. Johnson, M. Boissinot, R. A. Hallewell, J. R. Lepock, D. E. Cabelli, J A. Tainer, *Biochemistry*, **1996**, *35*, *14*, 4287

[4] J. T. Groves,W. J. Kruper, R. C. Haushalter, *J. Am. Chem. Soc.*, **1980**, 6375

[5] F. P. Guengerich, J. Biol. Chem., 1991, 266, 10019

[6] B. Meunier, *Chem. Rev.*, **1992**, *92*, 1411

[7] S. Signorella, C. Hureau, *Coord. Chem. Rev.*, **2012**, *256*, *11-12*, 1229

[8] A. J. Wu, J. E. Penner-Hahn, V. L. Pecoraro, *Chem. Rev.*, **2004**, *104*, 903

[9] T. D. H. Bugg, *Tetrahedron*, **2003**, *59*, 7075

[10] G. A. Hamilton, "Molecular Mechanisms of Oxygen Activation.", *Ed. O. Hayaishi, Academic: London*, **1974**, 405

[11] W. Kaim, B. Schwederski, "Bioinorganic chemistry: Inorganic Elements in the Chemistry of Life, 1st ed.", *John Wiley & Sons*, **1994**

[12] R. Yamahara, S. Ogo, H. Masuda, Y. Watanabe, *J. Inorg.Biochem.*, **2002**, *88*, 284

[13] M. G. Weller, V. Weser, *J. Am. Chem. Soc.*, **1982**, *104*, 1433

[14] L. S. White, P. V. Nilsson, L. H. Pignolet, L. Que Jr., *J. Am. Chem. Soc.*, **1984**, *106*, 8312

[15] D. D. Cox, L. Que Jr., *J. Am. Chem. Soc.*, **1988**, *110*, 8085

[16] H. G. Jang, D. D. Cox, L. Que Jr., *J. Am. Chem. Soc.*, **1991**, *113*, 9200

[17] P. Mialane, L. Tchertanov, F. Banse, J. Sainton, J. Girerd, *J. Inorg. Chem.*, **2000**, *39*, 2440

[18] T. Funabiki, A. Mizoguchi, T. Sugimoto, S. Tada, M. Tsugi, H. Sakamoto, S. Yoshida, *J. Am. Chem. Soc.*, **1986**, *108*, 2921

[19] A. Dei, D. Gatteschi, L. Pardi, *Inorg. Chem.*, **1993**, *32*, 1389

[20] M. Ito, L. Que Jr., *Angew. Chem. Int. Ed. Engl.*, **1997**, *36*, 1342

[21] G. Lin, G. Reid, T. D. H. Bugg, *J. Chem. Soc. Chem. Commun.*, **2000**, 1119

[22] T. Dhanalakshmi, M. Bhuvaneshwari, M. Palaniandavar, *J. Inorg. Biochem.*, **2006**, *100*, 1527

[23] R. Mayilmurugan, E. Suresh, M. Palaniandavar, *Inorg. Chem.*, **2007**, *46*, *15*, 6038

[24] P. C. A. Bruijnincx, M. Lutz, A. L. Spek, W. R. Hagen, B. M. Weckhuysen, G. van Koten, R. J. M. Klein Gebbink, *J. Am. Chem. Soc.*, **2007**, *129*, *8*, 2275

[25] M. Wagner, C. Limberg, T. Tietz, *Chem. Eur. J.*, **2009**, *15*, 5567

[26] S. Paria, P. Halder, T. K. Paine, *Inorg. Chem.*, **2010**, *49*, 4518

[27] H. Sakurai, S. Shimomura, T. Yoshimura, *Biochem. Biophys. Res. Commun.*, **1983**, *115*, *2*, 618

[28] A. E. M. Ramadan, I. M. El-Mehasseb, *Transition Met. Chem.*, **1998**, *23*, *2*, 183

[29] M Triller, D. Pursche, W.-Y. Hsieh, V. L. Pecoraro, A. Rompel, *Inorg. Chem.*, **2003**, *42*, 6274

[30] N. Shaikh, A. Panja, P. Banerjee, M. Ali, *Transition Met. Chem.*, **2003**, *28*, *8*, 871

[31] H. C. Kolb, M. G. Finn, K. B. Sharpless, *Angew. Chem. Int. Ed.*, **2001**, *40*, 2004

[32] D. D. Díaz, S. Punna, P. Holzer, A. K. McPherson, K. B. Sharpless, V. V. Fokin, M. G. Finn, *J. Polym. Sci. Part A: Polym. Chem.*, **2004**, *42*, *17*, 4392

[33] Y. Liu, D. D. Díaz, A. A. Accurso, K. B. Sharpless, V. V. Fokin, M. G. Finn, *J. Polym. Sci. Part A: Polym. Chem.*, **2007**, *45*, *22*, 5182

[34] J.-F. Lutz, *Angew. Chem. Int. Ed.*, **2007**, *46*, *7*, 1018

[35] See Introductory aspects of this Chapter.

[36] D. E. Bergbreiter, P. N. Hamilton, N. M. Koshti, *J. Am. Chem. Soc.*, **2007**, *129*, 10666

[37] J. Rosenthal, S. J. Lippard, *J. Am. Chem. Soc.*, **2010**, *132*, 5536

[38] A. L. Moore, D.-K. Bucar, L. R. MacGillivray, P. D. Benny, *Dalton Trans.*, **2010**, *39*, 1926

[39] S. Huang, R. J. Clark, L. Zhu, *Org. Lett.*, **2007**, *9*, *24*, 4999

[40] T. Dhanalakshmi, E. Suresh, M. Palaniandavar, *Dalton Trans.*, **2009**, 8317

[41] H. Struthers, B. Spingler, T. L. Mindt, R. Schibli, *Chem. Eur. J.*, **2008**, *14*, 6173

[42] M. Pascaly, M. Duda, A. Rompel, B. H. Sift, W. Meyer-Klaucke, B. Krebs, *Inorg Chim Acta*, **1999**, *291*, 289

[43] D. Q. Nguyen, H. W. Bae, E. H. Jeon, J. S. Lee, M. Cheong, H. Kim, H. S. Kim, H. Lee, *J. Power Sources*, **2008**, *183*, 303

[44] N. Wei, N. N. Murthy, Z. Tyekliir, K. D. Karlin, *Inorg. Chem.*, **1994**, *33*, 1177

[45] O. Seewald, U. Flörke, G. Henkel, T. Seshadri, *Acta Cryst.*, **2005**, *E61*, m1948

[46] M. Bartholomä, B. Ploier, H. Cheung, W. Ouellette, J. Zubieta, *Inorg. Chim. Acta*, **2010**, *363*, 1659

[47] I. Romero, M.-N. Collomb, A. Deronzier, A. Llobet, E. Perret, J. Pecaut, L. Le Pape, J.-M. Latour, *Eur. J. Inorg. Chem.*, **2001**, 69

[48] J.-Z. Wu, E. Bouwman, A. M. Mills, A. L. Spek, J. Reedijk, *Inorg. Chim. Acta*, **2004**, *357*, 2694

[49] G. A. van Albada, A. Mohamadou, W. L. Driessen, R. de Gelder, S. Tanase, J. Reedijk, *Polyhedron*, **2004**, *23*, 2387

[50] C.-M. Liu, S. Gao, D.-Q. Zhang, Z.-L. Liu, D.-B. Zhu, *Inorg. Chim. Acta*, **2005**, *358*, 834

[51] J. Qian, W. Gu, S.-P. Yan, D.-Z. Liao, P. Cheng, *Acta Cryst*., **2007**, *E63*, m687

[52] M.-M. Yu, Z.-H. Ni, C.-C. Zhao, A.-L. Cui, H.-Z. Kou, *Eur. J. Inorg. Chem.*, **2007**, 5670

[53] H.-Y. Wu, H.-Q. An, B.-L. Zhu, S.-R. Wang, S.-M. Zhang, S.-H. Wu, W.-P. Huang, *Inorg. Chem. Commun.*, **2007**, *10*, 1132

[54] A. W. Addison, T. N. Rao, J. Reedijk, J. van Rijn, G. C. Verschoor, *J. Chem. Soc. Dalton Trans.*, **1984**, *7*, 1349

[55] O. Kahn, "Molecular Magnetism", *Wiley-VCH*, **1993**

[56] J. Cano, "VPMAG", *University of Valencia, Valencia, Spain*, **2003**

[57] J. M. Herrera, A. Bleuzen, Y. Dromzée, M. Julve, F. Lloret, M. Verdaguer, *Inorg. Chem.*, **2003**, *42*, 7052

[58] E. Ruiz, J. Cano, S. Alvarez, P. Alemany, *J. Am. Chem. Soc.*, **1998**, *120*, 11122

[59] V. H. Crawford, H. W. Richardson, J. R. Wasson, D. J. Hodgson, W. E. Hatfield, *Inorg. Chem.*, **1976**, *15*, 2107

[60] T. K. Karmakar, B. K. Ghosh, A. Usman, H. K. Fun, E. Riviere, T. Mallah, G. Aromi, S. K. Chandra, *Inorg. Chem.*, **2005**, *44*, 2391

[61] R. Cortés, J. L. Pizarro, L. Lezama, M. I. Arriortua, T. Rojo, *Inorg. Chem.*, **1994**, *33*, 2697

[62] Z.-H. Ni, H.-Z. Kou, L. Zheng, Y.-H. Zhao, L. F. Zhang, R. J. Wang, A. L. Cui, O. Sato, *Inorg. Chem.*, **2005**, *44*, 4728

[63] A. Das, G. M. Rosair, M. S. El Fallah, J. Ribas, S. Mitra, *Inorg. Chem.*, **2006**, *45*, 3301

[64] J. L. Manson, A. M. Arif, J. S. Miller, *Chem. Commun.*, **1999**, 1479

[65] M. A. M. Abu-Youssef, A. Escuer, D. Gatteschi, M. A. S. Goher, F. A. Mautner, R. Vicente, *Inorg. Chem.*, **1999**, *38*, 5716

[66] G. Brouet, X. H. Chen, C. W. Lee, L. Kevan, *J. Am. Chem. Soc.*, **1992**, *114*, *10*, 3720

Chapter II:

Microwave irradiation for mesoporous silica synthesis

Introductory aspects

Porous materials are studied since the middle of the 18th century. A Swedish mineralogist called Cronstedt noticed that stilbite had the particular property of producing steam upon heating. He thus baptized them zeolites, meaning "boiling stone".[1] After this preliminary discovery, zeolites had to wait almost two centuries before chemists started to find interest in those porous materials. In 1925, Weigel and Steinhoff investigated the properties of chabazite and were the first to notice a sieve effect: whereas water, methanol ethanol and formic acid were adsorbed, neither acetone nor ether nor benzene underwent the same effect.[2] The term molecular sieve, though, was only proposed in 1932 by McBain.[3] With the pioneer work of Barrer in the 40's, a classification of zeolites was created, based on molecular size considerations.[4] In 1948, Barrer published the first total synthesis of an analogue of natural zeolites called mordenite.[5]

Along with a uniform pore diameter distribution, between 0.4 and 1.3 nm, these aluminosilicates possess acidic sites that can behave as potential catalysts for various reactions.[6,7] In addition, zeolites are rather adaptable materials, given that both pore size and acidic site density can be tuned. Hence zeolites can be employed either as efficient molecular sieves or catalysts.

This latter application contributed to the industrial development of zeolites in the 60's when they demonstrated selective activity toward hydrocarbon isomerization.[8,9,10,11] Backed by the petrochemistry research, zeolites became the most used catalysts for hydrocarbon reactions.[12,13] This interest born from industrial needs eventually spread to porous materials with larger specific surface area. In fact, beyond catalysis and sieves, porous behaviours can also find relevant applications in gas storage, adsorption and chromatography. Official nomenclature was then established in 1972 by the International Union of Pure and Applied Chemistry (IUPAC) to classify porous materials depending on their pore size. Solids with pore diameter below 2 nm are called microporous materials, whereas pore diameter between 2 and 50 nm are designed as mesoporous materials. Finally, above 50 nm, materials are considered as macroporous materials.

The first synthesis of a mesoporous material with ordered porosity was described in a patent by Chiola, Ritsko and Vanderpool in 1971.[14] Later in the beginning of the 90's, Kuroda *et al.* developed a mesoporous material starting from a lamellar clay called kanemite.

[15] The exchange of alkali ions contained in the clay by a cationic surfactant induced the hexagonal rearrangement of the silica layers. Finally, a real break-through occurred in 1992, when a research group from Mobil Oil led by Kresge synthesized mesoporous materials by sol-gel process followed by hydrothermal treatment. [16, 17] This new aluminosilicate family was called M41S. Amongst this family, silica-based solids, with pore diameter between 2 and 10 nm, are the most famous materials.

Basically, this sol-gel process consists in polymerizing silica precursors around a template formed by a supramolecular arrangement of surfactant molecules in aqueous solution. In the case of Mobil Oil materials, surfactants used are long lipophilic alkyl chains ended by a hydrophilic quaternary ammonium head, with a counter-anion to preserve the overall neutrality (Figure 1). Those molecules tend to auto-assemble in aqueous solution when a concentration, called critical micelle concentration (cmc), is reached (Figure 2). [18]

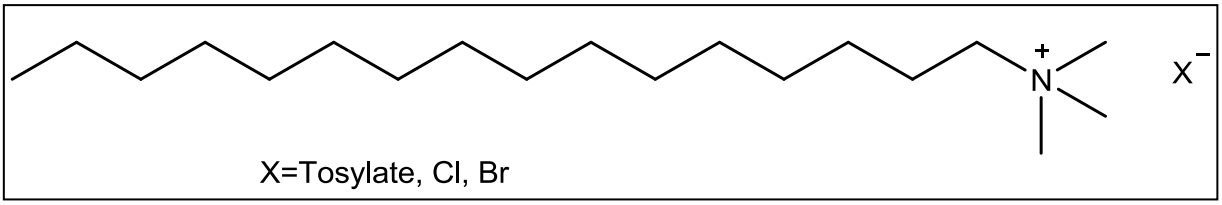

Figure 1: Surfactant molecule, cetyltrimethylammonium tosylate, chloride or bromide

A first cmc (cmc1) will correspond to the formation of spherical and cylindrical micelles. Under addition of surfactant, hence augmentation of concentration, those micelles will once again undergo an auto-assembly at a second critical micelle concentration (cmc2). Depending on the concentration, different liquid crystals can be formed (Figure 2):

- 2D hexagonal assembly, beehive lookalike, where all the micelles are independent one from another.
- 3D cubic assembly, where the micelles are interconnected.
- Lamellar assembly, where the micelles form layers.

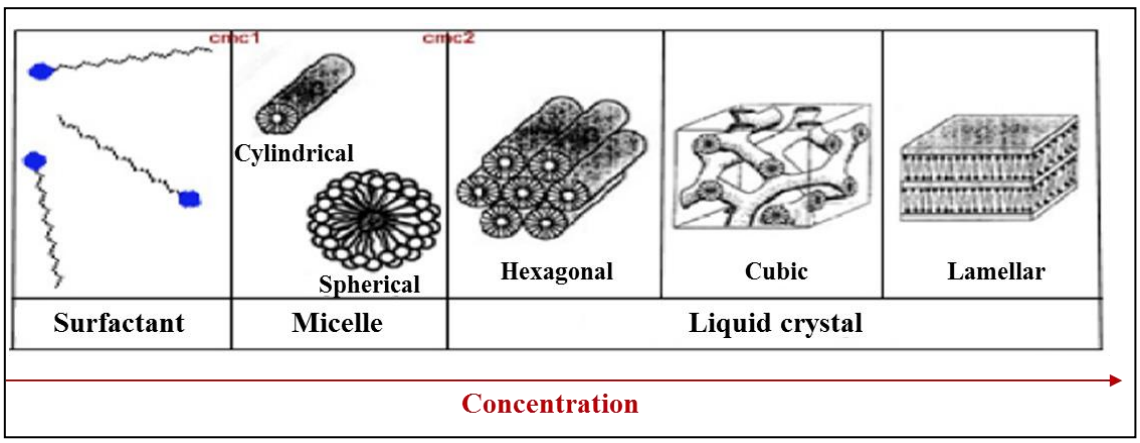

Figure 2: Surfactant phases depending on its concentration

Once the liquid crystal is formed, the silica precursor is then added and polymerize around the surfactant. Mobil Oil Compagny's materials (called MCM for Mobil Composition af Matter) are classified following the porous structure influenced by the template: MCM-41 for the 2D hexagonal arrangement, MCM-48 for the 3D cubic one and finally MCM-50 for the lamellar materials (Figure 4). These materials possess a narrow pore size distribution around 4 nm.

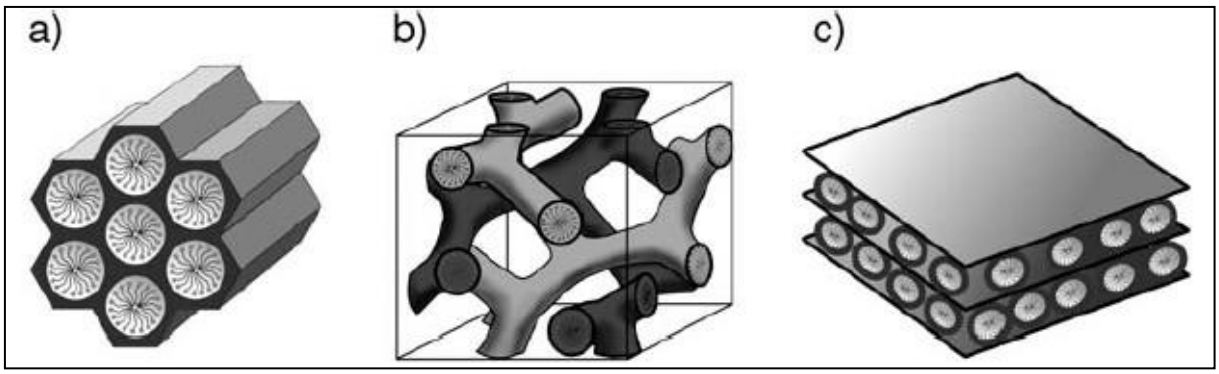

Figure 4: Different types of mesoporous silica developed by Mobil Oil, MCM-41 (a), MCM-48 (b) and MCM-50 (c)

This synthetic method, polymerizing silica around a template, has also been used with polymers instead of alkylammonium salts. One of the most famous polymer-based families is the SBA family (for Santa-Barbara University). [19, 20, 21, 22, 23] The polymer used in that synthesis is a tri-block co-polymer composed of glycol units. For instance, Pluronic® polymer (Figure 3) is an assembly of polyethylenglycol-polypropylenglycol-polyethylenglycol units that forms liquid crystals in aqueous solution. The SBA-15 material exhibits a 2D hexagonal arrangement similar to MCM-41 materials, though with larger pores (5 to 9 nm). Contrary to MCM-41 silicas, grown under basic conditions, SBA-15 is synthesized in acidic solution.

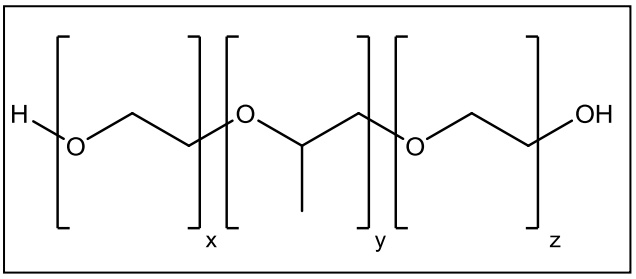

Figure 3: Pluronic® P-123

Though these materials usually polymerize upon oven heating, microwave irradiation started to emerge as an interesting alternative since the 90's. Compared to hydrothermal treatment, microwave heating provides materials within a much shorter time. Before detailing the reports involving microwave heating, this introduction will broach classical results from mesoporous materials studies. Silica interfaces and formation mechanism will be first explained, then microwave syntheses will be quickly reviewed.

II.0.1 Silica interfaces

Different kinds of interfaces can be encountered in a mesoporous material. Due to the variations in the preparation, the charges on both surfactant (S) and inorganic framework (I) will allow various possible interfaces (Figure 5). [18] For instance, in the case of MCM-41 materials, this interface will be represented as $\{S^+;I^-\}$, because of the cationic surfactant head and the anionic silanolates. However, depending on the surfactant's counter-cation, a variable proportion of the interface can be $\{S^+;X^-;I^0\}$. For mesoporous silicas synthesized in strongly acidic medium (pH<1), surface silanols are protonated, providing an interface $\{S^+;2X^-;I^+\}$.

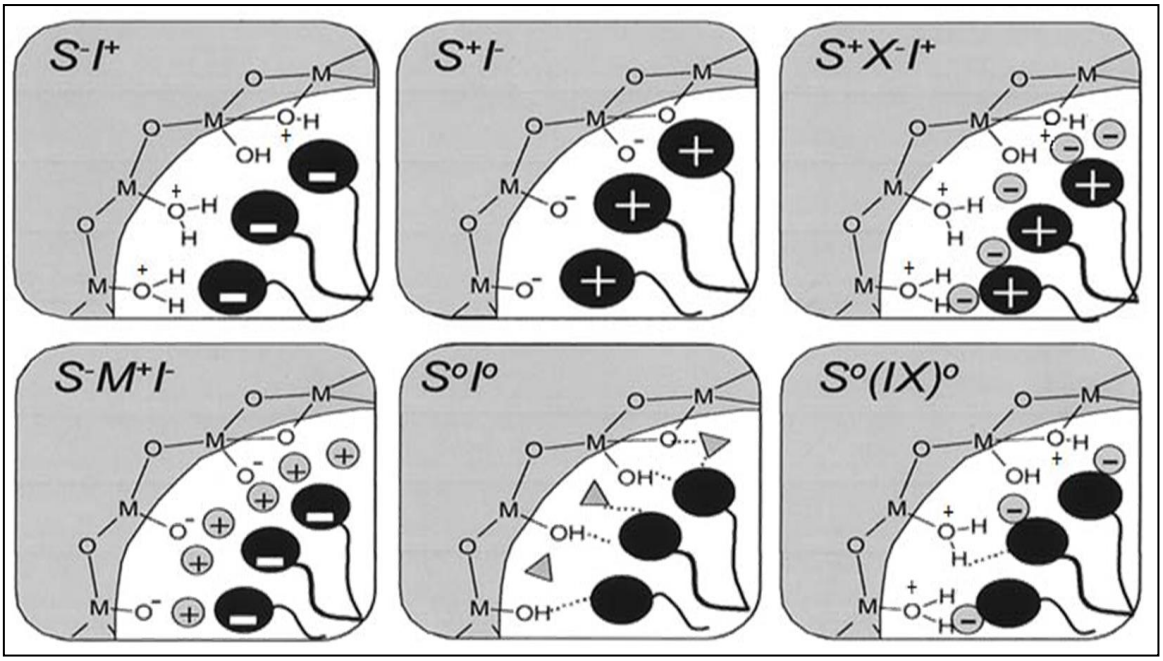

Figure 5: Possilbe surfactant/framework interfaces depending on the synthesis conditions

Non-charged surfactants like Pluronic will create a neutral interface $\{S^0;I^0\}$, if the surfactant is a neutral chain. Then, for charged surfactants and frameworks, interactions will be electrostatic, whereas they are mainly due to hydrogen bonding for neutral interfaces.

II.0.2 Formation mechanism

Formation mechanism of M41S materials has been intensively discussed by several groups since its discovery. Beck *et al.*, the initial research team from Mobil Oil Company, first proposed a mechanism where the liquid crystal is formed before polymerization, in absence of silica precursor. [16, 17] The precursor arranges itself around the template before condensation and creation of the solid. However, further reports of porous materials

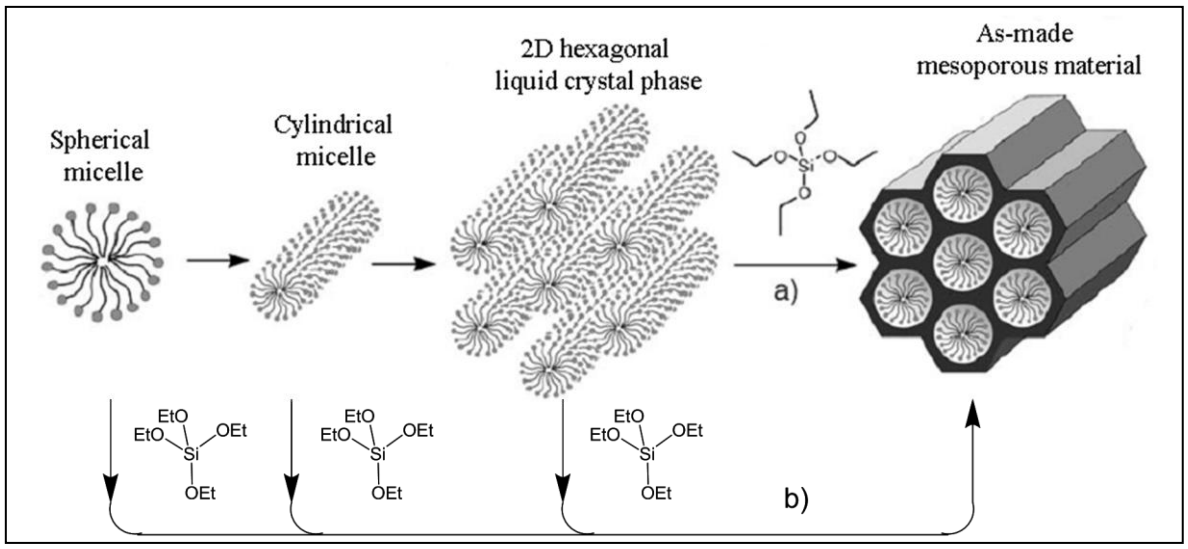

Figure 6: Formation mechanisms of MCM-41, liquid crystal phase (a) or cooperating (b) [25]

synthesized with a surfactant concentration far below cmc2 tend to contradict this proposition. [24] Therefore this research team proposed a second mechanism, involving the silica precursor in the formation of organized template structures. This mechanism would imply a cooperating effect between silica precursor and surfactant that explains the presence of liquid crystal phases at lower concentrations of surfactant (Figure 6). [25]

Those initial propositions have been followed by others as research teams began to study mesoporous materials. In 1993, Davis *et al.* proposed a new mechanism for this synthesis based on *in situ* ^{14}N NMR results. [26] In this hypothesis, cylindrical micelles directly interact with silica precursors, leading to the apparition of silica layers around them. Then, helped by the temperature, those micelles get closer and the silicates condensate to reach a hexagonal arrangement (Figure 7).

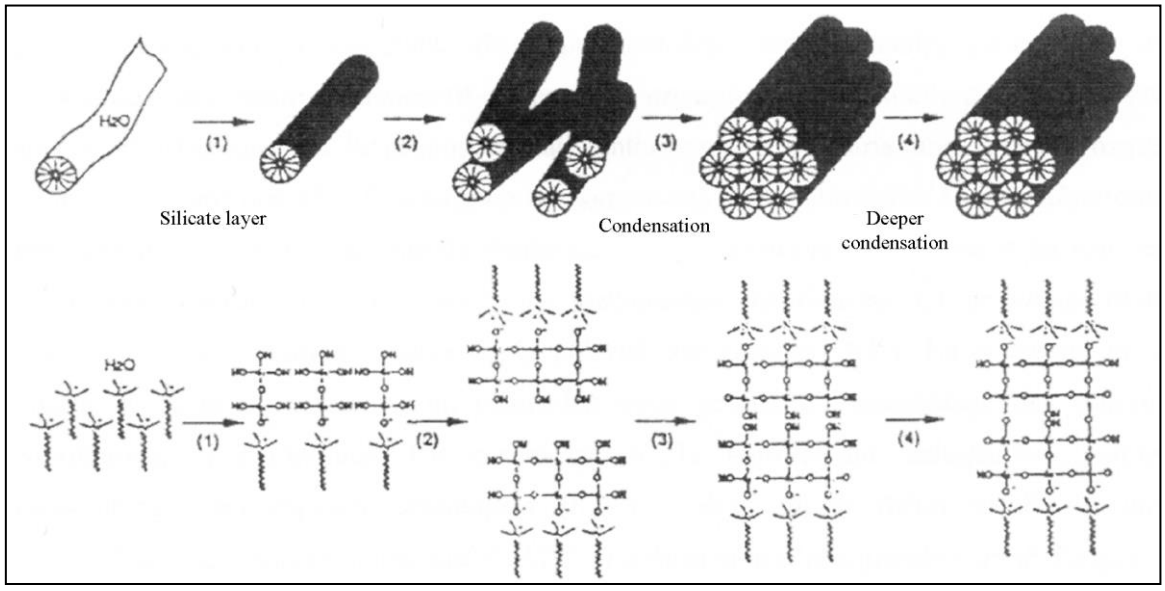

Figure 7: Formation mechanism proposed by Davis et al. [26]

The same year, Monnier *et al.* and Stucky *et al.* proposed another mechanism inspired from the work of Kuroda with kanemite. [27] Considering the transformation of this lamellar clay into a hexagonal material, they suggested a similar process for the synthesis of mesoporous silicas. This process is based on three main concepts: i) the existence of multiple bonds between silicate oligomers and surfactant heads, ii) the preferential polymerization at the silicate/surfactant interface and iii) the similar charge densities of silicate and surfactant. Hence starting from a lamellar arrangement, initiating the polymerization will decrease the charge density of silicates, leading to the introduction of curvature in the lamellar arrangement and eventually turning the solid into a hexagonally ordered material (Figure 8).

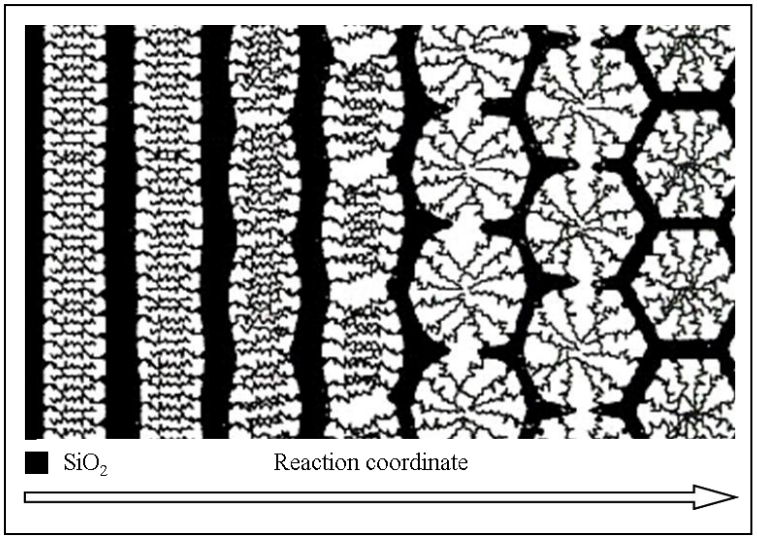

Figure 8: Formation mechanism proposed by Monnier et al. and Stucky et al. [27]

Two years later, Firouzi *et al.* demonstrated through ^{2}D and ^{29}Si NMR spectroscopy as well as neutron scattering that a micellar solution of cetyltrimethylammonium bromide (CTAB) turns into a hexagonal liquid crystal phase upon addition of silicate precursor. [28] They also demonstrated a remarkable affinity of D4R silicates (for Double-4-Ring, Figure 9) toward surfactant ammonium heads, due to the matching surface areas and charge densities of those two anionic and cationic species. Actually, this affinity is so strong that a CTAB solution in presence of a silicate solution containing no D4R silicate force the apparition of those double four rings. This assumption was backed by the successful synthesis of hexagonal, cubic and lamellar materials by Fyfe and Fu starting from D4R silicates. [29]

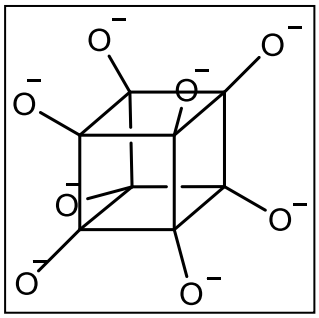

Figure 9: D4R silicate

More recent studies in 1999 and 2000 by Frasch *et al.* and Zhang *et al.*, using respectively *in situ* fuorimetry and EPR, unravelled a new aspect of the mechanism. [30, 31]

According to them, surfactant micelles exchange their counter-anion with silicate. Those silicates form oligomers that will eventually grow into polymers able to interact cooperatively with other micelles to create the hexagonal arrangement. Those polymers will then form aggregates that will precipitate when big enough and globally neutral.

II.0.3 Microwave synthesis

Microwave energy has been used recently for several chemical reactions, modifying selectivity and/or kinetics in a favourable way. From organic synthesis to polymerization or inorganic chemistry, many different processes are affected by this particular source of energy. By increasing reaction yields, selectivity or kinetics, microwave radiation possesses some of the environmentally friendly effects dear to green chemistry. Therefore, sturdy insights of its action are required in order to make the most of its potential.

In 1996, Stuerga and Gaillard published their investigations on wave/matter interactions. [32, 33] Their studies show that microwave energy is not sufficient to break covalent bonds but its absorption induces the motion of dipolar moments which is responsible for the transformation of electromagnetic energy into heat in lossy media.

Apart from a reduction of the necessary heating time, a more homogeneous distribution of size and shape of crystallites synthesized via microwave heating is reported. [34] From that observation, two possibilities arise: either microwave irradiation implies a faster nucleation of crystallites or the growth process is more uniform with this particular heating method. In 2006, Tompsett and Conner, in their review of microwave use for the synthesis of nanoporous materials, proposed a mechanism for crystallites undergoing such irradiation (Figure 10). [35]

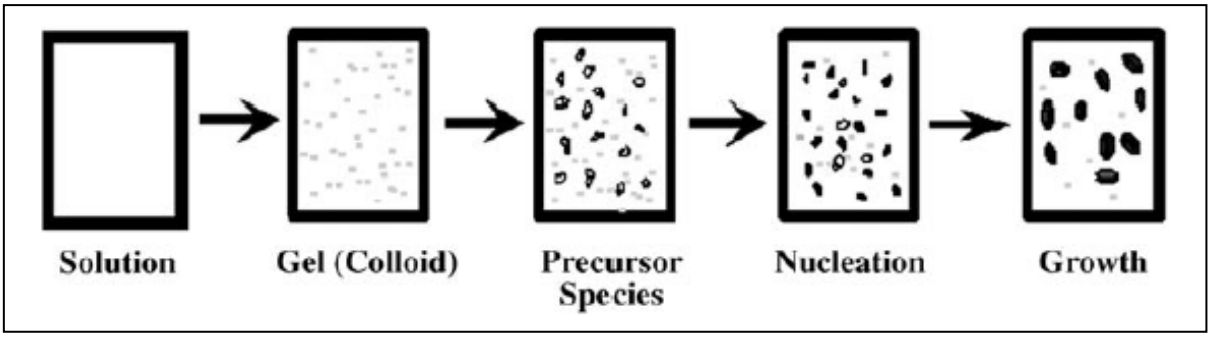

Figure 10: Proposed mechanism for a zeolite synthesis via microwave heating

The initial gel transforms into an assembly of ringlike structures, which will form the first structural cells. Nucleation of those cells occurs, creating small single crystals in the case of zeolites for instance. Then the growth step comes, by assembly of those single crystals. It is also supposed that a partial re-dissolution of the already formed crystallite may be involved in the growth of other crystals.

From this mechanism, microwave heating may have several influences:

- Increase of the heating rate in the solution.
- Better uniformity of the solution.
- Perturbation of interactions between species.
- Creation of hotter areas within the mixture.
- Increase of the precursor dissolution.
- Induction of specific reaction by absorption of microwave energy by the reacting species.

Development of microwave ovens for synthesis led material chemists to investigate the effect of this particular heating method. The first microwave-assisted synthesis of mesoporous silica was described in 1996 by Bein and Wu, with the synthesis of MCM-41 silica. [36] Synthesis time was reduced by an order of magnitude, the heating period at 150 °C only lasted around 80 min against 2 d in conventional ovens. Over the years, different types of mesoporous silica were then synthesized using microwave irradiation. Two years after this first reported utilisation, synthesis time was reduced to less than an hour, and heating temperature decreased down to 100-120 °C. [37] In 1998, Kim *et al.* tested the addition of ethylene glycol (EG) to the mixture. [38] This addition proved to be beneficial as both crystallinity and homogeneity of silica crystallites were improved (Figure 11). This optimization was attributed to the higher dissipation

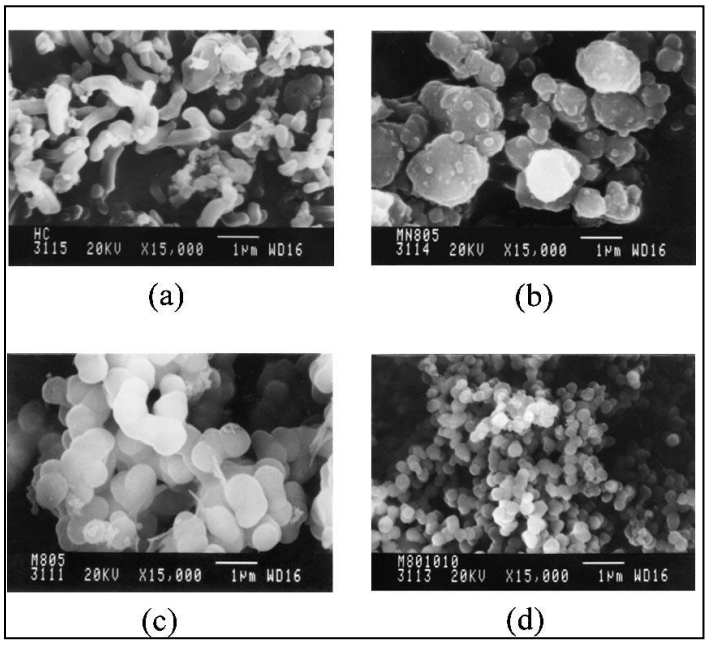

Figure 11: SEM images of MCM-41 silicas prepared by classical heating (a) and microwave heating with addition of ethylene glycol (EG), EG/H_2O=0 (b), EG/H_2O=0.02 (c), EG/H_2O=0.04 (d) [38]

factor of EG compared to the water one. Energy transfer was then more efficient, leading to a faster and more homogeneous nucleation and polymerization.

Microwave-assisted syntheses of SBA-15 were only reported from 2000, with the works of Kormarni *et al.* with heating times between 15 and 120 min at 100 °C. [39] Two years later, MCM-48 materials were successfully synthesized using microwave heating. [40] In all cases, better crystallization was observed which was translated into smaller crystals, faster and more homogenous nucleation as well as higher yields. This was actually coherent with previous results obtained with microwave-assisted syntheses of zeolites.

The main objective of this chapter is the adaptation of a mesoporous silica synthesis with a microwave heating method in order to provide a faster synthesis protocol for these materials. In particular, optimization of synthesis time and improvement of the porous characteristics of the materials will be key issues. Microwave-synthesized materials will then be compared with the classical ones to gauge the process efficiency.

II.1. Strategy

Our reference material is a MCM-41 type mesoporous silica, that presents a 2D hexagonal array. This kind of arrangement was chosen for three main reasons. Though it is comparable with MCM-48, its thermal stability is much better than lamellar MCM-50. [41] In addition, in the case of MCM-41, channels are more accessible than MCM-48 which favours both homogeneity in functionalization and diffusion of substrate for catalysis. Finally, this kind of mesoporous silica is much more reproducible in terms of synthesis as its existence domain is larger. For this work, an analogue of this silica type involving cetyltrimethylammonium tosylate (CTATos) instead of the usual bromide or chloride salt was used as surfactant. The synthesis protocol was first developed in the Laval University in Canada, where it was named LUS (for Laval University Silica). [42, 43] This synthesis is one of the shortest hydrothermal syntheses; as it lasts around twenty-two hours from the beginning of the surfactant dissolution to the end of the heating phase. As a comparison, MCM-41 or SBA-15 materials are synthesized in a couple of days. [16, 19]

A classic hydrothermal synthesis can be separated in four main steps: first the surfactant dissolution (1 hr at 60 °C), second the addition of the silica precursor and the preliminary stirring (1 hr at 60 °C), third the autoclave heating (20 hrs at 130 °C usually), and finally the filtration and washing of the as-made material with distilled water (Figure 12).

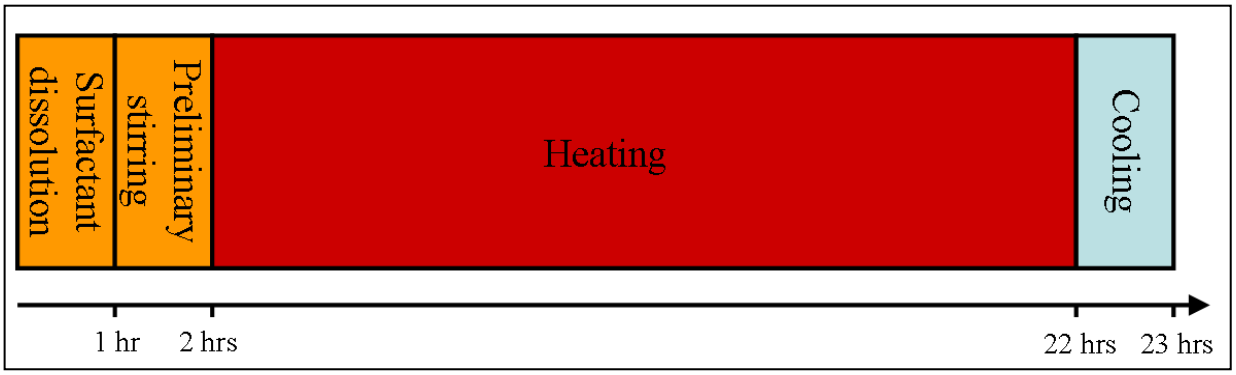

Figure 12: Synthesis steps for classical LUS mesoporous silica

Our initial aim was to improve the synthesis with microwave heating, to take advantage of both short synthesis time and homogeneity. Before explaining the results obtained with microwave heating, a description of the classical synthesis will be detailed.

II.2. Classical synthesis

As described above, cetyltrimethylammonium tosylate is used as surfactant to generate the mesostructure in LUS silica. The gel molar composition is $1SiO_2/0.05CTATos/0.5NaOH/79H_2O$. Surfactant is dissolved in water at 60 °C, the silica precursor is added and the resulting mixture is stirred for an hour to afford a rather homogeneously dispersed white suspension. This suspension is then introduced in an autoclave to be heated at 130 °C during 20 hrs. After autoclave cooling at room temperature, the solid is filtered, washed with water and dried at 80 °C overnight. The washing step removes every unreacted precursor and surfactant. The presence of remaining surfactant is quite easy to notice because of its very nature: the amphiphilic property of this molecule tends to form bubbles when dissolved and vigorously stirred in water, just like soap. Consequently the silica is considered clean when the filtrate does not bubble anymore. As a matter of fact, using tosylate salt instead of chloride or bromide salt presents some advantages: apart from structural reasons, the necessary amount of surfactant per precursor is lower and the bubbles do not form dense foam that slows down the filtration.

Once the material obtained, it is characterized with different techniques, such as powder X-ray diffraction, thermogravimetric analysis (TGA), and nitrogen adsorption and desorption. Considering that the latter consists in filling the mesopores with nitrogen, the as-made material has to be emptied from its surfactant which would prevent any sorption. In order to obtain the desired information, the surfactant is thus extracted, usually with hydrochloric acid in technical ethanol. Acid is used to protonate the surface silanolates and hence to destroy the electrostatic bond between the solid and the cationic surfactant. Without this interaction, the template is freed from the pore and dissolves in ethanol. For the other characterization techniques, the as-made silica can be used. The usual results will be presented below, as a reference for the comparison with microwave syntheses.

II.2.1 Powder X-Ray diffraction

This technique consists in analysing the diffraction of a monochromatic X-ray beam induced by the lattice planes of an ordered sample. Although the silica polymerizes in an amorphous fashion around the surfactant, the template itself presents a long-range order. In fact, the diffraction pattern comes from the 2D hexagonal arrangement of the pores. Bragg's

law allows us to link the angle θ between the incident ray and the scattering planes with the distance *d* between two planes and the radiation wavelength λ (Equation 1 and Figure 13).

$$2d\sin(\theta) = n.\lambda \qquad \textit{Equation 1}$$

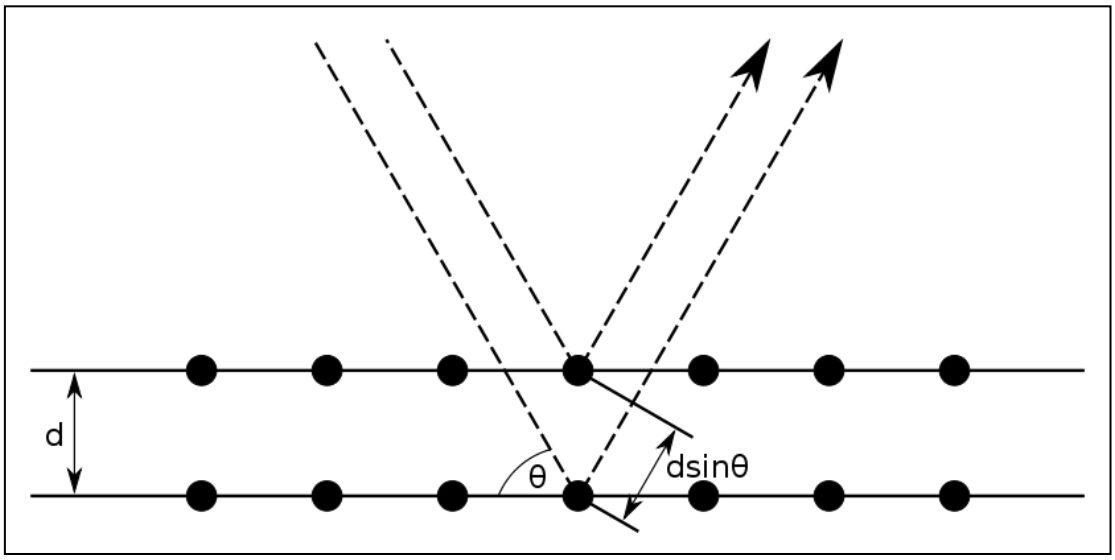

Figure 13: Diffraction of two lattice planes

In the case of a 2D hexagonal structure (P6mm symmetry), a = b, α = β = 90°, and γ = 120°, in the usual crystallographic notation (Figure 14). Furthermore, the distance between two planes of a same family of lattice, characterized by its Miller's index (h,k,l) can be linked to the lattice parameters through Equation 2. Hence from both Equations 1 and 2, the 2D arrangement can be verified by calculating the ratio of lattice distances deduced from the peak positions in the diffractogram. Basically, the ratio between d_{200} and d_{100} will be 0.5, and the ratio between d_{110} and d_{100} will be $\sqrt{3}$.

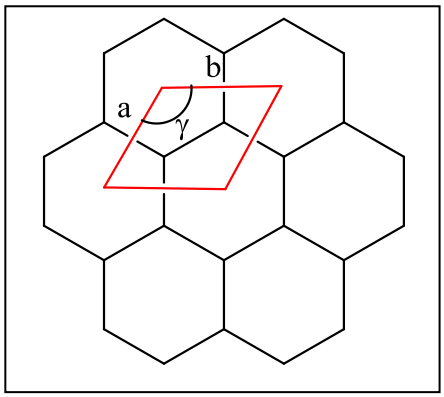

Figure 14: Example of a 2D hexagonal arrangement

$$\frac{1}{{d_{hkl}}^2} = \frac{4}{3}\left(\frac{h^2 + hk + k^2}{a^2}\right) + \frac{l^2}{c^2} \qquad \textit{Equation 2}$$

A whole X-ray diffractogram is measured for values of 2θ between 0.5 and 70° (Figure 15). However, characteristic peaks for hexagonal arrays can be found for values of 2θ below 10°, leading us to measure between 0.5 and 10° for routine analyses.

Mesoporous silica diffractogram displays four main peaks, around 2θ = 2.1°, 3.7°, 4.3° and 5.6°, corresponding to the diffraction of planes (100), (110), (200) and (210) respectively. There is also a fifth broad peak above 20°: this is not a diffraction peak but a diffusion peak

due to the Si-Si distances in the amorphous structure. Finally, lattice parameter a_0 can be calculated to measure the distance between the centres of two adjacent pores (Figure 14). Generally, lattice parameter for classical LUS-type silica is between 4.7 and 4.9 nm.

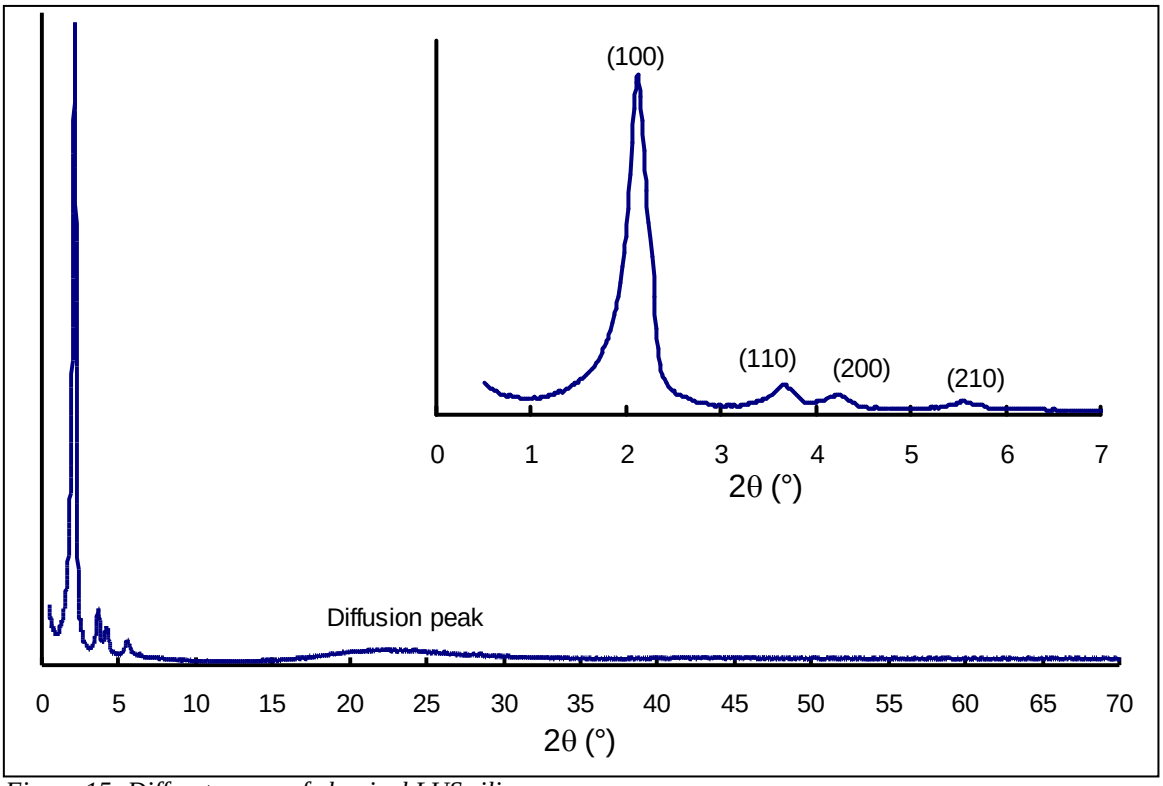

Figure 15: Diffractogram of classical LUS silica

II.2.2 Thermogravimetric analysis

Thermogravimetric analysis (TGA) is a characterization method that consists in heating the sample to measure the mass loss as a function of temperature. Although this is a destructive technique, it only requires few milligrams of material. Heating the sample under an air flux from 25 to 900 °C removes any absorbed solvent and also any organic function. Therefore, the final mass corresponds to the silica forming the mesoporous structure. Figure 16 displays classical mesoporous silica TGA profile. In order to have a better vision of the different mass losses, the derivative curve (dTG) is plotted. This curve emphasizes the changes in the TG curve's slope. Four main weight losses can be distinguished in the profile:

- 25-140 °C: this mass loss corresponds to solvent loss. In the case of an as-made LUS silica, it will therefore be attributed to a water loss. The amount of water lost in a LUS material is around 2.5 %, but this value can vary, depending on when the analysis was performed. For instance, a recently dried sample will lose less water than a sample let at air for some days.

- 140-310 °C: this is the main loss in a classical LUS, around 23 %. It is attributed to the degradation of surfactant in electrostatic interaction with the surface silanolates, *i.e.*, CTA^+.
- 310-430 °C: this loss is also assigned to the degradation of the surfactant, but in that case it corresponds to the surfactant that still contains its tosylate counter anion (CTATos). Indeed, the TGA of CTATos showed that this molecule starts to deteriorate at 300 °C. This latter profile actually exhibits a second loss which starts around 400 °C.
- 430-900 °C: this broad loss is attributed to two losses: one is the condensation of surface silanol groups which results in formation of water and consequently a detectable weight loss. As for the second loss, TGA coupled to mass spectroscopy proved that sulphonated compounds appear after 400 °C. As predicted by the thermogravimetric profile of CTATos, surfactant in interaction with tosylate makes part of this last loss as well as silanol condensation.

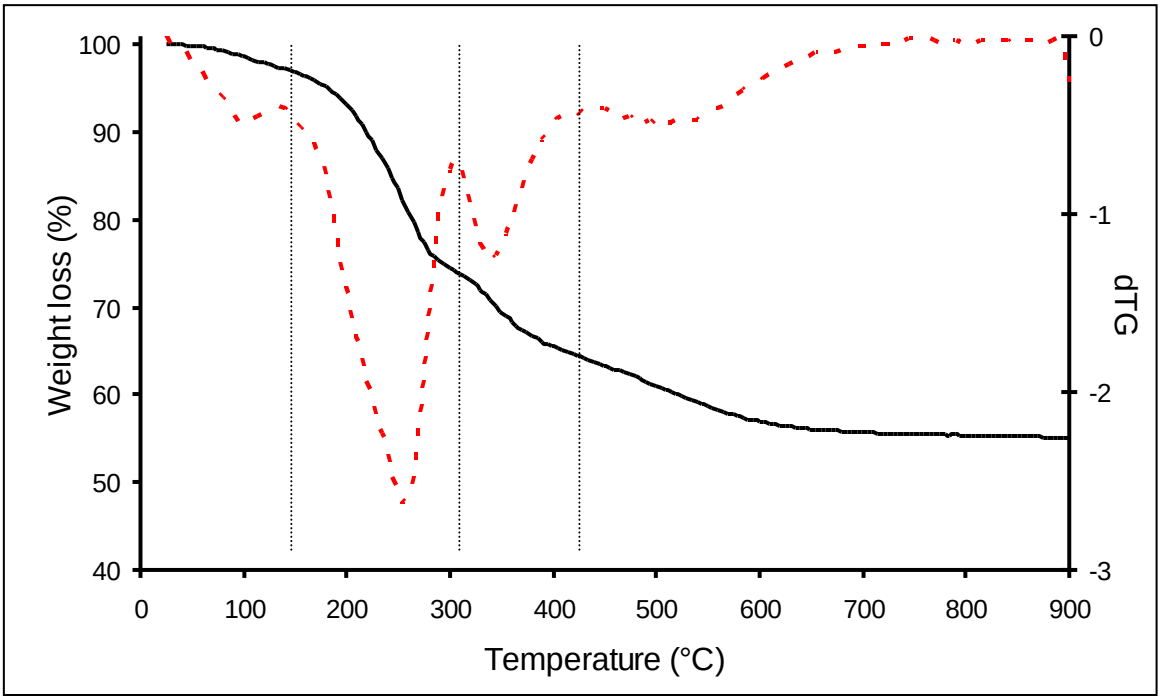

Figure 16: Thermogravimetric analysis of classical LUS silica (plain line) and its derivative curve (dashed line)

II.2.3 Nitrogen sorption isotherms

Nitrogen sorption is a key technique to obtain the mesoporous information. From this non-destructive analysis, properties such as pore surface, volume and diameter can be deduced. After surfactant extraction, a sample (around 100 mg) is pre-treated under vacuum

for one night at 80 or 130 °C, whether it contains or not any sensitive organic group. This pre-treatment allows eliminating any solvent left that could damage the equipment during the measure. In order to perform the latter, the sample is dropped into a liquid-nitrogen bath and put under vacuum. Small quantities of nitrogen are then added, and the resulting pressure is measured to provide the isotherm. LUS-type silica exhibits a type IV adsorption isotherm according to IUPAC nomenclature (Figure 17). [44] Three different volume rises can be observed, at low, medium and high relative pressure, respectively due to the filling of microporous, mesoporous and inter-grain volumes. The isotherm can exhibit a hysteresis loop stemmed from the difference between filling and emptying mechanisms. In fact, pore filling is done layer by layer whereas pore emptying is done by the displacement of a liquid nitrogen meniscus.

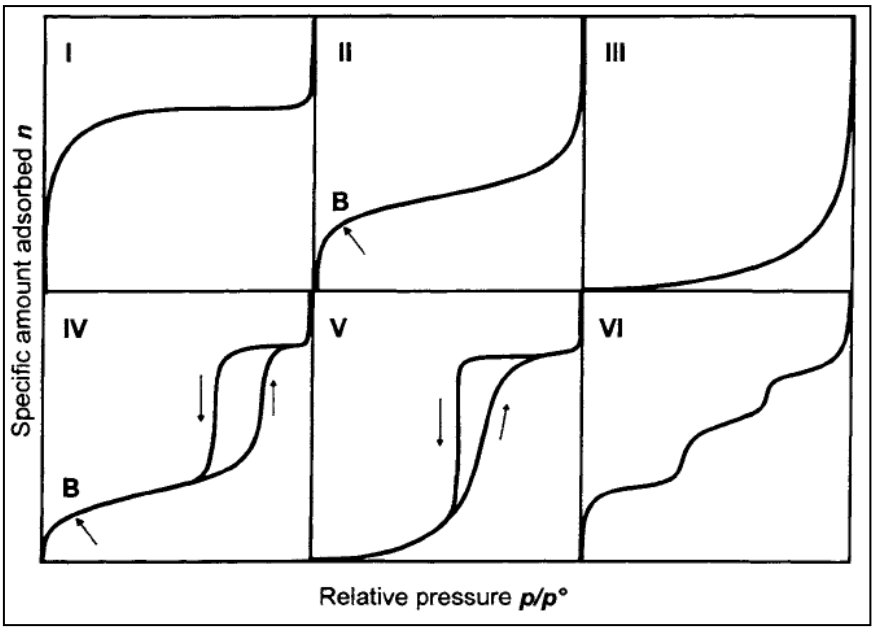

Figure 17: IUPAC nomenclature of gas sorption isotherms [44]

Figure 18 shows one of the isotherms measured with LUS silica. From what was explained before, two conclusion arise. First external volume is quite low compared to the internal porous volume, given the small value of adsorbed gas in the high-pressure region. Second, the similarity between adsorption and desorption indicates that both phenomenon are governed by similar mechanisms.

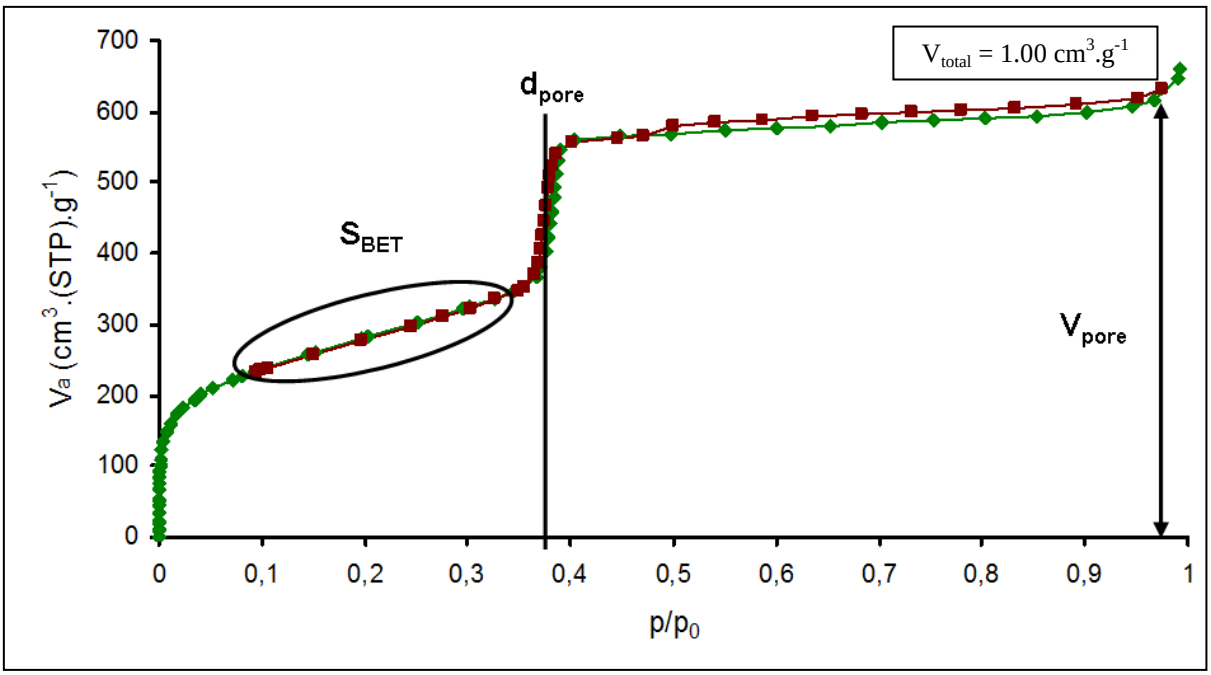

Figure 18: N_2 adsorption (green) and desorption (red) isotherms obtained with extracted LUS silica. S_{BET}, d_{pore} and V_{pore} indicate the portion of the curve used to determine the specific surface area, the porous diameter and the porous volume respectively

Different information can be extracted from this measure. From the curve itself, at p/p_0=0.99, the total amount of gas adsorbed by the sample V_{total} can be determined (*ca.* 1.00 $cm^3.g^{-1}$). One must note that the adsorbed volume reported on the y axis of a sorption isotherm is expressed in standard conditions of temperature and pressure (STP). As the measurement is performed at 77 K, the adsorbed gas will occupy much less volume than in STP condition, hence a difference between the adsorbed volume on the y axis and the actual pore volume. This latter is the sum of microporous, mesoporous and external volumes. One must be careful about those volumes: choosing to get the adsorbed volume at p/p_0=0.90, before the last external volume rise would not be relevant. In fact, the slight slope between p/p_0=0.45 and p/p_0=0.90 is a gaz adsorption also due to external volume. To determine each volume separately, and other characteristics such as surface area or pore diameter, some data treatment is necessary.

- **BET-plot:** the BET (for Brunauer-Emmett-Teller) method is based on the Langmuir mechanism of multilayer absorption: to cover the whole surface area, nitrogen molecules first form a monolayer, and then multilayers. [45] By plotting $p/[V_a(p-p_0)]$ as a function of p/p_0 and fitting the curve for $p/p_0 \in [0.05 ; 0.25]$ with a linear function (Figure 19), both specific surface area and adsorbed gas volume in a monolayer can be deduced. Surface area S_{BET} is more exploited in our case; a typical value is around 1000 $m^2.g^{-1}$. Like for

adsorbed gas volume, this surface area takes into account both porous and external surface areas. The external one can be known from t-plot, but actually its value is negligible in front of the porous one (around 40 $m^2.g^{-1}$, *i.e.*, 4 %). Intercept and slope of the linear fitting also provides the BET constant C. This constant traduces the affinity of the sorbent gas (N_2 in our case) with the silica surface. The higher the value of C, the better the affinity of N_2 with the surface will be. The measurement has been done on extracted silicas, meaning that the pore surface is composed of silanols which act like dipoles. When the nitrogen molecules come close to the surface during the adsorption process, their electron cloud is distorted by those surface dipoles which induce a dipolar moment in the N_2 molecule. The presence of those two dipoles, constant and induced, creates an interaction which increases the affinity of N_2 to the pore surface and the value of C in the same time. The intensity of this interaction depends on two factors: first the number of silanols and second their orientation. Indeed, this interaction will be improved when the silanols are orientated perpendicularly to the surface and when they are parallel one compared to another. In classical LUS extracted LUS silica, C is around 100.

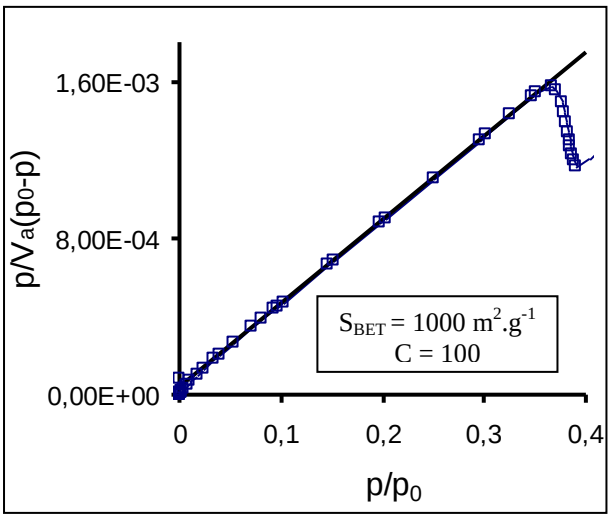

Figure 19: BET plot (blue) and its linear fitting (black) for extracted LUS silica

- **t-plot:** t-plot is a representation of the adsorbed volume V_a as a function of a standardized parameter. Shull suggested using the adsorption layer thickness t. [46, 47] To convert relative pressure p/p_0 into thickness t, a non-porous standard silica sample is used. From this standard isotherm, t value, in nanometres, is calculated using Equation 3:

$$t = \frac{V_a}{V_m} \times 0.354 \qquad \textit{Equation 3}$$

In this equation, V_a is the adsorbed volume, V_m the monolayer volume and the 0.354 value corresponds to the N_2 monolayer thickness. For mesoporous silicas such as LUS, a typical t-plot is shown on Figure 20.

There are two linear portions that can be fitted with two linear functions. The first one, below t=0.5, gives information about microporosity, whereas the second one, above t=1, gives information about external porosity. Microporosity in our case will not be well defined, it

would actually be more accurate to speak of roughness. This first fit gives us the specific surface (around 950 $m^2.g^{-1}$) and microporous volume (around 2.10^{-2} $cm^3.g^{-1}$). However, as this porosity is not regular, its filling will not be either and consequently those values have to be handled with care. The most reliable part will be the second linear fitting that informs us about external surface (around 40 $m^2.g^{-1}$) and porous volume (around 0.90 $cm^3.g^{-1}$).

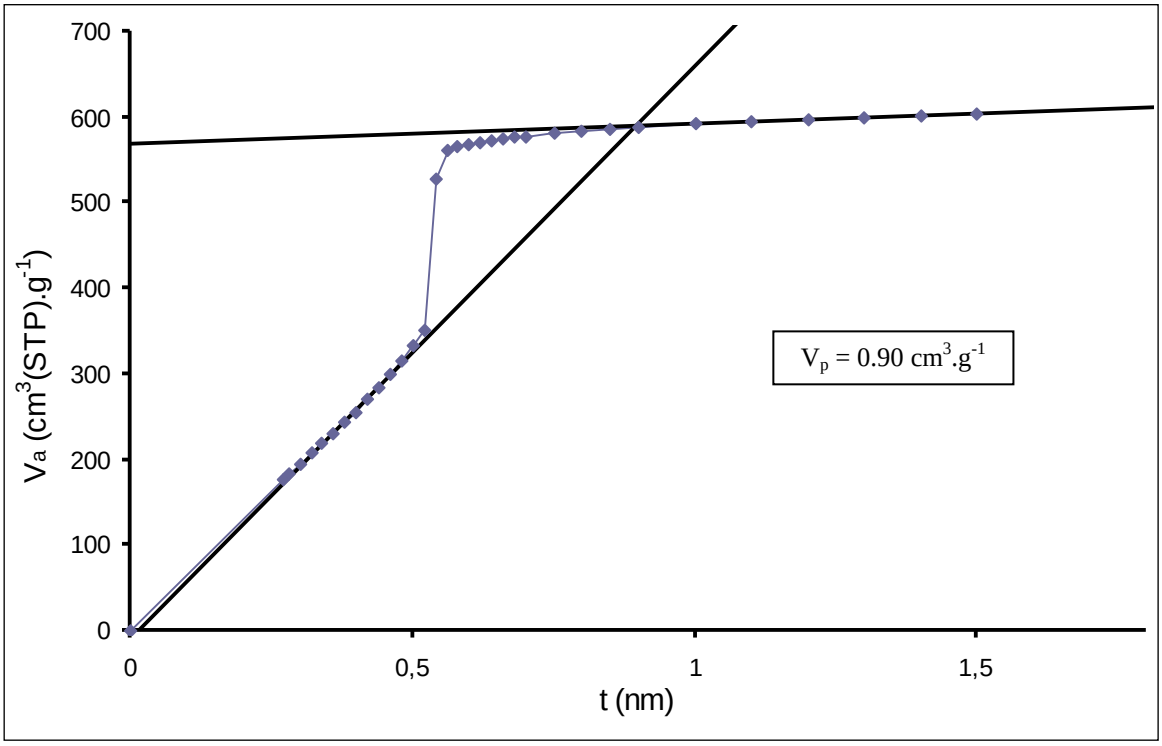

Figure 20: t-plot (blue) and its fitting (black) for extracted LUS silica

This volume in particular tells us a lot about the material, for it considers only the internal volume. Then checking its evolution after functionalization is a crucial step to verify the presence of remaining available pore volume.

- **Pore diameter:** this parameter can be calculated using different methods depending on the expected pore size, micro or mesoporous. The purpose of those methods is to obtain a relation between pore size and relative pressure. A usual method for microporous samples is the Horvath Kawazoe method (HK method). [48] This method was originally developed for the microporous filling in carbon sieves. In that case, relative pressure and pore size distribution are linked via the average potential inside the pores. For instance, with carbon sieves as adsorbate and nitrogen as adsorbent, the relation will be:

$$\ln\left(\frac{p}{p_0}\right) = \frac{62.38}{l - 0.64} \times \left[\frac{1.895 \times 10^{-3}}{(l - 0.32)^3} - \frac{2.7087 \times 10^{-7}}{(l - 0.32)^9} - 0.05014\right] \qquad \textit{Equation 4}$$

In this equation, l represents the distance between one side of a pore and the other side, which corresponds to the pore diameter for cylindrical pores. Although this method was designed for microporous samples, its results are quite accurate for LUS silicas, whose pores are in the lower limit of mesoporous range (3-4 nm). Because of this low diameter, capillary condensation does not induce a strong hysteresis and make the use of the HK method rather reliable. The distribution can be displayed by plotting dV_p/dd_p as a function of pore diameter d_p (Figure 21). Here V_p stands for porous volume. On this graphic, even though most of the points stand below the dV_p/dd_p peak, there is still a significant number of points after this same distribution peak which confirms the applicability of a microporous approach in this particular case. With this method, the pore diameter is evaluated around 3.5 nm for a classical LUS silica.

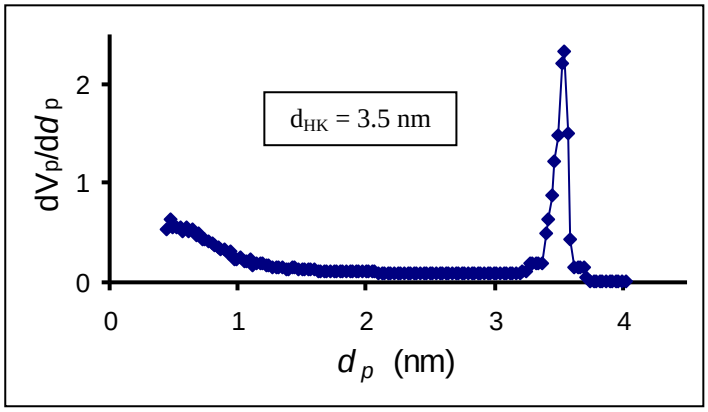

Figure 21: Pore size distribution calculated with HK method for extracted LUS silica

For mesoporous samples, the Barrett-Joyner-Halenda method (BJH) is more commonly applied. [49] This method exploits capillary condensation present in type IV isotherm. At low relative pressure, nitrogen adsorption occurs layer by layer. At a certain relative pressure, nitrogen starts to condensate inside the pores, creating a meniscus (Figure 22). Thus pore radius r_p will be the sum of adsorption layer thickness t, calculated as explained in t method, and meniscus radius r_m. Starting from Kelvin equation (Equation 5), the BJH method calculates the pore distribution.

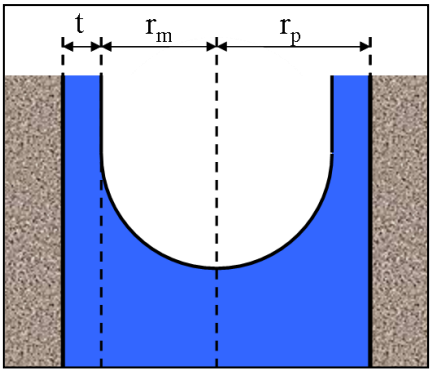

Figure 22: Meniscus inside a pore

$$\ln\left(\frac{p}{p_0}\right) = -\frac{2\gamma V_L}{RT}\frac{1}{r_m} \qquad \textit{Equation 5}$$

In this equation, r_m is meniscus radius, γ is surface tension, V_L is molar volume of liquid adsorptive, R is gas constant and T is absolute temperature. Considering nitrogen as adsorptive at 77 K, Equation 5 becomes:

$$r_m = 0.953/\ln\left(\frac{p_0}{p}\right) \qquad \textit{Equation 6}$$

BJH pore distribution will be plotted like HK distribution, *i.e.*, dV_p/dd_p as a function of d_p (Figure 23). Compared to HK distribution, this method displays much less points in the small diameter region. This comes from the initial hypothesis itself: for small pores, capillary condensation is not a reliable filling mechanism, thus the BJH calculation becomes irrelevant. Consequently, the few number of points below $d_p = 2$ nm will diminish the precision in the calculation of mean pore diameter. Actually, because of its lack of precision particularly for diameters smaller than 6 nm, the BJH method may reach the point where discrimination between different pore sizes becomes impossible. Indeed, same average pore size providing the exact same pore diameter value (2.57 nm) for different samples, leading us to favour other methods. Furthermore, this value is around 25 % less than HK method, although this latter considers in theory microporous materials.

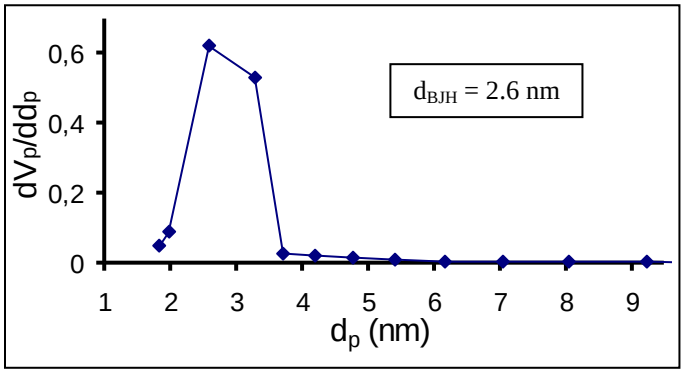

Figure 23: Pore size distribution calculated with BJH method for extracted LUS silica

The last method used in this study to calculate pore diameter distributions is the so-called BdB method (for Broekhoff and De Boer). [50] This method is based on a thermodynamic approach of the pore filling. It demonstrates that there is a difference between the thickness of layers adsorbed on a flat surface and on a cylindrical surface such as a pore. Depending on the diameter, capillary condensation will occur at a certain pressure as the result of the instability of the adsorbed film. The authors describe this method as valid for pore diameter above 1.5 nm, which is in between the HK and BJH ones. This calculation method can be simplified by using a polynomial approximation that links the pressure to the pore diameter: [51]

$$Y = 155.8457x^3 - 81.96198x^2 + 74.67812x + 14.60994 \qquad \textit{Equation 7}$$

where Y is the pore diameter (in Å) and x is the pressure at the inflexion point of the adsorption curve. Using this method provides a value of pore diameter around 4.0 nm for a classical LUS prepared hydrothermally with a single C_{16} alkyl chain CTATos, which is consistent with independent measurements and calculations on powder X-ray diffraction profiles. Furthermore, BdB method is not limited by pore sizes as small as those into consideration here, contrary to the BJH calculation.

II.2.4 Nuclear magnetic resonance

Crucial information can be deduced from ^{29}Si nuclear magnetic resonance (NMR) spectra. Silicon nucleus in mesoporous silicas can possess various environments which will tune their chemical displacement. Based on the number of oxygen atoms linked to the silicon and on the second neighbours linked to those oxygen atoms, a nomenclature has been established to designate the different silicon (Figure 24). Thus, silicon atoms linked to four,

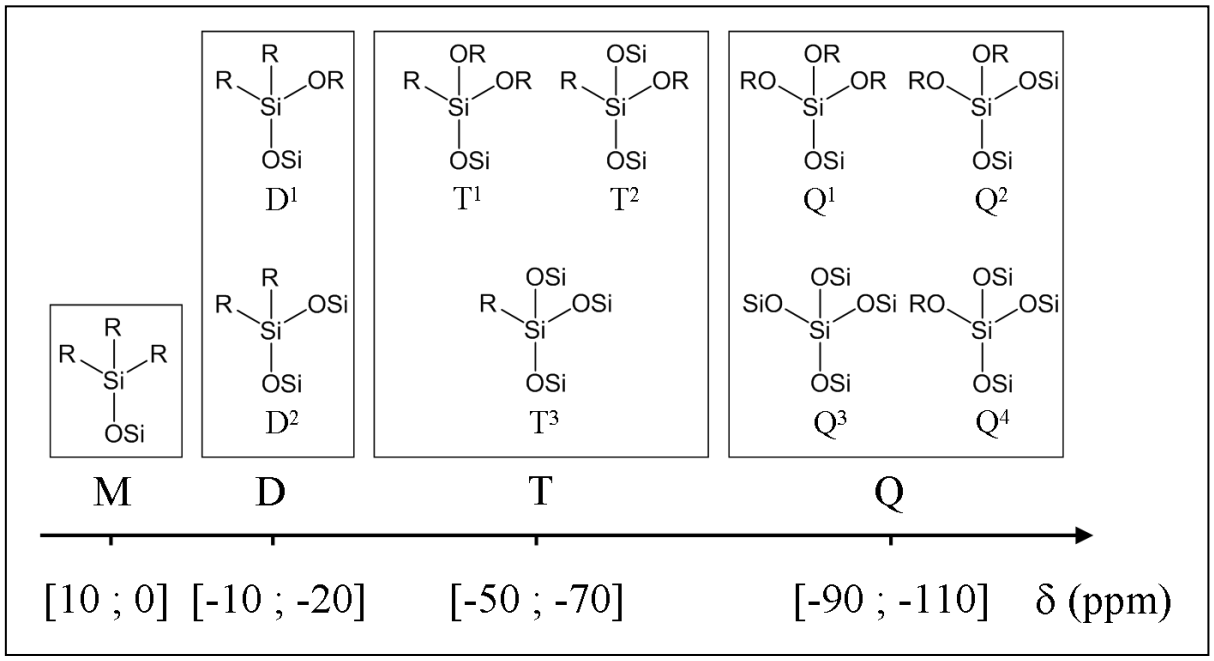

Figure 24: Silicon classification for NMR studies

three, two or one oxygen are named respectively Q, T, D and M. Then, the nature of the second atom after the oxygen one is indicated as follows: an exponent indicates the number of oxygen atoms linked to another silicon atom. In classical LUS material for instance, every silicon atoms are linked to four oxygen atoms. Therefore, only Q^1, Q^2, Q^3 and Q^4 species can occur. In practice, no Q^1 silicon is detected due to the low probability for silicates to possess three unreacted silanols.

Depending on the desired information, two kinds of ^{29}Si NMR spectra can be measured:

- Qualitative studies were carried out using a CP/MAS experiment (for Cross Polarization/Magic Angle Spinning). It consists in exciting the proton to transfer its polarization to the silicon, before decoupling the signal. Time of contact for proton to silicon transfer lasts 5 ms and relaxation time is the proton relaxation time, *i.e.*, 2 s.
- Quantitative studies are incontestably longer. In that case, an HPDEC experiment (for High Power Decoupled) was performed. This time, ^{29}Si is directly excited and the signal

is decoupled to avoid proton couplings. The length of this pulse finds its source in the 500 s relaxation time spent for silicon. However, signals obtained in those spectra can be deconvoluted with an adequate program (DMFit in our case) [52] to retrieve quantitative signals from each silicon species. All parameters were let free to vary except for the position of Q^2, which was set to 90 ppm.

For a classical LUS material, deconvolution of quantitative NMR spectra leads to an average distribution $Q^2/Q^3/Q^4$ around 5/40/55 %.

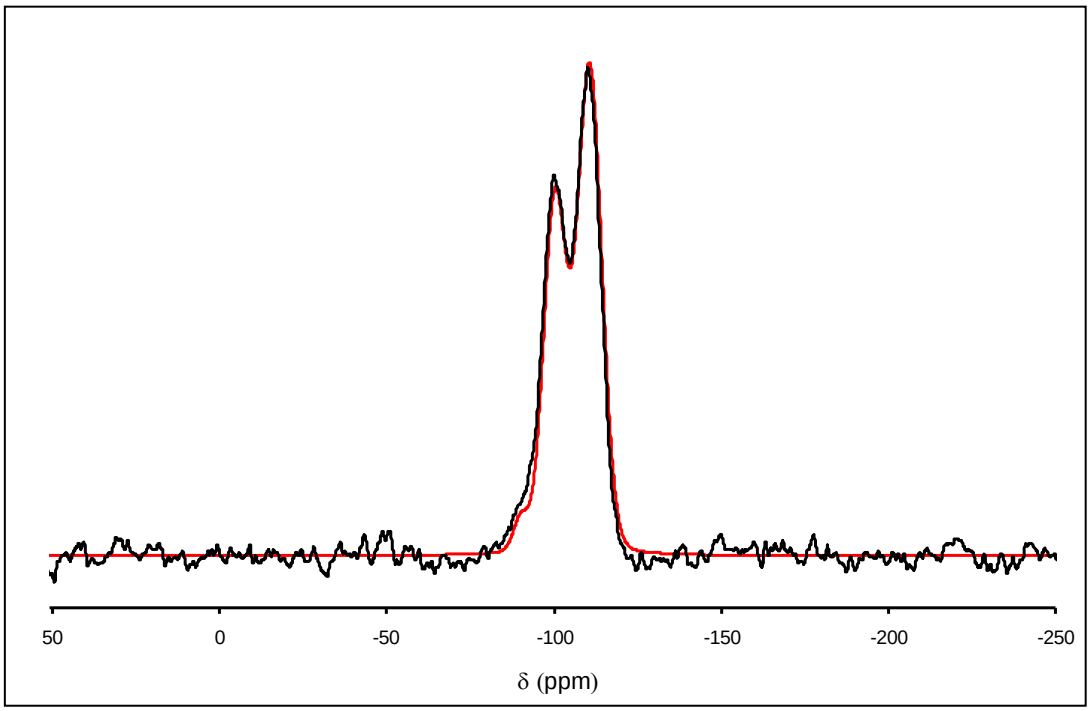

Figure 25: ^{29}Si HPDEC NMR spectra of an as-made classical LUS material (black) and its fit calculated with DMFit (red)

II.3. Microwave synthesis

Our first motivation was to develop a fastest synthesis that would keep similar structure and properties than the classical protocol. Therefore, reduction of the total synthesis time was studied first, followed by the influence of heating temperature. This section will describe the effects of microwave irradiation and the materials obtained with this method will be compared with the ones obtained using the classical synthesis.

II.3.1 Synthesis time reduction

In order to reduce the total synthesis time, we first focused on reducing the heating time, for it was the obvious parameter we could improve easily with the microwave heating. The microwave oven used in this study was a Speedwave four by Berghof providing a microwave irradiation at 2450 MHz with a power of 1450 W. This instrument allowed us to modify two distinct parameters apart from the temperature to control the heating profile: the ramp, *i.e.*, the time used to pass from room temperature to the chosen temperature, and the plateau, *i.e.*, the time spent at this desired temperature. Table 1 displays some of the conditions used in this study to synthesize microwave irradiated mesoporous silica. The silicas synthesized with different conditions were named $LUS_{MW}x$ where x is a digit. This nomenclature will only be used in this chapter.

Table 1: Principal synthesis conditions of silica via microwave heating

Silica	Addition [a]	Preliminary plateau (°C)	Temp. (°C)	Ramp (min)	Plateau (min)	Cooling[b]	Total [c] (min)
$LUS_{MW}01$	S	/	130	20	40	RT	240
$LUS_{MW}02$	F	60 (10 min)	130	10	40	RT	180
$LUS_{MW}03$	F	60 (10 min)	130	10	20	RT	160
$LUS_{MW}04$	F	/	130	1	14	RT	125
$LUS_{MW}05$	F	/	130	1	9	I	80
$LUS_{MW}06$	F	/	130	1	4	I	75
$LUS_{MW}07$	F	/	150	1	9	I	80
$LUS_{MW}08$	F	/	170	1	9	I	80
$LUS_{MW}09$	F	/	170	1	/	I	80
$LUS_{MW}10$	F	/	170	1	2	I	80
$LUS_{MW}11$	F	/	180	1	9	I	80
$LUS_{MW}12$	F	/	190	1	9	I	80

a) S=Slow, drop wise addition followed by a 1 hr stirring, F=Fast, addition on the edge of the beaker before putting the mixture in the autoclave, b) RT=Room Temperature, cooled at room temperature, I=Ice-bath, cooled in a ice-bath, c) Includes surfactant dissolution, heating and cooling before solid recovery.

II.3.1.1 Heating time

At the beginning of this study, the objective was to reduce the heating time without damaging the 2D hexagonal structure. Those materials were characterized by X-ray powder diffraction to make sure well-defined 2D hexagonal matrices were obtained. In the literature, microwave synthesis times vary between dozens of minutes to couples of hour at 130 °C. Thus, a first test was made using a total microwave time of one hour. Those conditions appeared to keep the long range order of the material, therefore we progressively reduced it. The preliminary temperature plateau for silicas $LUS_{MW}02$ and $LUS_{MW}03$ replaced the surfactant and precursor stirring step at 60 °C, but this preliminary heating was then abandoned when the $LUS_{MW}04$ silica, which was synthesized without any preliminary plateau, exhibited a good structure. Heating time was progressively reduced to reach minute-made silica. A ten minutes synthesis was finally considered because of the better temperature control that could be maintained. Indeed, the microwave oven used in this study could not reach temperatures above 140°C in only one minute, which was a problem when it came to study the influence of this latter. Though we kept a 10 minute heating time, in every case the

expected hexagonal pattern was observed, with only a small variation in the lattice parameter and/or the diffraction peak intensities. (Figure 26)

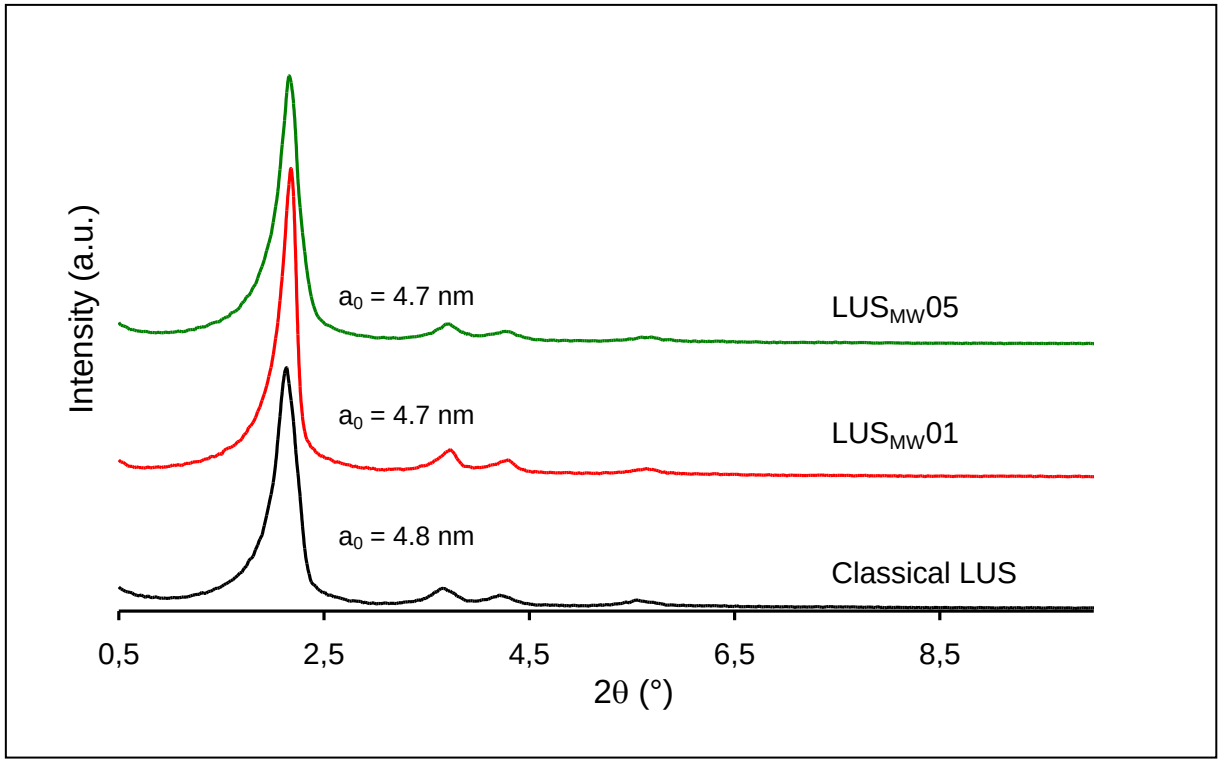

Figure 26: Comaprison of the diffraction patterns of three LUS mesoporous silicas: classical (bottom), $LUS_{MW}01$ (middle) and $LUS_{MW}05$ (top).

II.3.1.2 Precursor addition

To reduce even more the whole process time, the addition technique was modified. Instead of a slow addition followed by stirring, the precursor solution was added on the edge of the flask containing the surfactant solution. Following either the slow or fast addition, final mixtures presented a different texture: in the first case, the solution was a suspension of small and not discernable particles, while in the second case the suspension was made of bigger aggregates. In both cases the hexagonal structure was obtained, leading us to adopt the fast addition and to save one additional hour.

II.3.1.3 Autoclave cooling

Finally, the cooling process was modified. In the first tests or in the classical way, the autoclave was cooled at room temperature, which lasted around an hour. In order to cool the autoclaves in the minimum time an ice-bath was used. For the synthesis at 130°C, the autoclaves could be opened safely after 10 min; for temperatures above 170 °C, it was safer to

wait around 30 min to avoid steam jets. According to the diffracting patterns (Figure 26), no structure loss was observed, allowing us to save another 30 min.

Finally, fast precursor addition, ten minutes heating time (1 min for the ramp, 9 min for the plateau) and ice-bath cooling were chosen as basic conditions to study the influence of temperature on both structure and properties. Therefore, total synthesis time was reduced from 23 hrs to less than 2 hrs (Figure 27). In this new protocol, surfactant dissolution and autoclave cooling actually became the most time-consuming steps, while heating process is now a twelfth of the total synthesis time.

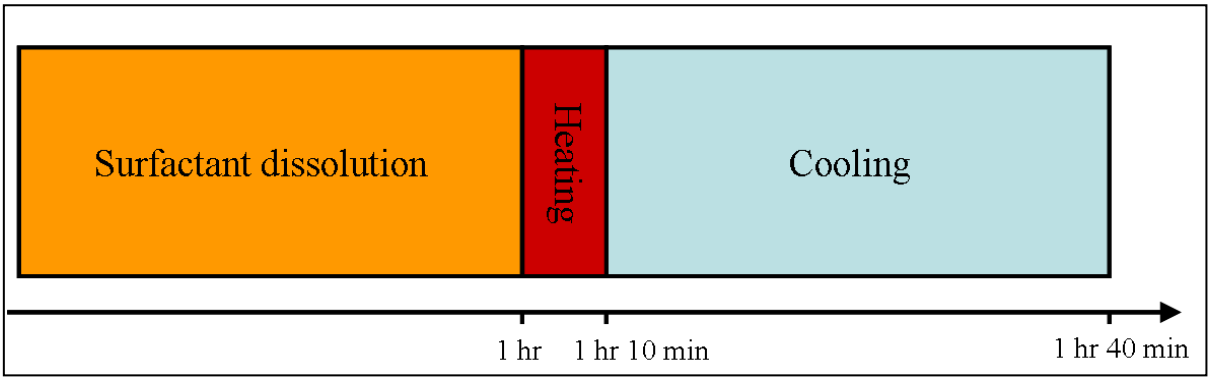

Figure 27: Synthesis steps for microwave LUS silica

II.3.2 Heating temperature influence

The influence of the temperature was studied for a heating time of 10 min. As explained before, shorter times did not permit reaching a stable set temperature above 140 °C, preventing any reliable conclusion about its effect on the final material.

The goal was to check whether or not higher temperatures would lead to better materials. Previous studies in the laboratory proved that temperatures around 190 °C in the classical conditions led to surfactant degradation by elimination of the quaternary ammonium and generation of a tertiary amine as well as a double bond C=C (Scheme 1). [53, 54, 55] Hence the classical method reached its limits at such temperature, given that the template degradation induces a loss in the mesoporous arrangement. Another inconvenient was the impossibility to recycle the surfactant by extracting it with chemical methods such as acidic treatment.

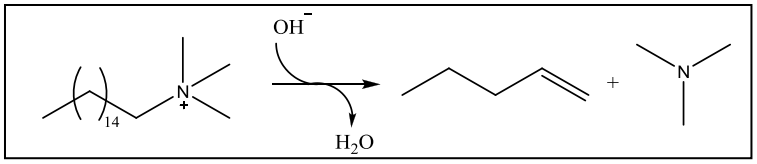

Scheme 1: Degradation of surfactant via Hoffmann elimination

Drastic reduction of the whole synthesis time has proven no to have any major influence on the 2D hexagonal structure. However properties such as pore volume, surface or diameter, which are key parameters to define the quality of mesoporous materials, still had to be investigated. The study was carried out on microwave silicas synthesized at 130, 150, 170, 180 and 190 °C alongside with classical silicas synthesized at 130, 150 and 170 °C used as comparison. For every material, synthesized either by hydrothermal treatment or using microwave, calcination at 550 °C was performed after extraction of its surfactant to determine its thermal stability. For non-calcined materials, surfactant was removed before they were characterized by X-ray diffraction and nitrogen sorption isotherms. Lattice parameter a_0 was measured by powder X-ray diffraction while total adsorbed volume (V_{total}), BET constant C as well as pore diameter (d_{HK} and d_{BdB}), volume (V_p) and surface (S_{BET}) were calculated from nitrogen adsorption and desorption isotherms. Table 2 displays the results obtained from those techniques. In this table, LUS_H stands for hydrothermal syntheses while LUS_{MW} stands for microwave syntheses. Numbers after the "@" correspond to the temperature of the synthesis. Samples containing the suffix "Cal" are samples calcined at 550 °C. Figure 28 illustrates the isotherms measured for some classical and microwave-synthesized mesoporous silicas.

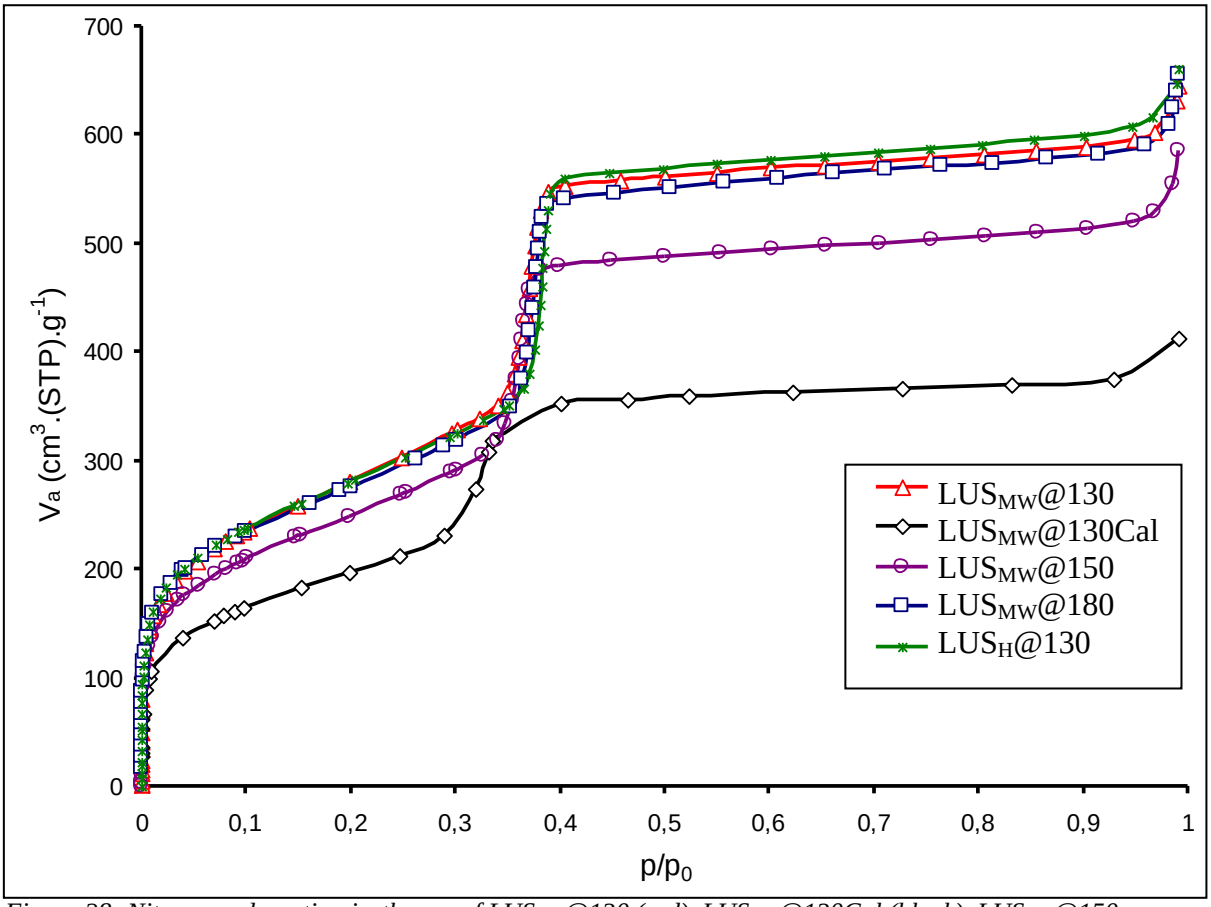

Figure 28: Nitrogen adsorption isotherms of LUS_{MW}@130 (red), LUS_{MW}@130Cal (black), LUS_{MW}@150 (purple), LUS_{MW}@180 (blue) and LUS_H@130 (green).

Table 2: Porosity data from N_2 sorption isotherms and XRD for extracted and calcined materials

Silica	a_0[a] (nm)	V_{total}[c] ($cm^3.g^{-1}$)	V_p[d] ($cm^3.g^{-1}$)	S_{BET}[b] ($m^2.g^{-1}$)	d_{HK}[e] (nm)	d_{BdB}[f] (nm)	$T_{w\ BdB}$[g] (nm)	C
LUS_H@130	4.8	1.00	0.88	1010	3.5	4.0	0.8	105
LUS_H@150	5.0	0.98	0.90	990	3.7	4.1	0.9	114
LUS_H@170	6.3	1.02	0.92	830	-	5.3	1.0	211
LUS_{MW}@130	4.7	0.98	0.87	1020	3.4	3.9	0.8	86
LUS_{MW}@150	4.6	0.90	0.75	910	3.3	3.8	0.8	88
LUS_{MW}@170	4.5	0.89	0.76	900	3.3	3.8	0.7	87
LUS_{MW}@180	4.6	1.00	0.86	990	3.5	3.9	0.7	135
LUS_{MW}@190	4.7	0.96	0.85	990	3.4	3.9	0.8	104
LUS_H@130 Cal	4.5	0.86	0.73	920	3.2	3.7	0.8	87
LUS_H@150 Cal	4.8	0.95	0.85	1000	3.5	3.9	0.9	94
LUS_H@170 Cal	6.2	0.99	0.91	860	-	5.2	1.0	165
LUS_{MW}@130 Cal	4.4	0.64	0.56	720	3.0	3.5	0.9	79
LUS_{MW}@150 Cal	4.5	0.82	0.70	930	3.1	3.6	0.9	71
LUS_{MW}@170 Cal	4.4	0.86	0.72	960	3.1	3.6	0.8	67
LUS_{MW}@180 Cal	4.6	0.93	0.79	1000	3.1	3.7	0.9	79
LUS_{MW}@190 Cal	4.6	0.93	0.80	1000	3.2	3.7	0.9	82

a) $a_0 = d_{100} \times 2/1.732$, hexagonal lattice parameter calculated from XRD, accuracy ± 0.1 nm, b) S_{BET} determined from BET equation surface applied in the relative pressure range of $0.05 \leq p/p_0 \leq 0.16$, accuracy ± 50 $m^2.g^{-1}$, c) V_{total} at p/p_0=0.99, accuracy ± 0.01 $cm^3.g^{-1}$, d) V_p extrapolated at $p/p_0 = 0$ on the adsorption plateau of the t-plot, accuracy ± 0.01 $cm^3.g^{-1}$, e) d_{HK} pore diameter extrapolated from the Horvath-Kawazoe method accuracy ± 0.1 nm, f) d_{BdB} extrapolated from the Broekhoff and De Boer method $Y = 14{,}60994 + 74{,}67812X - 81{,}96198X^2 + 155{,}8457X^3$, accuracy ± 0.1 nm, g) T_w, pore wall thickness obtained from the difference a_0-d_{BdB}, accuracy ± 0.2 nm.

Although this table does sum up all the relevant data to conclude about the quality of the materials mesoporosity, it is more exploitable when analysed by steps. To clarify the presentation, those results were plot as a function of temperature for each family of materials: microwave, hydrothermal, microwave calcinated and hydrothermal calcinated.

II.3.2.1 Pore diameter d_{BdB}

Table 2 presents pore diameters calculated either with the HK method or the BdB method. In order to compare the different materials, we chose to consider the BdB method, for it is applicable to a broader range of diameters. Indeed, for the LUS_H@170 material, pore diameter could not be calculated with the HK method.

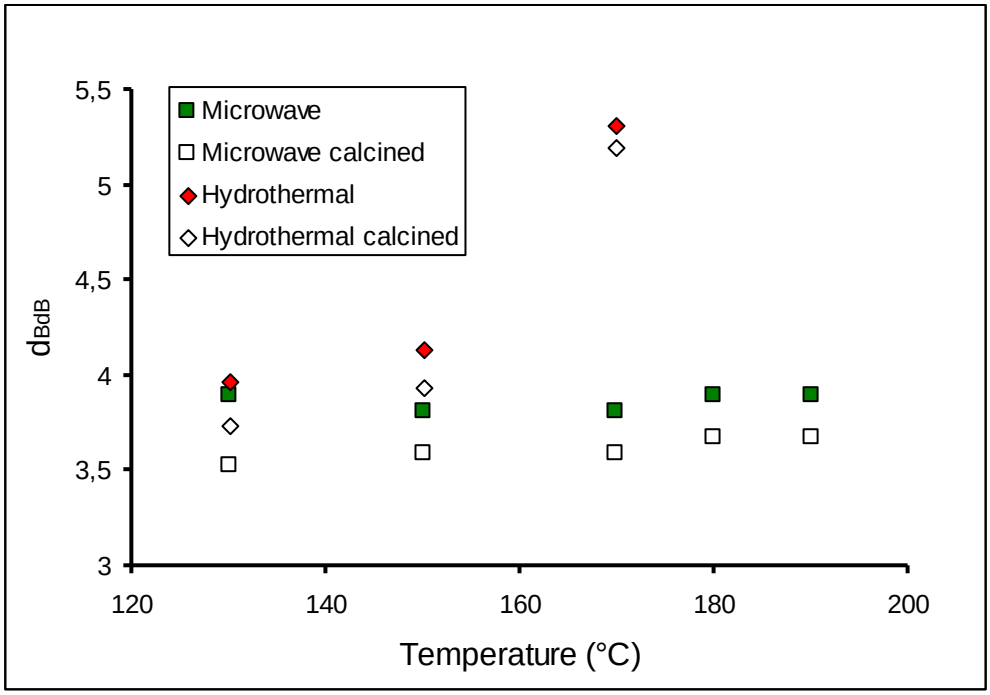

Figure 29: Pore diameter d_{BdB} as a function of synthesis temperature for microwave and classical materials as well as their calcined equivalents

When plotted as a function of synthesis temperature, one conclusion immediately arises (Figure 29). While d_{BdB} increased upon augmentation of temperature for hydrothermal materials (from 4.0 nm to 5.3 nm), it remains relatively constant (*ca.* 3.8 nm) for microwave-polymerised silicas. In the case of calcined samples, d_{BdB} slightly diminishes due to the contraction implied by the calcination treatment: upon heating at high temperature, adjacent silanols tend to condensate, which is proved by the mass loss starting from 450 °C up to *ca.* 650 °C in TGA. This contraction seems to be rather similar for each kind of material (difference *ca.* 0.2 nm in the case of hydrothermally treated samples and *ca.* 0.3 nm in microwave irradiated samples).

Lattice parameter a_0 tends to follow the same trend. Though the diffractogram presented in the previous section was measured from as-made silica (Figure 15), lattice parameters reported in Table 2 were calculated from diffractogram of extracted silicas. By doing so, we ensured that the same powders were used for each technique without modification such as acidic treatment, though this treatment does not have any noticeable

effect in the case of classical hydrothermal mesostructured silicas such as those from the LUS series. Similar trend for both diameter and lattice parameter implied a similar pore wall thickness in those materials. Indeed, pore wall thicknesses calculated from the difference a_0-d_{BdB} is quite constant, varying only by 0.2 nm, which is within the range of error of this calculation as precision for a_0 and d_{BdB} is ± 0.1 nm.

II.3.2.2 Porous volume V_p

Given that the evolutions of porous and total adsorbed volumes are similar, we will only focus on the porous volume V_p, *i.e.*, the total volume without inter-grain volume. In addition, similar evolution of both volumes means similar external volumes.

This porous volume does not vary much in hydrothermal syntheses; it slightly rises with a value around 0.9 $cm^3.g^{-1}$ (Figure 30). For microwave syntheses, the volume diminishes for 150 °C and 170 °C before rising up to values similar to those of the synthesis at 130 °C. However, calcined materials present the same behaviour: when the synthesis temperature increases, V_p increases likewise. This difference of behaviour emphasizes the fact that both microwave and hydrothermal-synthesised materials at 130 °C are not as stable as materials prepared at higher temperature. For instance, the LUS_{MW}@130 material loses half his porous volume after calcination (Figure 28). This loss of volume may be attributed to a partial collapse of the structure or merely to an overall framework shrinking, densifying the porous system. The latter case can be verified from the XRD value a_0. In fact, shrinkage occurs in both cases as a_0 decreases after calcination from 4.8 to 4.5 nm and from 4.7 to 4.4 nm respectively for LUS_H@130 and LUS_{MW}@130, *i.e.*, 0.3 nm or less than 7 %. In the mean time, pore diameter has also suffered a decrease of about 8 % which would produce a decrease of volume of about 15 % (for the same channel length). Therefore, volume should decrease from 0.88 down to 0.75 $cm^3.g^{-1}$, which is almost the case for LUS_H@130. This value nicely fits with a simple shrinking of the hexagonal network. In the case of LUS_{MW}@130, a similar decrease is observed for an initial volume of 0.87 $cm^3.g^{-1}$ that ends up at 0.56 $cm^3.g^{-1}$ instead of 0.74 $cm^3.g^{-1}$. Even by considering a longitudinal shrinkage around 8 %, the final volume would only decrease by 22 %, *i.e.*, to 0.68 $cm^3.g^{-1}$. These figures demonstrate that in addition to shrinkage, there is a decrease of pore volume coming from a partial structure collapse. This is also reflected by a higher surface area loss in the case of microwave-synthesized material. For syntheses performed at 150 or 170 °C, the same evolution occurs with less shrinkage and apparently no structural loss. Therefore, the solid maturation occurs at higher temperature when microwave heating is at work. The rational lies in the need for higher temperatures to

let the siliceous walls densify enough in compensation of such short synthesis time employed here (10 min).

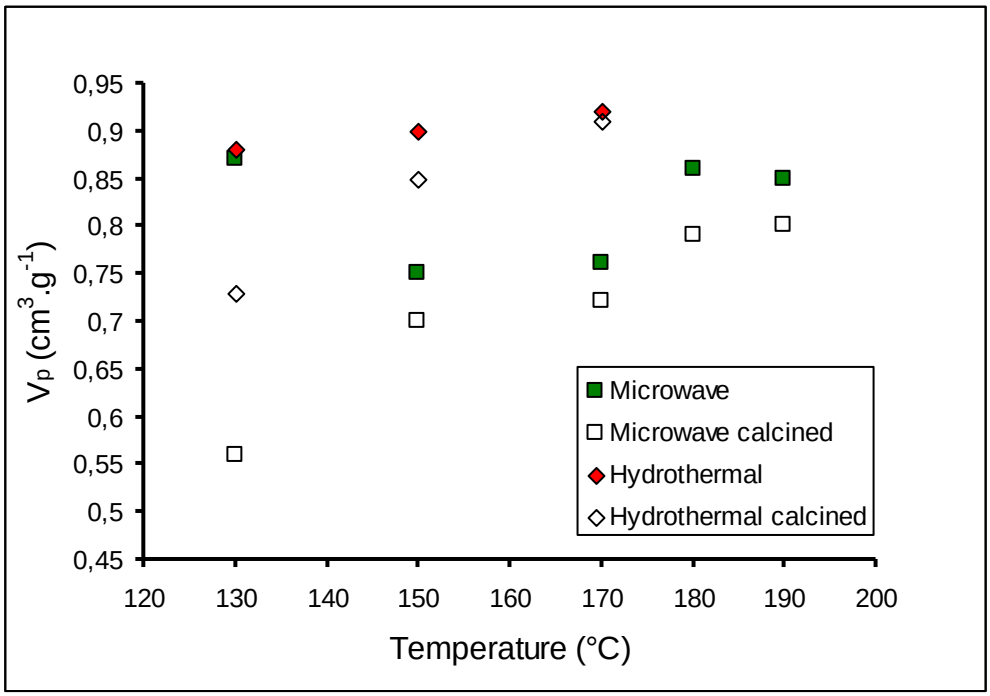

Figure 30: Porous volume V_p as a function of synthesis temperature for microwave and classical materials as well as their calcined equivalents

The case of higher temperature is a little bit different since classical and microwave heating method are not compared anymore. The reason lies into previous findings showing that the mesoporous structure tend to collapse above 170°C using a conventional oven heating. Indeed, the templating conditions do not survive long thermal effect (here 22 h). [55] However it is still possible to obtain good quality material in the microwave series mostly thanks to the short synthesis time. Indeed, materials with exceptional porous quality could be obtained at high temperature never explored for such systems. At both 180 and 190 °C, the structure is still there with even larger porous volume constantly increasing from low to high temperature in the microwave series (exception made from LUS_{MW}@130 which appeared to be an unstable phase). In parallel, the BET surface area is merely constant with apparently a slight increase just above measurement precision. In fact, the two highest temperature treatments generate the highest pore volumes which reach the values of the classical thermal series. In parallel, these conditions go along with the lowest shrinkage effect observed within the microwave series. Concomitantly, at such high temperatures the shrinkage is at the lowest and is also comparable with that of the LUS_H@150 heated classically for 22 hours.

Augmentation of pore volume upon increasing the temperature of synthesis is already described in the literature and discussed in detail by Tolbert *et al.* as a mere micelle dilatation that could be compared to a swelling effect (Figure 31). [56] The difference with classical

swelling comes from its origin that is not triggered by external molecules inserted in the micelles but rather by the dynamics of the single long carbon chain also called tail. In fact, thermal agitation produces an apparent shortening of the length of the tail which, by compensation, leads to a thickening of the dynamic diameter concentrated at the head side as represented in Figure 31.a. A larger head for each of the self assembled surfactant of the micelle produce an augmentation of the external surface and of the overall size of the micelle as represented in Figure 31.b. Note that it is inferred in this article that, once again by compensation, the middle of the micelle is empty or filled with something unidentified. [56]

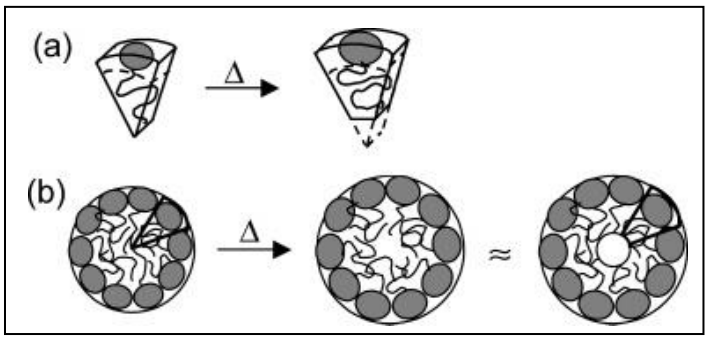

Figure 31: Effect of temperature on a) a simple surfactant molecule and b) a whole micelle [56]

The micelle "thermal swelling" effect is also clearly observed in our classical hydrothermal series. By contrast, this effect is not observed in the microwave series up to 180 °C. While this swelling effect should be instantaneous for a free micelle in response to the temperature, it is apparently not the case when micelles are confined in the siliceous matrix for synthesis time below 10 min. Nonetheless, the thermal swelling should create instantaneously an internal pressure, the driven force for pore dilatation. These results clearly demonstrate that the structure is already mature before the thermal swelling becomes important enough to be observed. The threshold temperature is provided by the classical thermal series and can be found in between 150 and 170°C, *i.e.*, when the framework is mature. Consistent with the picture drawn from the overall set of data, most of the events that determinate pore size and silica densification occurs during the temperature ramp. Conversely, the plateau kept after this ramp lasts in between 7 to 9 minutes within the microwave series and has little effect on the final characteristics of the materials. Note for example that at the lowest temperature investigate here, 130°C, despite a total time longer than the ramping time, there is not enough energy to let the silica polycondensate and densify enough, while 150 °C is already enough to get such stabilization as revealed by the resistance to calcination. This is consistent with a highly activated process where temperature is more important than duration to reach stabilisation. Time is rather required when diffusion (a weakly activated process) is at stake. This is obviously observed for the thermal swelling effect. That is also apparently combined with a pore wall densification. This remark is backed by the ^{29}Si MAS NMR

spectra, which exhibit a higher Q^4 proportion in LUS_H@170 (*ca.* 66 %) than in LUS_H@130 (*ca.* 58 %).

II.3.2.3 Pore wall densification and ^{29}Si solid state NMR investigation

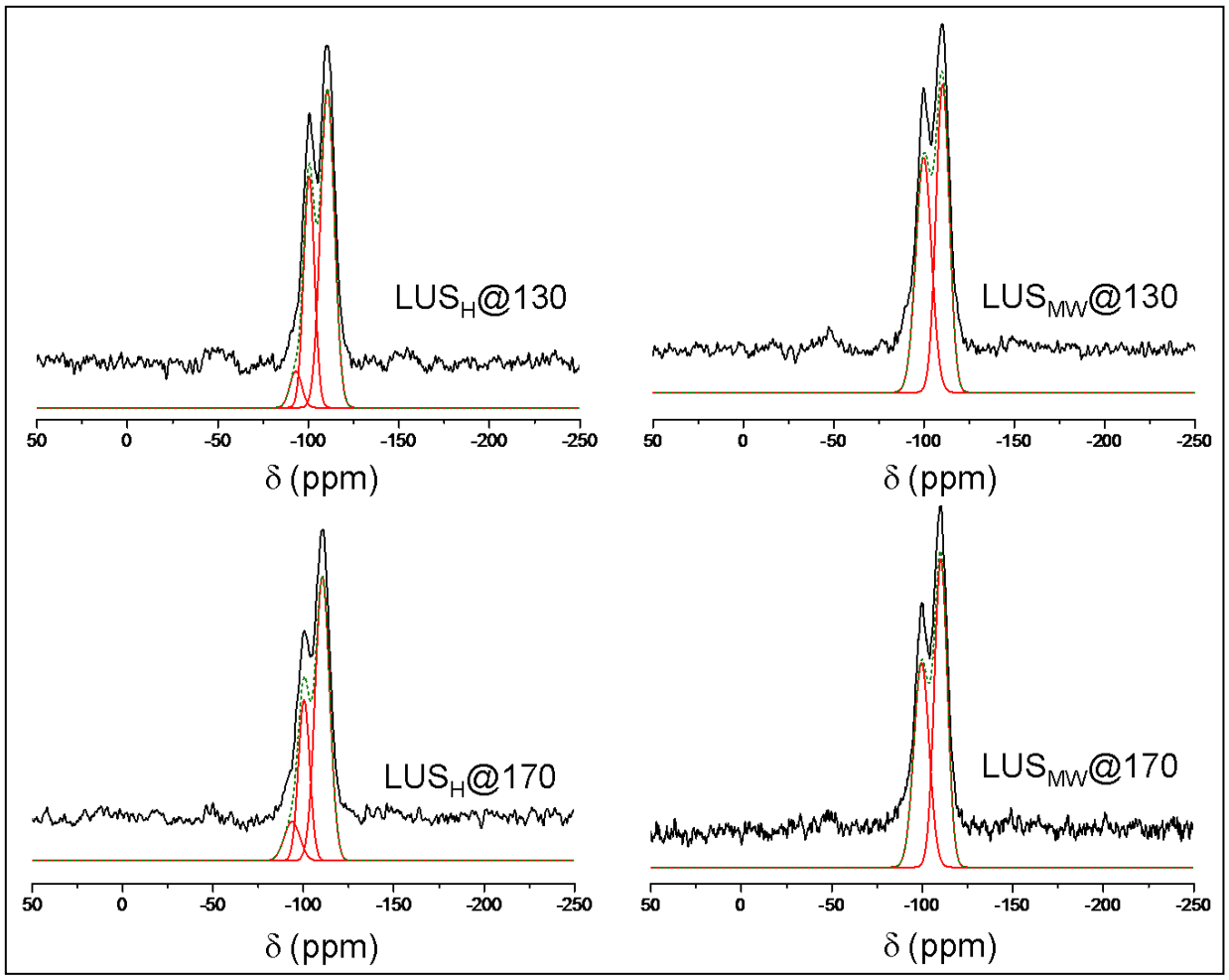

Figure 32: ^{29}Si HPDEC NMR spectra (black line), simulation (red line) and deconvolution (green dotted line) of LUS_H@130, LUS_H@170, LUS_{MW}@130 and LUS_{MW}@170.

In order to quantify the proportion of silicon species in the classical and microwave mesoporous materials, ^{29}Si HPDEC NMR spectra of the samples were measured (Figure 32 and 33). Deconvolution of the signal provided the percentage of Q^2-Q^4. Proportion of Q^4 is especially interesting to monitor the pore wall thickness as these silicon atoms are only surrounded by O-Si species, *i.e.*, they compose the silica wall. Proportions of Q^4 silicon are reported in Table 3.

Though the pore wall thickness deduced from the difference a_0 - d_{BdB} did not allow any reliable conclusion about an eventual pore wall densification due to the lack of precision in the measured parameters, ^{29}Si NMR spectroscopy confirms that the proportion of Q^4 silicon increases by *ca.* 14 % (from 58 to 66 %) along the classical family. However, this proportion

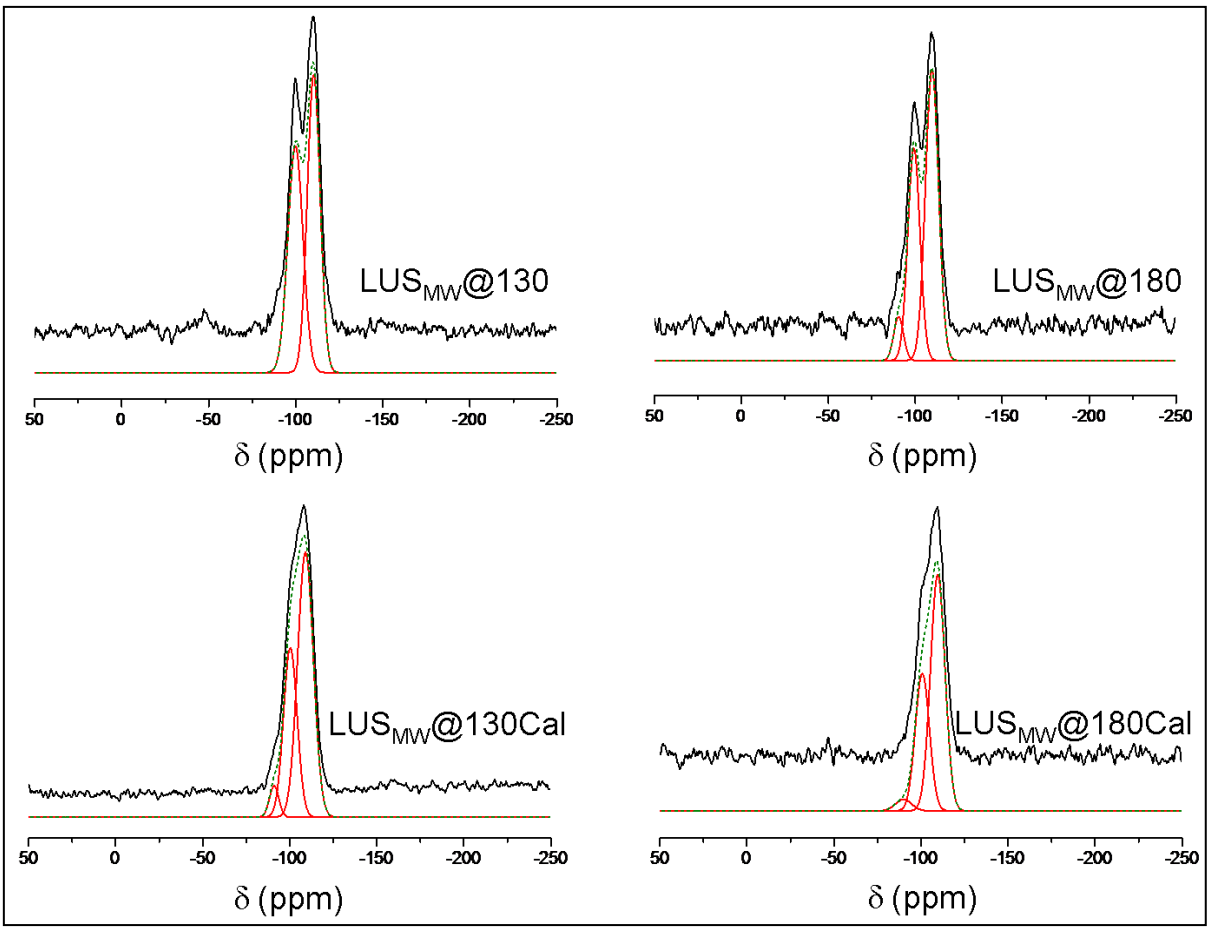

Figure 33: ^{29}Si HPDEC NMR spectra (black line), simulation (red line) and deconvolution (green dotted line) of LUS$_{MW}$@130, LUS$_{MW}$@130Cal, LUS$_{MW}$@180 and LUS$_{MW}$@180Cal.

remains relatively constant in microwave materials upon increase of the synthesis temperature with a slight decrease in LUS$_{MW}$@180 (-5 % compared to LUS$_{MW}$@130).

Therefore there are definitely two different behaviours in microwave and classical materials: while pore wall thickness and pore diameter increase with the temperature in classical silicas, microwave irradiation allows keeping similar pore size and pore wall thicknesses even at higher temperature.

Table 3: Q^4 silicon proportion of selected silica materials.

Silica	δ (ppm) / Q^4 (%)
LUS$_H$@130	110.6 / 58.3
LUS$_H$@170	110.8 / 66.0
LUS$_{MW}$@130	109.8 / 57.9
LUS$_{MW}$@170	109.9 / 58.9
LUS$_{MW}$@180	109.7 / 55.0
LUS$_{MW}$@130Cal	109.3 / 57.7
LUS$_{MW}$@180Cal	109.6 / 61.2

II.3.2.4 Specific surface area S_{BET}

A large part of the interest aroused by mesoporous materials comes from their large specific surface area. Hence new synthetic methods must preserve this advantage. When prepared using hydrothermal synthesis, LUS materials lose some of this surface upon augmentation of the temperature (Figure 34). The same tendency is observed for microwave syntheses until 180 °C, where it rises again and stabilises to reach values comparable to the classical synthesis at 130 °C (*ca.* 1000 $m^2.g^{-1}$). This diminution could be caused by a difference in the surface roughness: indeed, for the same pore volume, higher surface area can be achieved by tuning the roughness. This is for instance what happens in the small intestine: the wall of this organ is folded to maximize the surface and therefore optimize adsorption of nutriments.

Back to mesoporous silicas, a decrease in the specific surface area can occur in a smoother material. The higher the temperature, the less rigid will be the micelles because of thermal agitation. Therefore it is understandable that roughness, and thus S_{BET}, decreases when temperature rises. Howbeit, this phenomenon could not explain why LUS_{MW}@180 and LUS_{MW}@190 possess higher surface area (990 $m^2.g^{-1}$). Given that this trend only occurs in microwave syntheses, we supposed that a second phenomenon counter-balances the thermal agitation. Indeed, increasing the temperature does not only improve thermal agitation but also polymerization rate. Our hypothesis is the following: for a high enough temperature, polymerization occurs so quickly that it freezes the silica around the surfactant heads and prevent thermal agitation from smoothing the surface. During a classical synthesis, temperature gradient within the autoclave does not allow such a fast thermal rise and Brownian movement still has the high ground on polymerization. At lower temperature, polymerization is not as affected by thermal agitation as for higher temperatures, what would explain the greater surface area obtained.

Calcination process also brings interesting information. First, and this could be predicted with the pore volume information, both syntheses at 130 °C lose a lot of specific surface area after calcination. Once again, partial collapse of the structure is responsible for this loss. Actually, this loss only occurs for those two materials. For higher temperature, the tendency changes and calcination allows gaining specific surface. However a problem arises: this gain in specific surface goes along with a loss in porous volume and in pore diameter. Indeed, calcination, and condensation of surface silanols, slightly reduces the pore size while it creates additional roughness for materials that can support the thermal treatment.

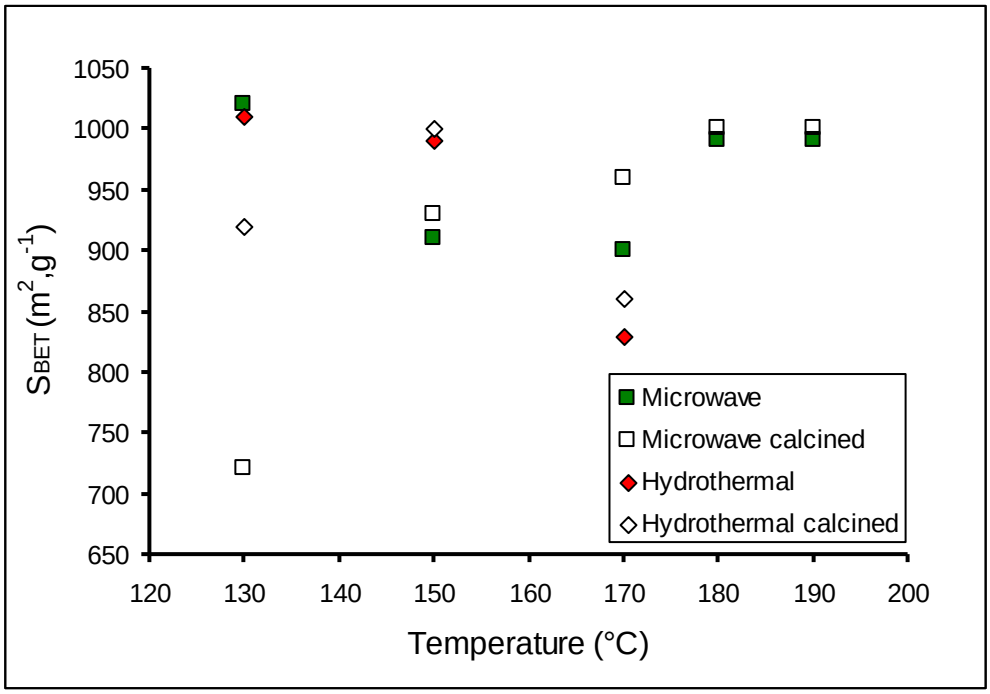

Figure 34: Specific surface area S_{BET} as a function of synthesis temperature for microwave and classical materials as well as their calcined equivalents

II.3.2.5 BET constant C

Results reported in Table 2 show a trend in the classical family. Increasing the temperature of the synthesis implies an important rise in the values of C, from 105 to 211. This evolution can be understood by the larger pore size along the LUS_H materials. Larger pore diameter implies a lower curvature. Therefore, the surface in LUS_H@170 is much flatter than the one in LUS_H@130, which was already proved with the specific surface. Increasing the temperature reduces the roughness, and prevents the silanols from mutually cancelling their effect. Actually, the C value in LUS_H@170 is quite close to the values measured for amorphous silica materials which do not present particularly concave areas.

Microwave materials do not seem to be especially affected by the change of temperature, which is expected from the similar values of pore diameter. This constancy traduces a similarity of surfaces in LUS_{MW} silicas. However this rule does not apply to the silica synthesized at 180 °C. This silica is really close to the LUS_{MW}@190 sample in terms of specific surface, pore diameter and porous volume, but not in C value. From NMR spectra, we can rule out a greater density of surface silanols, therefore this better affinity toward N_2 can be explained by their orientation: such material would present silanol moieties that would better cooperate in the induction of dipoles in N_2 molecules.

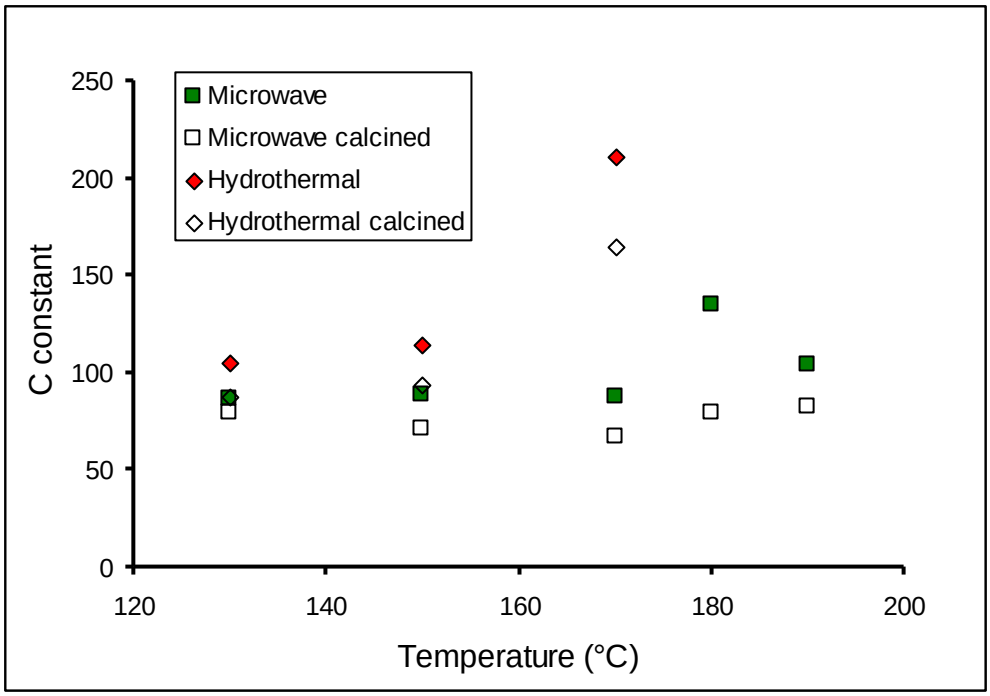

Figure 35: C constant as a function of synthesis temperature for microwave and classical materials as well as their calcined equivalents

Finally, reduction of C value after calcination can be explained by the silanol condensation implied by the process: the overall number of silanols is reduced and so is the C value.

II.3.2.6 Scanning Electronic Microscopy (SEM)

SEM pictures of classical silica and microwave LUS synthesized at 130, 150 and 170 °C are presented on Figure 36.

Classical silica particles do not appear larger than silica microwave particles. They often look like long fibres. In the meantime, the shape of microwave silica changes according to the temperature: at 130 °C, small fibres are observed (Figure 36.b), without any specific arrangement or special ordering. The overall particles are a jumble of those fibres which create a sort of web. At higher temperatures, no more fibres are found. LUS_{MW}@150 seems to be a packing of small tiles, which looks like slate rocks, while LUS_{MW}@170 is composed of a multitude of small spherical particles (Figure 36.c and d). In any case, the higher the temperature, the smaller the entities which form the material, which is coherent with the homogeneity of microwave heating: better homogeneity leads to numerous nucleation points, are therefore smaller particles.

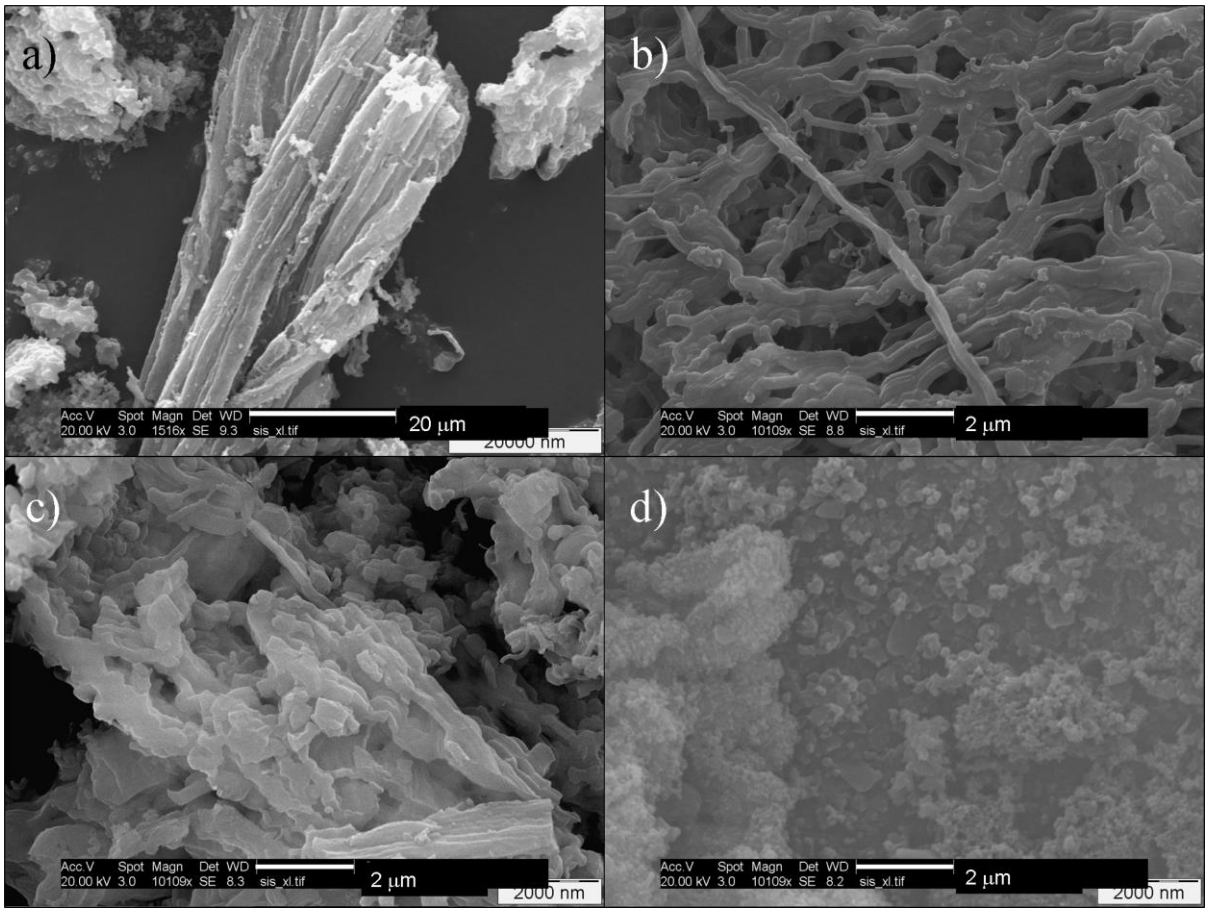

Figure 36: SEM pictures of LUS_H@130 (a) and LUS_{MW}@130 (b), LUS_{MW}@150 (c) and LUS_{MW}@170 (d)

II.4. Experimental part

Synthesis of classical LUS_H silicas (LUS_H@130, LUS_H@150 and LUS_H@170). Ludox (15.5 g, 0.26 mol), was added to sodium hydroxide (2 g, 50 mmol) in 50 mL of distilled water, then stirred at 40 °C until clear (about 24 hr). A second solution of hexadecyltrimethylammonium p-toluenesulfonate (CTATos) (1.96 g, 4.3 mmol) in distilled water (71 mL) was stirred at 60°C during 1 hour. In the meantime, the first solution (49 mL) was also stirred at 60°C during 1 h. Then the second solution was slowly added to the first one. The resulting mixture was further stirred at 60 °C for 1h and transferred in an autoclave to be heated in an oven at the desired temperature (130, 150 or 170 °C) for 20 h. Then the autoclave was allowed to cool first in air for about 1 hr and then under water for about 10 min. The solid was filtered on Büchner, washed with 100 mL of water and dried overnight at 80 °C to obtain 3.8 g of white powder. Elemental analysis (wt%): LUS_{MW}05: Si: 23.61, C: 30.88, H: 6.56, N: 1.80, S. 0.39.

Synthesis of microwave LUS_{MW}01 silica. The protocol is similar than for LUS_H except that the solution was transferred in a DAP-100 pressured vessel and heated in the microwave oven as described in Table 1. The autoclave was then cooled at air, and the solid was recovered by following the protocol described above.

Synthesis of microwave LUS_{MW}02-04 silicas. The protocol is similar than previously, except that the first solution is added to the second one by pouring it on the edge of the recipient containing this latter. After vigorous hand shaking, the mixture was transferred in the autoclave and the solid was recovered by following the protocol described above.

Synthesis of microwave LUS_{MW}05-12 silicas. The protocol is similar than for LUS_{MW}02-04, except that the autoclave was cooled in an ice-bath for 30 to 45 min depending on the synthesis temperature. The solid was recovered by following the protocol described above. Elemental analysis (wt%): LUS_{MW}05: Si: 23.63, C: 30.91, H: 6.31, N: 1.72, S. 0.20. LUS_{MW}07: Si. 23.71, C: 31.08, H: 6.41, N: 1.71, S: <0.20. LUS_{MW}08: Si: 24.17, C: 29.83, H: 6.17, N: 1.64, S: <0.20.

Extraction and calcination protocols. The surfactant was extracted by stirring 1 g of LUS and 2 mL of HCl 1M in 200 mL of technical ethanol during 1 h. The solid was then filtered on Büchner, washed twice with 50 mL of technical ethanol and dried overnight at 80 °C to obtain the extracted material suitable for N_2 sorption isotherm and X-ray powder diffraction. The extracted solids were then calcined at 550 °C under an air flow for 5 h.

Conclusion

This chapter compares two synthetic ways of LUS mesoporous silica, the first one using a conventional oven, the second using microwave irradiation. This latter has been optimized following two main criteria:

- Total synthesis time, which provides a material in a shorter time.
- Synthesis temperature, which has important effect on the material properties and thermal resistance.

While the classical method requires at least 22 hrs to provide a mesoporous material, the total synthesis time was reduced to a couple of hours using the microwave irradiation. Time was gained on different steps: heating time, which is the most drastic time economic step, but also precursor addition and autoclave cooling steps. Mesoporous properties are maintained through the process, *i.e.*, the final materials possess similar pore sizes (between 3 and 4 nm), porous volumes (between 0.7 and 0.9 $cm^3.g^{-1}$) and specific surface areas (900 to 1000 $m^2.g^{-1}$). This conservation of mesoporosity is a crucial issue to ensure the advantages of this microwave assisted method.

Effect of temperature synthesis provided much different information. A maximal temperature of 190 °C was reached in microwave syntheses, while the same temperature led to the degradation of the surfactant in classical syntheses. Therefore, shortening the synthesis time allows to heat at higher temperature without any effect on the surfactant integrity. Increasing the temperature in both protocols enlightened different behaviours:

- In the classical synthesis, the pores tend to enlarge upon such increase, the porous volume remains quasi-unchanged, and the specific surface area drops. The first effect can be explained by the temperature effect on surfactant micelles, which occupy more space due to the thermal agitation (swelling effect). Porous volume does not vary because of the larger pore size: this is a volume per gram, thus materials with both larger walls and larger pore size will not necessary possess a greater porous volume. Surface area decrease can also be caused by the augmentation of temperature: thermal agitation increases, and micelles will tend to smooth the silica surface, leading to less roughness, and therefore less surface area.
- In microwave synthesis, no micelle swelling is observed. Porous volume and surface area follow the same trend: a decrease between 130 °C and 170 °C followed by an increase until 180 °C and stabilization at 190 °C. Hence increasing temperature has not the

same effect than for classical syntheses and the interpretation is different: two effects are at stake in microwave synthesis. The first one is the thermal effect, which was already present in the original method. However, due to the homogeneous heating and fast temperature increase in the autoclave provided by microwave heating, polymerization speed is greatly increased and thermal agitation does not have the same impact on the final material. In this case micelles cannot swell as previously observed. This effect can be due to a polymerization fast enough so the micelles are encapsulated in the solid before they can grow by thermal agitation. This interpretation is coherent with the fact that microwave radiation impacts more polar molecules such as water and much less apolar alkyl chains, responsible for micelle expansion. In addition, microwave heating does not create larger pore walls. This fact is attributed to the homogeneity of this particular heating method: precursors are consumed in every point of the solution and there is no more temperature gradient like in classical heating. Nucleation/growth process occurs the same way regardless from the temperature. Finally increase in the surface area at higher temperature can be explained by the roughness: the higher the temperature, the faster the polymerization, and therefore the highest encapsulation of micelles. Then, at high temperature one can assume that condensation of the precursors occurs much faster and create a sort of mould of the micelle. However, the fact that smoothing of the surface does not happen like in classical syntheses let us suppose that this smoothing is a process that occurs at a much larger time scale and thus cannot be observed within the ten minutes of microwave synthesis.

Microwave irradiation is therefore a method that allows synthesis of mesoporous silica in much shorter time with a better homogeneity of the final material. The effects of thermal agitation become much less visible compared to the condensation speed ones.

Bibliography

[1] A. F. Cronsted, *Kongl. Svenska Vetenskaps Akademiens Handlingar Stockholm*, **1756**, *17*, 120

[2] D. W. Breck, *J. Chem. Educ.*, **1964**, *41*, *12*, 678

[3] J. N. McBain, "The Sorption of Gases and Vapors by Solids", *George Rutledge and Sons Ltd., London*, **1932**

[4] R. M. Barrer, *Proc. Roy. Soc. London*, **1938**, *A167*, 393

[5] R. M. Barrer, *J. Chem. Soc.*, **1948**, 2158

[6] A. Corma, H. Garcia, J. Primo, *J. Chem. Res.-S*, **1988**, *1*, 40

[7] G. J. Kramer, R. A. Vansanten, C. A. Emeis, A. K. Nowak, *Nature*, **1993**, *363*, 529

[8] R. Beecher, A. Voorhies Jr., *Ind. Eng. Chem. Prod. Res. Dev.*, **1969**, *8*, *4*, 366

[9] C. Dimitrov, H. F. Leach, *J. Catal.*, **1969**, *14*, 336

[10] M. A. Lanewala, A. P. Bolton, *J. Org. Chem.*, **1969**, *34*, 3107

[11] L. B. Young, S. A. Butter, W. W. Kaeding, *J. Catal.*, **1982**, *76*, 418

[12] L. Bonetto, M. A. Camblor, A. Corma, J. P. Pariente, *Appl. Cat. A: Gen.*, **1992**, *82*, 37

[13] M. A. Camblor, A. Corma, A. Martinez, F. A. Mocholi, J. P. Pariente, *Appl. Cat.*, **1989**, *55*, 65

[14] V. Chiola, J. E. Ritsko, C. D. Vanderpool, US Patent N° 3 556 725, **1971**

[15] T. Yanagisawa, T. Shimizu, K. Kuroda, C. Kato, *Bull. Chem. Soc. Jap.*, **1990**, *63*, 988

[16] C. T. Kresge, M. E. Leonowicz, W. J. Roth, J. C. Vartuli, J. S. Beck, *Nature*, **1992**, *359*, 710

[17] J. S. Beck, J. C. Vartuli, W. J. Roth, M. E. Leonowicz, C. T. Kresge, K. D. Schmitt, C. T. W. Chu, D. H. Olson, E. W. Sheppard, S. B. McCullen, J. B. Higgins, J. L. Schlenker, *J. Am. Chem. Soc.*, **1992**, *114*, 10834

[18] Q. S. Huo, D. I. Margolese, U. Ciesla, D. G. Demuth, P. Y. Feng, T. E. Gier, P. Sieger, A. Firouzi, B. F. Chmelka, F. Schuth, G. D. Stucky, *Chem. Mater.*, **1994**, *6*, 1176

[19] D. Y. Zhao, J. L. Feng, Q. S. Huo, N. Melosh, G. H. Fredrickson, B. F. Chmelka, G. D. Stucky, *Science*, **1998**, *279*, 548

[20] D. Y. Zhao, Q. S. Huo, J. L. Feng, B. F. Chmelka, G. D. Stucky, *J. Am. Chem. Soc.*, **1998**, *120*, 6024

[21] P. D. Yang, D. Y. Zhao, D. I. Margolese, B. F. Chmelka, G. D. Stucky, *Chem. Mater.*, **1999**, *11*, 2813

[22] A. Taguchi, F. Schuth, *Micropor. Mesopor. Mater.*, **2005**, *77*, 1

[23] A. Galarneau, N. Cambon, F. Di Renzo, R. Ryoo, M. Choi, F. Fajula, *New J. Chem.*, **2003**, *27*, 73

[24] G. D. Stucky, A. Monnier, F. Schüth, Q. Huo, D. Kumar, D. Margolese, M. Krishnamurty, P. Petroff, A. Firouzi, M. Janicke, B. F. Chmelka, *Mol. Cryst. Liq. Cryst.*, **1994**, *240*, 187

[25] F. Hoffmann, M. Cornelius, J. Morell, M. Froba, *Angew. Chem.-Int. Ed.*, **2006**, *45*, 3216

[26] C. Y. Chen, S. L. Burkett, H. X. Li, M. E. Davis, *Micropor. Mater.*, **1993**, *2*, 27

[27] A. Monnier, F. Schuth, Q. Huo, D. Kumar, D. Margolese, R. S. Maxwell, G. D. Stucky, M. Krishnamurty, P. Petroff, A. Firouzi, M. Janicke, B. F. Chmelka, *Science*, **1993**, *261*, 1299

[28] A. Firouzi, D. Kumar, L. M. Bull, T. Besier, P. Sieger, Q. Huo, S. A. Walker, J. A. Zasadzinski, C. Glinka, J. Nicol, D. Margolese, G. D. Stucky, B. F. Chmelka, *Science*, **1995**, *267*, 1138

[29] C. A. Fyfe, G. Fu, *J. Am. Chem. Soc.*, **1995**, *117*, 9709

[30] R. Zana, J. Frasch, M. Soulard, B. Lebeau, J. Patarin, *Langmuir*, **1999**, *15*, *8*, 2603

[31] J. Zhang, Z. Luz, H. Zimmermann, D. Goldfarb, *J. Phys. Chem. B*, **2000**, *104*, *2*, 279

[32] D. A. C. Stuerga, P. Gaillard, *J. Microwave Power Electromagn. Energy*, **1996**, *31*, 87

[33] D. A. C. Stuerga, P. Gaillard, *J. Microwave Power Electromagn. Energy*, **1996**, *31*, 101

[34] K. J. Rao, B. Vaidhyanathan, M. Ganguli, P. A. Ramakrishnan, *Chem. Mater.*, **1999**, *11*, 882

[35] G. A. Tompsett, W. C. Conner, K. S. Yngvesson, *Chem. Phys. Chem.*, **2006**, *7*, 296

[36] C. G. Wu, T. Bein, *Chem. Commun.*, **1996**, 925

[37] Y. Sun, W. Lin, J. Chen, Y. Yue, W. Pang, "Studies in Surface Science and Catalysis", *Elsevier, Amsterdam*, **1997**, *105*, 77

[38] S. E. Park, D. S. Kim, J. S. Chang, W. Y. Kim, *Catal. Today*, **1998**, *44*, 301

[39] B. L. Newalkar, S. Komarneni, H. Katsuki, *Phys. Chem. Chem. Phys.*, **2000**, *2*, 2389

[40] X.-W. Yan, X.-W. Han, Y. Cao, Y.-L. Wei, J.-H. Zhu, *Wuji Huaxue Xuebao*, **2002**, *18*, 1101

[41]

[42] L. Bonneviot, M. Morin, A. Badiei, Patent WO 01/55031 A1, **2001**

[43] P. Reinert, B. Garcia, C. Morin, A. Badiei, P. Perriat, O. Tillement, L. Bonneviot, *Stud. Surf. Sci. Catal.*, **2003**, *146*, 133

[44] K. S. W. Sing, *Pure Appl. Chem.*, **1982**, *54*, *11*, 2201

[45] S. Brunauer, P. H. Emmett, E. Teller, *J. Am. Chem. Soc.*, **1938**, *60*, 309

[46] C. G. Shull, *J. Am. Chem. Soc.*, **1948**, *70*, *4*, 1405

[47] B. C. Lippens, J. H. de Boer, *J. Catal.*, **1965**, *4*, 319

[48] G. Horváth, K. Kawazoe, *J. Chem. Eng. Japan*, **1983**, *16*, 470

[49] E. P. Barrett, L. G. Joyner, P. P. Halenda, *J. Am. Chem. Soc.*, **1951**, *73*, 373

[50] J. C. P. Broekhoff, J. H. De Boer, *J. Catal.*, **1967**, *9*, 15

[51] L. Nicole, PhD Thesis, "Adsorption d'une molécule hydrophobe modèle, le C60, sur des matériaux aux tensioactifs structurants : les MCM-41.", *Université des Sciences et Techniques du Languedoc*, *Montpellier*, *France*, **2002**

[52] D. Massiot, F. Fayon, M. Capron, I. King, S. Le Calvé, B.Alonso, J. O. Durand, B. Bujoli, Z. Gan, G. Hoatson, *Magn. Reson. Chem.*, **2002**, *40*, 70

[53] M. Kruk, M. Jaroniec, A. Sayari, *Micropor. Mesopor. Mater.*, **1999**, *27*, 217

[54] N. Xiao, L. Wang, S. Liu, Y. C. Zou, C. Y. Wang, Y. Y. Ji, J. W. Song, F. Li, X. Meng, F. S. Xiao, *J. Mater. Chem.*, **2009**, *19*, 661

[55] K. Zhang, H.-L. Chen, B. Albela, J.-G. Jiang, Y.-M. Wang, M.-Y. He, L. Bonneviot, *Eur. J. Inorg. Chem.*, **2011**, *2011*, 59

[56] A. M. Lapeña, A. F. Gross, S. H. Tolbert, *Langmuir*, **2005**, *21*, 470

Chapter III:

Silica functionalization and catalytic tests

Introductory aspects

Contrary to zeolites, as-made mesoporous silicas are not used as catalysts. Due to the larger pore size, confinement is not as efficient as in microporous solids. Nonetheless their ability to be functionalized quickly offered numerous possibilities for chemists. Then depending on the modification, various families of materials can be synthesized. Purely inorganic materials have proven to be efficient catalysts, using metal oxides such as vanadium, titanium or aluminium to provide catalytic sites. [1, 2, 3, 4, 5] Those metallic sites can be incorporated either by co-condensation (addition of the metal oxide precursor before silica polymerization) or by post-reaction (reaction of the metal oxide precursor after silica polymerization).

Our study brought us to focus on hybrid materials, *i.e.* materials containing both an inorganic part (silica framework) and an organic one (organic functions to form metal complexes). In fact, due to the greater range of grafting options, those materials are much more interesting in terms of selectivity and yield. Hybrid materials offer the possibility to immobilize efficient catalysts onto a surface and consequently increase the concentration of active sites while keeping an overall catalytic quantity of catalyst. In addition, the very nature of those solids brings another advantage when it comes to recycle the catalyst, for homogeneous catalysts cannot be recovered in many syntheses. Immobilizing catalysts on such silicas is not without consequences though. [6] For instance, some grafted manganese catalysts have been reported to be more active than their homogeneous counterparts. [7]

The interaction between the function and the support can be weak (adsorption of complexes at the surface) or strong (covalent support-function bonds). In order to functionalize mesoporous silicas by creating covalent bonds, different strategies can be considered (Figure 1):

- A direct condensation between a desired organosilane and the silica precursor, called one-pot strategy or direct synthesis, that will provide a material containing protruding organic functions, like rock outcrops.
- A direct condensation between a polysilylated organosilane and the silica precursor, leading to an encapsulation of the function inside pore walls. These materials are often called periodic mesoporous organosilicas (PMOS).

- A post-grafting strategy, where the surfactant is removed before reaction involving a chosen organosilane to anchor the function on the pore surface.

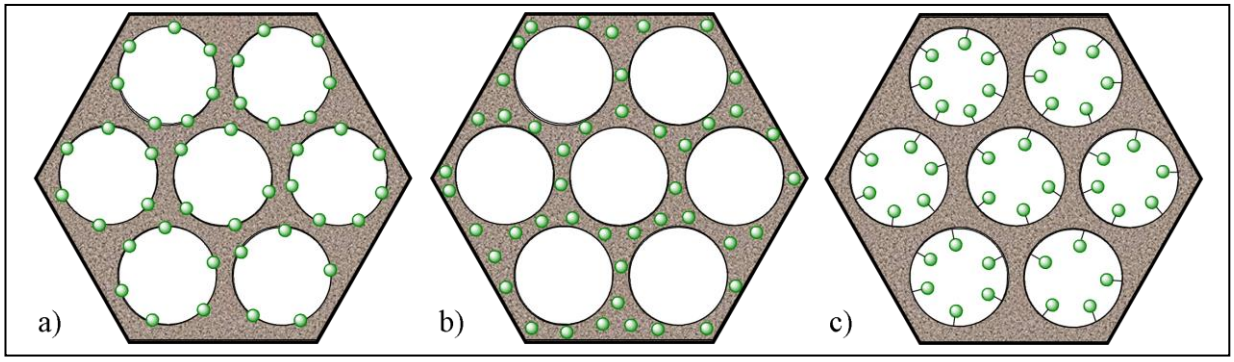

Figure 1: Function positioning depending on the functionalization strategy, protruding (a), encapsulated (b) or inside the pore (c)

The first two methods are in principle the easiest ones in terms of synthesis because they can provide a functionalized material in one step. However, function distribution cannot be controlled for it will be statistically spread in the final solid. This lack of control also brings the question of equivalence between two sites: environment cannot be controlled and hence it can be different one from another. Therefore we chose to functionalize our material via the post-grafting method. This method offers *a priori* more possibilities to control both function distribution and environment.

There is not a unique way to post-functionalize a mesoporous material, and the chosen method has to answer three main criteria, especially in the case of multi-functionalizations:

- The active sites must be isolated one from another.
- The environment must be equivalent for every function.
- The distribution and relative position of two functions must be controlled.

Therefore, those requirements imply controlling the synthesis at both short and long range. Short range control ensures the environment equivalence while long range control allows keeping a uniform distribution all along the material pores.

In order to afford site isolation, two approaches can be though of. The first one consists in diluting the desired function while the second restricts the number of available bonding sites in the material. Obviously, the first one is the simplest, but it also presents disadvantages. Though dispersion of the function will be achieved by incorporating a limited amount of desired precursor, it can also be tuned by using an appropriate solvent. For instance, Asefa *et al.* showed that density and distribution of functions was different depending of the solvent. [8, 9, 10] In fact, when a polar-protic solvent such as ethanol or isopropanol was used, amine functions could by isolated, whereas functionalization in non-polar solvent such as

toluene led to bring the amines closer one from another. In ethanol, site isolation was achieved while toluene caused the amines to form small blocks at the pore surface. Similar solvent effects were observed by Sharma *et al.* as well as Salmio and Brühwiler, with THF and toluene. [11, 12]

A wise choice of silane precursor can also allow controlling the functions distribution. Thus, Hicks *et al.* diluted their desired silane with a spacing silane to afford isolation. [13] However, physico-chemical differences between those silanes come along with possible aggregation, as well as variations in diffusion throughout pores. Those disparities contributed to the observation of random distribution of both functions.

Another approach consists in reducing the numbers of binding sites, in other terms decreasing the density of surface silanols. This principle is the base of Surface Organo Metallic Chemistry (SOMC). [14, 15, 16] Thermal treatment at 700 °C forces the dehydration of the initial material by reaction between two adjacent silanols. An Si-O-Si bond is formed by reaction of two Si-OH upon heating. Remaining Si-OH are thus isolated and considered as ligands for further functionalization with metal complexes $[MX_nL_n]$ to provide $Si\text{-}OMX_{n-1}L_n$ and XH. Coperet and Basset have largely developed such approach for the synthesis of metathesis catalysts. [17, 18] However, the direct link between metal and oxygen from the surface emphasizes the influence of close siloxanes. [15] A solution to this problem was developed by Anwander *et al.* with the degradation of heteroleptic complexes to control the vicinity of the metallic site (Figure 2). [19] A complex containing a strong chelating ligand (such as salen) and a reactive one (such as silylamines) will bind to the silica surface by

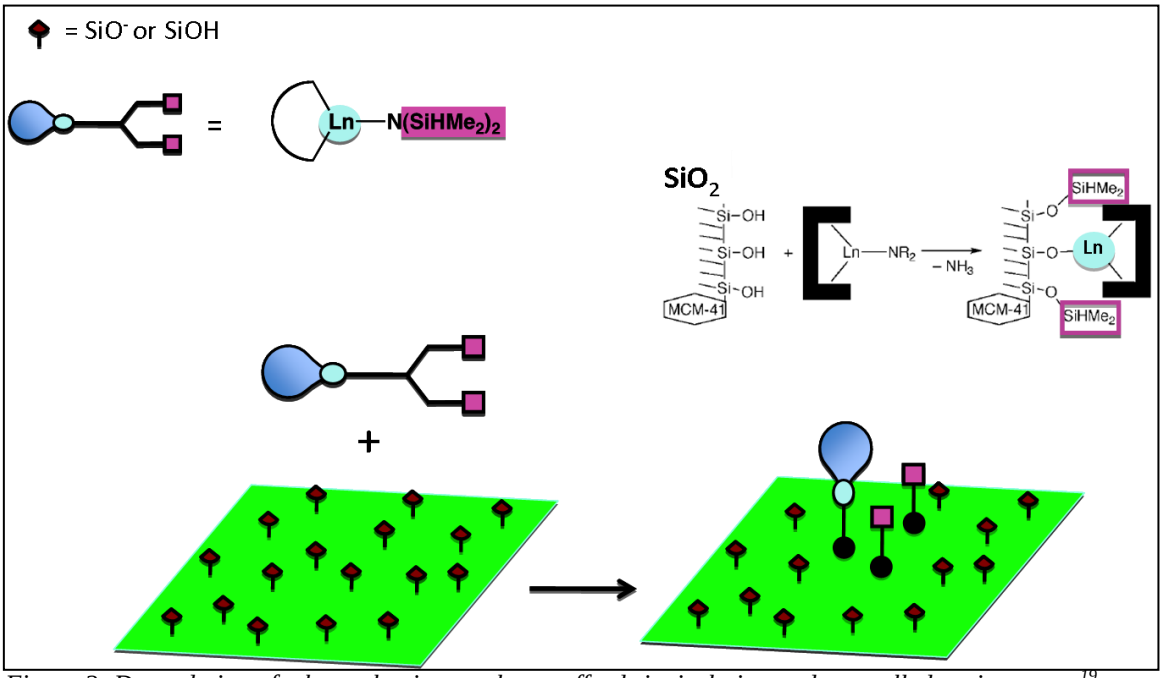

Figure 2: Degradation of a heteroleptic complex to afford site isolation and controlled environment [19]

replacement of the silylamine, which will create a controlled environment around the newly formed complex by reacting with the surrounding silanols. By carefully designing the silylamine, *i.e.* by controlling the functional groups linked to the silicon atom, hydrophobicity of the metal vicinity can thus be tuned.

Wulff proposed to control the distribution of the functions with a sacrificial spacer (Figure 3). [20, 21] Several functions are connected to a spacer that can be removed under mild conditions after grafting. This technique was extended to the synthesis of materials for chiral recognition or catalysis. Stack *et al.* developed a similar technique that employs a metal ion as sacrificial spacer: this sacrificial metal is only meant to be replaced by the desired one. [22, 23] They modified silica with a L_2Cu complex to anchor the two ligand molecules close one to the other, before exchanging copper by the desired metal. Although these methods have proven to be efficient in terms of control, their limitation lies in the small amount of functions that can be grafted and in the difficulty of the organosilane syntheses.

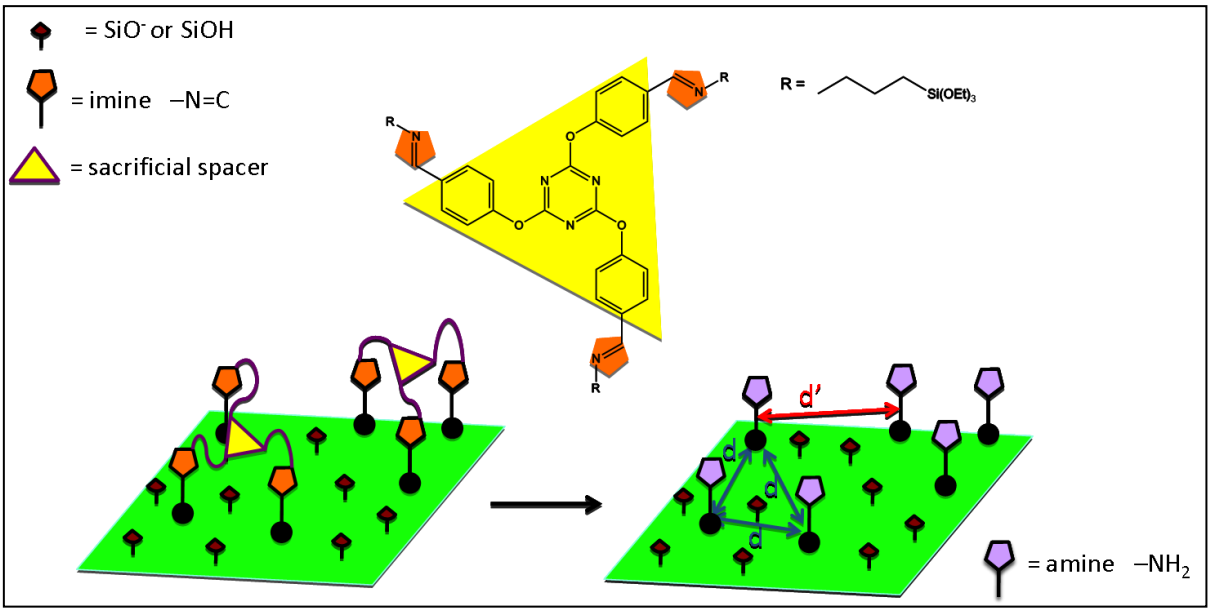

Figure 3: Use of a sacrificial spacer to control the distance between two functions [20]

To counter those disadvantages, Jones and McKittrick worked on a different approach. The desired function was not diluted anymore, but it was modified with a bulky group. This approach was called "protection-deprotection" method (Figure 4). [24, 25] An amine function was linked to a phenyl-containing alkyl chain and grafted to a SBA-15 material. Steric hindrance prevented two amine functions to get close during the grafting reaction and hydrolysis of the C=N bond yield to a material with a high amount of amine (around 1.3 $mmol.g^{-1}$). There is a side-advantage of the protection of amines: the double-bond C=N avoids interactions between amines and surface silanols. Though this method has proven to be

efficient, it has only been used for amine functions up to now. Therefore, grafting other kinds of functions can be quite problematic for they must possess the ability to be protected and deprotected easily. In addition, even by using two different grafted functions, the relative distribution of those two functions will be governed by statistics, which does not guarantee any homogeneity.

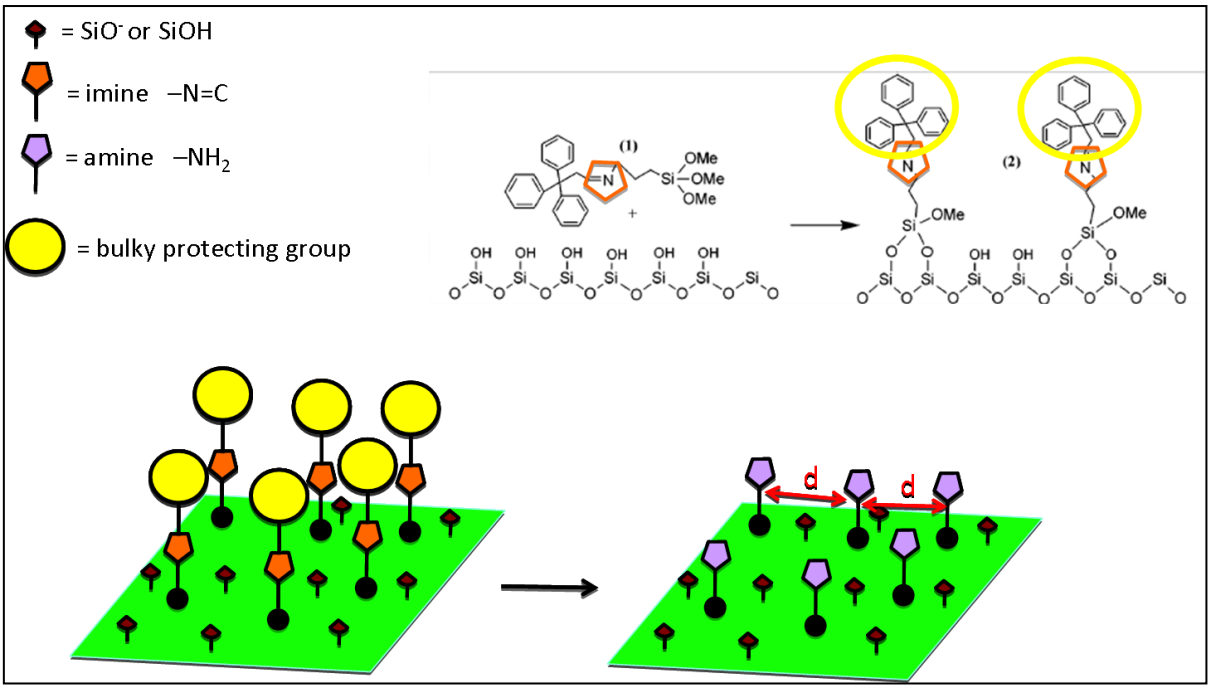

Figure 4: Protection-deprotection strategy using a bulky protecting group [25]

In 2004, Ariga *et al.* reported a pioneer approach for silica functionalization. [26, 27] Instead of adding the organosilane as an independent precursor during the polymerization step, they included it in the very templating molecule. In order to do so, they designed a surfactant containing a cationic organosilane linked to a peptide (or an amino acid), itself linked to a long alkyl chain by an ester moiety. Acid treatment after polymerization leads to the cleavage of the alkyl chain by saponification, providing a bio-functionalized material. However, once again, this method is effective for only one kind of function at a time.

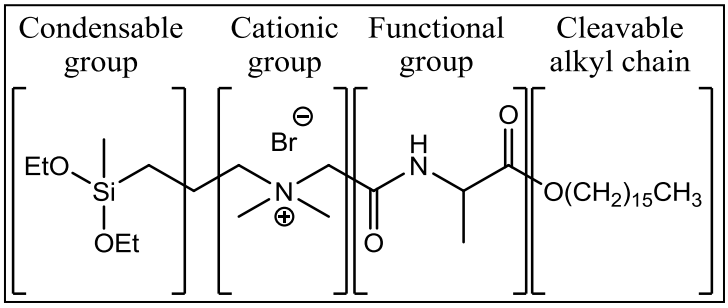

Figure 5: Surfactant molecule designed by Ariga et al. [26]

Though the methodology to afford mono-functionalization of mesoporous materials has been developed over the years, multi-functionalization still remains problematic in terms of organization and vicinity control. To solve this problem, our group developed a new grafting strategy called Molecular Stencil Patterning

(MSP). This strategy takes advantage of the electronic charge carried by the ammonium head of the templating agent. It creates an electrostatic repulsion between the surfactant molecules that can be exploited to organize the pore surface. Indeed, when part of this surfactant is extracted, the remaining template will reorganize inside the silica pores to minimize those interactions. To prove this concept, trimethylsilyl (TMS) groups from hexamethyldisilazane (HMDS) were grafted in a partially extracted mesoporous material. [28, 29] Those TMS moieties could be incorporated with a minimal displacement of CTA^+ molecules. ^{13}C and ^{29}Si NMR studies also proved that both signals from TMS were shifted compared to a fully silylated silica, due to the difference in the environment. [29] The presence of CTA^+ molecules modifies the Si-O-Si angle, which reverberates on the TMS, modifying its chemical displacement in NMR. The presence of a unique displaced signal proves the homogeneity of the function distribution. After this first functionalization, extracting the remaining surfactant will free some surface area. This latter will be surrounded by previously grafted TMS groups and therefore be organized. A second grafting reaction can be carried out, to obtain a double-functionalized mesoporous material. The homogeneity of the distribution provided by this method has been proven by using a europium complex with 1,10-phenanthroline grafted to a TMS-functionalized silica surface as a probe for transmission electron microscopy (TEM). [30] In agreement with the expected result, europium content was constant all along the analyzed fibre, and luminescence properties of the material validated the overall grafting method to afford single-sites.

This chapter is dedicated to the functionalization of the support as well as the preliminary catalytic tests. In a first part, the entire silica functionalization strategy will be detailed as well as the characterization of the intermediate materials. An optimal functionalization has to respect the homogeneity of the function distribution along with the optimization of the overall grafted surface area. In a second part, catalysis results with manganese(II) complexes as well as their grafted counterparts will be broached.

III.1. Strategy

Once the support synthesized and characterized, further functionalization was necessary to host manganese complexes. We decided to choose a post-grafting strategy over a direct synthesis to control the silica functionalization (Scheme 1).

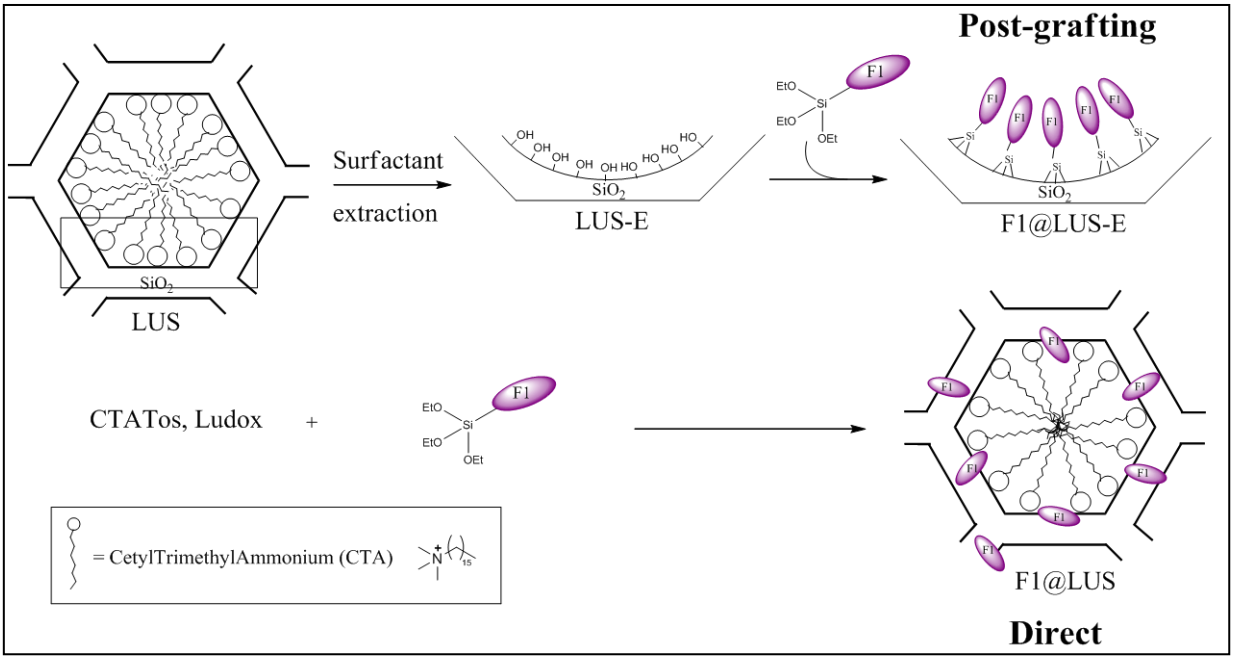

Scheme 1: Silica functionalization strategies, post-grafting (top) or direct synthesis (bottom)

In order to isolate the complexes, two functions are necessary:

- A first function F1 that will fulfil a spacing role.
- A second function F2 that will be a tether to anchor the manganese(II) complexes.

Complex isolation and homogeneity of their vicinity require controlling the functionalization at a molecular level. Therefore, amongst all the methods presented in the introductory aspects of this chapter, the Molecular Stencil Patterning (MSP) strategy was preferred for its versatility and effectiveness.

As introduced with the ligand synthesis in the first chapter, the Huisgen copper catalyzed cycloaddition was chosen as grafting reaction (Scheme 2). [31] Indeed, this reaction offers many advantages such as high yields and specificity which ensure an efficient supporting reaction.

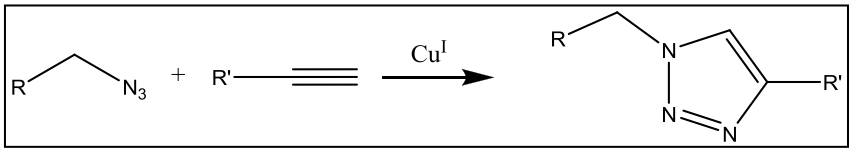

Scheme 2: Click chemistry reaction

III.2. Silica functionalization

III.2.1 Double-functionalization strategy

III.2.1.1 Site isolation

The post-grafted strategy used in this study was the so-called molecular stencil patterning, or MSP (Scheme 3). This strategy takes advantage of the cationic nature of the surfactant. This is a four step strategy:

i) First, the template is partially removed with hydrochloric acid. Due to electrostatic repulsion, the remaining surfactant rearranges making some silica surface available.

ii) Second, a first organosilane is grafted on this previously freed surface.

iii) Third, all of the remaining surfactant is removed, releasing once again free silica surface.

iv) Finally, the second function is grafted, providing a double functionalized material.

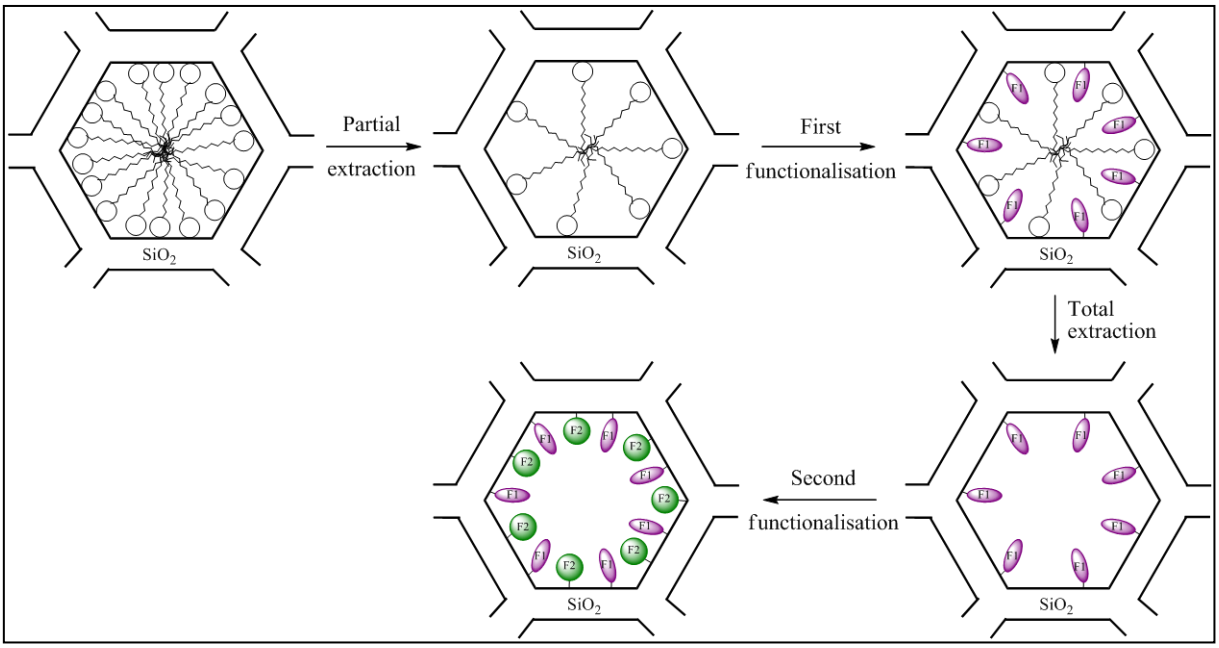

Scheme 3: Molecular Stencil Patterning (MSP) double-grafting strategy

Adjusting the amount of removed surfactant in the first step leads to distribution control. If grafted groups are modelled by spheres arranged in a 2D hexagonal packing on the surface (Figure 6), isolating a F2 function means to have it surrounded by six F1 functions. Every F1 function being adjacent to 3 F2 functions, the F1/F2 molar ration will be 2. In other words, 66 % of silica surface will be occupied by F1 against 33 % by F2. In conclusion, to isolate a F2 function, first extraction must remove at least 66 % of the surfactant.

In this work, a slightly different protocol was applied. Before the first partial extraction, CTA^+ was exchanged with tetramethylammonium (TMA^+). [32] In other terms, the whole surfactant molecule was replaced by another cation equivalent to the charged head of CTA^+ without its long hydrophobic chain. This modification has two main effects:

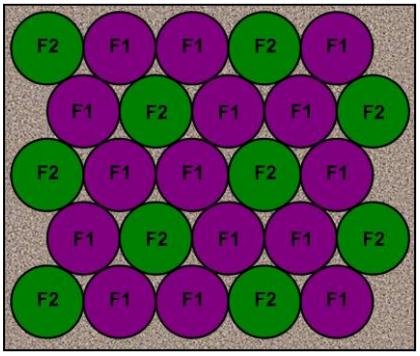

Figure 6: Site isolation in a 2D hexagonal packing, where F2 is the isolated function

- Diffusion of the F1 grafting function is all the more favoured that there is more available pore space.
- Removal of the long alkyl chain also removes some interactions between the molecules. Therefore, electrostatic interactions between ammonium cations are no longer counterbalanced as in the raw material, increasing the space between adjacent TMA^+. This results in a TMA^+ concentration lower than the original CTA^+ one. Consequently, the surface area made available by this operation has to be taken into account in the first TMA^+ extraction.

As for the nomenclature used in this chapter, the as-made material will be named LUS_{MW} (for LUS MicroWave). These silicas were synthesized using the condition described in Chapter II for the synthesis of LUS_{MW}@180, *i.e.*, a microwave mesoporous silica synthesized in 10 min at 180 °C. Material exchanged with TMA^+ will be noted LUS_{MW}-TMA. Partial extraction is represented by an –Ex suffix where x is the percentage of extracted TMA^+. For instance a material where 80 % of TMA^+ has been extracted would be named LUS_{MW}-TMA-E80. Totally extracted materials are simply noted LUS_{MW}-E. Likewise, when the remaining TMA^+ is removed from a material LUS_{MW}-TMA-Ex, the resulting material will be denoted as LUS_{MW}-Ey. Grafting reactions are symbolized by prefixes. For instance, azide-functionalized silica will be named N_3@ LUS_{MW}. In the case of several functionalizations, the more recent is placed at the beginning of the name: a material functionalized with F1 and then with F2 will thus be called F2-F1@ LUS_{MW} (the last two examples do not consider eventual ion exchanges and extractions).

III.2.1.2 Grafted functions

Grafting the manganese complexes inside the porous matrix required a previous modification of the silica material. In fact, these complexes were not directly grafted to the silica surface; a tether function was employed instead. Therefore, incorporating the complex was a two-steps synthesis. The first one consisted in grafting the tether function inside the

pores to provide a host material and the second one was an anchoring reaction between the tether function and the complex.

At first several options were thought of to choose the most relevant tether. Using the reaction of an aldehyde with an amine to form a Schiff base had already been used to graft europium complexes. In that case, the amine played the role of tether while the ligand complexed to the europium contained an aldehyde arm. [30] However, syntheses of amine-based ligands containing an aldehyde are not the simplest ones because of the reactivity of the very aldehyde. In addition, it has been noticed that grafting aminopropyltriethoxysilane on a partially TMS-capped silica surface tended to break some TMS-silica bonds. [33] Therefore, this operation lets free some surface silanols, which are able to interact via hydrogen bonds with the amine function. This interaction will bend the functional arm and hence reduce its availability toward yet unreacted aldehydes. The linking yield will then be reduced, diminishing the potential activity of the overall material.

Then another anchoring method was investigated: the copper-catalyzed Huisgen cycloaddition. The high usual yields obtained with this reaction would provide a material with a maximum amount of grafted complex compared to the number of available tethers, while its good selectivity would prevent any unwanted side reactions during both complex synthesis and silica functionalization.

Given that histidines from the second coordination sphere around the active site in the MndD stabilizes the reactive dioxygen species to allow the catechol cleavage, [34] we aimed at mimicking this coordinating effect in our material. One function, F2, will be the tether function, *i.e.* an azide silane (represented as N_3 in the material names) for click chemistry, whereas the second one (F1) could play two roles: it can be employed as a basic spacer and/or a stabilizing agent. Hence two host materials were targeted. The first one would contain a tether function and a simple spacing function, and the second one would contain once again a tether function, but also a coordinating and spacing function (Figure 7). With those two kinds of materials, the coordinating role of the second function could be investigated.

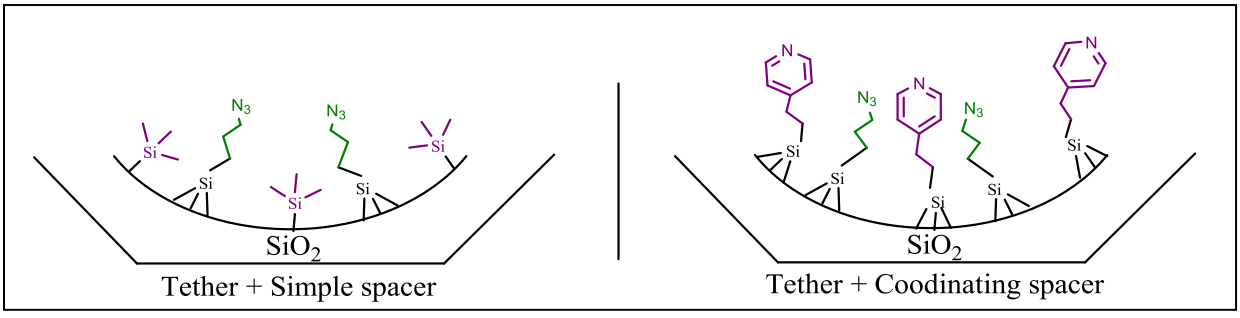

Figure 7: Targeted host materials.

In order to space without possible coordination to a metal ion, trimethylsilane (TMS in the material names) is a usual choice. To bind this function onto the silica surface, a silazane precursor is used. This family of precursors was used instead of chlorotrimethylsilane to avoid the formation of HCl that could extract the remaining surfactant and prevent him from filling its masking role. In comparison, using a silazane precursor generates NH_3 which implies much less displacement of the masking agent. To mimic the histidine, pyridine (Py in the names) was chosen as spacing and coordinating function for it was also one of the few commercially available aromatic heterocycles (Figure 9) at that time.

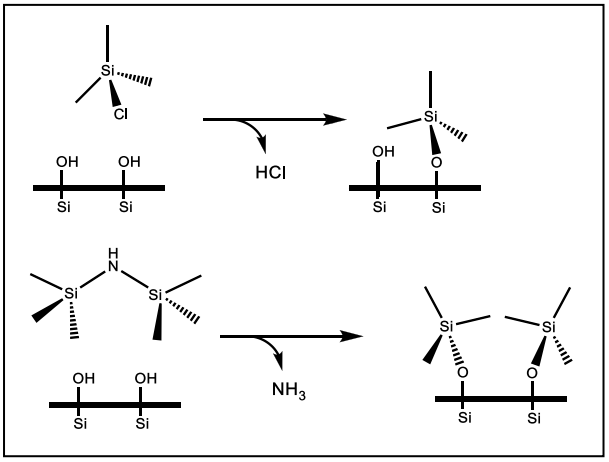

Figure 8: Reaction of silica surface with chlorotrimethylsilane (top) or hexamethyldisilazane (bottom).

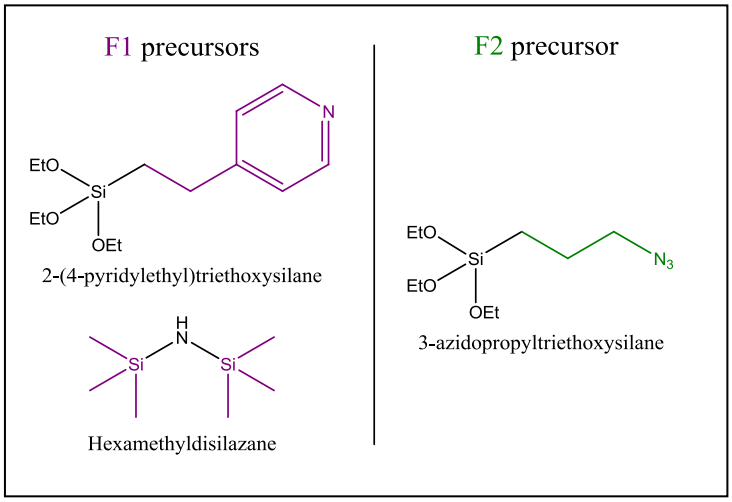

Figure 9: Organosilanes used as precursors for to generate F1 and F2 in the mesoporous materials

III.2.1.3 Synthesis of the host material

The azidopropyltrietoxysilane precursor was first synthesized starting from the chloropropyltriethoxysilane. [35] The synthesis was a nucleophilic substitution of a chlorine atom from chloropropyltriethoxysilane by an azide moiety from the sodium salt (Scheme 4). Reaction was done in butanone and ^{13}C NMR spectrum of the product proved the purity of the desired organosilane.

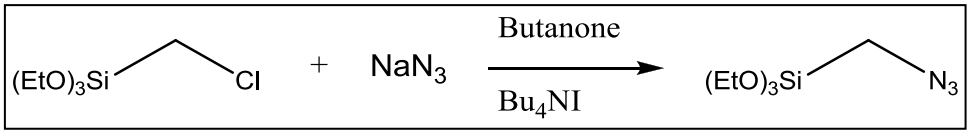

Scheme 4: Synthesis of the azidopropyltriethoxysilane.

Previous studies in the laboratory have proved that grafting TMS using hexamethyldisilazane (HMDS) on TMA-exchanged silicas still removes a small amount of TMA^+: thermogravimetric analysis (TGA) of an as-made LUS_{MW} indicates that there is around 2.6 mmol of surfactant per gram of silica SiO_2 while TGA of LUS_{MW}-TMA proves that there are only 2.1 mmol of TMA^+ per gram of SiO_2. Another aspect must also be considered to have the correct F1/F2 grafting proportion: TMS is grafted to the support with only one covalent bond, whereas triethoxysilanes can be attached with two or three covalent bonds. This means that if surface silanols are considered, obtaining a final F1/F2 molar ratio of 2 corresponds to a F1/F2 "required silanol" ratio of 2/3. Keeping in mind that TMA-exchange already frees some surface silanols, TMS functionalization was performed without any partial extraction. However, in the case of pyridine, which possesses a triethoxysilane linking function, 15 % of TMA^+ was extracted before the functionalization reaction. In other words, TMS functionalization was performed on LUS_{MW}-TMA materials while pyridine functionalization was carried out with LUS_{MW}-TMA-E15 materials.

After exchange of CTA^+ by TMA^+, three intermediate materials could be synthesized: N_3@LUS_{MW}-TMA, TMS@LUS_{MW}-TMA or Py@LUS_{MW}-E15. We tried the three possibilities and actually the second and third ones, which are equivalent in term of strategy, were the most relevant. It is in general more interesting to graft the tethering function after the isolating one. In fact, this latter is present in larger quantities in the final material because of its very role. Consequently, if grafted first, the isolating function will react on a pore surface with more accessible sites, given that it must isolate the tethering function.

Finally, the host materials were prepared as shown on Scheme 5.

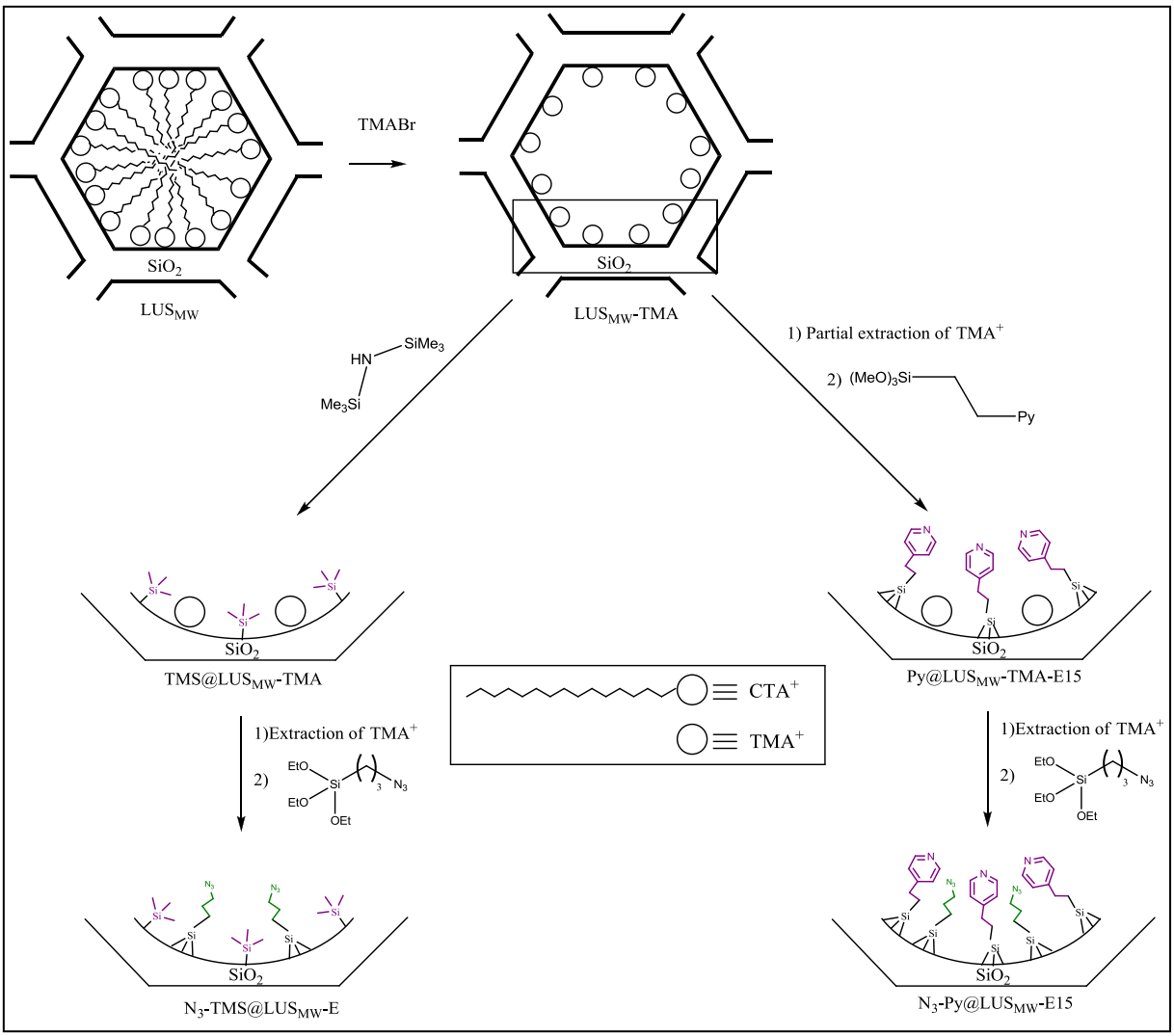

Scheme 5: Synthesis of the two families of host materials.

While surface modifications like TMA^+ exchange or extraction as well as azide and pyridine functionalizations could be followed by TGA (Figure 10), TMS functionalization could not be detected with the same accuracy due to the low mass of organic groups inserted in the silica: TMS mass loss occurs in a larger range of temperature which make it challenging to quantify with TGA. However, contrary to triethoxysilanes which can provide either T^2 or T^3 silicon species, TMS can only be present as M silicon species, which will give a unique peak on the ^{29}Si HPDEC NMR spectrum (Figure 11). Integration of M and Q massifs could give a estimation of the quantity of TMS functions grafted per gram of SiO_2.

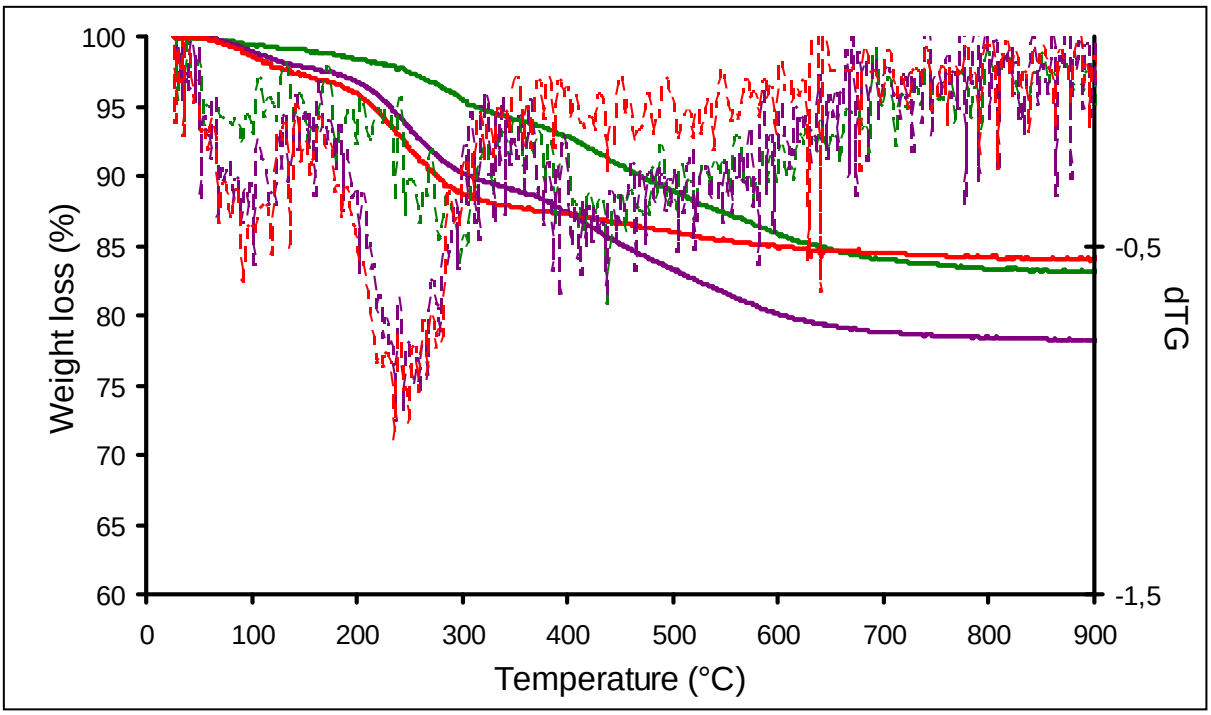

Figure 10: TGA profiles of materials LUS_{MW}-TMA-E15 (red), Py@LUS_{MW}-TMA-E15 (purple) and N_3-Py@LUS_{MW}-E15 (green) as well as their derivative curves (dotted lines).

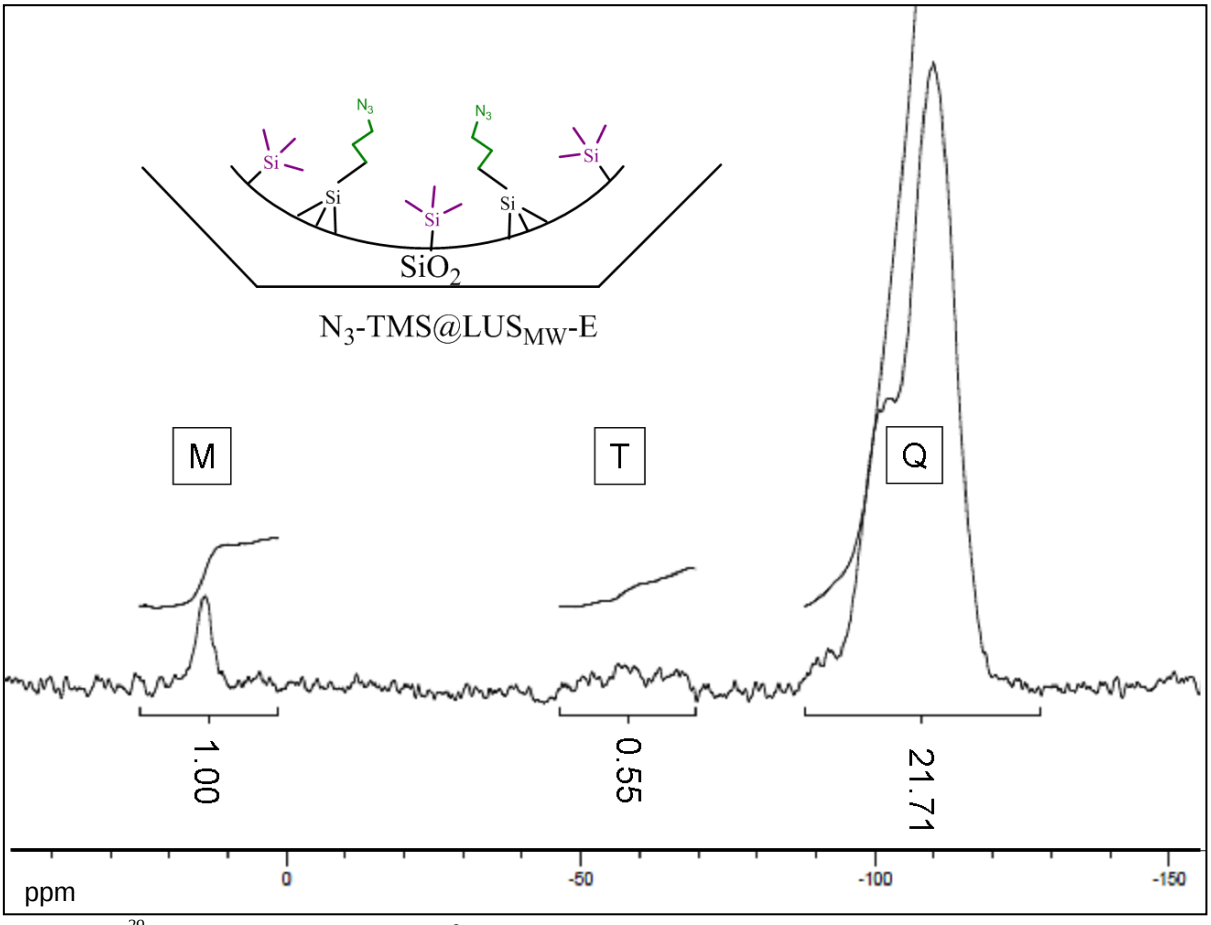

Figure 11: ^{29}Si HPDEC NMR spectrum of N_3-TMS@LUS_{MW}-E.

In the case of N_3-Py@LUS_{MW}-E15, mass losses corresponding to the degradation of pyridine and azide functions were 9,5 and 4 % respectively. After conversion in molar percentage, the ratio Py/N_3 becomes 88/47, i.e., 1.9, which is close from the desired ratio of 2. The case of N_3-TMS@LUS_{MW}-E requires both TGA profile and NMR spectrum. Given that the NMR peak corresponding to the T species is quite broad, its integration is not as accurate as for the M species. This latter provides a molar ratio TMS/Si (which is equal to the TMS/SiO_2 ratio) of 1/21.71 = 0.046. TGA profile of the material indicates a loss of azide function of 3 % and a residual mass of 89 %, corresponding to the SiO_2 mass. From those figures, we can calculate a molar ratio N_3/SiO_2 of 0.025. Therefore, the molar ratio TMS/N_3 will be 1.8, which is once again really close to the desired ratio of 2.

III.2.2 Anchoring reaction

Even though click-chemistry is known to be efficient, one must be careful about the conditions underlying in those reactions. For instance, the copper-catalyzed Huisgen cycloaddition has proven to be really sensitive to coordinating molecules when the classical copper catalyst is used. In principle, copper(II) sulphate or acetate is directly used and reduced to copper(I) *in situ*, most of the time by treatment with sodium ascorbate. For instance, reaction with L^1 and benzyl azide has been reported and performed under those conditions. [36] Instead of sodium ascorbate, methanol can also be sued as reductant. [37] This protocol could be repeated successfully with L^1. However, after our attempt to perform the cycloaddition of L^2 or L^3 with benzyl azide, the broad peaks in the ^{1}H NMR spectrum of the crude product indicated clearly the presence of copper(II) coordinated to the ligand (See appendix for the ^{1}H NMR spectrum). Although this coordination could be expected, it was nonetheless a basic problem, as those classical reaction conditions seemed to suit only with L^1.

Therefore, new synthesis conditions were tried. The use of copper(I) bromide gave the same result. Every test led to the coordination of copper with the ligand. A change in the catalyst was then necessary: given that copper(I) and copper(II) salts were too easily complexed by the clickable ligands, a complex of copper(I), $CuBr(PPh_3)_3$, was employed as catalyst. This change of catalyst was inspired by organic syntheses of triethoxysilanes using Huisgen copper-catalyzed reaction. [38] Given that triethoxysilanes are particularly sensitive to water and to many chemical functions such as alcohols or carboxylic acids, this kind of syntheses was an actual challenge. However, using microwave irradiation and a

tris(triphenylphosphine) copper(I) bromide as catalyst, the desired organosilanes were obtained in typical yield for click chemistry (above 90 %).

First tests were directly made using **C1** and N_3@LUS_{MW}-E (Scheme 6). After a reaction overnight with $CuBr(PPh_3)_3$, the IR spectrum of the resulting material still exhibited a band around 2100 cm^{-1} characteristic of the presence of azide moieties. After one week, no absorption occurred in this region, proving that all the azide moieties had reacted. This long reaction time can be explained by the porous nature of the material: the reactive sites at the silica surface are not all as accessible as in solution and diffusion inside the porous material becomes a non-negligible parameter.

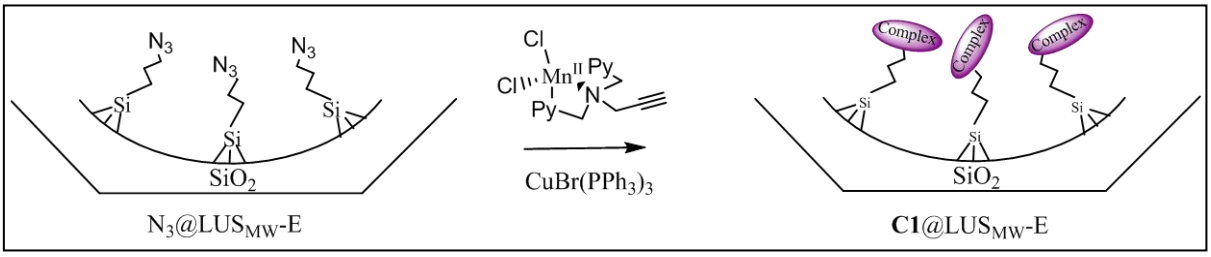

Scheme 6: First test of Huisgen azide-alkyne cycloaddition.

Once the cycloaddition made possible with our molecules, the total removal of the copper catalyst needed to be ensured. Washing with methanol turned out to be efficient enough to remove the catalyst, as confirmed by EDX microscopy and elemental analysis: no trace of copper could be found beyond the detectable threshold. Furthermore, elemental analysis proved that the synthesized material possessed a manganese loading of 1.7 to 2.4 %.

However, though manganese was indeed detected by the analytical techniques mentioned above, we had no proof that the metal ion kept its oxidation state after reaction. Hence the EPR spectrum of the material was measured, and the six characteristic bands of an isolated Mn(II) centre were observed (Figure 12). Then this method provided an isolated complex in solid state, which was not possible for the free equivalent such as **C1**, which

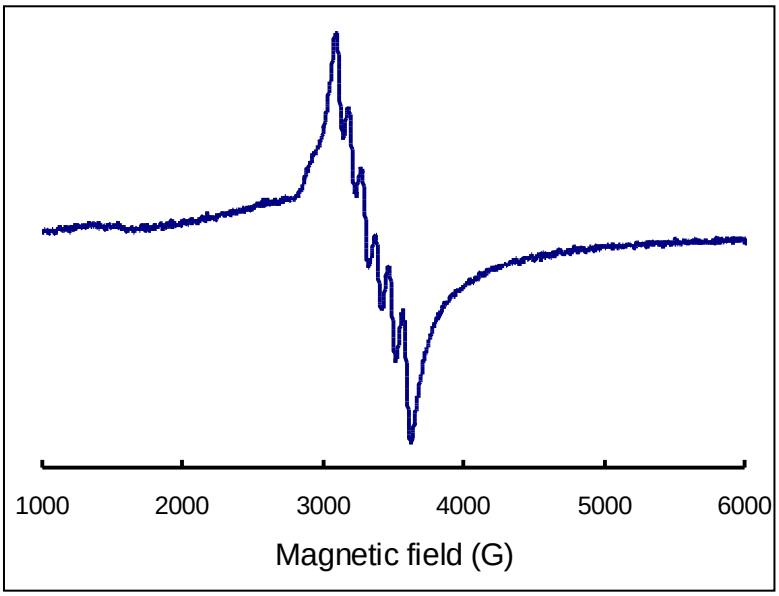

*Figure 12: Solid state EPR spectra of **C1**-TMS@LUS_{MW}-E) at 298 K. Microwave frequency: 9.41 GHz, amplitude modulation: 5 G, gain: 60 dB, power: 2 mW.*

crystallized only as dinuclear species.

Though EPR proved the presence of manganese(II) complexes grafted to the silica pore, a different analytical technique is required in order to characterize the manganese environment. Due to the low concentration of metal complex compared to the silica one, many characterizations are not as accurate as for free complexes. One choice method is EXAFS experiment, which takes advantage of the synchrotron energy to provide X-ray beams of high intensity. ALBA synchrotron in Spain accepted our project to measure the absorption of our species when irradiate by such X-ray beam. However, this experiment will be done at the beginning of 2014 and will not be reported in this manuscript.

Nitrogen sorption isotherms were finally performed to measure the remaining porous volume of the final material. Figure 13 displays the isotherm of LUS_{MW}-E (initial material extracted without any modification), N_3-Py@LUS_{MW}-E15 (host material) and **C1**-Py@LUS_{MW}-E15 (final material). Both host and final materials exhibit a similar total volume of *ca.* 0.45 $cm^3.g^{-1}$. Pore volume given by t-plot clearly indicates a volume loss caused by the surface functionalization as this volume drops from 0.87 in the initial silica to *ca.* 0.27 $cm^3.g^{-1}$ in the host and final materials. However, there is still enough pore volume to allow the diffusion of substrate and access to the manganese(II) centres for catalytic applications.

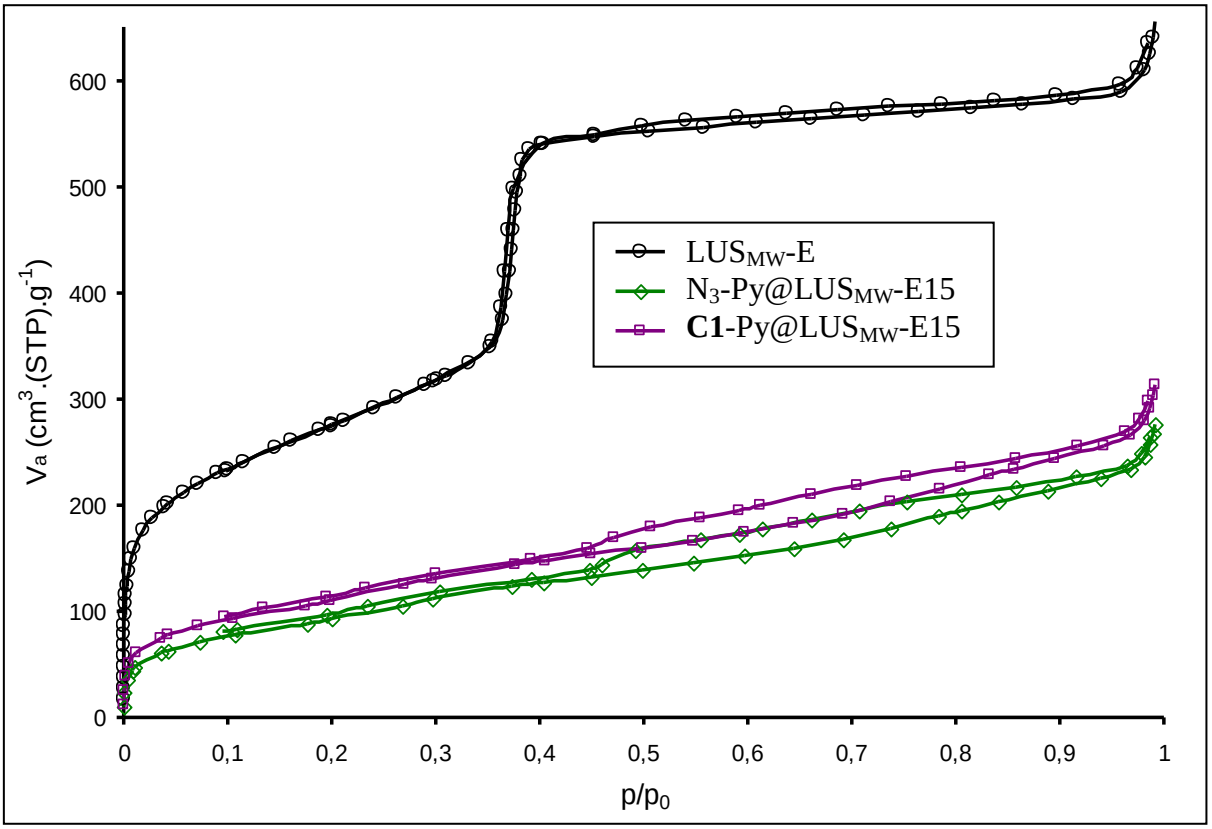

Figure 13: N_2 sorption isotherms of LUS_{MW}-E (black), N_3-Py@LUS_{MW}-E15 (green) and Py@LUS_{MW}-E15 (purple).

III.3. Catalytic tests

This section reports the previous results obtained for the oxidation catalysis of two different catechol derivatives, 4-*ter*-butylcatechol (4-TBC) and 3,5-di-*ter*-butylcatechol (3,5-DTBC) as shown on Figure 14. This work has been done in collaboration with Dr. Fabienne Fache, from the University Claude Bernard Lyon I, and Marie Gourgues from the chemistry Institut Universitaire de Technologie of Grenoble.

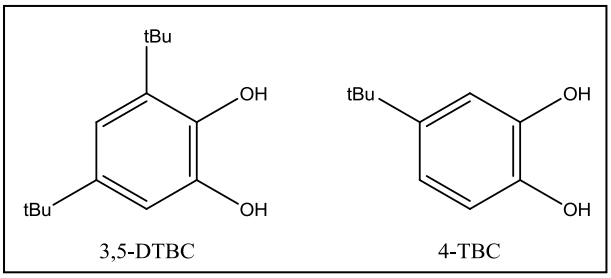

Figure 14: Catechol derivatives used in the study

Our objective was to verify the activity of the synthesized catalysts in reaction of catechol oxidation using O_2 as cheap and easily available oxidant. First, manganese(II) complexes were directly used as catalysts and a panel of reaction conditions were explored. Conditions such as reaction time, temperature, quantity of catalyst or substrate were investigated with those free complexes. In a second time, preliminary tests have been performed with supported analogues.

III.3.1 Free manganese(II) complexes

All experiments are summed up in Table 1. Four complexes, $[Mn_2(\mu\text{-}Cl)_2(Cl)_2(L^1)_2]$ (**C1**), $[Mn(NO_3)(H_2O)_2L^1]\cdot NO_3$ (**C5**), $[MnCl_2L^2]$ (**C6**) and $[Mn(H_2O)_3L^1]\cdot(BPh_4)_2$ (**C7**) were tested as catalysts. Scheme 7 depicts the general catalytic reaction.

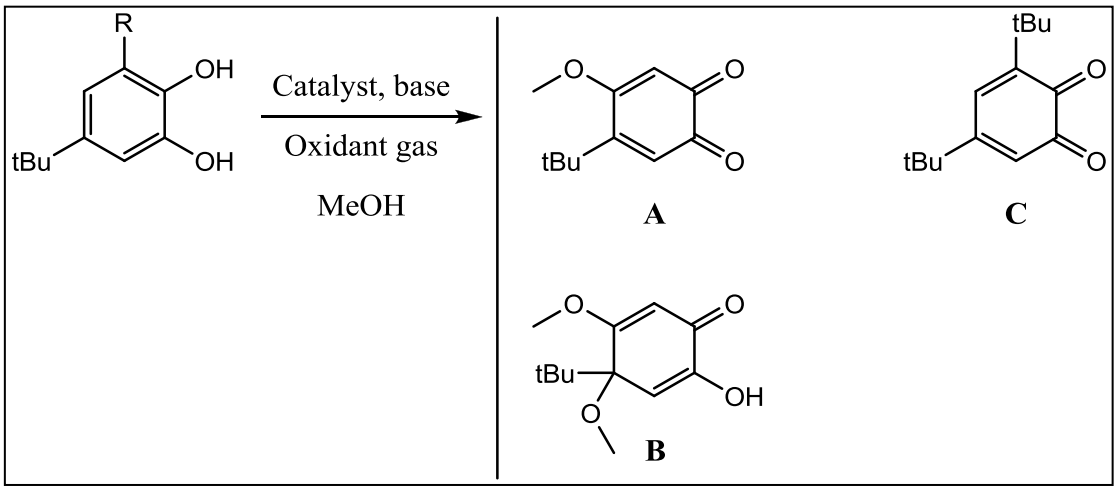

Scheme 7: Generic catalytic test reaction

Table 1: Reaction conditions used in the preliminary catalytic tests

Entry	R	Catalyst [a]	Time (h)	Temperature (°C)	Gas	Base [b]	Products
1	H	**C1** 1 eq	18	25	O_2	/	4-TBC
2	H	**C1** 1 eq	18	25	O_2	TMP	**A**/**B** 9/1
3	H	**C1** 0.1 eq	5	25	O_2	TMP	**A**/**B** 3/2
4	H	/	5	25	O_2	TMP	4-TBC
5	H	$MnCl_2$ 0.1 eq	5	25	O_2	TMP	**A**/**B**/others
6	H	$Mn(NO_3)_2$ 0.1 eq	5	25	O_2	TMP	4-TBC
7	H	**C1** 0.1 eq	5	25	Air	TMP	**A**/**B** 3/1
8	H	**C1** 0.1 eq	3	25	Air	TMP	**A**/**B** 2/3
9	H	**C1** 0.05 eq	5	25	Air	TMP	**A**/**B**/4-TBC
10	H	**C1** 0.01 eq	5	25	Air	TMP	**A**/4-TBC
11	H	**C1** 0.1 eq	5	45	Air	TMP	**A**/**B** 7/3
12	H	**C1** 0.1 eq	5	65	Air	TMP	**A**/**B** 7/3
13	H	**C5** 0.1 eq	5	25	O_2	TMP	**A**/**B**/others
14	H	**C6** 0.1 eq	5	25	O_2	TMP	**A**/**B** 3/2
15	H	**C7** 0.1 eq	5	25	O_2	TMP	**A**/**B**/others
16	*t*Bu	**C1** 0.1 eq	5	25	O_2	TMP	**C**
17	*t*Bu	**C5** 0.1 eq	5	25	O_2	TMP	**C**
18	*t*Bu	**C6** 0.1 eq	5	25	O_2	TMP	**C**
19	*t*Bu	**C7** 0.1 eq	5	25	O_2	TMP	**C**
20	*t*Bu	**C1** 0.1 eq	5	25	O_2	Py	**C**

a) **C1**, **C5**-**C7** correspond to the nomenclature used in Chapter I, b) TMP = 2,2-6,6-tetramethylpiperidine, Py = Pyridine.

III.3.1.1 Analysis of the obtained products

In the case of 4-TBC, a mixture of two main products was obtained. The first one was easily identified as the 4-*tert*-butyl-5-methoxy-*o*-quinone. Let us name this product **A**.

The second major product, called **B**, appeared to be a little more difficult to characterized, as it had never been reported in the literature with such dioxygenase models. Simple ^{1}H and ^{13}C NMR and IR spectra were not conclusive as for the characterization of the product. Therefore, 2D HSQC (for Heteronuclear Single-Quantum Correlation**)** and HMBC (for Heteronuclear Multiple-Bond Correlation) experiments were performed, which allowed us to link ^{1}H and ^{13}C NMR peaks. While the HSQC experiment only correlates directly bound

carbon and hydrogen atoms, the range of HMBC extends from 2 to 4 covalent bonds. Both experiments are represented on Figure 15. Finally we could identify this product **B** as the 4-*tert*-butyl-2-hydroxy-4,5-dimethoxycyclohexa-2,5-dienone.

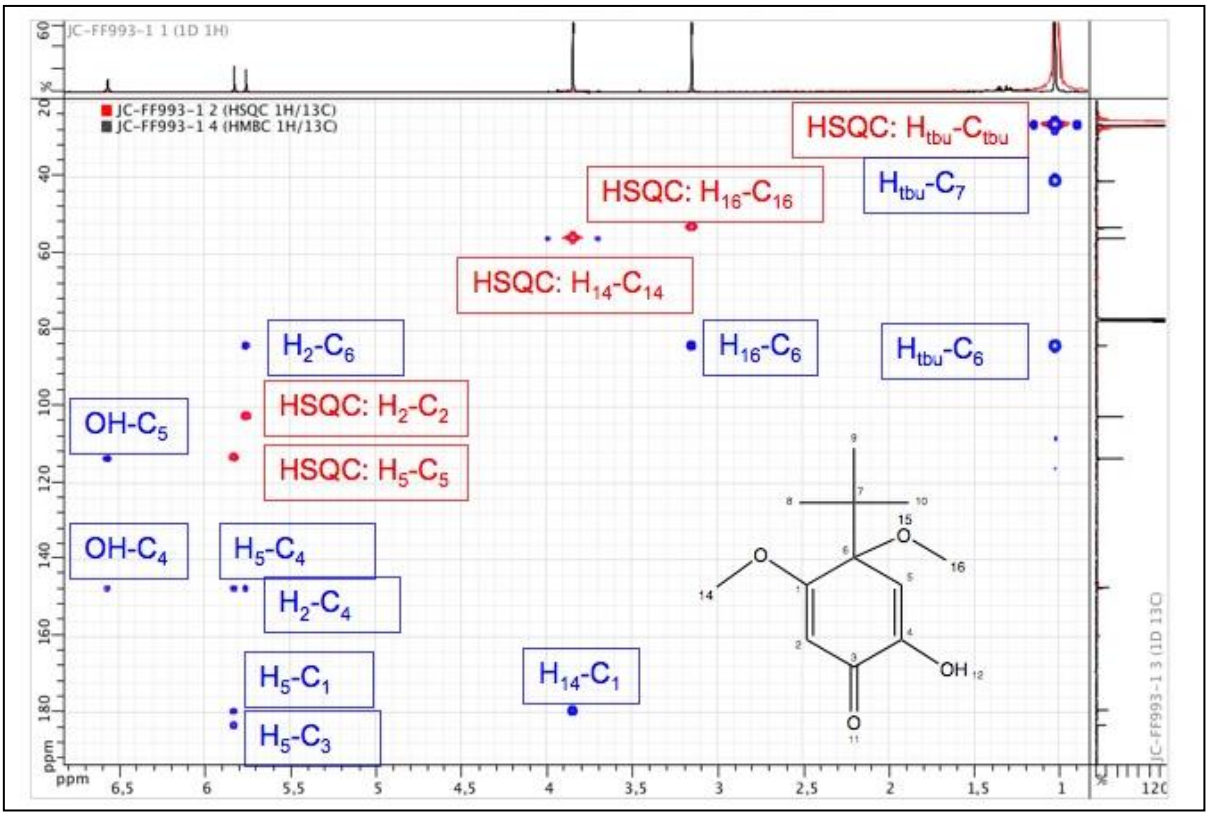

*Figure 15: HSQC (red) and HMBC (blue) spectra of product **B**. X axis correspond to the ^{1}H NMR spectrum while Y axis is the ^{13}C NMR spectrum*

When 3,5-DTBC was used as substrate, oxidation reaction only provided one product which was the *o*-quinone derivative, called **C**.

With both substrates, the products remained cyclic. The oxidation of alcohol groups to ketone would exemplify an oxidase activity rather than a dioxygenase one. Similar activities have been reported with iron or manganese-based models. [39]

Proportion of **A** and **B** were deduced from the NMR spectra of the crude product. Each product has been isolated and the ^{1}H NMR spectra are presented in appendix. To avoid NMR peaks overlapping problems in the integration, the proportion of **A** and **B** were deduced respectively from the peak at 6.25 ppm (1H) and from the peak at 3.07 ppm (3H) respectively. The NMR spectrum of the crude product obtained using the conditions of entry 3 is displayed in Figure 16. Infrared and NMR spectra of products **A**, **B** and **C** are presented in appendix.

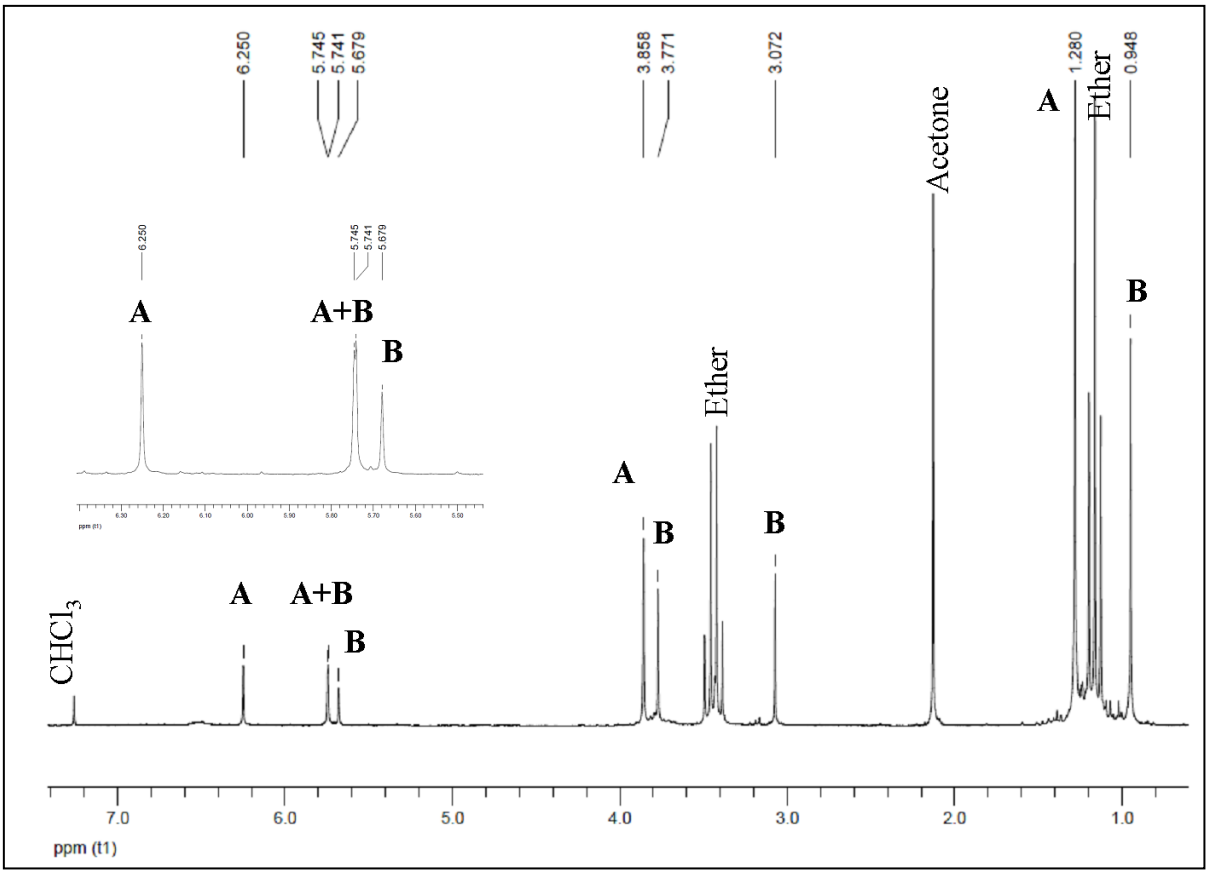

Figure 16: ^{1}H NMR spectrum of the crude product obtained using the conditions in entry 3. The inset is a zoom around 6 ppm

III.3.1.2 Reaction conditions

Default reaction conditions needed to be set up to monitor the activity of the complexes and to provide an experiment which would be considered as a reference. Except for the first two entries, which used a mixture MeOH/H_2O 9/1, every other entry used methanol alone. Comparison of entry 1 and 2 clearly indicated that presence of a base was required to observe an oxidation. 2,2-6,6-tetramethylpiperidine was chosen as a base for it could not coordinate the manganese centre due to the steric hindrance induced by the four methyl groups. Then the question of the quantity of complex arose. While entry 1 and 2 involved one equivalent of complex (which cannot be called catalyst in that case), the rest of the entries were done using 0.1 equivalent or less. Similar activity was observed with 0.1 equivalent, which shows a catalytic activity of **C1**.

Blank tests were performed without catalyst (entry 4) and with manganese chloride (entry 5) and manganese nitrate (entry 6). While tests 4 and 6 did not seem to have any effect on catechol, the use of manganese chloride allowed oxidizing the 4-TBC into in mixture of product **A**, **B** and other subproducts in minority which were not identified.

III.3.1.3 Influence of oxidative gas

Though O_2 was used for the first tests, it was replaced with air. This gas is even cheaper, which could be an asset for a potential larger utilisation. In the end, the oxidation of 4-TBC catalysed by **C1** provided again products **A** and **B**, but in a different proportion. While the ratio **A**/**B** was 3/2 with oxygen, it changed to 3/1 with air.

III.3.1.4 Influence of reaction time

Very first tests were done by bubbling dioxygen in the reactive mixture for 5 h, before stirring overnight under static O_2. Due to the length of the experiment, reaction time was studied first. Therefore stirring overnight was suppressed, and product **A** and **B** were not anymore obtained in a 9/1 ration but in a 3/2 proportion. Reaction time was then decreased to 3 h under air, and products **A** and **B** were obtained in a ratio 2/3 which have to be compared to the 3/1 ration obtained for the 5 h reaction under air. In both cases, with air or with dioxygen, increasing the reaction time also increases the proportion of **A**, which may suggest that **B** is likely an intermediate in the formation of **A**.

III.3.1.5 Influence of the proportion of catalyst

Keeping in mind that the complex could be used in catalytic quantity, we tried to reduce the number of equivalents necessary for the reaction to occur in 5 h under air. Entry 7, 9 and 10 will therefore be compared as these experiments were done using 10, 5 and 1 % of catalyst. However, in both cases, presence of remaining substrate incited us to maintain a 10 % proportion of catalyst for the rest of the tests.

III.3.1.6 Influence of temperature

Temperature did not seem to have an important influence on the proportion of both product **A** and **B** after reaction: both reactions at 45 and 65 °C (entry 11 and 12) provided **A** and **B** in a 7/3 ratio, which is really close to the proportion obtained at room temperature.

III.3.1.7 Influence of catalyst

Apart from **C1**, complexes **C5**, **C6** and **C7** were used as catalysts. While reactions involving **C1** and **C6** provided **A** and **B** (ratio 3/2) in a similar large majority, many subproducts were present after in the reactions catalyzed by **C5** and **C7**. However, these subproducts were not further characterized as we did not manage to isolate them.

Reaction with 3,5-DTBC (entry 16-19) provided product **C** and non-identified subproduct in minority with every catalyst tested.

III.3.1.8 Influence of base

In order to verify whether the coordinating ability of the base could be of any importance in the reactivity, pyridine was used as base instead of tetramethylpiperidine in the oxidation of 3,5-DTBC. This exchange did not have any effect on the product as product **C** was once again obtained along with some subproducts in minority.

III.3.2 Grafted complexes

Two catalysts were tested in the oxidation of 3,5-DTBC. The first one involved **C6**-TMS@LUS$_{MW}$-E while the second one used **C6**-Py@LUS$_{MW}$-E15. The reaction was performed in methanol, with 0.1 equivalent of manganese per substrate, calculated by considering 2 wt% of manganese in the material. No base was added. As for the gas, dioxygen was bubbled in the mixture during 5 h. The solution was then filtered to remove the material, the solvent was evaporated under reduced pressure and the obtained product was passed on a short silica column. The ^{1}H NMR spectra proved that product **C** alone was obtained with both catalysts (Figure 17), without trace of other subproducts present in the tests with free complexes.

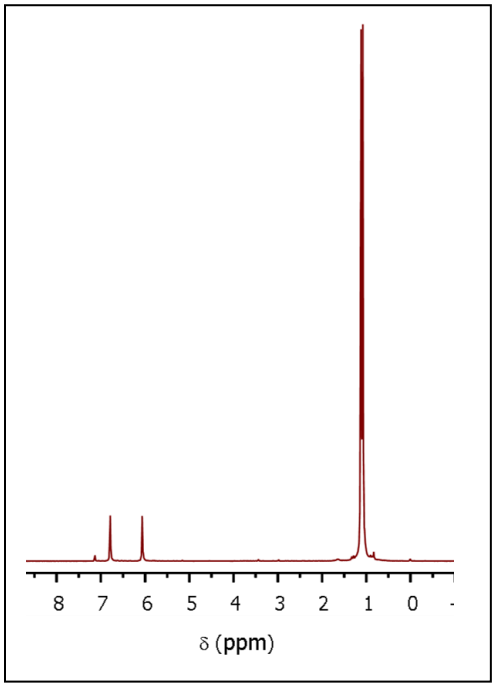

*Figure 17: NMR spectrum of the product obtained after oxidation of 3,5-DTBC using **C6**-Py@LUS-E15 as catalyst.*

Therefore, our materials, like the free complexes, exhibited an oxidase activity rather than a dioxygenase one. However, only two catalytic tests have been carried out, hence the reaction conditions are far from being optimal. In particular, contrary to free complexes, the supported manganese complexes are much less accessible due to their incorporation inside the silica mesopores. Though this incorporation permits to recover the now solid catalyst, diffusion problems have to been taken into account. For instance, simple O_2 bubbling might not be enough to achieve a suitable dioxygen concentration at the active site. In that case, higher pressure of dioxygen would be preferable.

III.4. Experimental part

In this experimental part, general procedure will be described for the modification and functionalization of mesoporous silica.

Synthesis of 3-azidopropyltriethoxysilane. [35] Sodium azide (27 g, 0.41 mol) was added portionwise to a solution of 3-chloropropylethoxysilane (20 g, 83 mmol) and tetrabutylammonium iodide (153 mg, 0.42 mmol) in 220 mL of butanone. The mixture was then stirred at reflux for 5 d under nitrogen. The solution was then filtered over celite and the solvent was removed under reduced pressure. The resulting oil was redissolved in 400 mL CH_2Cl_2 and quickly washed twice with 20 mL of distilled water. The organic phase was dried over Na_2SO_4 and the solvent was removed under reduced pressure to afford the 3-azidopropyltriethoxysilane (84 mg, 0.34 mmol) as a pale yellow oil in a 80 % yield. ^{13}C NMR (200 MHz, $CDCl_3$): δ (ppm) 58.16, 53.54, 22.39, 17.97, 7.33.

Synthesis of LUS_{MW}-TMA. [32] Tetramethylammonium bromide (1.7 g, 11 mmol) was dissolved in 150 mL of EtOH 70 % and stirred for 10 min at 40 °C. The LUS_{MW} mesoporous silica (3 g) was added and the resulting suspension was stirred for 45 min at 40 °C. The solid was filtered on Büchner and washed twice with 50 mL of EtOH 70% and twice with 50 mL of acetone. This procedure was repeated three times to ensure a total exchange. The solid LUS_{MW}-TMA obtained was finally dried in at 80 °C overnight.

Synthesis of TMS@LUS_{MW}-TMA. [32] Before any reaction, the solid was pretreated as follows: the LUS_{MW}-TMA solid (1.5 g) was stirred at 130 °C under argon for 2 h, then at 130 °C under vacuum for 2 h. The solid was let to cool to room temperature under argon, before addition of hexamethyldisilazane (2.42 mg, 15.0 mmol) in 20 mL of dry toluene. The suspension was further stirred at room temperature for 1 h, then 60 mL of toluene were added. The suspension was stirred under argon at 80 °C for 18 h, before being filtered and washed twice with 20 mL of toluene, 20 mL of technical EtOH and 20 mL of acetone. The solid was dried overnight at 80 °C to afford the TMS@LUS_{MW}-TMA silica.

Synthesis of TMS@LUS_{MW}-E. Hydrochloric acid (2 mL of 1M solution) was added to a suspension of TMS@LUS_{MW}-TMA (1 g) in 200 mL of technical EtOH and stirred at RT for 1

h. The solid was then filtered and washed twice with 100 mL of technical EtOH, before being dried overnight at 80 °C.

Synthesis of N_3-TMS@LUS_{MW}-E. TMS@LUS_{MW}-E (500 mg) was pretreated following the same procedure used in the synthesis of TMS@LUS_{MW}-TMA. After cooling under argon, a solution of 3-azidopropyltriethoxysilane (371 mg, 1.5 mmol) dissolved in 10 mL of dry toluene was added. The suspension was stirred for 1 h, 20 mL of toluene were added, and the mixture was stirred at 80 °C during 18 h. After filtration and washing twice with 20 mL of toluene, 20 mL of technical EtOH and 20 mL of acetone, the solid was finally dried overnight at 80 °C. Elemental analysis: C: 5.18 %, H: 1.80 %, N: 2.06 %.

Synthesis of C1-TMS@LUS_{MW}-E. N_3-TMS@LUS_{MW}-E (300 mg) was stirred in a mixture MeOH/MeCN (60 mL/20 mL). After 10 min, complex **C1** (176 mg, 0.5 mmol) was added and the suspension was stirred during 1 hr, before addition of $CuBr(PPh_3)_3$ (93 mg, 0.10 mmol). Then the mixture was stirred at 60 °C for 6 days before filtration. The pale brown solid was washed with 200 mL of MeOH and dried overnight at 80 °C. Elemental analysis: C: 6.42 %, H: 1.75 %, N: 1.44 %, Mn: 2.43 %, Cl: 0.74 %. Similar procedure was followed for the synthesis of **C6**-TMS@LUS_{MW}-E.

Synthesis of LUS_{MW}-TMA-E15. Hydrochloric acid (0.25 mL of 1M solution) was added to a suspension of LUS_{MW}-TMA (1 g) in 200 mL of technical EtOH and stirred at RT for 1 h. The solid was then filtered and washed twice with 100 mL of technical EtOH, before being dried overnight at 80 °C.

Synthesis of Py@LUS_{MW}-TMA-E15. LUS_{MW}-TMA-E15 (500 mg) was pretreated following the same procedure used in the synthesis of TMS@LUS_{MW}-TMA. After cooling under argon, a solution of 2-(4-pyridylethyl)triethoxysilane (459 mg, 1.7 mmol) dissolved in 10 mL of dry toluene was added. The suspension was stirred for 1 hr, 20 mL of toluene were added, and the mixture was stirred at 80 °C during 18 h. After filtration and washing twice with 20 mL of toluene, 20 mL of technical EtOH and 20 mL of acetone, the solid was finally dried overnight at 80 °C.

Synthesis of Py@LUS_{MW}-E15. Hydrochloric acid (2 mL of 1M solution) was added to a suspension of Py@LUS_{MW}-TMA-E15 (1 g) in 200 mL of technical EtOH and stirred at RT

for 1 h. The solid was then filtered and washed twice with 100 mL of technical EtOH, before being dried overnight at 80 °C.

Synthesis of N_3-Py@LUS_{MW}-E15. Py@LUS_{MW}-E15 (500 mg) was pretreated following the same procedure used in the synthesis of TMS@LUS_{MW}-TMA. After cooling under argon, a solution of 3-azidopropyltriethoxysilane (371 mg, 1.5 mmol) dissolved in 10 mL of dry toluene was added. The suspension was stirred for 1 h, 20 mL of toluene were added, and the mixture was stirred at 80 °C during 18 h. After filtration and washing twice with 20 mL of toluene, 20 mL of technical EtOH and 20 mL of acetone, the solid was finally dried overnight at 80 °C. Elemental analysis: C: 9.78 %, H: 1.99 %, N: 2.14 %.

Synthesis of C1-Py@LUS_{MW}-E15. N_3-Py@LUS_{MW}-E15 (300 mg) was stirred in a mixture MeOH/MeCN (60 mL/20 mL). After 10 min, complex **C1** (176 mg, 0.5 mmol) was added and the suspension was stirred during 1 hr, before addition of $CuBr(PPh_3)_3$ (93 mg, 0.10 mmol). Then the mixture was stirred at 60 °C for 6 days before filtration. The pale brown solid was washed with 200 mL of MeOH and dried overnight at 80 °C. Elemental analysis: C: 9.86 %, H: 1.84 %, N: 1.68 %, Mn: 1.66 %, Cl: 0.74 %. Similar procedure was followed for the synthesis of **C6**-Py@LUS_{MW}-E15. Elemental analysis: C: 10.15 %, H: 1.76 %, N: 1.79 %, Mn: 2.13 %, Cl: 1.22 %.

Conclusion

This last chapter details the design of host materials to support the manganese(II) complexes synthesized in the first chapter. Mesoporous LUS silica synthesized at 180 °C using microwave irradiation described in chapter II were functionalized using the Molecular-Stencil Patterning (MSP) strategy. This multi-steps strategy takes advantage of the electrostatic repulsion between cationic heads of surfactant molecules to partially mask the silica surface allowing an homogeneous distribution of the grafted functions.

Host materials synthesized in this study were separated in two families:

- The first contained the tethering azide function and a simple spacing function trimethylsilyl (TMS).
- The second contained the azide function and a spacing and coordinating function pyridine (Py). This latter was meant to mimic the histidine amino acid present in the second coordination sphere in the MndD enzyme.

Prior to the first functionalization, surfactant was exchanged by tetramethylammonium (TMA^+) to diminish the steric hindrance inside the pores. Then, TMA^+-exchanged materials were partially extracted before reaction with 2-(4-pyridyl)ethyltriethoxysilane or used as it is with hexamethyldisilazane. Total extraction of the remaining TMA^+ provided newly freed silica surface that could react with azidopropyltriethoxysilane to afford the host material. All along these modifications, X-ray powder diffraction allowed controlling the integrity of the porous structure.

Once the host materials ready to welcome the manganese(II) complexes, Huisgen copper-catalyzed cycloaddition was adapted to the grating of complexes onto silica surface. In particular, different reaction conditions than the classical $CuSO_4$/ascorbate couple were used to avoid reaction of copper with the silica surface or replacement of the manganese(II) ion in the complex. Therefore tris(triphenylphosphine) copper bromide was employed as catalyst for this ultimate grafting step. EPR study showed that isolated manganese(II) species were indeed present in the final material, and nitrogen sorption isotherm demonstrated that the complexes were inside the pores and that there was enough remaining porous volume to allow catalytic reactions inside the mesopores of the solid. Complex **C1** ($[Mn_2(\mu\text{-}Cl)_2(Cl)_2(L^1)_2]$) and $[MnCl_2L^2]$ (**C6**) were grafted on different host materials, providing solids with an average manganese content of 2 wt%.

Catalytic reactions were then carried out using **C1**, **C5**, **C6** and **C7** as catalyst and 4-*ter*-butylcatechol (4-TBC) and 3,5-di-*ter*-butylcatechol (3,5-DTBC) as substrates. From these tests, reaction conditions were scoped and several conclusions arose:

- Presence of base is necessary for the oxidation reaction to occur.
- All these complexes are active in catalytic proportion.
- The complexes exhibit an oxidase activity, contrary to the dioxygenase one in the enzyme: the substrate is oxidized from alcohol to ketone without incorporation of oxygen atoms from dioxygen.
- Oxidation by O_2 provides two main products in the case of 4-TBC, including one which has never been reported with such manganese-containing models, and only one product in majority (the *o*-quinone derivative) in the case of 3,5-DTBC; these catalysts are thus relatively specific compared to other model catalysts described in literature.

Oxidation of 4-TBC with supported complexes **C6**-TMS@LUS-E and **C6**-Py@LUS-E15 only provided the *o*-quinone. However, while the free catalysts also provided by-products, this is no longer the case as supported complexes exclusively oxidize the catechol to its quinone form. An oxidase activity is therefore at stake with those materials.

Bibliography

[1] C.-H. Lee, T.-S. Lin, C.-Y. Mou, *J. Phys. Chem. C*, **2007**, *111*, *10*, 3873

[2] C. Hess, *Chem. Phys. Chem.*, **2009**, *10*, 319

[3] A. Corma, *Chem. Rev.*, **1997**, *97*, *6*, 2373

[4] K. Moller, T. Bein, *Chem. Mater.*, **1998**, *10*, 2950

[5] M. Anpo, M. Takeuchi, *J. Catal.*, **2003**,*216*, *1–2*, 505

[6] M. Basset, F. Lefebvre, C. Santini, *Coord. Chem. Rev.* **1998**, *178*, 1703

[7] Q. Tang, S. Hu, Y. Chen, Z. Guo, Y. Hu, Y. Chen, Y. Yang, *Micropor. Mesopor. Mater.*, **2010**, *132*, 501

[8] K. K. Sharma, T. Asefa, *Angew. Chem. Int. Ed.*, **2007**, *46*, 2879

[9] K. K. Sharma, R. P. Buckley, T. Asefa, *Langmuir*, **2008**, *24*, 14306

[10] Y. W. Xie, K. K. Sharma, A. Anan, G. Wang, A. V. Biradar, T. Asefa, *J. Catal.*, **2009**, *265*, 131

[11] K. K. Sharma, A. V. Biradar, S. Das, T. Asefa, *Eur. J. Inorg. Chem.*, **2011**, 3174

[12] H. Salmio, D. Bruehwiler, *J. Phys. Chem. C*, **2007**, *111*, 923

[13] J. C. Hicks, R. Dabestani, A. C. Buchanan, C. W. Jones, *Inorg. Chim. Acta*, **2008**, *361*, 3024

[14] J. M. Basset, R. Psaro, D. Roberto, R. Ugo, "Modern Surface Orfganometallic Chemistry", *John Wiley & Sons, Weinheim*, **2009**

[15] D. Gajan, C. Coperet, *New J. Chem.*, **2011**, *35*, 2403

[16] O. Clause, M. Kermarec, L. Bonneviot, F. Villain, M. Che, *J.Am. Chem. Soc.*, **1992,** *114*, *12*, 4709

[17] C. Coperet, M. Chabanas, R. P. Saint-Arroman, J. M. Basset, *Angew. Chem. Int. Ed.*, **2003**, *42*, 156

[18] J.-M. Basset, C. Coperet, D. Soulivong, M. Taoufik, J. Thivolle-Cazat, *Angew. Chem. Int. Ed.*, **2006**, *45*, 6082

[19] R. Anwander, *Chem. Mater.*, **2001**, *13*, 4419

[20] G. Wulff, B. Heide, G. Helfmeier, *J. Am. Chem. Soc.*, **1986**, *108*, 1089

[21] G. Wulff, B. Heide, G. Helfmeier, *Reactive Polymers*, **1987**, *6*, 299

[22] T. J. Terry, G. Dubois, A. Murphy, T. D. P. Stack, *Angew. Chem. Int. Ed.*, **2007**, *46*, 945

[23] T. J. Terry, T. D. P. Stack, *J. Am. Chem. Soc.*, **2008**, *130*, 4945

[24] M. W. McKittrick, C. W. Jones, *Chem. Mater.*, **2003**, *15*, 1132

[25] J. C. Hicks, R. Dabestani, A. C. Buchanan, C. W. Jones, *Inorg. Chim. Acta*, **2008**, *361*, 3024

[26] Q. M. Zhang, K. Ariga, A. Okabe, T. Aida, *J. Am. Chem. Soc.*, **2004**, *126*, 988

[27] W. Otani, K. Kinbara, Q. M. Zhang, K. Ariga, T. Aida, *Chem. Eur. J.*, **2007**, *13*, 1731

[28] S. Abry, B. Albela, L. Bonneviot, *C. R. Chimie*, **2005**, *8*, 741

[29] A. Badiei, L. Bonneviot, N. Crowther, G. M. Ziarani, *J. Organomet. Chem.*, **2006**, *691*, 5911

[30] S. Abry, F. Lux, B. Albela, A. Artigas-Miquel, S. Nicolas, B. Jarry, P. Perriat, G. Lemercier, L. Bonneviot, *Chem. Mater.* **2009**, *21*, 2349

[31] H. C. Kolb, M. G. Finn, K. B. Sharpless, *Angew. Chem. Int. Ed.*, **2001**, *40*, 2004

[32] K. Zhang, B. Albela, M. Y. He, Y. M. Wang, L. Bonneviot, *PCCP*, **2009**, *11*, 2912

[33] S. Abry, A. Thibon, B. Albela, P. Delichère, F. Banse, L. Bonneviot, *New J. Chem.*, **2009**, *33*, 484

[34] J. P. Emerson, M. L. Wagner, M. F. Reynolds, L. Que Jr., M. J. Sadowsky, L. P. Wackett, *J. Biol. Inorg. Chem.*, **2005**, *10*, 751

[35] M. Ortega-Muñoz, J. Lopez-Jaramillo, F. Hernandez-Mateo, F. Santoyo-Gonzalez, *Adv. Synth. Catal.*, **2006**, *348*, 2410

[36] S. Huang, R. J. Clark, L. Zhu, *Org. Lett.*, **2007**, *9*, 4999

[37] W. S. Brotherton, H. A. Michaels, J. T. Simmons, R. J. Clark, N. S. Dalal, L. Zhu, *Org. Lett.*, **2009**, *11*, *21*, 4954

[38] K. Burglova, N. Moitra, J. Hodacova, X. Cattoen, M. W. C. Man, *J. Org. Chem.*, **2011**, *76*, 7326

[39] See Introductory aspects of Chapter I

Conclusions and perspectives

IV.1 Conclusions

In this study, we have designed and synthesize new materials that mimic the manganese-dependent dioxygenases, enzymes that oxidize catechol derivatives with dioxygen. This study did not only focus on modelling the sole active site of the enzyme, but it also took in consideration the importance of the second enzymatic coordination sphere which plays a major role during the extradiol cleavage of catechol derivatives. In order to do so, we separated our strategy in two main phases:

- The synthesis of new ligands and the corresponding manganese(II) complexes, models of the enzymatic active site;
- The synthesis and functionalization of a mesoporous silica followed by the grafting of the previously synthesized complexes.

Three ligands were synthesized in this study: *N*,*N*-bis((pyridin-2-yl)methyl)prop-2-yn-1-amine (L^1), *N*-((1-methyl-1H-imidazol-2-yl)methyl)-*N*-(pyridin-2-ylmethyl)prop-2-yn-1-amine (L^2) and 2-(prop-2-ynyl(pyridin-2-ylmethyl)amino)acetate (L^3). These ligands were synthesized *ad hoc* for the complexation of different manganese(II) salts and grafting on a silica surface. Therefore, they are composed of both coordinating moieties (pyridine, imidazole, carboxylate and tertiary amine) and an anchoring moiety (an alkyne arm for Huisgen cycloaddition). This orthogonal approach allowed minimizing the interference between the complexation and grafting reactions. The compounds syntheses provided both mono and dinuclear complexes depending on the reaction conditions. Four dinuclear complexes were crystallized and their magnetic properties were further studied: $[Mn_2(\mu\text{-}Cl)_2(Cl)_2(L^1)_2]$ (**C1**), $[Mn_2(\mu\text{-}Br)_2(Br)_2(L^1)_2]$ (**C2**), $[Mn_2(\mu\text{-}N_3)_2(N_3)_2(L^1)_2]\cdot 2CH_3OH$ (**C3**) and $[Mn_2(\mu\text{-}N_3)_2(N_3)_2(L^2)_2]$ (**C4**). The same structural pattern is observed in these four crystals: two manganese(II) centres complexed by two ligand molecules and two anions, and bridged by two additional anions. To our knowledge, only a few examples of bromide-bridged manganese(II) dinuclear complexes are reported, and **C2** is the first of complex of such kind to be magnetically studied. From a magnetic point of view, while **C1** turned out to present a weak antiferromagnetic behaviour at low temperature, a ferromagnetic coupling between the two bridged manganese(II) ions was observed in all other complexes **C2**-**C4**. However, though complex **C1** crystallized as a dinuclear unit, EPR spectroscopy proved that this

complex becomes a mononuclear species when dissolved. This behaviour allowed us to validate its use as model in the oxidation of catechol.

In addition to dinuclear complexes, two mononuclear complexes were crystallized: $[Mn(NO_3)(H_2O)_2L^1]$ NO_3 (**C5**) and $[MnCl_2L^2]$ (**C6**), which are hepta and pentacoordinated manganese(II) complexes, respectively. Two last manganese(II) complexes were synthesized with L^1 and L^3 using tetraphenylborate as counter-anion and were obtained as powders. Given the low coordinating ability of this particular anion, one can suppose that ligand and solvent are part of the coordination sphere of the metal ion.

The second part of this project was the synthesis and functionalization of the mesoporous silica support. As mesoporous silicas are usually synthesized in conventional ovens in a couple of days, we optimized the synthesis by using microwave irradiation. The total synthesis time was therefore reduced from 22 h to 2 h without damaging the porous structure. Once the synthesis time reduced, the influence of temperature was studied to monitor its effect on the quality of the final material. Several conclusions can be withdrawn from this study:

- Microwave synthesis allows using higher temperatures than classical heating without alteration of the templating agent;
- Upon temperature augmentation, no micelle swelling is observed by microwave synthesis while it was the case in classical materials;
- While increasing the temperature in classical synthesis leads to a loss of surface area, such loss in microwave-assisted syntheses is only observed until 170 °C. At 180 or 190 °C, surface area are similar to the classical ones prepared at 130 °C;

Therefore, a microwave synthesis at 180 °C provided a material comparable with the classical one, synthesized in conventional oven at 130 °C. This microwave material was further used for functionalization.

Different functionalized materials were synthesized. The functionalization strategy used was the so-called Molecular Stencil Patterning (MSP) which allows both long and short range control on grafting, as well as a high coverage of the silica surface. Before grafting the complex itself, host materials were synthesized. Two different families of materials were designed:

- A material containing both a tethering function and a spacing one, *i.e.*, an azide-terminated alkyl chain and trimethylsilyl, respectively;
- A material containing both a tethering function and a spacing and coordinating one, *i.e.*, an azide-terminated alkyl chain and pyridine, respectively. This latter was used to mimic the histidine present in the second coordination sphere in the enzyme, which allows the stabilization of intermediate species during the enzymatic oxidation.

This functionalization strategy is a multi-step synthesis involving successive modification of the silica surface. All the intermediate materials were characterized by powder X-ray diffraction, thermogravimetric analysis, infrared spectroscopy, ^{29}Si and ^{13}C NMR as well as nitrogen sorption to ensure the conservation of the porous quality. The porous structure was maintained along the numerous steps, providing a material with both large porosity and organic functions able to host the complexes.

Complex grafting was achieved by adapting the Huisgen cycloaddition to our manganese(II) complexes. In order to do so, the copper catalyst used was different than the usual couple $CuSO_4$/ascorbate, and tris(triphenylphosphine) copper bromide was preferred to avoid any complexation of copper by our ligands. Characterization techniques such as X-ray diffraction and nitrogen sorption led us to conclude that this complex incorporation conserves the 2D hexagonal arrangement of the silica and that in spite of these different pore surface modifications, the remaining porous volume is suitable for further catalytic reactions. The EPR spectra of the **C1**-supported material revealed the presence of isolated manganese(II) centres. Hence by anchoring the complexes onto the silica surface, we managed to isolate them in solid state while the complex alone precipitated or crystallized as a dinuclear species.

Preliminary catalytic tests were finally performed using both complexes and materials. From these results, two conclusions were drawn:

- First, both material and complexes exhibit an oxidase catalytic activity rather than a dioxygenase activity, meaning that the substrate does undergo an oxidation, but oxygen atoms are not incorporated in the molecule;
- Second, these catalysts, supported or free, are more specific than other models found in the literature: depending on the conditions, oxidation of 4-*tert*-butylcatechol only provided two main products, including an original one, the 4-*tert*-butyl-2-hydroxy-4,5-dimethoxycyclohexa-2,5-dienone, an oxidation o 3,5-di-*tert*-butylcatechol provided the *o*-quinone in all cases, though with an better selectivity in the case of supported complexes.

IV.2 Perspectives

Several points are worth being investigated to reach a ring opening with this type of material for further applications in depollution:

- New ligands can be synthesized, to provide better mimics of the enzymatic active site. Likewise, the side functions in the materials, models of the second coordination sphere of the enzyme, can be modified for a more precise imitation of the amino acids present in the dioxygenase.
- Insights of the manganese complexation after grafting are actually really difficult to obtain due to the silica matrix that prevents most analytical techniques to be effective. To counter this difficulty, an EXAFS study has been accepted by the ALBA Spanish synchrotron in Barcelona (proposal n°2012100442), and should be performed at the beginning of 2014. This study might provide information on grafted complexes as well as their behaviour toward catechol;
- Catalytic studies with materials should be deepened, in particular for the optimization of the conditions of reaction. Given that the supported complexes are much less accessible than in solution, simple O_2 bubbling might not be the optimal condition for efficient oxidation. Higher pressure of oxygen or material impregnation could improve the reactivity. Temperature could also help to overcome the diffusion problems inside the porous matrix.
- Finally, the possible utilizations of the synthesized ligands can be extended due to the versatility provided by their orthogonal design. For instance, different metals can be coordinated to those ligands and different coupling reactions can be performed using the Huisgen cycloaddition. For example, these ligands could become building blocks in the synthesis of MOFs (Metal-Organic Framework), or could potentially be grafted to any surface, polymer or material that would contain an azide function.

Appendix

Appendix A: Apparatus

Low angle X-ray powder diffraction (XRD) experiments were carried out using a Bruker (Siemens) D5005 diffractometer using Cu K monochromatic radiation.

Infrared spectra were recorded from KBr pellets using a Mattson 3000 IRTF spectrometer and on a JASCO FT-IR 4200 containing an monoreflexion high pressure ATR-pro-470-H Attenuated Total Reflectance (ATR) device.

Nitrogen sorption isotherms at 77 K were determined with a volume device Micromeritics ASAP 2010M on solids that were dried at 80 ºC under vacuum overnight.

TGA measurements were collected from Al_2O_3 crucibles on a DTA-TG Netzsch STA 409 PC/PG instrument, under air (30 $mL.min^{-1}$), with a 25-1000 ºC (10 $ºC.min^{-1}$) temperature range.

EPR spectra were recorded using a Brucker Elexsys e500 X-band (9.4 GHz) spectrometer with a standard cavity. The simulated spectra were calculated using the Easyspin toolbox from Matlab. The spin Hamiltonian used was:

$$\hat{H} = \sum_i \left[\hat{H}_{\mathrm{EZI}}(i) + \hat{H}_{\mathrm{ZFI}}(i)\right] + \sum_k \left[\hat{H}_{\mathrm{NZI}}(i) + \hat{H}_{\mathrm{NQI}}(i)\right] + \sum_{i>j} \hat{H}_{\mathrm{EEI}}(i,j) + \sum_{i,k} \hat{H}_{\mathrm{HFI}}(i,k)$$

With :

- $H_{EZI}(i)$: Electron Zeeman Interaction (EZI) of electron spin i
- $H_{ZFI}(i)$: Zero-Field Interaction (ZFI) of electron spin i
- $H_{NZI}(k)$: Nuclear Zeeman Interaction (NZI) of nuclear spin k
- $H_{NQI}(k)$: Nuclear Quadrupole Interaction (NQI) of nuclear spin k
- $H_{EEI}(i,j)$: Electron-Electron Interaction (EEI) between electron spins i and j
- $H_{HFI}(i,k)$: Hyperfine Interaction (HFI) between electron spin i and nuclear spin k

Powder X-ray diffraction was measured using a Bruker 8 Advance that uses the monochromatic Kα copper radiation (λ=0,154184 nm).

SEM pictures were recorded on a field emission microscope FEI ESEM XL30. Samples were previously metalized with a gold layer.

Solid NMR spectra were measured on an Advance III Bruker 500MHz Wide Bore spectrometer, with a CP/MAS DVT (double resonance, variable temperature) probe 4 mm. The delay time between pulses (pulse width 5 μs) in HPDEC experiments was set to 500 s. Spinning speed was set to about 5 kHz and the number of scans was 5000. Frequency ^{13}C = 125.76 MHz, ^{29}Si = 99.36 MHz.

Liquid NMR spectra were recorded on a Bruker AC 200 spectrometer.

Magnetic measurements:

The measurement of magnetic susceptibility as a function of temperature χ(T) is the most employed characterization technique for coordination compounds exhibiting magnetic properties. These measurements can be realized in direct current (DC), where the sample is placed in a static magnetic field, and in alternating current (AC), where an oscillating magnetic field is added to the static one which leads to the apparition of a time-dependent magnetic moment in the sample. This latter utilization is especially useful for slow magnetic relaxation studies (dynamic effects).

Nowadays, Superconducting Quantum Interference Device (SQUID) are used for samples measurement due to their high sensitivity, and high range of measurement temperaturas (from 2 to 400 K by using liquid helium). Furthermore, the samples can be studied undergoing different perturbations such as strong magnetic fields.

SQUID magnetometers quantify the magnetic flux within a superconducting ring. Therefore this flux can only adopt value that are integer multiples of a determined value called fluxon. The flux of one fluxon is given by:

$$\frac{h}{2c} = 2 \cdot 10^{-7}\ Oe \cdot cm^2$$

This magnetometer contains a 3 cm long coil composed of four superconducting spirals. Inside the coil, the magnetic flux is constant: the introduction of the sample creates a variation which is traduced in electric current transmitted to the SQUID device. This latter possesses a closed superconducting ring with a small discontinuity known as Josephson junction, which is crossed by an electric current. Infinitesimal magnetic field variations, and by extension small voltage oscillations, current intensities or magnetic susceptibility, can be detected through quantum processes by a SQUID.

During the measurement, samples are placed in the magnetic flux and the magnetometer realizes a series of successive sample oscillations to provide an average value of the measured

variable. Small magnetic field variations produce strong electric signals, which grant those devices such sensitivity in magnetic susceptibility measurements.

The magnetic susceptibility presented in this work were measured using Quantum Design MPMS-XL-5 SQUID.

Appendix B: Crystallographic tables

Table B1. Crystal data and refinement results for complexes **C1-C4**.

	1	**2**	**3**	**4**
Formula	$C_{30}H_{30}Cl_4Mn_2N_6$	$C_{30}H_{30}Br_4Mn_2N_6$	$C_{32}H_{38}Mn_2N_{18}O_2$	$C_{28}H_{32}Mn_2N_{20}$
Molecular weight ($g.mol^{-1}$)	726.3	904.1	816.7	758.6
Crystal system	monoclinic	monoclinic	triclinic	monoclinic
Space group	$P2_1/c$	$P2_1/c$	P-1	C2/c
a (Å)	9.930(1)	10.1360(4)	9.0552(2)	10.2453(6)
b (Å)	17.060(2)	17.2803(6)	10.1744(2)	18.4200(9)
c (Å)	10.008(2)	10.2664(4)	11.1141(2)	18.674(1)
α (deg.)	90	0	85.550(1)	90
β (deg.)	109.00(2)	109.062(2)	81.656(1)	95.597(4)
γ (deg.)	90	90	69.687(1)	90
V ($Å^3$)	1603.0(5)	1699.6(1)	949.70(3)	3507.3(3)
T (K)	150	293	293	293
Density	1.505	1.767	1.428	1.437
F(000)	740	884	422	1560
Data collected	5610	3268	8630	23413
Unique data	3034	2741	3467	1821
R_{int}	0.051	0.031	0.029	0.065
S	0.92	1.04	1.11	1.01
R	0.0526	0.0239	0.0337	0.0315
R_w	0.0648	0.0545	0.0868	0.0639
No. data used	2285	3268	4352	1830
No. refined parameters	190	190	260	221
$\Delta\rho_{max}$ ($e^-.Å^{-3}$)	0.98	0.44	0.41	0.16
$\Delta\rho_{min}$ ($e^-.Å^{-3}$)	-0.72	-0.42	-0.60	-0.21
Absorption correction	analytical	multi-scan	multi-scan	multi-scan

Table B2. Crystal data and refinement results for complexes **C5-C6**.

	C6	**C5**
Formula	$C_{14}H_{16}Cl_2MnN_4$	$C_{15}H_{29}MnN_5O_8$
***M*$_r$ (g)**	366.15	451.29
***T* (K)**	293(2)	293(2)
λ (Å)	0.71073	0.71073
Crystal System	Monoclinic	Monoclinic
Space Group	*P*21/c	*C 2/c*
***a* (Å)**	8.6117(6)	29.7559(12)
***b* (Å)**	13.6718(10)	9.2430(3)
***c* (Å)**	15.1597(11)	16.8703(6)
α (º)	90	90
β (º)	109.715(4)	121.541(3)
γ (º)	90	90
***V* (Å^3)**	1680.2(2)	3954.4(2)
Z	4	8
ρ_{calc} (Mg/m^3)	1447	1.519
μ (mm^{-1})	1.101	0.721
***F*(000)**	748	471
Crystal size (mm^3)	0.06 x 0.00 x 0.02	0.12 x 0.08 x 0.06
Theta range for data collection (º)	2.06 to 31.31°	1.44 to 28.37
Index ranges	-11<=h<=12, -17<=k<=18, -21<=l<=19	-43<=h<=43, -13<=k<=12, -24<=l<=23
Reflections collected	23298	40197
Independent reflections	4677 [*R*(int) = 0.1747]	6326 [R(int) = 0.0374]
Completeness to theta = 25º	99.9%	100.00%
Max. and min. transmission	0.982 and 0.936	0.963 and 0.917
Goodness-of-fit on *F*^{2}	1.076	1.024
Final R indices [*I* > 2.0σ(*I*)]	*R*1 = 0.0715, *wR*2 = 0.1854	R1 = 0.0372, wR2 = 0.0827
***R* indices (all data)**	*R*1 = 0.1094, *wR*2 = 0.2323	R1 = 0.0605, wR2 = 0.0923
Largest diff. peak and hole (e Å^{-3})	0.873 and -0.826	0.564 and -0.326

Table B3. Important bond lengths (Å) and bond angles (deg.) in complexes **1**-**4**.

	C1	**C2**	**C3**	**C4**
Bond lengths (Å)				
Mn1-N1	2.27(1)	2.26(6)	2.26(5)	2.28(4)
Mn1-N2	2.280(4)	2.269(2)	2.265(2)	2.185(3)
Mn1-N3	2.388(3)	2.389(2)	2.384(2)	2.463(3
Mn1-Cl1/X1	2.574(1)	2.6641(5)		
(bridge)	2.515(2)	2.7333(5)		
Mn1-Cl3/X3	2.423(1)	2.5740(5)		
Mn1-N9			2.225(2)	2.201(3)
(bridge)			2.244(2)	2.221(3)
Mn1-N6			2.153(2)	2.119(3)
Bond angles (°)				
Mn1-X-Mn1	97.52(4)	95.88(1)	104.50(6)	104.0(1)
X = Cl1, Br1, N9				
N-Mn1-N	72.6(1)	98.84(8)	103.33(6)	69.7(1)
(N1,N2,N3)	70.9(1)	72.95(8)	72.86(5)	72.2(1)
	98.1(1)	71.45(8)	72.89(6)	101.5(1)
N-Mn-N			97.84(6)	101.6(1)
(N1,N2,N3 = ligand			105.08(6)	91.5(1)
N6,N9 = N_3 groups)			75.50(6)	154.7(1)
			93.54(6)	161.8(1)
			90.62(6)	88.0(1)
			157.98(6)	90.2(1)
			90.02(6)	98.3(1)
			163.57(6)	103.3(1)
			88.55(6)	156.4(1)
			154.43(6)	101.8(1)
			103.72(6)	90.3(1)
			93.60(6)	76.1(1)
N-Mn-Cl/Br	86.09(8)	95.11(6)		
	93.56(8)	95.14(6)		
	98.17(8)	159.85(5)		
	94.91(8)	87.70(5)		
	163.87(7)	165.10(6)		
	161.76(7)	98.05(5)		
	89.48(8)	162.13(6)		
	157.83(7)	85.78(6)		
	92.30(8)	92.47(5)		
Cl/Br-Mn-Cl/Br	82.48(5)	97.61(2)		
	99.99(5)	101.69(2)		
	102.57(4)	84.12(1)		

Table B4. Important bond lengths (Å) and bond angles (deg.) in complexes **C5-C6**

	C5	**C6**
Bond lengths (Å)		
Mn(1)-N(1)	2.262(1)	2.217(3)
Mn(1)-N(2)	2.387(1)	2.450(3)
Mn(1)-N(3)	2.250(1)	2.150(3)
Mn(1)-N(4)	2.866(1)	
Mn(1)-O(1)	2.185(1)	
Mn(1)-O(2)	2.154(1)	
Mn(1)-O(3)	2.295(1)	
Mn(1)-O(4)	2.601(1)	
Mn(1)-Cl(1)		2.3926(10)
Mn(1)-Cl(2)		2.3431(11)
Bond angles (°)		
N(1)-Mn(1)-N(2)	72.09(4)	72.38(10)
N(1)-Mn(1)-N(3)	144.30(5)	124.76(11)
N(1)-Mn(1)-N(4)	108.45(1)	
N(1)-Mn(1)-O(1)	92.12(5)	
N(1)-Mn(1)-O(2)	89.10(5)	
N(1)-Mn(1)-O(3)	83.37(5)	
N(1)-Mn(1)-O(4)	133.350(1)	
N(1)-Mn(1)-Cl(1)		94.15(8)
N(1)-Mn(1)-Cl(2)		113.60(8)
N(2)-Mn(1)-N(3)	72.63(5)	73.24(10)
N(2)-Mn(1)-N(4)	173.636(2)	
N(2)-Mn(1)-O(1)	88.07(4)	
N(2)-Mn(1)-O(2)	98.01(5)	
N(2)-Mn(1)-O(4)	154.56(2)	
N(3)-Mn(1)-N(4)	107.22(1)	
N(3)-Mn(1)-O(1)	91.96(5)	
N(3)-Mn(1)-O(2)	90.53(5)	
N(3)-Mn(1)-O(3)	153.15(4)	
N(3)-Mn(1)-O(3)	132.30(5)	
N(3)-Mn(1)-O(4)	82.02(1)	
N(4)-Mn(1)-O(1)	85.57(1)	
N(4)-Mn(1)-O(2)	88.35 (1)	
N(4)-Mn(1)-O(3)	25.45(1)	
N(4)-Mn(1)-O(4)	25.61(1)	
O(1)-Mn(1)-O(2)	173.88(5)	
O(1)-Mn(1)-O(3)	81.99(5)	
O(1)-Mn(1)-O(4)	90.85(1)	
O(2)-Mn(1)-O(3)	92.21(5)	
O(2)-Mn(1)-O(4)	83.97(1)	
O(3)-Mn(1)-O(4)	51.05(1)	
N(2)-Mn(1)-Cl(1)		154.87(7)
N(2)-Mn(1)-Cl(2)		96.91(7)
N(3)-Mn(1)-Cl(1)		99.36(8)
N(3)-Mn(1)-Cl(2)		112.32(9)
Cl(1)-Mn(1)-Cl(2)		108.01(4)

Appendix C: IR spectra

Ligand L^1

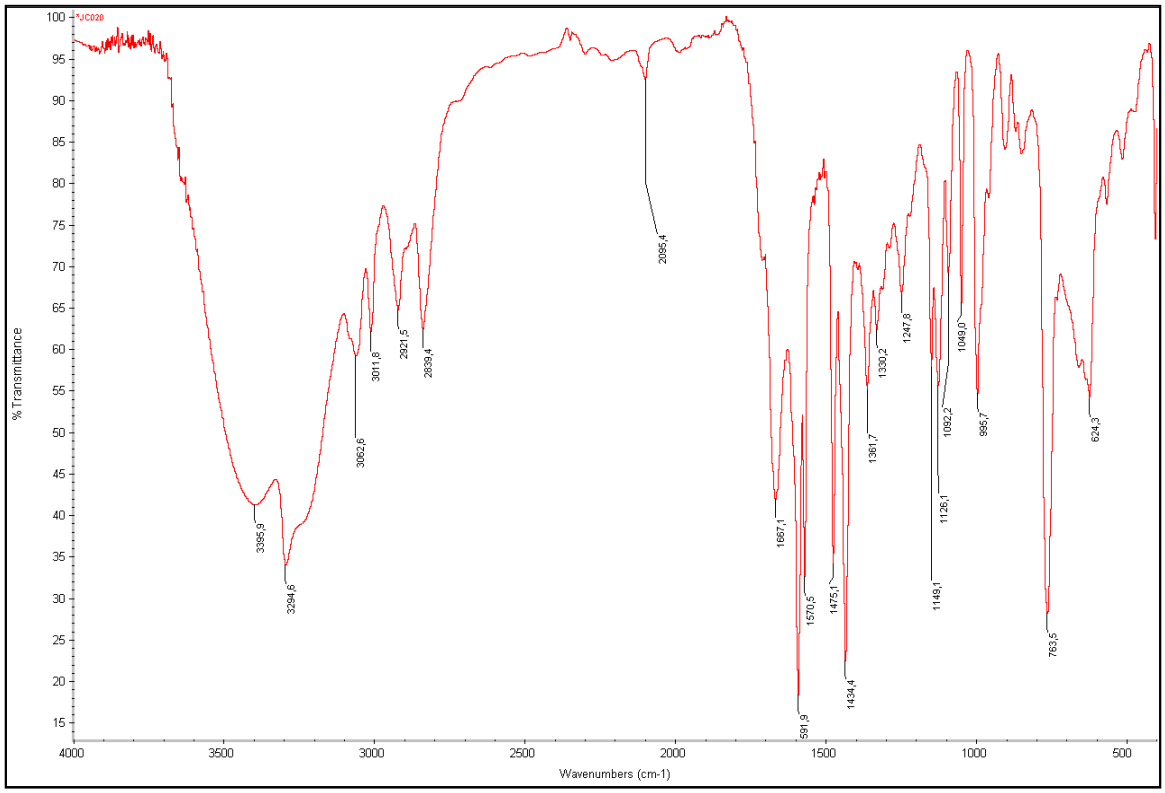

Ligand L^2

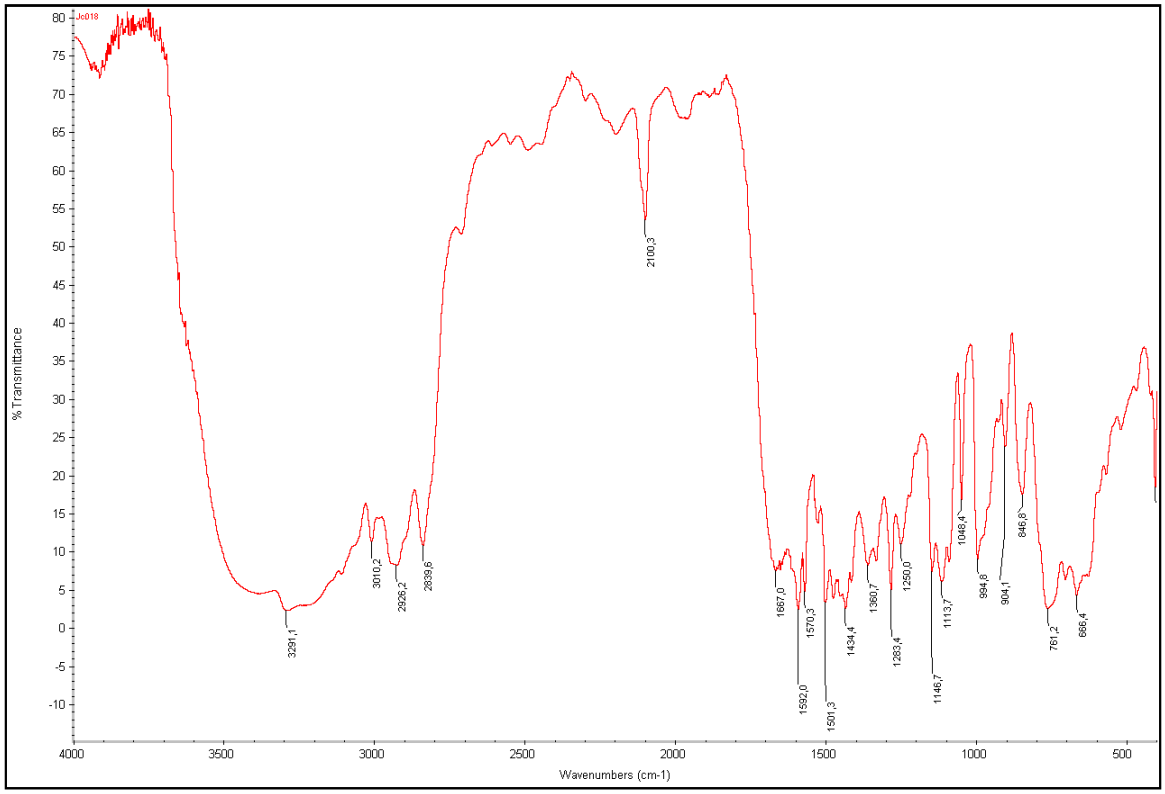

Complex **C1**

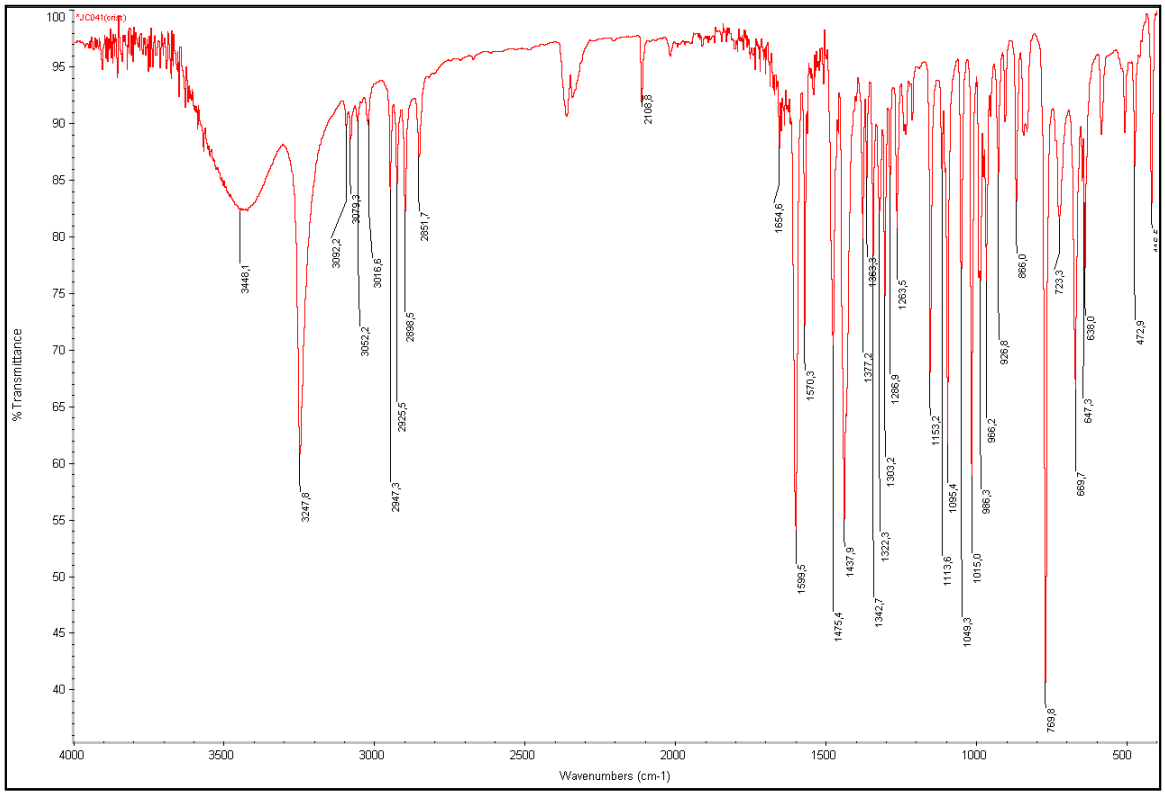

Complex **C6**

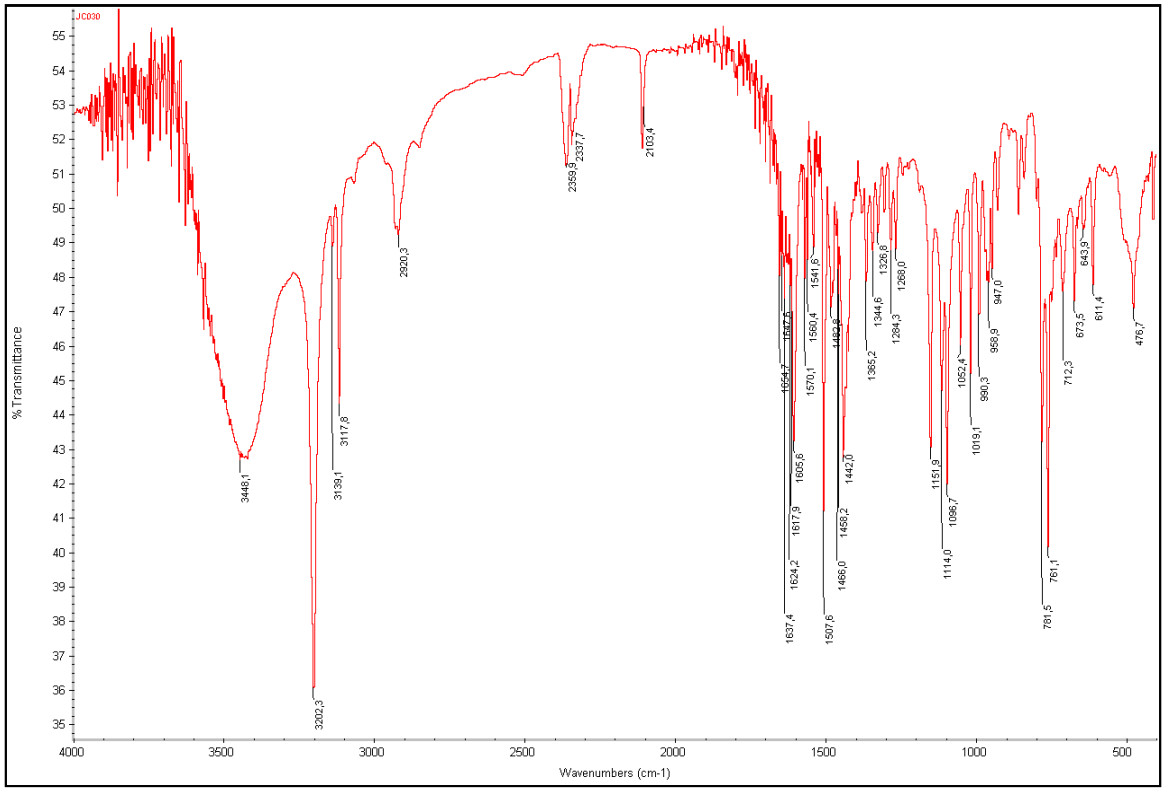

Complex **C7**

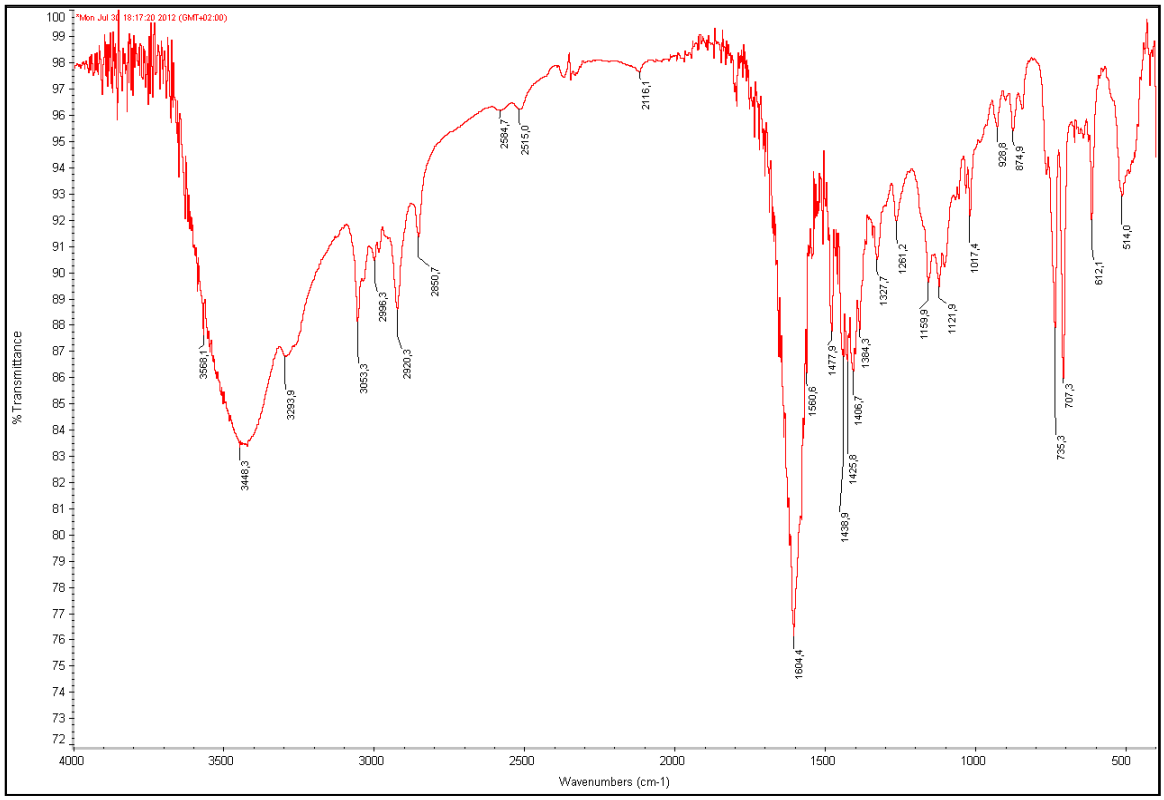
% Transmittance
Wavenumbers (cm-1)
3568,1
3448,3
3293,9
3053,3
2996,3
2920,3
2850,7
2584,7
2515,0
2116,1
1604,4
1560,6
1477,9
1438,9
1425,8
1406,7
1384,3
1327,7
1261,2
1159,9
1121,9
1017,4
928,8
874,9
735,3
707,3
612,1
514,0

Product **A**

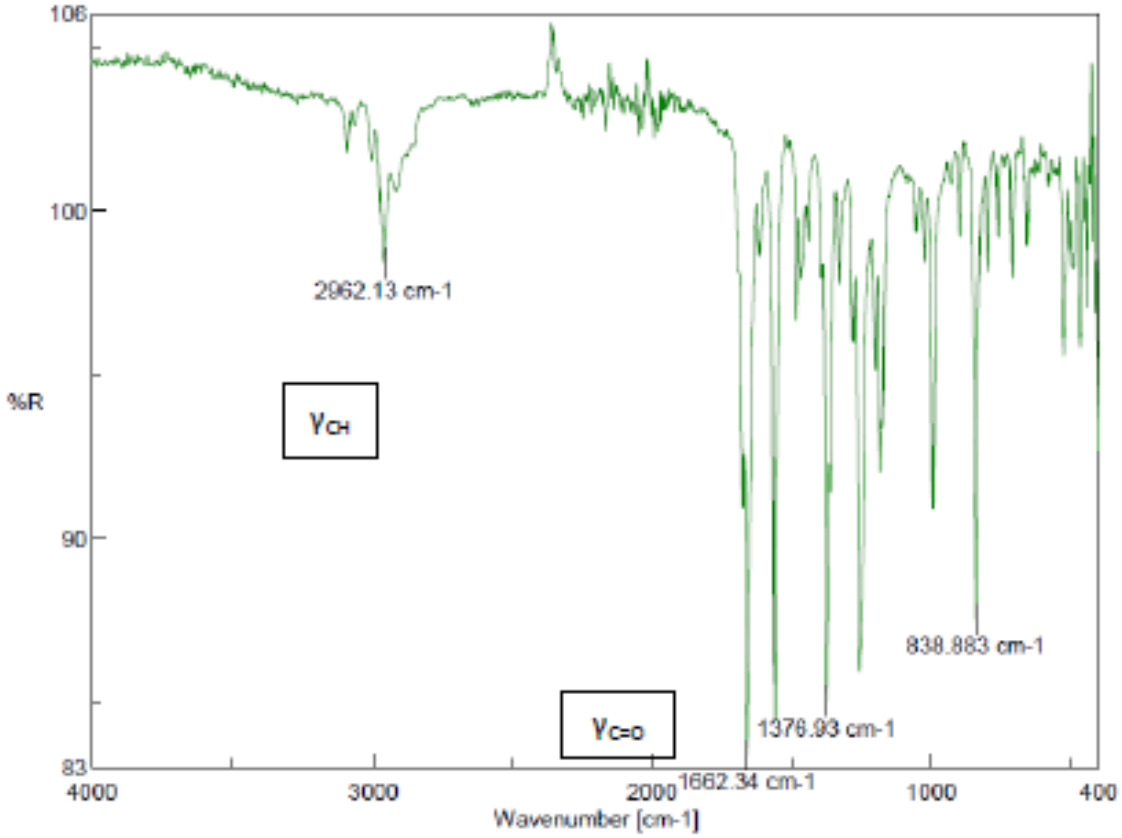

Product **B**

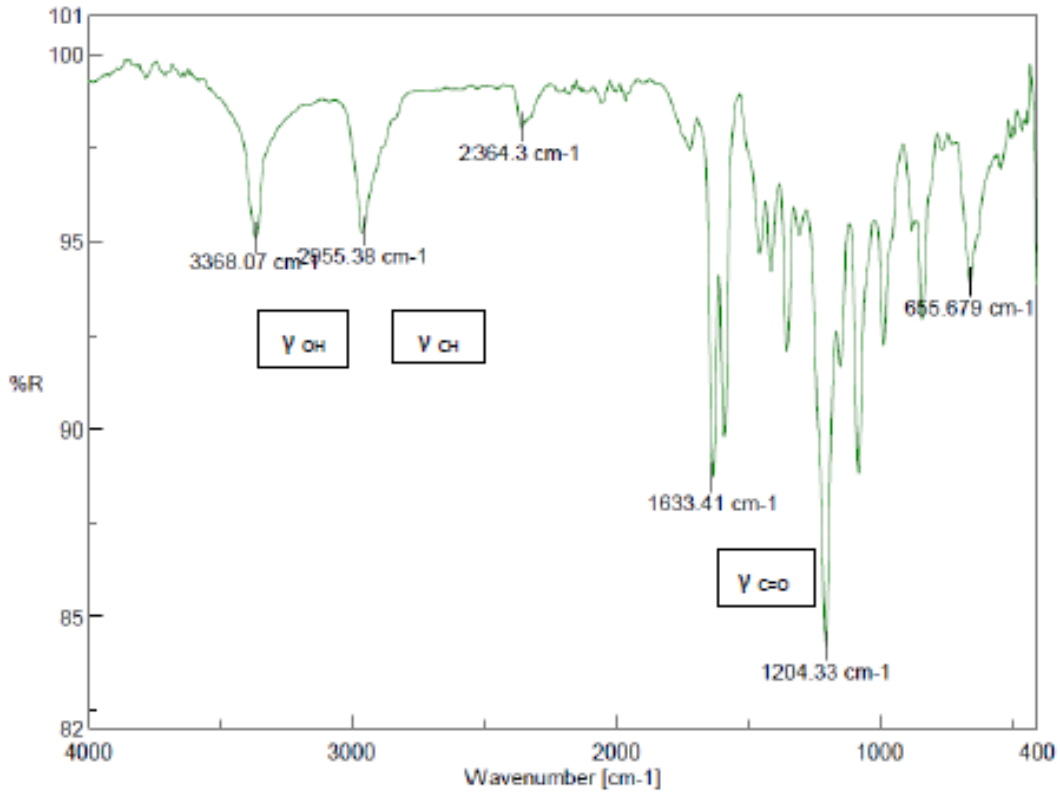

Product **C**

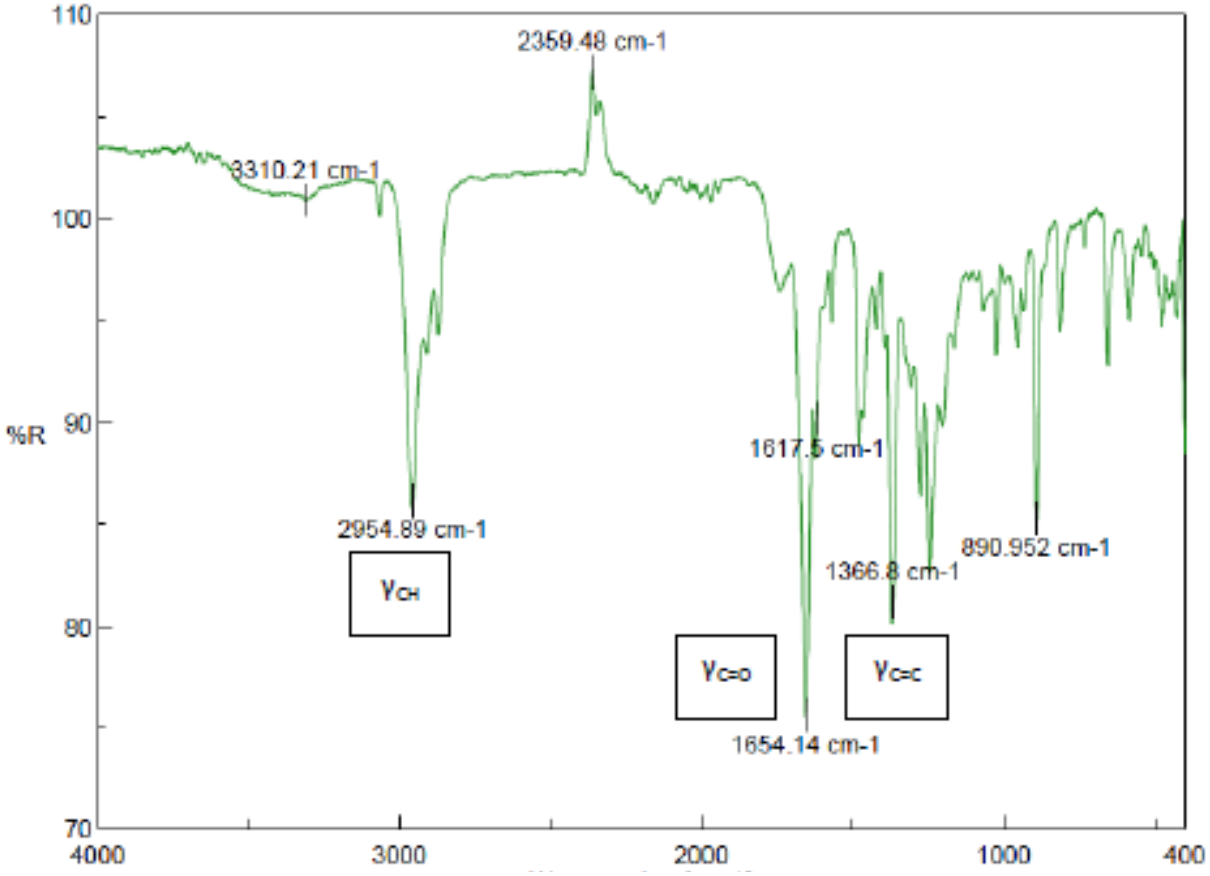

Material synthesized with the Huisgen cycloaddition between **C5** and an azide functionalized silica after 1 night.

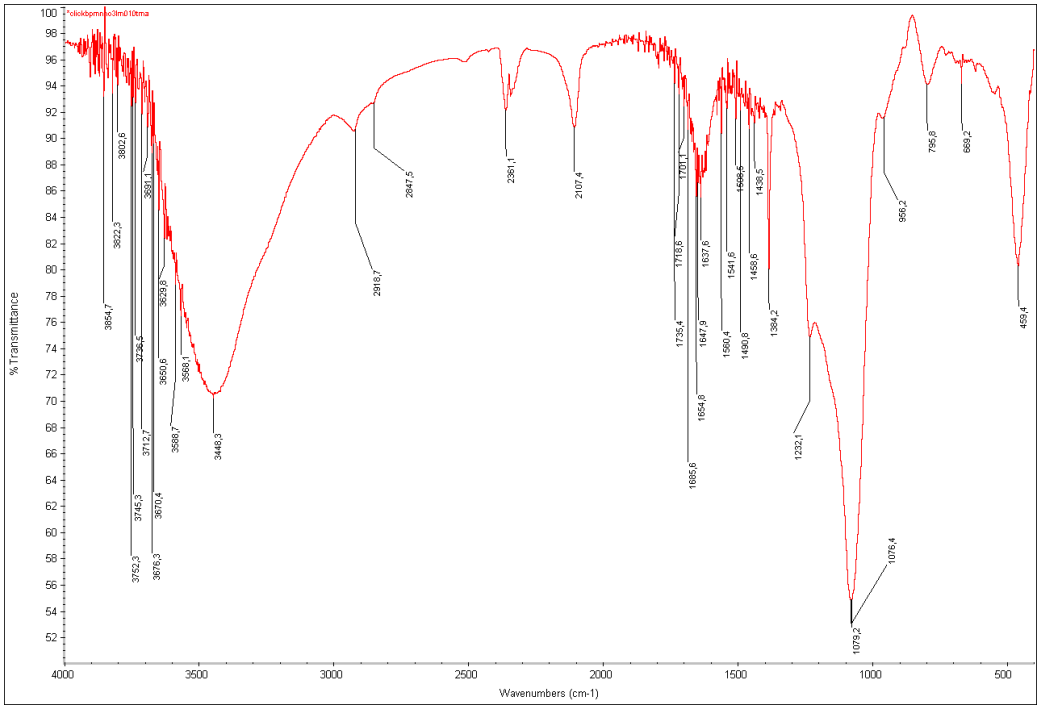

Appendix D: NMR spectra

Ligand L^1: ^1H and ^{13}C

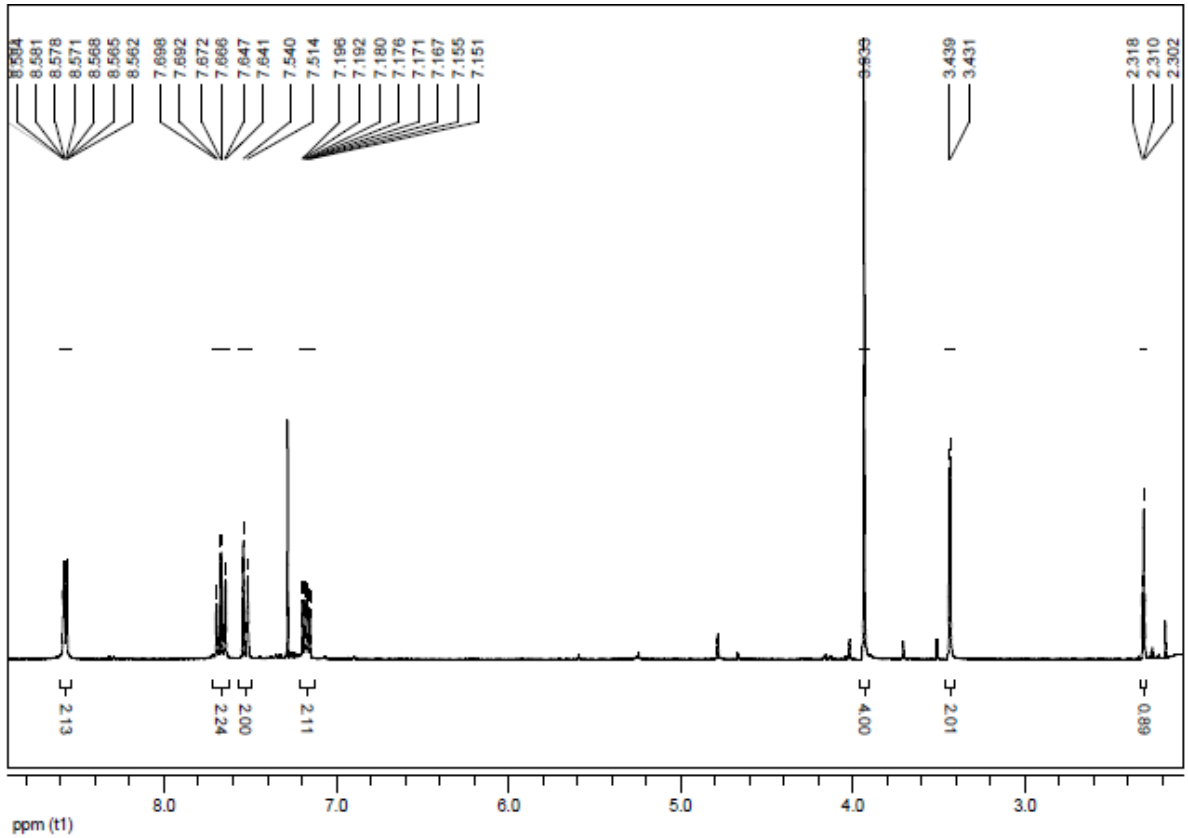

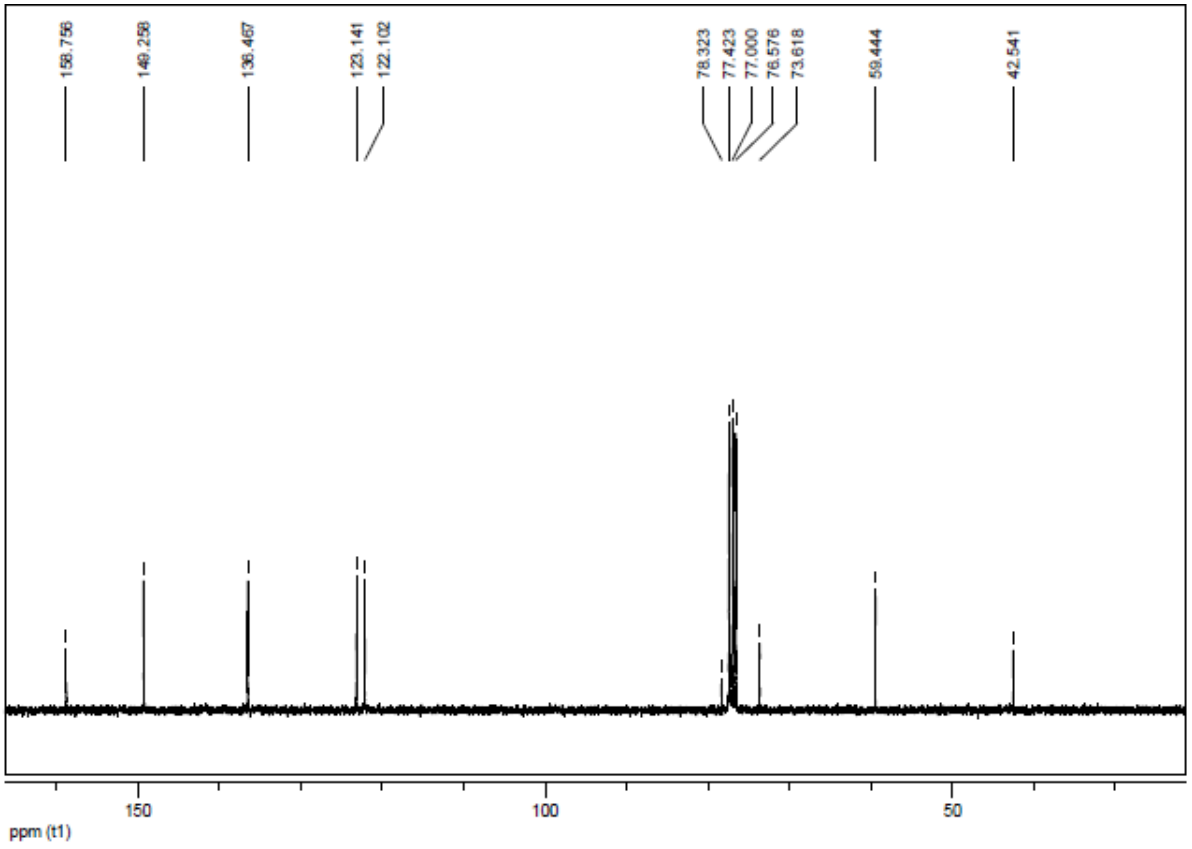

Ligand L^2: ^1H and ^{13}C

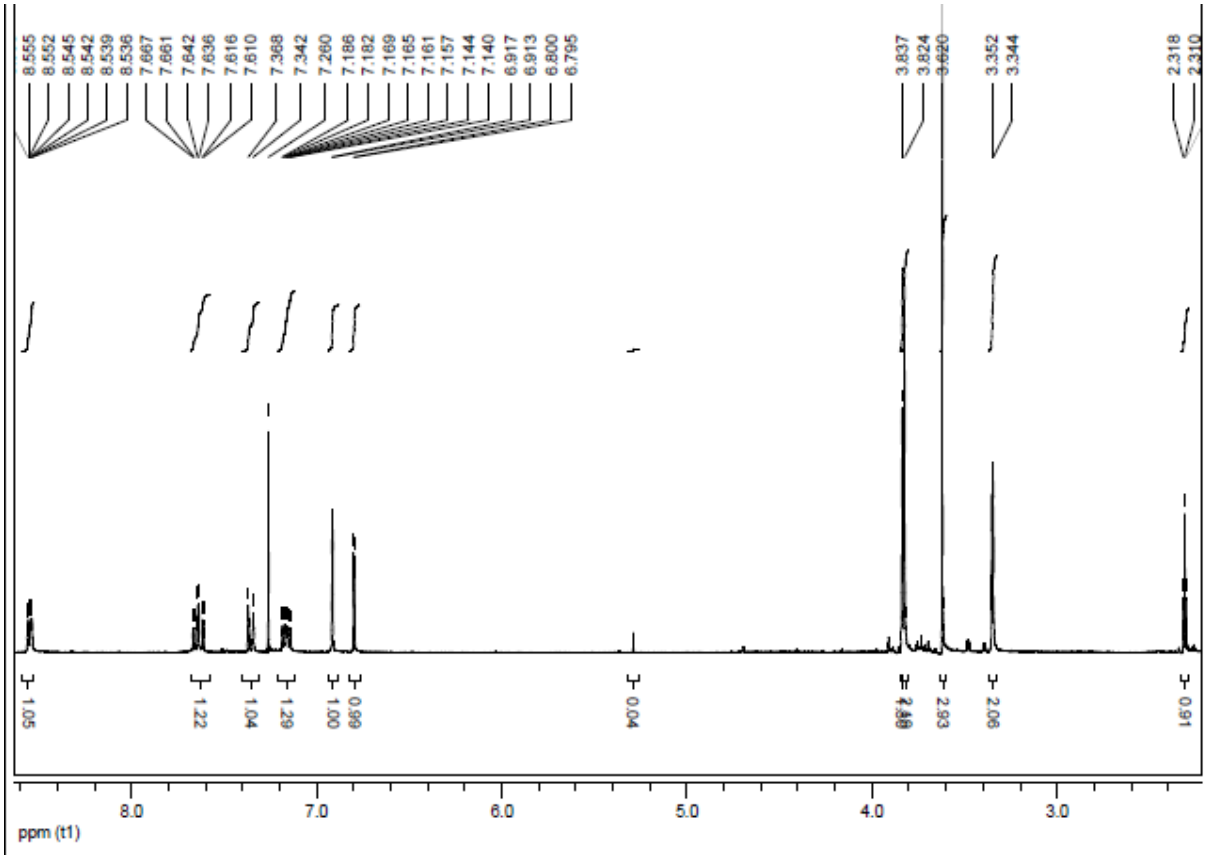

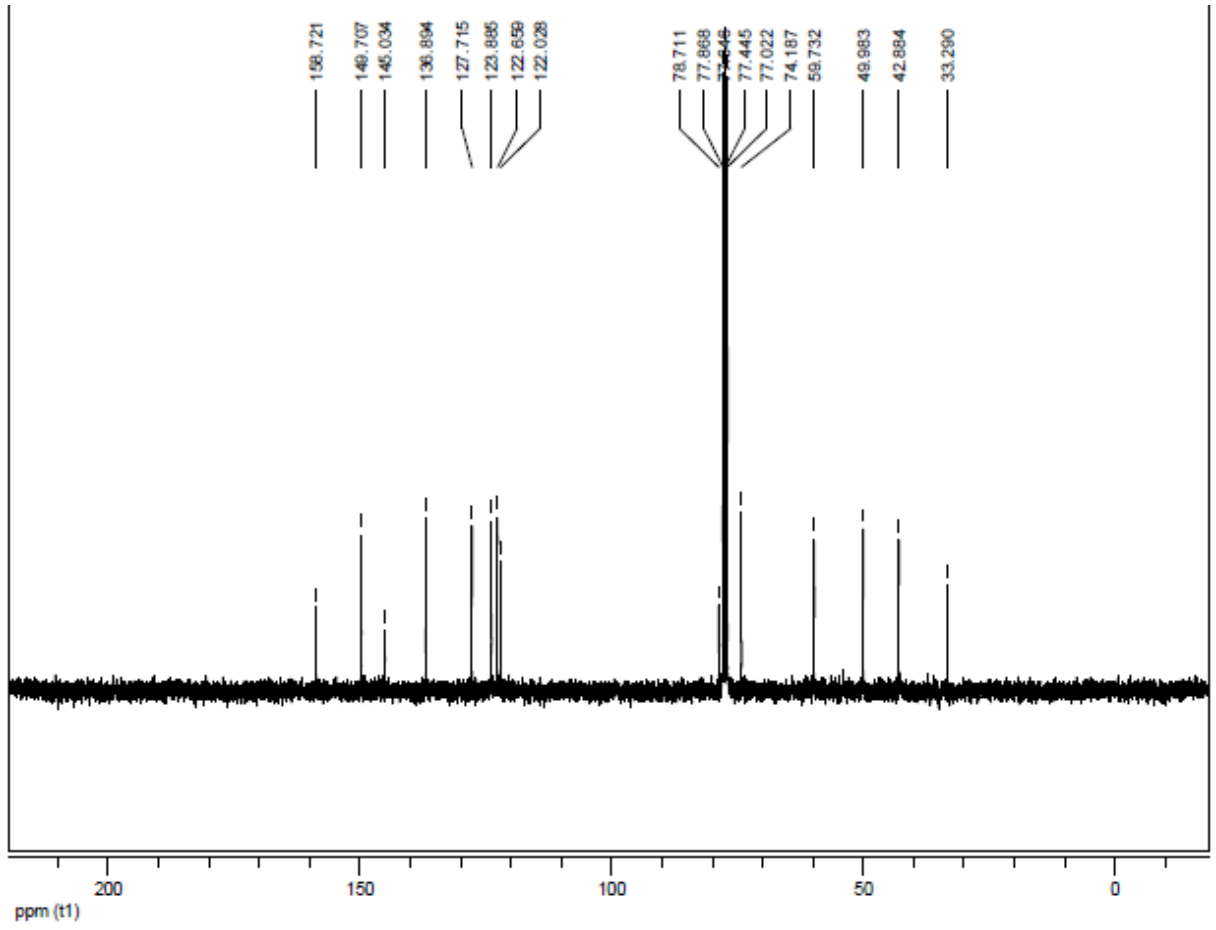

Ligand L^3

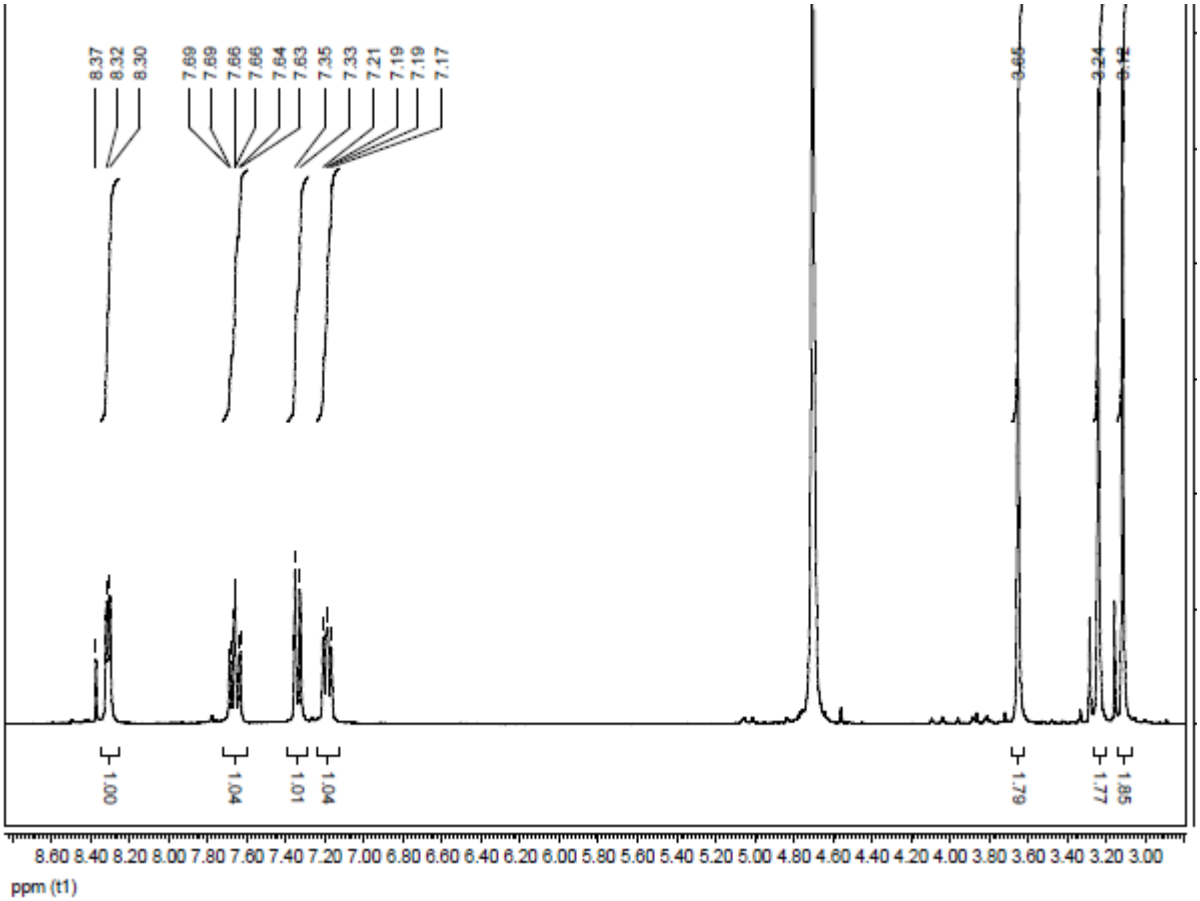

Crude product of the copper-catalyzed reaction between L2 and benzyl azide

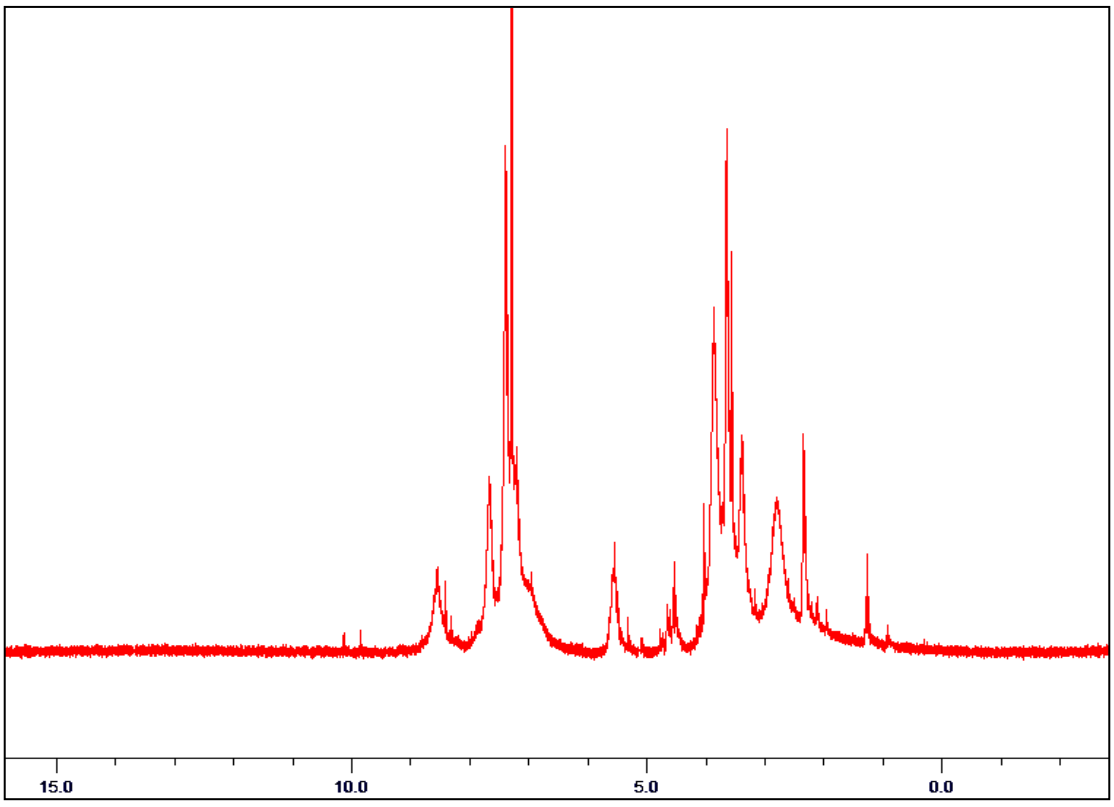

Product **A**

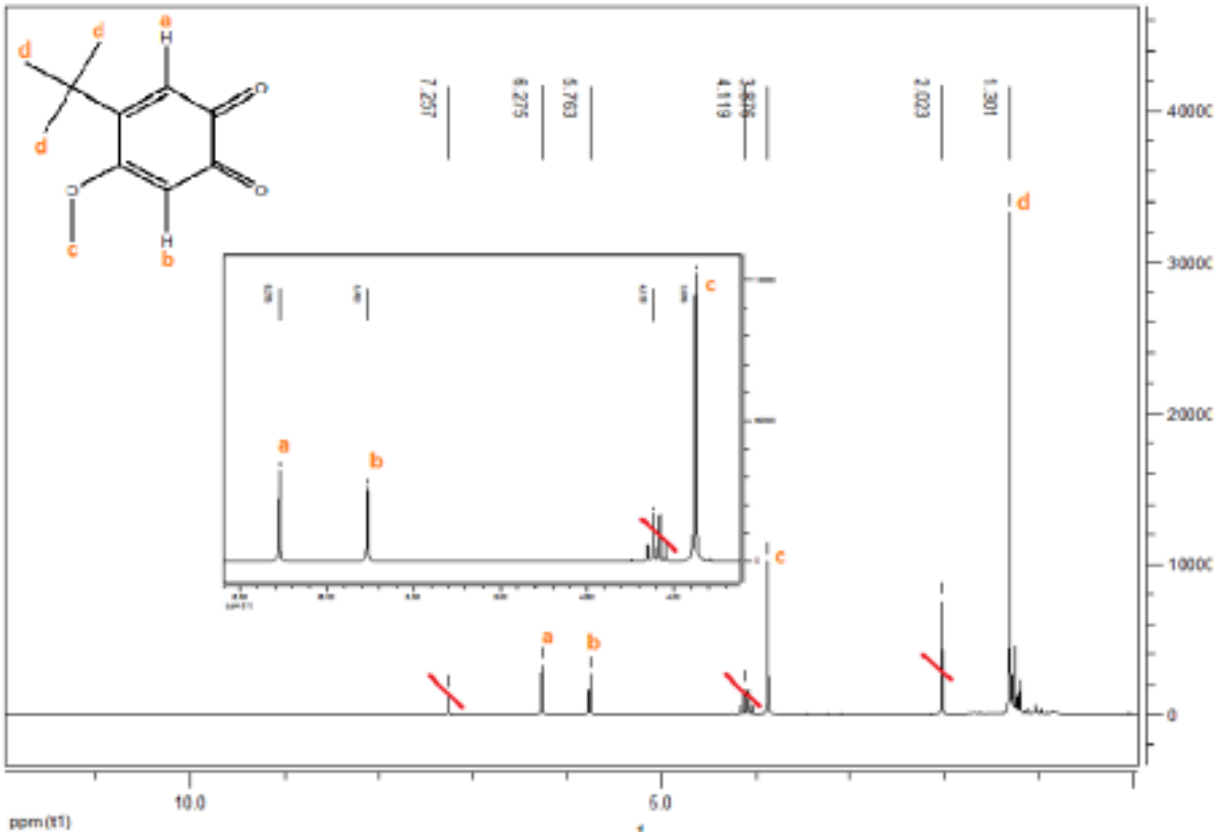

Product **B**

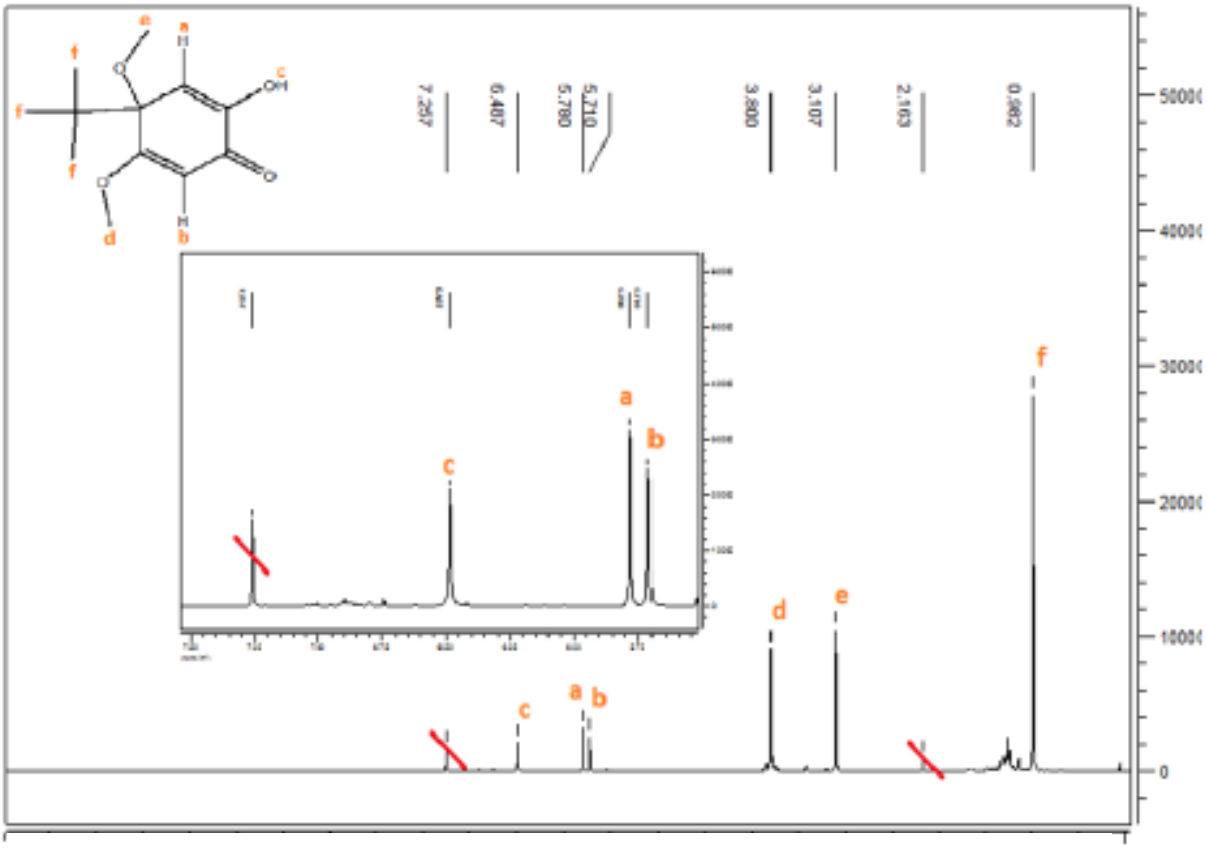

Product **C**

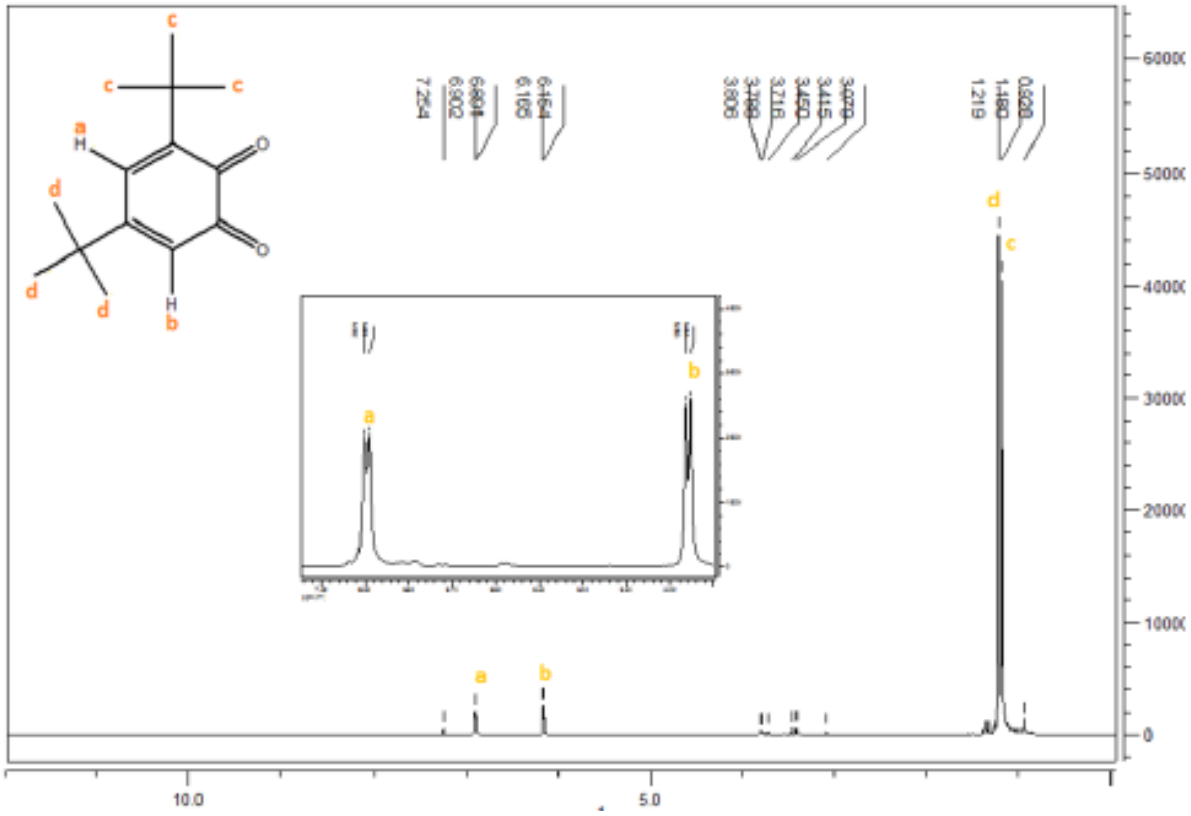
c
c
c
a
H
O
O
d
d
d
H
b
7.254
6.902
6.884
6.164
6.160
3.806
3.788
3.716
3.450
3.415
3.072
1.219
1.180
0.920
a
b
d
c
60000
50000
40000
30000
20000
10000
0
10.0
5.0

Appendix E: Powder XRD patterns

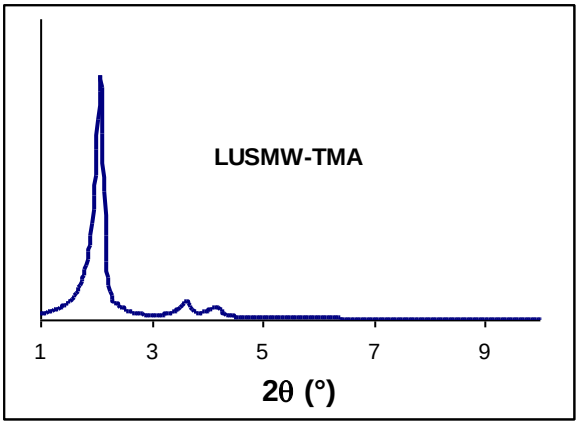

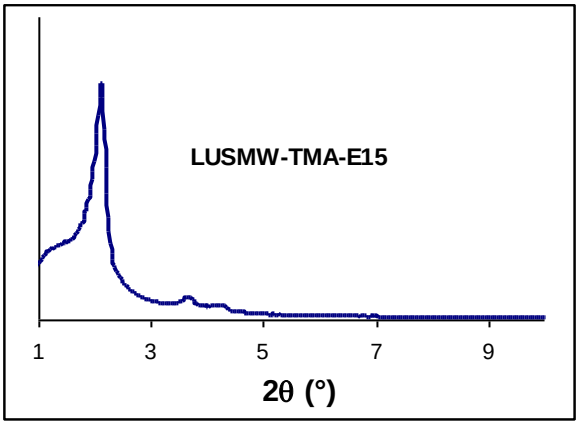

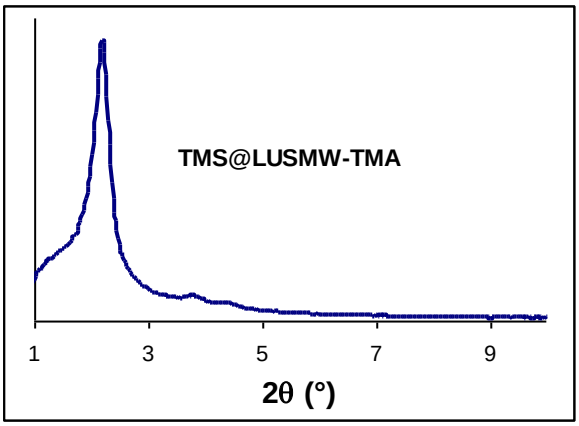

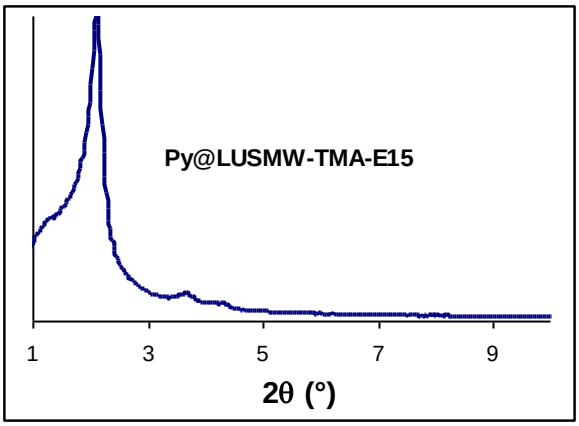

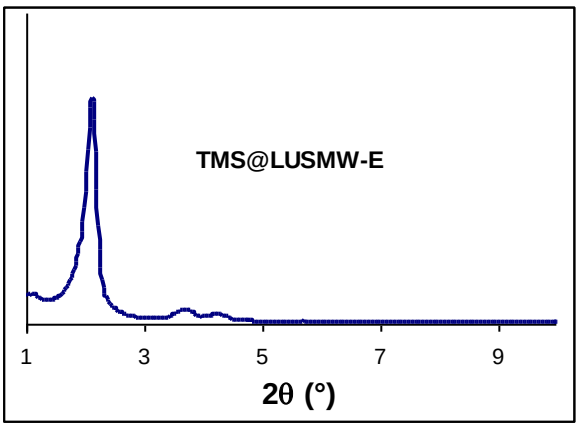

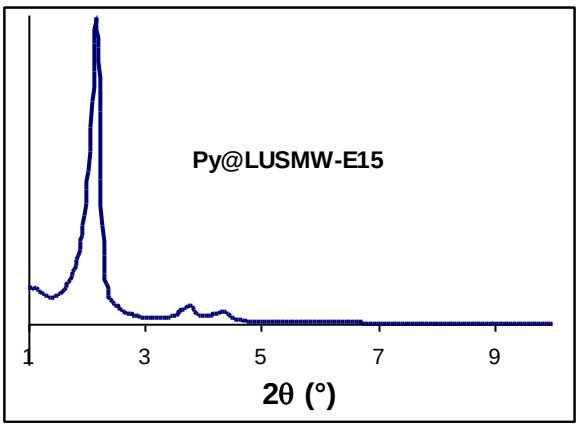

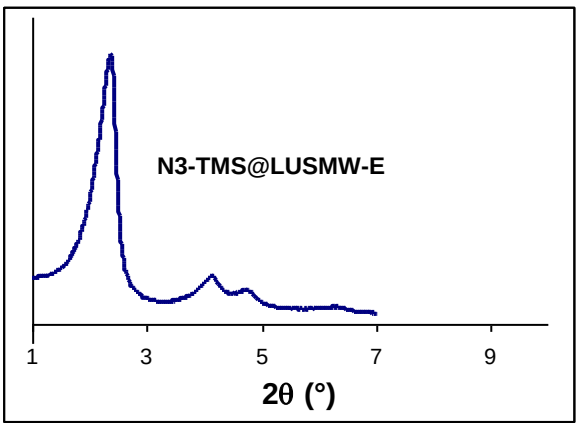

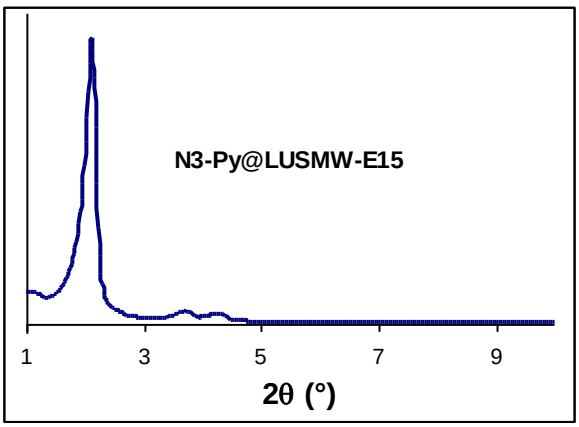

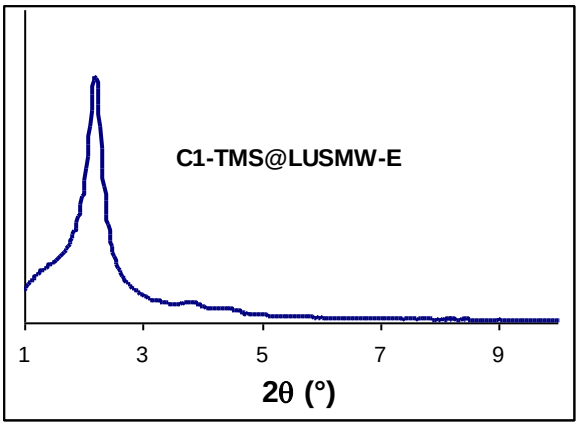
C1-TMS@LUSMW-E
1
3
5
7
9
2θ (°)

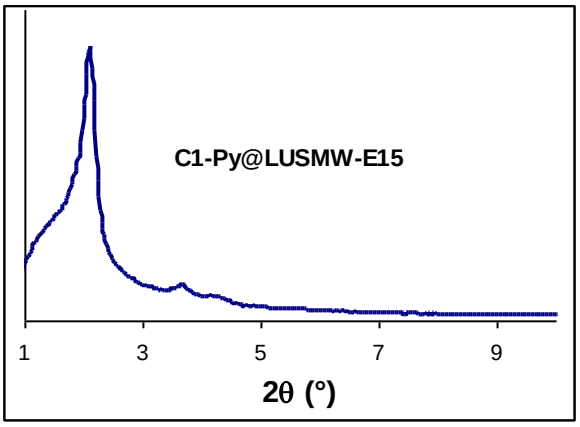
C1-Py@LUSMW-E15
1
3
5
7
9
2θ (°)

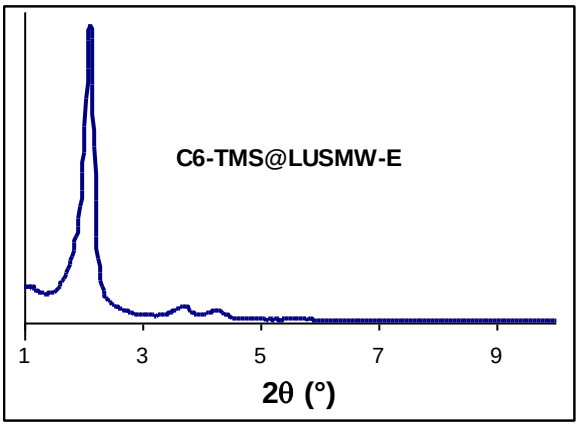
C6-TMS@LUSMW-E
1
3
5
7
9
2θ (°)

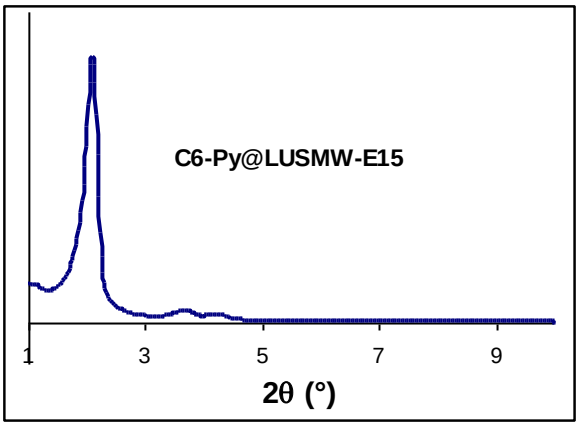
C6-Py@LUSMW-E15
1
3
5
7
9
2θ (°)

Table E1: Values of a_0 and diffraction peak positions for microwave synthesized silicas

Silica	a_0 (Å)	d200/d100	d110/d100	d100	d110	d200
$LUS_{MW}01$	4.72	0.51	0.58	40.84	23.73	20.67
$LUS_{MW}02$	4.58	0.51	0.59	39.70	23.36	20.38
$LUS_{MW}03$	4.76	0.51	0.58	41.21	23.79	20.89
$LUS_{MW}04$	4.41	0.52	0.60	38.19	22.75	19.89
$LUS_{MW}05$	4.72	0.51	0.58	40.84	23.83	20.71
$LUS_{MW}06$	4.55	0.51	0.59	39.42	23.31	20.30
$LUS_{MW}07$	4.71	0.51	0.58	40.77	23.66	20.63
$LUS_{MW}08$	4.40	0.53	0.61	38.08	23.19	20.20
$LUS_{MW}09$	4.69	0.51	0.58	40.60	23.61	20.64
$LUS_{MW}10$	4.79	0.50	0.57	41.50	23.84	20.68
LUS_{H}@130	4.78	0.51	0.58	41.38	24.11	20.95